Detailed population balance modelling of industrial titania synthesis

Astrid Anne Boje

Department of Chemical Engineering & Biotechnology
University of Cambridge

This dissertation is submitted for the degree of
Doctor of Philosophy

Churchill College

November 2019

Declaration

I hereby declare that except where specific reference is made to the work of others, the contents of this dissertation are original and have not been submitted in whole or in part for consideration for any other degree or qualification in this, or any other, university. This dissertation is my own work and contains nothing which is the outcome of work done in collaboration with others, except as specified in the text and acknowledgements.

This dissertation contains approximately 40,000 words, 53 figures and 17 tables. Some of the work in this thesis has been published:

Paper 1
Astrid Boje, Jethro Akroyd, Stephen Sutcliffe, John Edwards and Markus Kraft (2017). Detailed population balance modelling of TiO_2 synthesis in an industrial reactor. *Chemical Engineering Science*, 164:219–231. doi: 10.1016/j.ces.2017.02.019.

Paper 2
Astrid Boje, Jethro Akroyd, and Markus Kraft (2019). A hybrid particle-number and particle model for efficient solution of population balance equations. *Journal of Computational Physics*, 389:189–218. doi: 10.1016/j.jcp.2019.03.033.

Paper 3
Astrid Boje, Jethro Akroyd, Stephen Sutcliffe, and Markus Kraft (2020). Study of industrial titania synthesis using a hybrid particle-number and detailed particle model. *Chemical Engineering Science*, 219:115615. doi: 10.1016/j.ces.2020.115615.

Astrid Anne Boje
November 2019

Detailed population balance modelling of industrial titania synthesis

Astrid Anne Boje

This thesis presents an efficient and robust detailed population balance framework for simulating aerosol synthesis of structured particles using a stochastic method. This is developed in the context of the industrial titania (TiO_2) process to enable extensive numerical characterisation of the pigmentary product.

A reactor network model is used to provide a modular treatment of the reactor and account for key features, including multiple reactant injections, and tubular reaction and cooling zones. This approach simplifies the flow field in order to focus computational effort on resolving particle structure using a high-dimensional particle model and its modularity offers flexibility to investigate different configurations. Initial results are presented using a pre-defined temperature profile in the network, and the particulate product is characterised by its property distributions. Numerical performance is studied, highlighting the high computational cost of simulating strong phase-coupling, fast process rates, and broad particle size distributions.

A novel hybrid particle model is developed to address these challenges. The hybrid particle model employs a univariate description of small particles and switches to a detailed particle model to resolve morphology of more complicated, aggregate particles. New simulation algorithms are presented to manage interactions between particles of each type. The hybrid model is shown to improve efficiency (resolution versus computational cost) and robustness (sensitivity to numerical parameters), while generating the same solutions and convergence behaviour as earlier models.

The reactor model is extended, utilizing the superior numerical performance of the new hybrid particle model to enable inclusion of a system energy balance for more accurate study of a broad range of process conditions, and a more sophisticated particle model to resolve particle geometry. These contributions facilitate the study of particle structure and its sensitivity to reactor design and operational choices, providing insight into how operation affects characteristics of the particles and allowing direct comparison with experimental images of the pigmentary product.

Acknowledgements

I would like to thank my supervisor, Prof. Markus Kraft, for providing guidance during my Ph.D., for conversations that helped me out of the weeds, and for treating me as a peer. I would also like to thank Dr Jethro Akroyd for many useful discussions and for supporting me over the past four years. I am grateful to the members of the CoMo group and of Cambridge CARES for much tea-time levity and many fruitful conversations. Further thanks to Dr Rob Patterson for helping me to understand the theory of stochastic particle systems.

I would like to acknowledge financial support from the National Research Foundation (NRF), Prime Minister's Office, Singapore under its Campus for Research Excellence and Technological Enterprise (CREATE) programme. This funding allowed me to spend two years in Singapore, which was a rewarding experience. I would like to thank Venator for funding me, for providing the opportunity to visit their plant, and for supporting me in publishing and presenting work studying their process. I am grateful to Dr Stephen Sutcliffe, Dr John Edwards and Dr Tony Jones for helpful discussions and advice about my project.

It is challenging to spend half of a Ph.D. on a different continent and I appreciate the support I received with logistics from Mrs Amanda Taylor, Dr Sebastian Mosbach and Dr Jethro Akroyd at CEB, Mrs Rebecca Sawalmeh and Prof. Alex Webb at Churchill College, and Mrs Xiang Ning Leong at Cambridge CARES in Singapore.

This Ph.D. has been a dominant feature of my life for four years and I want to thank the people closest to me for supporting me throughout. To my parents, Ashley and Edward, thank you for sharing my successes and counselling me through my challenges. Thank you for reading drafts of my work and for your encouragement over the past four years, as in all of my life. To my siblings, Alexa, Oliver and Dave, thank you for your support and friendship.

Finally, to JP, without whom I could not have reached this point. Thank you for your companionship, your endless support and patience, and all of your help reading and listening to my work. I am so fortunate that you are my partner in life.

Table of contents

List of figures

List of tables

Chapter 1

Introduction

1.1 Motivation

Particulate matter is ubiquitous across modern society and the natural world, arising in aerosol [76, 115], crystallization [128], combustion [157], atmospheric [26, 28] and astrophysical [14, 84] processes. Particle size, morphology and composition are determined by process conditions. As these characteristics govern system-specific properties such as pigment opacity, photocatalytic propensity and respiratory toxicity, it is critical to understand formation and growth dynamics for process design and control. This requires consideration of complex interactions between chemistry, heat transfer, fluid dynamics and particle structure [18, 126]. Particles are frequently multicomponent, non-spherical or fractal-like. The structured titania particle in Fig. 1.1 is typical of an aerosol product [18].

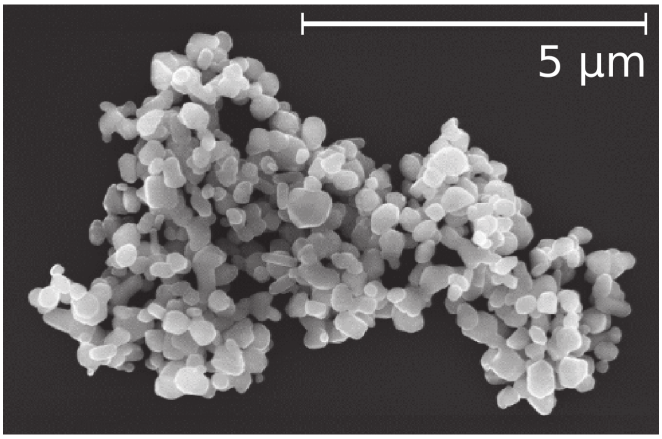

Fig. 1.1: Scanning electron microscopy (SEM) image of a titania particle aggregate (image courtesy of, and with permission from, Venator).

Population balance modelling is a versatile, widely-used numerical tool for investigating particle synthesis and a necessary complement to experiment to develop process understanding. Moment-based [40, 85, 88], sectional [53, 68, 152] and stochastic [2, 21, 63, 83, 121] methods have been applied to solve the formation and growth dynamics. Each method has inherent advantages and disadvantages in terms of computational complexity, resolution of particle properties and closure of the governing equations. Stochastic (Monte Carlo) methods are attractive for simulating non-spherical particle systems given their ability to accommodate detailed particle models with thousands of internal coordinates.

Detailed models describe an aggregate particle by the list of its primary particles, each defined by composition, and their connectivity. Connectivity can be described by combined surface area and extent of cohesion [133] or by relative position of primary particles and their degree of overlap [81]. These models can thus resolve features that determine end-product quality, and have been used with coupled gas phase and stochastic population balance solvers to study combustion synthesis of soot [22, 52, 134, 172], silicon [101], silica [133, 140, 141] and titania [81, 160]. Such simulations are computationally expensive and cost scales with increasing process rates – more stochastic events must be performed at higher rates, and resolution of broad particle size distributions requires a large ensemble of computational particles. Techniques to enhance efficiency [120] are of ongoing importance.

Pigmentary titania (TiO_2, titanium dioxide) is a multi-million ton per annum commodity product with properties that are sensitive to synthesis conditions. Industrial titania synthesis is a salient example of an aerosol process that is challenging to study due to process conditions including temperatures above 1000 K, residence times under a second and a hazardous chlorine environment. Non-spherical, chemically bonded aggregate particles (Fig. 1.1) form from collision and adherence of particles followed by high-temperature sintering [50, 122]. Structure affects particle growth and, critically, has implications for refractive properties and size consistency of the end-product. Post-process cooling and energy-intensive milling steps are required to control important particle characteristics [8].

Detailed particle modelling would be beneficial to inform understanding of developed particle structure under a wide range of process design and operating conditions. Challenges to detailed modelling include multi-injection reactor geometry, sharp temperature gradients, high precursor concentrations with significant mass conversion (high process rates), strong phase coupling and broad, non-spherical particle size distributions.

The **objective of this thesis** is to develop a framework that enables simulation of particle synthesis using detailed population balance models. This framework should address challenges posed by complex reactor geometry, high simulation cost, and sensitivity to numerical parameters (lack of robustness). This thesis seeks to overcome numerical difficulties when the stochastic algorithm is applied to the study of industrial titania synthesis, and to propose a new reactor model that is capable of providing insights about particle size and morphology under relevant industrial conditions, and flexible to changes in reactor configuration.

1.2 Novel aspects of the thesis

This thesis presents the following **novel developments**:

- It demonstrates the ability to simulate a multi-injection industrial titania reactor, with detailed models for particle structure and gas phase chemistry, using a network of ideal reactors to approximate key features of the flow field and a stochastic numerical method to simulate the dynamics of physical particle formation and growth. Numerical performance is investigated for the reactor network with industrially relevant conditions and insights are used to identify computational challenges.
- It addresses these challenges by developing a new hybrid particle model for population balance simulations. The hybrid particle model tracks simple and complex particles separately using particle-number and detailed particle models respectively. An adapted Monte Carlo method is derived by adding suitable algorithms to treat interactions between particles described by each model. The new model is shown to be exact in the sense that it generates the same solutions as existing particle models. It improves efficiency and reduces sensitivity to choice of numerical parameters, enabling resolution of particle structure in the presence of high process rates and broad particle size distributions.
- It extends the reactor model, exploiting performance gains from the hybrid particle model to provide better resolution of particle structure and more flexibility in exploring the process design space. The quasi steady state system energy balance is modelled for gas and solid (particle) phases, and heat release from particle processes is added to the operator splitting algorithm for the first time. This energy balance detail is critical for studying the industrial process where temperature and control of exothermic behaviour by reactant injections are important considerations, and where the particle mass fraction is not negligible. A more sophisticated particle model is used to capture particle geometry, allowing industrially relevant characterisation of product structure.

1.3 Structure of the thesis

The remainder of this thesis is structured as follows. Chapter 2 provides background on titania synthesis, popular particle models and numerical methods for solving the population balance equation.

Chapter 3 describes existing modelling tools that are used in this work, including details about the particle models, the gas phase mechanism and particle processes, and the stochastic numerical algorithm.

Chapter 4 presents a first model for an industrial-scale, multi-injection titania reactor using a network of ideal reactors to simplify treatment of the flow field and an imposed temperature profile in line with insights from industry. Development of particle structure is described and a parameter study is used to provide initial assessment of process conditions. The statistical error, numerical convergence and solver time are investigated to characterise computational performance.

Chapter 5 develops a novel hybrid particle model with separate descriptions for simple and complex particles. New algorithms are presented to use the hybrid particle model with a stochastic method. These include particle selection, surface growth, and an adapted waiting time algorithm to choose and perform discrete events. The new approach is demonstrated to agree with the conventional particle model using a convergence study and comparing particle size distributions. Improvements in robustness and efficiency are highlighted and performance is benchmarked for different process rate regimes.

Chapter 6 returns to modelling an industrial titania reactor, using performance gains of the newly developed hybrid model to enable model extensions. An energy balance is incorporated to allow more flexible study of different process design choices and a more complicated, overlapping-spheres particle model is used to resolve aggregate structure. Particle property distributions are assessed in detail and simulated particle structures are compared visually with a real aggregate particle. Robustness of the new model in simulating the industrial system is illustrated in terms of transient ensemble loading in each ideal reactor.

Chapter 7 presents conclusions and provides recommendations for future work in the areas of model extensions, method developments and new applications. A table of nomenclature can be found after Chapter 7. This is followed by a list of definitions for words used in this thesis. Appendices A–C contain algorithms, mathematical expressions and tables respectively.

Chapter 2

Background

This thesis will develop population balance modelling tools for studying industrial aerosol synthesis. These are used to investigate formation of particulate titanium dioxide via the chloride process. In this chapter, the importance of titanium dioxide as an inorganic chemical is highlighted and key features of the synthesis process are provided. Although it is a mature technology, process design remains a challenging problem due to the complex relationship between the operating environment, the product structure and the product quality. This chapter discusses existing studies, both experimental and numerical, that have been conducted to aid process understanding. The approach developed in this thesis concerns population balance modelling with a detailed particle model and a stochastic numerical method, and this modelling framework is contextualised by presenting an overview of different particle models and popular numerical methods. The specific tools and theory developed in previous work and used in this thesis are presented in more detail in Chapter 3.

2.1 Titanium dioxide

Titanium dioxide (TiO_2, titania) is a white powder that is used ubiquitously in pigments, as well as in ceramics and catalysts. Its importance as a pigment stems from its strong light scattering properties, its chemical stability and its non-toxicity [8]. Light scattering imparts product whiteness, brightness and opacity. It results from a high refractive index and diffraction – features that are influenced by the crystal phase and range of particle sizes [29]. Coatings (such as paints, lacquers and primers) are the predominant pigmentary application (ca. 60 %), followed by plastics (ca. 24 %) and paper (ca. 8 %) [8]. Titania catalysts are used to remove nitrogen oxides in exhaust gas of power stations, incinerators and diesel engines [75, 125] and titania photocatalysts have been developed to aid water and air purification [72, 97, 163]. Crystal phase and particle size are critical to determining catalytic behaviour.

Titania occurs in three main crystal phases: rutile, anatase and brookite, but rutile and anatase dominate commercial interest for applications such as pigments and catalysis respectively. Auer et al. [8] describe titania as one of the "Top 5" inorganic chemicals, with global sales above $\$12 \times 10^9$ in 2007 and an upward trend in production capacity, already in the order of millions of tons per annum (Fig. 2.1). Industrial titania synthesis is the second largest industrial aerosol process by value and volume after carbon black production [50]. Synthesis occurs via two processes, both of which are well-established industrial technologies.

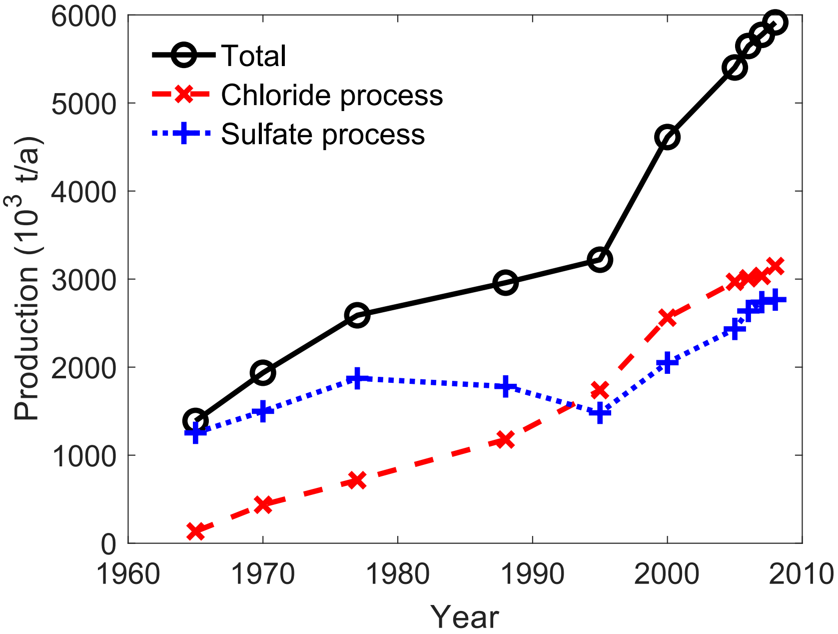

Fig. 2.1: Global production (pre-2000) and production capacity (2000–) of titanium dioxide by the chloride and sulfate processes (based on data from Auer et al. [8]).

2.1.1 Synthesis process

The sulfate process (Fig. 2.1, dotted line) is an older route that uses concentrated sulfuric acid to dissolve titanium from a titanium-containing raw material. This process is used to produce printer ink because it creates less abrasive particles, and for (anatase) catalyst preparation [8]. The chloride process reacts chlorine with a titanium-containing raw material. Its importance can be inferred from the trend in increasing global production values since the mid-1960s (Fig. 2.1, dashed line). The chloride process is popular for pigment synthesis because it yields a (rutile) particle product with better optical properties and durability, and has lower environmental impact [8]. As this thesis considers the industrial production of pigmentary titania via the chloride process, this route will be described further here (with reference to steps labelled in Fig. 2.2).

The chloride process proceeds via (a) chlorination of titanium-containing raw material to form titanium tetrachloride ($TiCl_4$) in the presence of excess oxygen and a carbon reducing agent. This high temperature (ca. 1273 K) step is followed by (b) quenching with liquid $TiCl_4$ and (c) two-stage purification with evaporation to remove chlorides and dissolved chlorine, and reduction and evaporation to remove vanadium tetrachlorides and oxychlorides. The subsequent step (d) is the oxidation of $TiCl_4$ in either a flame, or by stage-wise addition to a plasma [4, 42]. The oxygen and $TiCl_4$ streams are preheated – $TiCl_4$ to 773 K–1273 K and O_2 to above 1273 K – and introduced to the reactor separately (1) with a 110 %–150 % stoichiometric excess of oxygen [8]. The TiO_2-forming reaction has the overall stoichiometry:

$$\mathrm{TiCl_4} + \mathrm{O_2} \rightarrow \mathrm{TiO_{2(particles)}} + 2\mathrm{Cl_2}. \tag{2.1}$$

The oxidation reaction is exothermic and the reactor operates at temperatures in the range 1173 K–1673 K [8]. To prevent excessive particle growth, the products are cooled rapidly (2). These steps are critical to establishing characteristics of the final particle size distribution, and aggressive conditions combined with short residence times make studying the process dynamics very challenging. Further cooling (e) is followed by (f) another separation step to remove and recycle the chlorine formed as a by-product in the oxidation reaction. This is either redistributed to the chlorinator, or used to aid cooling in the reactor. Pigment particles undergo several further steps, including (g) coating to improve durability and enhance binder dispersion, and (h) post-process washing, drying and milling to achieve suitable particle sizes for the end-product.

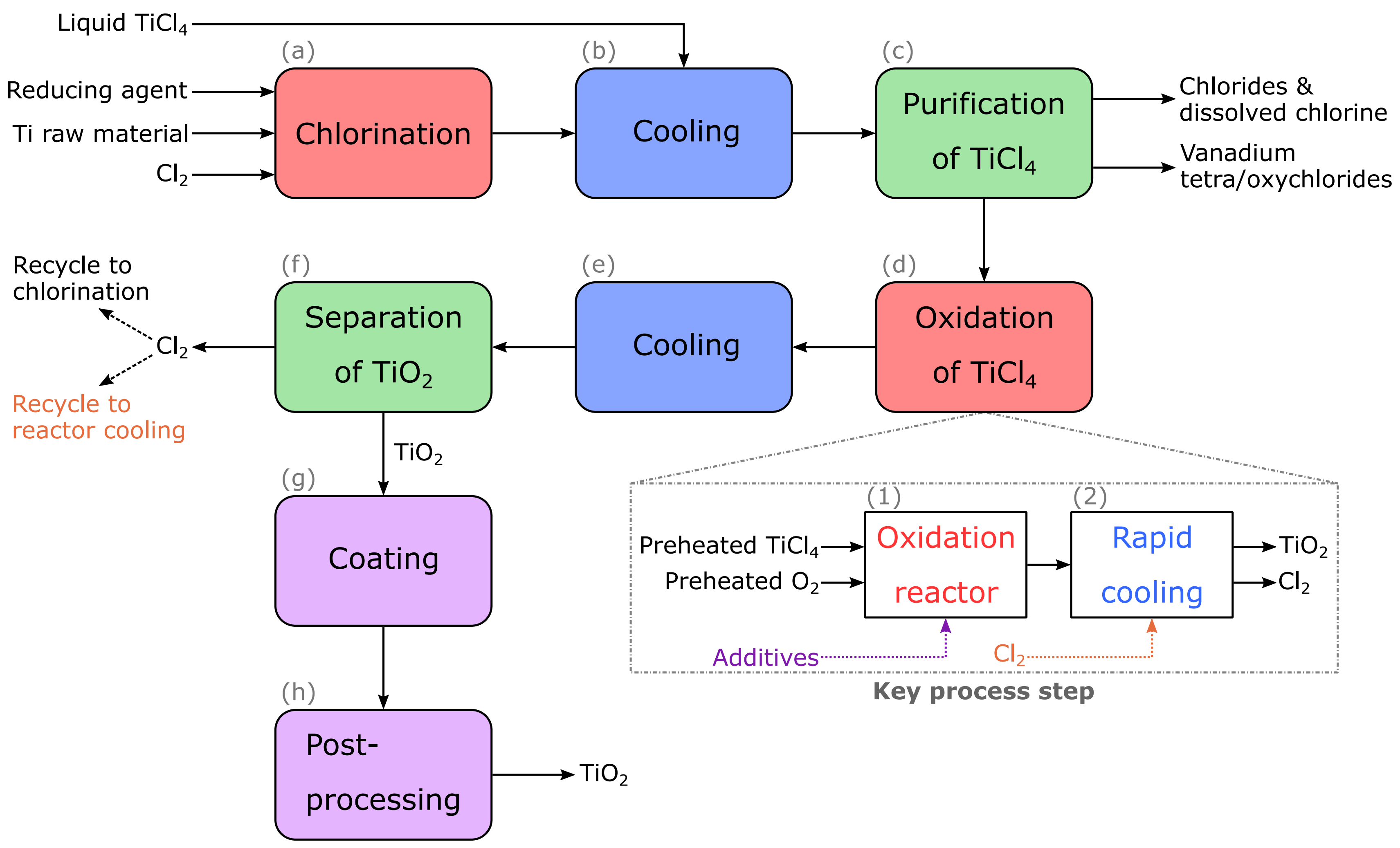

Fig. 2.2: Steps in the chloride process for production of titanium dioxide (TiO_2) pigmentary particles starting from formation of titanium tetrachloride ($TiCl_4$) by chlorination of raw titanium-containing material with chlorine (Cl_2) (stages as in Auer et al. [8]).

2.1.2 Design considerations

The optical properties of titania are determined by particle size and morphology, for example tint depends on the particle size distribution (PSD), and the crystal phase determines the magnitude of the refractive index and the photocatalytic nature of the product [24, 57, 160]. Milling is required as a post-process in the industrial synthesis in order to achieve a suitable PSD for light scattering (optimally 0.2 µm [8]). Milling has a significant impact on the energy cost of the product; thus, ease of milling is an important consideration [25, 47]. The rapid cooling employed to quench the system after reaction completion helps to prevent excessive particle growth and reduce milling requirements [50].

Many factors influence the size and morphology of the particles, including the gas phase reaction rates, particle process dynamics, operating conditions, reactor configuration, type of plasma-forming gas, and use of chemical additives. Park and Park [115] discuss the role of these different factors and summarise the difficulties inherent in understanding and controlling the synthesis process. Additives, e.g. $AlCl_3$ and $SiCl_4$, act to promote/inhibit anatase-to-rutile phase transformation and reduce/enhance surface area [122]. As noted by Auer et al. [8], the many patents for TiO_2 synthesis [25, 47, 107] indicate the complexity of this process and the degree of attention it has received. In particular, the oxidation step (d) offers many design choices and parameters for optimisation including mixing strategies, choice of additives and cooling scheme. Thus, this is the “key process step” [8]. Collision and sintering processes that occur in this step directly affect the milling energy requirements to achieve a suitable product size distribution.

Reactors for industrial titania synthesis have multiple feed points, with independently controlled feed rates and pre-heat temperatures [160]. Operating conditions such as temperature ranges around 1000 K–1500 K, pressures of up to 4.5 bar (absolute) and residence times in the millisecond-range limit industrially relevant studies; thus most published experimental work is under milder laboratory-scale and flame synthesis conditions. Even then, high temperatures and short process times confound sample collection and characterisation [122].

2.1.3 Experimental studies

Experimental studies on TiO_2 formation were tabulated by Pratsinis [122] and Park and Park [115]. These include premixed and diffusion flames as well as hot wall reactors, with $TiCl_4$ and titanium tetraisopropoxide (TTIP) precursors. Heating in flame experiments is provided by combustion of the reactants directly, while hot wall reactors control the temperature using an external heat element. As highlighted by Pratsinis [122], early studies considered TiO_2 particle growth in flames and suggested different dominant processes. Examples from the 1970s include work by George et al. [44] that found coagulation to be the dominant process in determining particle size distributions, and work by Formenti et al. [37], who investigated the photocatalytic nature of TiO_2. Vemury and Pratsinis [155] characterised the effect of additives on particle size and crystal phase, demonstrating how dopants can be used to control product character. Flame studies have continued over the last twenty years [41, 51, 87, 154]. For example, Manuputty et al. [86] characterised polymorphism of titania in a stagnation flame – in addition to the common anatase, rutile and brookite phases, a metastable phase named TiO_2-II was observed.

Two important studies include the thin film experiment of Ghoshtagore [45] and the hot wall reactor of Pratsinis et al. [124]. These provided valuable insights into the kinetics of surface growth and the overall oxidation reaction. Thin film experiments study the deposition of layers of titania crystals onto specially prepared silicon wafers and can be used to study the dynamics of particle formation from gas phase processes. A first-order rate expression was proposed for surface growth at temperatures in the range 673 K–1123 K [45]. The oxidation reaction was found to be first-order in $TiCl_4$ and independent of oxygen up to a ten-fold excess at temperatures in the range 973 K–1273 K [124]. The kinetics and experimental data from these studies have been widely used for parameter fitting and modelling studies [103, 123, 147, 161] including recent work [4, 78]. Despite this, West et al. [161] reasonably advise caution when using the kinetic expressions at temperatures beyond the ranges covered by the original experiments (e.g. the higher temperatures relevant to the industrial process).

Nakaso et al. [109] used a hot wall reactor to investigate development of particle size and morphology for a range of temperatures (873 K–1473 K) for both TTIP and $TiCl_4$ precursors. They presented a clear set of transmission electron microscopy (TEM) images showing changes in morphology with temperature and primary particle sizes are extracted from these for analysis. Interestingly, the results suggest that there is a mid-range temperature for which primary particle size is minimized and that temperature does not have a substantial differential effect on particle size above 1273 K.

Kartaev et al. [57] investigated laboratory-scale synthesis in different plasmas, calling attention to the dependence of the growth processes on plasma composition, precursor flow rate, quench gas, reactor length and reactor temperature. These design choices control crystal phase and particle size. Their study is notable for features that are similar to the industrial process, including radial injection of precursor into a hot gas stream (at relevant conditions), a working zone for reactions to be completed and a cooling zone to quench the product.

The industrial process operates at high precursor concentrations in near-stoichiometric proportion to the oxygen and achieves full precursor conversion under high production rates

[50]. The rates of the particle growth processes are significantly different under industrial conditions. Modelling studies by Pratsinis and Spicer [123] and Morgan et al. [103] found substantially increased surface growth rates at high $TiCl_4$ concentrations. In the absence of published experimental data for the industrial synthesis of titanium dioxide, it is useful to compare the available literature to numerical studies under the high temperatures, pressures and precursor concentration used in the industrial process. In addition to allowing direct study of particulate properties, for example by imaging, such studies provide a means of testing and building numerical models [1, 79, 137] which allows for rapid investigation of process conditions that are expensive or challenging to realize experimentally.

2.1.4 Modelling studies

Many numerical studies of titania synthesis have been presented. Factors such as high temperatures and rates, multiple phases and complex flow fields challenge modelling efforts in the same way as they frustrate experimental studies. It is currently challenging-to-intractable to address all issues simultaneously. Kraft [64] lists pertinent examples of titania modelling studies, in addition to examples for other particulate syntheses, up to the early 2000s, highlighting features such as reactor type, particle model dimensionality and method. Differentiating features of common numerical methods are discussed further in Section 2.2.

Several modelling studies have been presented for TiO_2 formation in a plug flow reactor (PFR) using different numerical methods [64]. These include one- and two-dimensional sectional methods with and without gas phase coupling [108, 152] (as well as the earlier work of Xiong and Pratsinis [166, 167]); a one-dimensional, uncoupled finite element method [5]; and a one-dimensional, uncoupled weighted stochastic method [103]. Comparison to the experimental systems is qualitative [168], although the two-dimensional sectional model of Nakaso et al. [108] could also differentiate between different precursors ($TiCl_4$ vs. TTIP). The principal drawback of this approach was a long run time (3 h–11 h) – by comparison, the one-dimensional version employed by Tsantilis and Pratsinis [152] for TTIP may have been quite far off at predicting experimental results, but the authors showed that it was not much worse than more complex models and was considerably cheaper (under 1 h). Likewise, Mühlenweg et al. [106] compared one- and two-dimensional sectional methods for coupling titania studies with fluid dynamics and found that the two-dimensional method was infeasible, requiring an incredible 112 days to run on a 300 MHz alpha workstation in 2002 [161].

Spicer et al. [147] used a moving sectional method to study the competition between the surface and gas phase oxidation pathways for titania synthesis. The surface reaction was shown to be dominant for high precursor concentrations. Comparison with a monodisperse model identified low temperature and low precursor concentration as regions with the biggest discrepancies. Monodisperse models are widely used in theoretical studies [62, 65, 123, 147]. Heine and Pratsinis [50] used a monodisperse model with global kinetics to study titania synthesis under industrially relevant conditions via oxidation, and under more dilute conditions via hydrolysis. A fractal relationship was used to account for aggregate size in the coagulation dynamics. An almost-stoichiometric mixture of $TiCl_4$ and O_2, heated to 2000 K, was used to model the industrial process, and post-reactor cooling of $2700\,\mathrm{K\,s^{-1}}$ was applied to achieve a linear temperature decrease. The authors highlighted the importance of particle contributions to gas phase properties under industrially relevant conditions, where complete conversion yields solid (particle) mass of 34 % by weight of the initial gas mass.

Researchers initially used global chemical kinetics, typically [103, 166, 167] first-order in $TiCl_4$ for TiO_2 formation, based on observations from experimental work [45, 124]. A thermodynamically consistent detailed kinetic mechanism was proposed by West et al. [160, 161, 162] for the oxidation of $TiCl_4$ via titanium oxychloride intermediates. The authors believed that the global approach was insufficient to assess temperature and concentration dependencies or the influence of additives on the chemical reactions. They quantified the mechanism with thermochemical data from density functional theory (DFT) investigations and further extended it using kinetic information from variational transition state theory (VTST) and DFT to propose new rate expressions, stable intermediate species and elementary reactions. Modifications have subsequently been suggested including further reactions and improved thermodynamic data [16, 17, 114]. Shirley et al. [143] used DFT to study $TiCl_4$ adsorption on the surface of TiO_2 and proposed a mechanism for the surface chemistry and Shirley et al. [142] used DFT to supplement the detailed kinetics with an $AlCl_3$ mechanism to describe additive chemistry.

A key study providing foundations for this thesis work is that of West et al. [161], which is the first holistic model of the industrial titania process to couple detailed gas phase and surface chemistry with multidimensional population balance modelling. The authors combined their previously-introduced reaction mechanism with a stochastic solver for the particle phase to provide a comprehensive description of titania formation and growth in the chloride process. They also extended the particle model to include primary particle sizes (a multidimensional particle model). An extensive model for inception was proposed using collision theory and considering titanium oxychloride species as precursors. Surface growth was assumed to be first-order with Arrhenius parameters from Ghoshtagore [45] and the hot wall experiment of Pratsinis et al. [124] was simulated as a test case; however, no comment was provided on level of agreement with the original data. More industrially representative conditions were also considered (1500 K, 3 bar, equimolar reactant mixture), and found to produce particles much smaller than the industrial size. However, it was noted that the kinetic model was incomplete and had not been fitted to experimental data. In later work [162], the authors returned to the Pratsinis experiment and fitted surface kinetic parameters; however, the resulting simulations were unable to match the experiment, with as much as four orders of magnitude disagreement between the first-order rates fitted to the experimental and simulation data respectively.

While some researchers have focussed on tackling the gas phase and particle kinetics, others have worked towards addressing the flow. Computational fluid dynamics (CFD) simulations have been used to model the flow fields in titania synthesis in laboratory-scale plasma-chemical reactors [57, 58], flame reactors [95, 171] and an industrially representative slot reactor [4]. The non-ideal flow patterns observed in the reactor cases suggest that treatment of flow is an important consideration for a model of the industrial system. For example, Kartaev et al. [58] showed mixing in a recirculation zone induced by the injection of quench gas by eight perpendicular jets into the main stream and global first-order kinetics with three species, while Akroyd et al. [4] illustrated circulation in the velocity field near the reactant injection site, with axial flow in the direction of the main stream further downstream, using detailed kinetics and thirty species.

The computational cost of solving the flow with CFD limits the complexity of the chemistry and particle models that can be used. Unfortunately, these detailed descriptions are suggested [96] to be necessary to describe experimentally-observed behaviour in TiO_2 flame synthesis. Mehta et al. [95, 96] utilized an idealized reactor modelling framework to simplify the treatment of turbulent reacting flows so that an acceptable level of detail could be obtained in the chemistry and particle models, allowing description of trends in flame aerosol synthesis. To date, this approach has not been used to incorporate detailed particle models for titania.

2.2 Population balance framework

The description of the particle phase is crucial to studying the relationship between the synthesis process and the product properties. The most general way to describe the evolution of a particle system through time and space is by its population balance equation (PBE), also sometimes called the general dynamic equation (GDE). The PBE is an integro-partial differential equation that accounts for state-space changes to the particle system.

The particle state-space refers to the mathematical description of possible particle properties (coordinates). The particle state-space can include external coordinates, ω, specifying physical locations in a domain Ω and internal coordinates, x, specifying “quantitative characteristics of distinguishing traits” [127], i.e. particle types such as mass, surface area, chemical composition and structure. The mathematical description of possible particle types is called the type-space, $\mathcal{E}$. As demonstrated by the preceding examples, the type-space can include both continuous and discrete coordinates.

The particle state-space is characterized by its number density, which maps from possible particle states to the quantity of particles of this state in the given system. That is, for a given particle of type $x \in \mathcal{E}$, at position $\omega \in \Omega$, the number density (concentration) of particles is $n(x,\omega) : (x,\omega) \mapsto \mathbb{R}_0^+$. In general terms, the number density of particles of a given state evolves due to convective, birth and death processes, i.e. the PBE describes:

$$\begin{matrix}\text{state number} \\ \text{density change}\end{matrix} + \begin{matrix}\text{type-space} \\ \text{convection}\end{matrix} + \begin{matrix}\text{physical} \\ \text{convection}\end{matrix} = \begin{matrix}\text{birth} \\ \text{processes}\end{matrix} - \begin{matrix}\text{death} \\ \text{processes.}\end{matrix}$$

Type-space convection, e.g. particle growth, changes the particle type but does not alter the overall particle count. Birth and death processes include particle inception and aggregation – particles of a specific state are created by aggregation of smaller particles and destroyed by aggregation to form larger ones. Aggregation is a nonlinear functional of the number density and requires consideration of (i.e. summation/integration over) different particle states [127]. The particle system is typically dispersed within another environment; thus, the PBE is frequently coupled to conservation equations for this continuous phase. Particle inception is independent of the number density but may depend on the continuous phase (e.g. particles formed by collision of gas phase precursor species).

For the processes discussed above, which will be relevant to this thesis work, the PBE takes the general form [126]

$$\begin{aligned}\frac{\partial n}{\partial t} + \underbrace{\frac{\partial}{\partial x} \cdot \left[S_x(x,\mathbf{C},T)\,n\right]}_{\mathcal{S}} + \underbrace{\frac{\partial}{\partial \omega} \cdot \left[u_\mathrm{p}(x,\mathbf{C},T)\,n - D_\mathrm{p}(x,\mathbf{C},T)\,\frac{\partial n}{\partial \omega}\right]}_{\mathcal{F}_\mathrm{p}} \\ = \underbrace{\int_{\mathcal{E}} K(x-y,y,T)\,n(x-y)\,n(y)\,dy - \int_{\mathcal{E}} K(x,y,T)\,n(x)\,n(y)\,dy}_{\mathcal{K}} \\ + \underbrace{I(x,\mathbf{C},T)}_{\mathcal{I}},\end{aligned} \tag{2.2}$$

where $\mathcal{S}$ is the growth term, defined by growth rate S_x which may be a function of the gas phase environment, $\mathbf{C}$, and temperature, T; $\mathcal{F}_\mathrm{p}$ is the flow term, including particle velocity, u_p, and diffusion, D_p; $\mathcal{K}$ is particle aggregation, defined by the coagulation kernel K; and $\mathcal{I}$ is particle inception, defined by the inception rate I. The particle velocity is defined as the sum of the gas phase velocity and the themophoretic movement of the particle due to the spatial temperature gradient. The PBE will be revisited in Chapter 3, where the precise form used in this thesis will be provided along with models for the titania-specific processes.

The PBE is specified by defining rates for the convective, birth and death processes, an initial condition for the distribution of particles across the state-space at time zero, and boundary conditions at the physical boundaries (the PBE is typically hyperbolic because of the advective terms). The framework for modelling such a system requires three principal components: (i) a model for the particle type-space (Fig. 2.3); (ii) a mechanism for the particle processes that is consistent with the choice of type-space; and (iii) an analytical solution to, or a numerical method for solving, the population balance equation formulated in terms of relevant particle processes for particles of types described by the particle model.

2.2.1 Particle models

The real particle type-space is typically high-dimensional, with each particle characterised by up to thousands of internal coordinates which correspond to the diversity of morphologies and surface chemistries that can be formed [64]. Type-space models of varying complexity have been used to provide a numerical description of the particles (Fig. 2.3).

The simplest type-space model is a coalescent sphere or spherical particle model (Fig. 2.3, left), which represents particles as spheres of constant composition and density; thus only a one-dimensional type-space is required. This assumes that lasting collision (i.e. coagulation) events are followed by instantaneous coalescence to a larger spherical particle [40, 123]. More detail is incorporated into surface area and volume models (Fig. 2.3, centre), where these properties are added for coagulating particles [65, 167]. This allows more structural information to be tracked; however, these models require adaptations to deal with processes such as surface reaction and sintering. Particles are assumed to have a fractal-like structure that can be defined in terms of the tracked variables and this is used to describe their geometry for surface processes.

The most detailed particle models are primary particle models (Fig. 2.3, right). These resolve the connectivity of ‘primary particles’ (particles formed by inception) following coagulation events and describe particle structure e.g. combined surface area and centre-to-centre distance between particles [78]. Detailed particle models have been shown to provide important additional information when the particle system is polydisperse (composed of non-uniform particles) or the coagulation and sintering timescales are similar [98]. Lindberg et al. [81] presented an overlapping-spheres, primary coordinate-tracking particle model which provides further resolution in the particle type-space and eliminates assumptions on fractal dimension in calculating particle collision rates. This level of detail naturally poses additional challenges to the modelling framework, but it is essential for understanding the coupling between process design choices and (experimentally) observable particle properties.

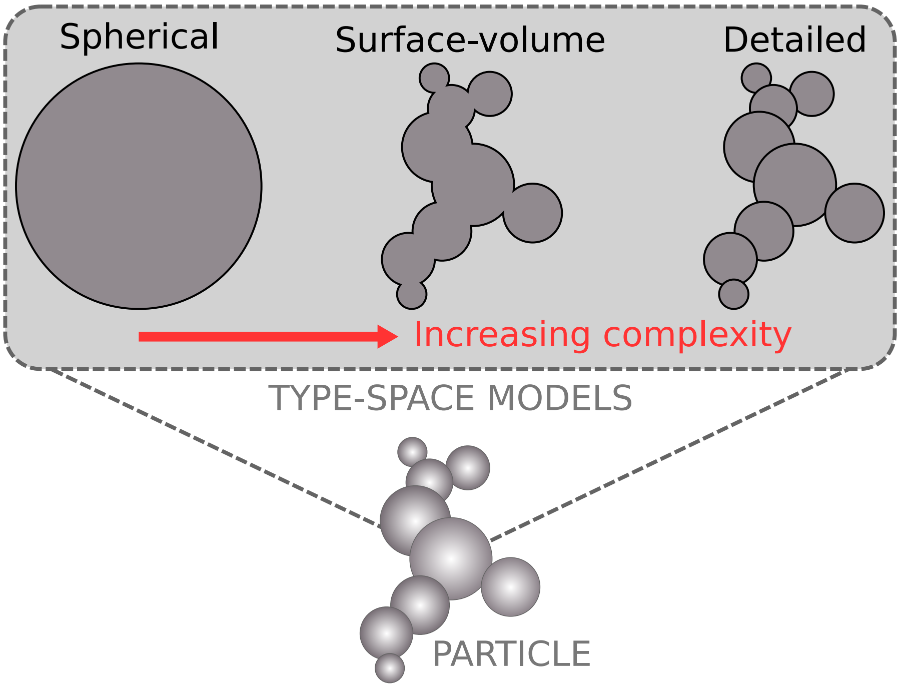

Fig. 2.3: Particle type-space models of varying complexity

2.2.2 Numerical methods

This section considers numerical methods for solving the homogeneous PBE. Transport will be discussed in Section 2.2.3. Analytical and perturbative solutions are available for simple problems and these can be used as benchmark cases to validate numerical methods [130]. The complexity of real systems precludes analytical solutions; thus numerical methods must be developed.

Direct approaches such as Laplace transforms can be applied to simple, linear problems [127]. Stadnichuk et al. [148] and Smith et al. [145] describe iterative schemes for efficient steady state solutions. Another numerical technique employs low-rank, separable approximations to the coagulation and fragmentation kernel matrices to reduce computational cost and memory requirements by speeding up matrix-vector operations and increasing matrix sparsity [61].

Simple models can be developed by assuming that the particle system is monodisperse [65]. Expressions for the overall particle number density, surface area and volume can be formulated with terms for inception, coagulation, and sintering accommodated by assuming a fixed primary particle size and (fractal) relationship between the primary particle and aggregate particle sizes. The limitation of this approach is that it cannot describe polydisperse particle systems and imposes restrictions on particle structure. However, it is computationally efficient and consequently is typically used with CFD simulations [56, 106, 135].

Several classes of integral, discretization-based and stochastic methods are widely used [127]. In all cases, numerical solution of the PBE becomes more challenging with increasing type-space dimensionality.

Moment methods

The method of moments (MOM) approach solves for finitely many moments of the number density function. A moment transport equation is formulated by multiplying the PBE by k^{th} powers of a property, ξ, (e.g. mass, diameter, etc.) and integrating over the type-space [127], converting it to an equation in terms of the k^{th} moments,

$$M_k = \int_{\mathcal{E}} \xi\,(x)^k n\,(x)\,dx.$$

Moment methods typically solve for the first few moments, including the number and mass density (M_0, M_1). This approach is computationally efficient and stable [105], but truncation of the infinite moment series prevents exact reconstruction of the number density function [126]. This introduces closure problems for coagulation kernels involving fractional or negative moments and processes requiring the point-wise particle concentrations (e.g. shrinkage). ‘Closure’ in this context refers to having all of the information necessary to solve an equation without approximations or coupling to unknown variables. Moment methods experience closure problems when the equation for a given moment depends on higher-order or fractional moments that are not known because the method tracks only the first few moments, or when information is required about a specific particle type because the point-wise values of the particle size distribution are unknown. Closure problems are typically treated by modelling the missing information.

Closure issues have been treated by polynomial approximation, the method of moments with interpolative closure (MOMIC) [4, 39, 40, 85] and Gaussian quadrature (QMOM) – parametrizing the unknown distribution with weights and abscissas that can then be used to compute the moments [89, 93]. The direct quadrature version (DQMOM) [3, 88] avoids expensive matrix inversion by direct solution for the quadrature parameters [130]. It can provide more accurate solutions for multi-modal distributions, and in particular this allows resolution of a nucleating mode in problems where this is important [105]. The moment projection method has been proposed to handle shrinkage problems by specifically tracking the number of particles at the smallest size [164].

In addition to potential closure issues for realistic particle dynamics, an important limitation of moment methods is that they track only scalar quantities representing the particle distributions. More detailed size information is not readily available, and, since the time history of particles is not recoverable, multidimensional particle morphology cannot be described without further assumptions.

Discretization methods

Discretization methods are an alternative option that can provide greater resolution of the particle size distribution but with a trade-off in computational efficiency. These include methods that discretize the state-space by sub-dividing the particle coordinates into discrete grid cells, and methods that discretize the function space, by representing the number density function by finite-dimensional approximations.

Sectional methods are a popular choice in the former category. These methods discretize the PSD into sections or 'bins' within which it is modelled either with step functions or polynomials. Sectional methods allow resolution of the PSD and can be accurate for fine partitioning; however, they have a number of drawbacks. Properties of the PSD must be approximated within each section and this can cause numerical diffusion when modelling convection [151] because exact values cannot be assigned at each point. They are expensive compared with moment methods, and higher-order variants can suffer from stability issues [64]. A number of adaptations have been proposed, for example to conserve mass and particle number [53], to handle discontinuities in the number distribution and numerical diffusion due to surface reaction [68–70], and to treat sintering [152].

Finite difference [91] and finite volume [13] methods are also used for low-dimensional type-spaces. Matveev et al. [91] propose low rank skeleton approximations for the kernel matrix to exploit fast convolutions and reduce complexity. Such techniques can accommodate multidimensional problems with several internal coordinates in the particle model (e.g. 25 coordinates in Matveev et al. [92]).

Global approximation uses weighted residual approaches, e.g. collocation [43] and the Galerkin method [131], on finite elements to formulate a piecewise approximation to the number density function at a set of nodal points in terms of basis functions. The Galerkin finite element method (FEM) has been packaged into a solver called PARSIVAL [165] which was used to study surface energy effects for titania [5, 6] – the authors of these studies argued that surface shielding is important in the industrial synthesis, requiring a particle model that could resolve aggregate structure to model structural effects.

Discretization methods become prohibitively expensive for high-dimensional type-spaces for example, the thousands of dimensions required to describe aggregate particle structure, including all possible configurations and sizes of the constituent primary particles. Stochastic methods are required to incorporate high-dimensional type-space models.

Stochastic methods

Stochastic (Monte Carlo) methods solve the PBE by performing process events probabilistically on a finite ensemble of computational particles in a representative sample volume. These particles retain their time history [177] and can have arbitrarily many internal coordinates; thus this class of methods is currently the only viable option for using very high-dimensional particle type-spaces [161]. They have been used to study formation of soot [21], silica [140], silicon [101], and titania [2, 160] particles. Yapp et al. [173] used a detailed population balance model to compute the optical band gap of polycyclic aromatic hydrocarbons in an ethylene diffusion flame – providing possibilities for useful direct comparison with experimental observations.

Stochastic methods are based on direct simulation Monte Carlo (DSMC) methods developed in the 1970s by Gillespie [46], who presented the theory and computational steps for stochastic modelling of droplet coalescence and inception, and Shah et al. [139], who presented an algorithm to simulate coalescence in dispersed phase mixing in a flow reactor. The statistical accuracy of these methods is controlled by the number of computational particles used, and the number of repeat runs with different random seeds. Stochastic methods can be computationally taxing for high process rates and strong phase coupling (as in industrial TiO_2 synthesis) because a large particle ensemble is required to resolve the polydisperse PSD and the surface structure of the particles evolves very rapidly. In Monte Carlo methods, convergence to the exact solution is expected with increasing sample size. This can be demonstrated numerically [101, 140], and has been shown theoretically in several studies [34, 116, 159].

Using a finite ensemble of particles naturally limits the resolution that can be obtained. Coagulation, which involves collision and sticking of a pair of particles, depletes the ensemble with successive events. Conversely, breakage, which splits particles into smaller fragments, increases the number of simulation particles and can exceed a pre-defined storage quota. Particle inception is equally problematic if it continuously adds new simulation particles to the finite ensemble [63]. Variance reduction techniques have been introduced to improve the precision of a Monte Carlo simulation for a given computational cost. Smith and Matsoukas [146] proposed constant ensemble top-up following coagulation events, extending this ‘constant-number’ approach to cover other processes in subsequent work. Maisels et al. [83] presented a stepwise constant-volume version that duplicates the ensemble if it drops below half-filled and simultaneously doubles the sample volume to maintain the correct number concentrations. This was found to provide superior performance compared to the previous constant-number approach.

Random removal, or ‘contraction’, is typically employed to treat the problem of exceeding ensemble capacity. This involves removing a particle at random from the ensemble and rescaling the sample volume to account for the change [77]. Merging [175] is an alternative approach wherein two (similar) particles are combined and their concentration is adjusted accordingly. Kotalczyk and Kruis [63] proposed a ‘low weight’ merging technique that selects particles to merge so as to minimise the error introduced in the PSD. This was deployed using a parallelized algorithm to compare errors for different particle pairs in a cached list of low (statistical) weight particles, and was shown to reduce the statistical noise compared to random removal.

Variance has also been addressed by mass flow algorithms [34] and, more generally, weighted particle methods [28, 63, 71, 121, 176]. These methods differ in details; however they all use the concept that each simulation particle can represent a different physical concentration by using statistical weights associated with each simulation particle to provide better resolution of certain regions of the particle size distribution. The statistical weights can be linked to a physical property of the particles (e.g. mass), as in the original mass flow algorithms, or can be used to conserve the particle number and other properties such as mass introducing concepts of ‘weight transfer functions’ [121] or ‘stochastic resolution’ [63] in defining coagulation rates and behaviour.

Rules need to be derived to govern coagulation for weighted particles [177] in order to ensure that the event frequency and symmetry of the real coagulation process is represented [121]. The more complicated the formulation of the PBE and rate expressions, the less easy it is to show that the method remains exact in the limit of large ensembles. However, theoretical work by Patterson et al. [121] and DeVille et al. [27] has shown convergence to the correct behaviour for some formulations using mathematical notions of convergence. Additionally, empirical studies have shown agreement with deterministic methods for various growth mechanisms [63].

In previous work, stochastic methods have been refined with several techniques to improve efficiency e.g. fictitious jumps and majorant kernels [33, 99, 121, 132], and the linear process deferment algorithm (LPDA) [120]. These techniques are used in this thesis; thus, further details will be provided with the theory in Section 3.5. Performance enhancement has also been reported using a smart book-keeping approach that calculates all coagulation rate contributions upfront and only updates the rate to account for contributions from particles that are affected by an event [66]. Wei and Kruis [158] subsequently parallelized this on graphics processing units (GPUs), reporting 100–1000 times speed-up. Xu et al. [170] also presented a GPU-parallelized approach, using a weighted majorant for the coagulation kernel, and studied optimal choice of parallel threads (128). Irizarry [54] proposed a point ensemble Monte Carlo technique in which computational particles are grouped into size classes that are used to compute the process rates instead of summing over an ensemble of distinct properties. Particle movement during jump events is determined probabilistically (e.g. a particle is picked randomly from the chosen size class) and this was shown to maintain reasonable accuracy – at least for a low-dimensional problem – at lower cost.

Hybrid methods

The numerical methods discussed in the previous subsections offer different attractive features in terms of accuracy and efficiency. Each approach also has inherent limitations including loss of size information, instability and presence of unclosed terms. This has motivated some researchers to look to combine methods for better across-the-board performance.

A split solution method was proposed for studying gelation processes, to reduce the chance of stochastic effects forming metastable states [9]: the equations for particles smaller than size N_1 are treated deterministically, those for particles of sizes between N_1 and N_2 are treated stochastically, and particles larger than N_2 are removed (the gelled mass).

A hybrid method in which treatment depends on particle size was proposed by Mueller et al. [105] to treat problems such as soot formation where the particle system is bimodal with a primary particle mode and an aggregate particle mode. The hybrid method of moments (HMOM) aims to combine the stability of MOMIC with the multi-modality of DQMOM. It uses a MOMIC formulation with inclusion of a DQMOM-type Dirac delta function at the nucleating size to capture the smallest particle statistics. This also permits a new handling of collision that exploits the two-regime nature of the method. HMOM was shown to provide better accuracy than MOMIC and, whilst noticeably less accurate than DQMOM or high-fidelity Monte Carlo, it is more efficient and thus allows better resolution than DQMOM for a given computational cost.

Hybrid sectional and moment methods have been developed with both QMOM [7] and DQMOM [15]. These apply quadrature moment methods within each section to predict local moments of the particle size distribution using the quadrature points to supply finer resolution than the sections provide. The numerical solution of the moment integrals is intended to be better conditioned because of the smaller size of the localized problem. Despite this, Bruns and Ezekoye [15] report that the sectional quadrature method of moments (SQMOM) is slow and unstable. These methods also require adaptation to handle growth or loss processes. Nguyen et al. [110] proposed further improvements in numerical efficiency for these algorithms but noted that further developments are necessary for handling high-dimensional PBEs and flow coupling.

Bouaniche et al. [12] proposed a hybrid stochastic and sectional method to handle the problem of numerical diffusion. This uses two separate discretization schemes for the particle size space and probability density function (PDF) – a fixed grid and a discrete particle ensemble, updated with sectional and Monte Carlo methods respectively. Surface growth is treated separately from inception and aggregation using operator splitting. Surface growth is handled deterministically by growing each of the discrete particles, and inception and aggregation are performed by using rates computed with a conventional sectional method to redistribute the particles randomly to different sections in a sequential step. The movement process introduces a residual due to round-off, which is tracked and redistributed when it gets sufficiently large. The authors demonstrated superior performance compared to standard sectional methods in terms of reduced artificial diffusion and showed that the residual tracking feature improves agreement with the exact solution for small ensembles.

2.2.3 Transport of particles

Particle systems tend not to exist in isolation and coupling to a continuous phase commonly results in physical transport of particles through space. This further couples the population balance equation to the continuous phase both directly, through the velocity, and indirectly, through variations in local chemistry. Methods have been developed to treat both laminar and turbulent flow for different systems. Turbulence is an inevitable consequence of the high velocities used in aerosol synthesis, resulting in chaotic flow fields with a variety of gas phase conditions and residence times which can be exploited to control mixing of reactants and transport through the reactor [126]. This can help to prevent caking of the reactor walls [8] and increase efficiency of precursor conversion by more rapid mixing – i.e. transport of precursors to overcome mixing limitations and control of particle exposure high temperature regions where growth, collision and sintering occur to achieve suitable sizes [126].

Modelling of turbulent transport is central to the numerical treatment of turbulent reacting flows and several approaches are used. Direct numerical simulation (DNS) directly solves the discretized transport equations for the velocity, species compositions in the continuous phase, and moments of the number density function (NDF). This is prohibitively computationally expensive for realistic systems because of the broad range of length and time scales involved [126]. Two-dimensional DNS has been used to study formation of TiO_2 in a methane-air flame using one step, global kinetics and discretization-based particle tracking [41, 156] and detailed chemistry without particle tracking [144]. These studies do not provide resolution of the particle size properties, but can inform understanding of precursor consumption and local flow characteristics. As an indication of the computational cost, the simple chemistry study of Wang and Garrick [156] required 9600 CPU hours on a Cray X1 in the early 2000s.

It is generally necessary to simplify the detailed system model to obtain a more computationally tractable problem [64]. Equations can be derived for the statistical properties of the system and closed using physics-based modelling. For a turbulent system, each quantity can be modelled as a random variable defined by a probability density function (PDF). As outlined in Rigopoulos [130], there are three modelling choices to be made. Firstly, a model is obtained for the flow field by applying one of two averaging techniques: Reynolds decomposition or small-scale filtering. These lead to Reynolds-averaged Navier-Stokes (RANS) and large-eddy simulation (LES) formulations respectively. The resulting equations must be closed, and this requires a model for turbulence-particle formation coupling. The two approaches used for this are flame structure (e.g. flamelet) and statistical (e.g. PDF transport) models [126]. The former reduces complexity by considering local simplified flame structures and the latter use the joint probability density function for the transported scalars. Finally, a modelling strategy for the PBE is required e.g. MOM, QMOM or discretization, described in Section 2.2.2.

RANS is the least computationally expensive option – thus it is useful for modelling complex reactor geometries; however, it is sensitive to choice of model parameters and this can present significant challenges in the context of modelling fine particle formation [126]. Despite this, Raman and Fox [126] report that good agreement has been observed with experiments for some flame studies. Johannessen et al. [56] studied flame synthesis of titania using a single-step combustion model and calibrating with experimental data. They represented particles as a pseudo gas phase species in the CFD simulation, using the differential Reynolds stress turbulence model. The results were post-processed with a monodisperse, Lagrangian particle model to recover more detailed particle size information. Despite the relatively simplistic model, this approach was able to achieve reasonable agreement with measured properties for four different flame studies.

Filtering of the smallest scales of the flow yields the LES approach. Despite its popularity, this technique is not ideally suited to the study of fine particle formation where the smallest scales influence the reaction kinetics [126]. It also suffers from numerical discretization errors at scales near the filtered size. Sung et al. [150] used LES with a flamelet model and QMOM for the particle moments to study $TiCl_4$-methane flames using the detailed kinetics of West et al. [162] and Mehta et al. [95], finding that precursor oxidation occurs near the injection site and suggesting that particle characteristics would agree better with experimental data if sintering and surface growth were modelled. Their computations ran for around five days on 256 processors (the authors do not provide more detail about the computer architecture). Loeffler et al. [82] compared DNS and LES simulations of titania formation and found the latter to be reasonably accurate for less than one thousandth of the computational cost. However, the authors conclude that particle processes such as sintering may be poorly resolved with the LES approach.

PDF transport modelling shows promise for coupling transport to particle dynamics. This involves forming a joint PDF for all relevant random variables and deriving the transport equations in terms of this quantity. This provides more flexibility than assuming the flame or PDF structures; however, it also increases the dimensionality of the system by converting dependent variables into independent ones [126, 130]. The PDF approach can be simplified by assuming there are no spatial gradients in the PDF of physical quantities, trading information about the flow field for lower computational cost [64]. An example of this so-called stochastic reactor model (SRM) approach is the partially stirred plug flow reactor used by Balthasar et al. [10] to model a carbon black furnace. Rigopoulos [129] and Sewerin and Rigopoulos [138] included discretized and functional forms of the number density in the joint PDF ("PBE-PDF") to better resolve particle size distributions.

Coupling of transport to stochastic PBE methods has recently been achieved by several groups, from the weighted random walk, constant-number Monte Carlo method of Kruis et al. [67], to flame synthesis of titania [169] with a simple model for phase transformation [171] and laminar flow in a crystallizer [11]. Patterson and Wagner [119] reported better performance using a weighted particle method compared to direct simulation algorithms. In all cases, the particle models used were simple and although the extension to detailed particle models may be straightforward in theory, this has not been achieved to date due to the significantly higher computational cost. Computational cost and memory overhead limit the size of ensemble that can be used, restricting attainable accuracy [67]. The coupling is typically one-way – operator splitting is used to establish the flow field and chemistry; following this the particle system is evolved.

A full representation of the flow, chemistry and particle dynamics is the ideal for studying particle systems. However, this is currently limited by available processing power, especially for realistic problems such as aerosol synthesis. The equivalent reactor network (ERN) approach provides a simpler treatment of the flow, coupling ideal reactors, such as continuously stirred tank reactors (CSTRs) and plug flow reactors (PFRs), to approximate the flow behaviour observed experimentally or by CFD. Novosselov et al. [113] and Novosselov and Malte [112] used CFD to guide their network development and were able to match experimental results for complex combustion processes in engines. Other studies of this kind include compartmental models [55], ideal reactor networks [101] and Lagrangian particle tracking [96] including post-processing of flame streamlines with detailed particle models [79]. Menz et al. [101] provided a comprehensive investigation of convergence and error behaviour in different stochastic reactor network models demonstrating propagation of error to downstream reactors, effect of recycles and transient behaviour. This thesis follows this approach in order to enable simulation with a highly detailed particle model.

Chapter 3

Theory

A key contribution of this thesis is a new strategy for describing the particle type-space and an algorithm for solving the population balance equation for this "hybrid" type-space model. These novel elements are built on top of existing population balance modelling tools including: (i) detailed particle models; (ii) gas phase and particle mechanisms; and (iii) a coupled solver for the two-phase system. The aim of this chapter is to provide additional detail about the existing modelling framework. New model developments are presented in Chapters 4–6. This chapter begins with an overview of modelling the gas and particle phases. It then describes the spherical particle model and two multivariate particle models used in this thesis. The first tracks primary particle connectivity and combined surface area, and the second tracks primary particle coordinates and the degree of overlap of adjacent primary particles. The latter is a more recent model that provides more detail about particle structure. This is followed by a description of mechanisms defining the chemical reactions and particle growth processes. Finally, this chapter describes features of the operator splitting algorithm that is used to couple the ordinary differential equation solver for the gas phase and the stochastic solver for the particle phase.

3.1 Overview of phase models and coupling

As outlined in Section 2.2, a description of the systems of interest to this work requires consideration of both the continuous, gas phase environment and the dispersed, discrete particle phase. In this chapter, models are presented to describe components of both phases and how they interact (Fig. 3.1). The flow behaviour depends on the type of reactor and two types of idealised flow reactor will be employed in models developed in this work: the continuously stirred tank reactor (CSTR) and the plug flow reactor (PFR). These two reactor models represent extremes of mixing behaviour. In a CSTR, all concentrations are spatially homogeneous, while a PFR represents perfect 1D flow without any back-mixing. The combinations of these two archetypes can be used to approximate real, partially-mixed flow systems [36]. PFRs are commonly modelled using a third simple reactor model – a batch reactor – and exchanging the time and displacement variables to obtain steady-state axial profiles as required. This is the approach used in the current work; thus models for a CSTR will be presented in this chapter since the batch reactor equations are identical excepting absence of flow. It is not necessary to consider physical positions of particles so the particle state-space only includes internal coordinates (types, x).

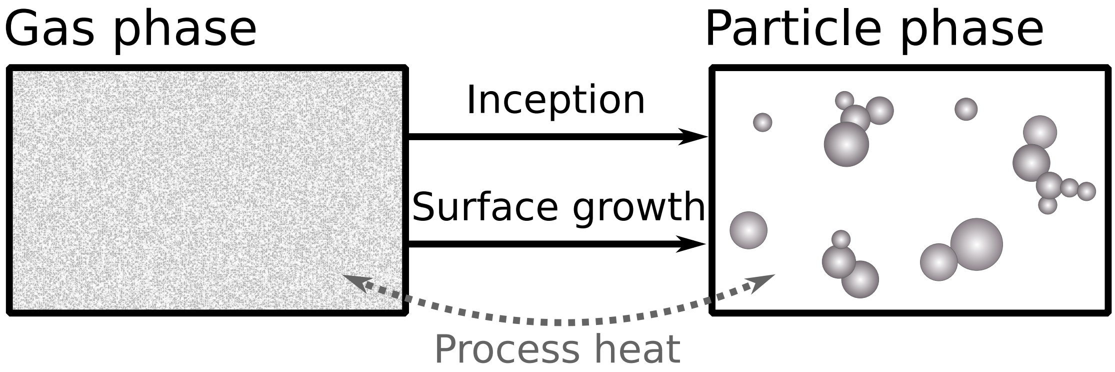

Fig. 3.1: Overview of interactions between continuum gas phase and dispersed particle phase. The solid arrows show the direction of mass transfer and the dotted arrow indicates heat transfer.

Gas phase

The gas phase consists of different chemical species including reactants, intermediates and products. The species compositions are tracked as a function of the system temperature and pressure. The gas phase mechanism specifies reactions that convert reactants to intermediates and/or products. Thermodynamic and kinetic parameters are required to specify the reaction rates and behaviour of the chemical species at different temperatures. The gas phase is also affected by particle processes and flow, i.e.

$$\frac{dC_k}{dt} = \mathcal{W}(\mathbf{C},T) + \mathcal{G}(\mathbf{C},T,n) + \mathcal{F}_{\mathrm{g}}(C_k). \tag{3.1}$$

Here, consumption or production of species k changes its concentration, C_k, according to gas phase, particle phase and flow processes represented by the generic operators $\mathcal{W}$, $\mathcal{G}$ and $\mathcal{F}_{\mathrm{g}}$ respectively. These processes are affected by the gas phase concentrations of all N_{sp} species, $\mathbf{C} = \left(C_1, \ldots, C_{N_{\mathrm{sp}}}\right)$, and particle phase concentrations, $n(x)$. For a constant volume CSTR, with residence time τ_{CSTR} and N_{in} inflow streams, the concentration of each gas phase species develops according to

$$\frac{\mathrm{d}C_k}{\mathrm{d}t} = \dot{w}_k(\mathbf{C},T) + \dot{g}_k(\mathbf{C},T,n) + \frac{1}{\tau_{\mathrm{CSTR}}} \sum_{j=1}^{N_{\mathrm{in}}} f^{[j]} \left(C_{k,\mathrm{in}}^{[j]} - C_k\right), \tag{3.2}$$

where, $\dot{w}_k$ and $\dot{g}_k$ are the molar production rates of species k by gas phase and particle reactions respectively and $C_{k,\mathrm{in}}^{[j]}$ is the concentration in the j^{th} inflow stream. The energy balance will be developed in Chapter 6, before which only isothermal systems are studied.

More detail is provided for the titania system in Section 3.3.

Particle phase

Solid particles are formed by collisions between certain gas phase (precursor) species, leading to stable arrangements of molecules larger than a system-specific critical size. This process is termed inception. The particles grow via collisions that result in lasting contact, referred to as coagulation, which produces non-spherical, fractal-like structures. Suitability of different formulations of the coagulation rate kernel depends on particle size and gas phase conditions, such as pressure [161]. Heterogeneous reaction with the gas phase, termed surface growth, increases the surface area of individual particles. Connected particles undergo structural changes due to surface growth and sintering processes in order to satisfy surface energy requirements. These processes thus create different particle types and, in order to study the evolution of the particle system, a model is required for the particle type-space that is capable of describing relevant particle structures. This is the subject of Section 3.2.

Mathematically, particles are ascribed types, x, in the type-space, $\mathcal{E}$, i.e. $x \in \mathcal{E}$. Particle types encompass distinct properties such as mass, composition, crystal phase and structure which can be either discrete (e.g. number of molecules) or continuous (e.g. particle radius). In this thesis, structured particles will be defined by their constituent primary particle compositions (i.e.

discrete number of TiO_2 monomers), connectivity and degree of cohesion (i.e. relative positions of primary particle centres of mass and particle radii). Thus the type-space will be multivariate and comprise both discrete and continuous coordinates (see Fig. 3.2 for a representative element of the type-space and Section 3.2 for further details). The number density of particles of this type, $n(x) : x \mapsto \mathbb{R}_0^+$, is tracked as they undergo changes due to inception ($\mathcal{I}$), coagulation ($\mathcal{K}$), surface changes ($\mathcal{S}$) and flow ($\mathcal{F}_{\mathrm{p}}$),

$$\frac{dn(x)}{dt} = \mathcal{I}(x,\mathbf{C},T) + \mathcal{K}(x,n,T) + \mathcal{S}(x,\mathbf{C},T) + \mathcal{F}_{\mathrm{p}}(n). \tag{3.3}$$

The operators $\mathcal{I}$, $\mathcal{K}$, $\mathcal{S}$ and $\mathcal{F}_{\mathrm{p}}$ provide a generic reference to the rates of the respective processes which can depend on the particle type, and the concentrations of gas phase species and other particles. A mechanism is needed to specify how different processes affect the particles and these processes are described in more detail in Section 3.4 which furnishes specific rate expressions for the processes considered in this thesis. In a simplification of the expression given in Eq. (2.2), the population balance equation for a constant volume CSTR takes the form

$$\begin{aligned} \frac{\mathrm{d}n(x)}{\mathrm{d}t} =& I(x,\mathbf{C},T) + \frac{1}{2} \sum_{\substack{y,z\in\mathcal{E}:\\ y+z=x}} K(y,z,T)\,n(y)\,n(z) - \sum_{y\in\mathcal{E}} K(x,y,T)\,n(x)\,n(y) \\ &+ \sum_{\substack{y\in\mathcal{E}:\\ g_{\mathrm{SG}}(y)=x}} \beta_{\mathrm{SG}}(y,\mathbf{C},T)\,n(y) - \beta_{\mathrm{SG}}(x,\mathbf{C},T)\,n(x) \\ &+ \frac{1}{\tau_{\mathrm{CSTR}}} \sum_{j=1}^{N_{\mathrm{in}}} f^{[j]} \left(n_{\mathrm{in}}^{[j]}(x) - n(x) \right), \end{aligned} \tag{3.4}$$

where, I is the inception rate, K is the coagulation kernel, $g_{\mathrm{SG}} : \mathcal{E} \to \mathcal{E}$ describes change in particle type, β_{SG} is the rate of change in type due to surface processes (growth/sintering), and $f^{[j]}$ is the volumetric feed fraction of inlet stream j, $j \in [1, N_{\mathrm{in}}]$. This assumes that the particles travel at the gas velocity and their residence time in the reactor is not influenced by their mass or shape.

Coupled phase dynamics

Section 2.2.2 highlighted numerical challenges to solving the coupled equations for the gas phase chemistry and particle population dynamics. A stochastic method is required when the high-dimensional particle type-space is described by a detailed model. Section 3.5 discusses the operator splitting technique used to connect the phases and the direct simulation algorithm used for the particles.

3.2 Particle models

The particle model is a key ingredient in the modelling framework because it determines the maximum amount of information that can be obtained directly about product morphology without requiring further assumptions on shape.

3.2.1 Spherical particle models

Spherical particle models [98] describe particles using a single internal coordinate such as mass. This provides an efficient mathematical model for the type-space, but restricts treatment of surface-changing processes such as growth (Section 3.4.2) or sintering (Section 3.4.4). In the spherical particle model for titania, a particle, P_q, is defined by the number of TiO_2 molecules, $\eta_q \in \mathbb{N}_0$, it contains,

$$P_q = P_q\left(\eta_q\right). \tag{3.5}$$

The diameter, d_p, of a spherical particle can be computed from its mass, m,

$$m\left(P_q\right) = \frac{\eta_q \mathrm{MW}}{N_\mathrm{A}} \implies d_\mathrm{p}\left(P_q\right) = \left(\frac{6}{\pi}\frac{m\left(P_q\right)}{\rho}\right)^{1/3}. \tag{3.6}$$

Here, N_A is Avogadro's constant and the first expression converts the number of molecules tracked by η_q to moles and multiplies by the molecular mass, MW, to yield mass. The second expression converts mass to volume and thus finds the volume-equivalent spherical diameter using the particle mass density, ρ. The molecular weight of titania is $79.87\,\mathrm{g\,mol^{-1}}$ and the density of rutile is used, $4.26\,\mathrm{g\,cm^{-3}}$.

3.2.2 Detailed particle models

Detailed particle models provide particle descriptions at two levels: primary particles (primaries), which consist of chemically bonded units of TiO_2 and are described by the number of atoms they contain (Fig. 3.2(a)), and aggregate particles which are formed from multiple, independently-tracked primaries with arbitrary connectivity (Fig. 3.2(b)).

Single primary particles, p_i, are the simplest elements in the particle type-space and are modelled as spheres of constant density. Each particle, P_q, is described by the list of its constituent primary particles, p_i, $i = 1, \ldots, n_q$, and a data structure, $\mathbf{C}_q$, that provides further information about connectivity of adjacent primary particles in the aggregate:

$$P_q = P_q\left(p_1, \ldots, p_{n_q}, \mathbf{C}_q\right). \tag{3.7}$$

The definition of the primary particles and their connectivity depends on the choice of detailed particle model. Two variants of detailed particle model are used in this thesis – a combined surface area model (Section 3.2.3) and a primary coordinate-tracking, or overlapping-spheres, model (Section 3.2.4).

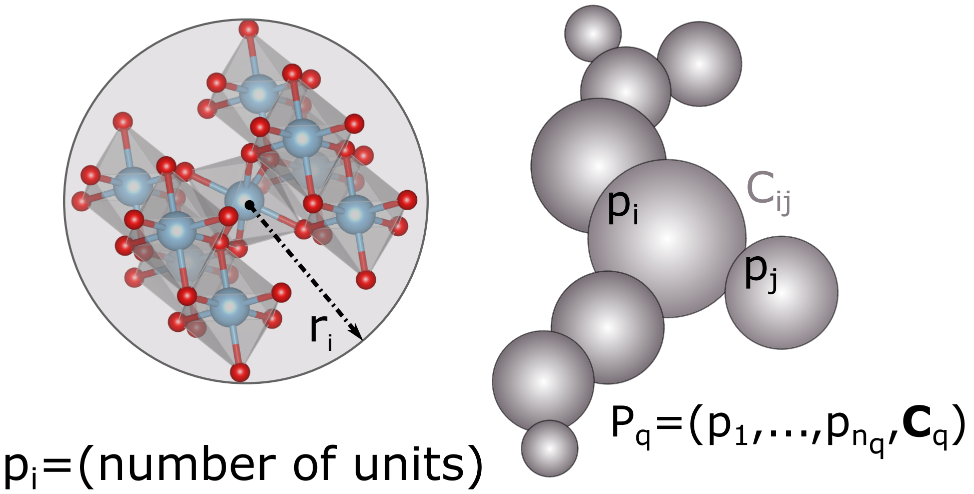

(a) Spherical primary particle (b) Detailed aggregate particle

Fig. 3.2: Particle model components showing (a) primary particle, p_i, composed of TiO_2 units and represented as a volume-equivalent sphere; and (b) particle, P_q, composed of a list of primary particles with connectivity information stored in $\mathbf{C}_q$.

3.2.3 Combined surface area particle model

The combined surface area model was developed and used to study several particulate systems including SiO_2 [133, 141], TiO_2 [78, 162], silicon [99] and soot [22]. In it, primary particles, p_i, are defined by a single internal coordinate, $\eta_i \in \mathbb{N}_0$, which tracks the number of units of the chemical species contained,

$$p_i = p_i\left(\eta_i\right). \tag{3.8}$$

Properties of the primary particles can be derived as for the spherical particle model (Eq. (3.6)). The connectivity, degree of sintering and surface area for each pair of neighbouring primary particles is tracked by storing: the surface area at initial point contact, the current combined surface area and the surface area of a volume-equivalent sphere (Fig. 3.3). The combined surface area refers to the total exposed surface area of the two primary particles. For primary particles in point contact, it is the sum of their surface areas. For primary particles with a larger degree of cohesion, less of their original surface area is exposed and the combined area is reduced.

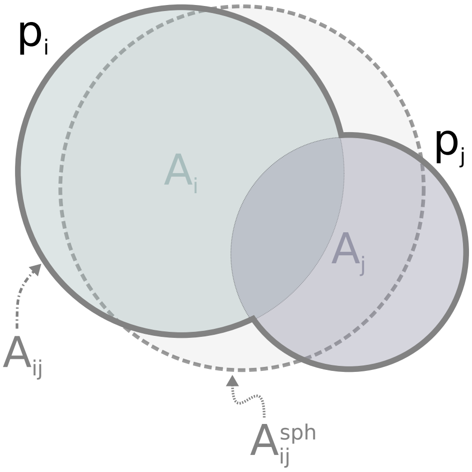

Fig. 3.3: Connected primaries p_i and p_j, with spherical areas A_i and A_j respectively, have combined surface area, A_{ij}, and volume-equivalent spherical surface area, A_{ij}^{sph}.

As the primary particles sinter (described in more detail in Section 3.4.4), the current surface area is updated and the degree of sintering can be computed – the sintering process is modelled on the assumption that the combined surface area will approach that of a volume-equivalent sphere for energetic reasons. A detailed implementation of $\mathbf{C}_q$ is provided by Sander et al. [133] and consists of storing three symmetric, square matrices with dimension equal to the number of primary particles belonging to the particle. The elements in the i^{th} row and j^{th} column of each of the three matrices represent the surface area at point contact ($A_{ij}^{(0)}$), the current time (A_{ij}), and after coalescence (A_{ij}^{sph}) respectively for primary particles p_i and p_j. The elements in row i and column j are zero if the primaries are not adjacent.

For non-spherical particles, the collision diameter, d_c, is frequently used as a measure of aggregate size and to evaluate collision propensity (Section 3.4.3). The collision diameter of each particle is computed from the total particle volume, V_q, and area, A_q, [133]

$$d_c\left(P_q\right) = \frac{6V_q}{A_q} n_q^{\frac{1}{1.8}}. \tag{3.9}$$

V_q and A_q are calculated by summation of the particle's primary particle volumes and surface areas, adjusted for the effect of sintering (Section 3.4.4). Eq. (3.9) assumes a fractal dimension of 1.8 [133, 154]. This is the fractal dimension typical of particles formed from an initially monodisperse (uniform) particle system by diffusion-limited cluster-cluster agglomeration (DCLA), one of the two dominant mechanisms for aerosol growth which is favoured in the continuum regime [31]. Constant and variable fractal dimensions were studied by Goudeli et al. [49] using interpolation between regimes and mesoscale simulations. It was found that changing the fractal dimension had little effect on primary particle and agglomerate diameters but under-predicted the aggregate diameter under certain conditions. Expressions for the collision diameter are compared by Patterson and Kraft [118] where it was suggested that the specific choice for approximating aggregate structure does not have a significant effect relative to the current understanding of the formation and growth processes. This is also observed by Tsantilis et al. [154].

3.2.4 Overlapping-spheres particle model

A primary coordinate-tracking or overlapping-spheres model was recently developed to provide more detailed information about particle geometry [81]. This extends earlier overlapping-spheres models [32, 102, 104] that were applied to study aggregation with surface growth or sintering. The overlapping-spheres model describes three-dimensional aggregate structure in terms of the relative coordinates and sizes of constituent primary particles, which allows surface-changing processes to be modelled with consideration of features that affect them. This is particularly useful in the late stages of particle development, as well as for providing direct comparison with experimental results and images [80]; whereas, in previous work [161], particle shape was visualised by post-process positioning of the primary particles in each particle. This model has been used to study flame synthesis of titania [79] and soot [52].

In addition to their chemical composition, η_i, primaries are further described by their radius, r_i, and position, $\mathbf{z}_i$,

$$p_i = p_i\left(\eta_i, r_i, \mathbf{z}_i\right). \tag{3.10}$$

The coordinates, $\mathbf{z}_i$, specify the location of the primary centre relative to the centre of mass of the aggregate (Fig. 3.4) and do not provide information about the spatial location of particles. The radius r_i can change independently of the composition η_i to permit conservation of mass during sintering by redistributing it to the surface.

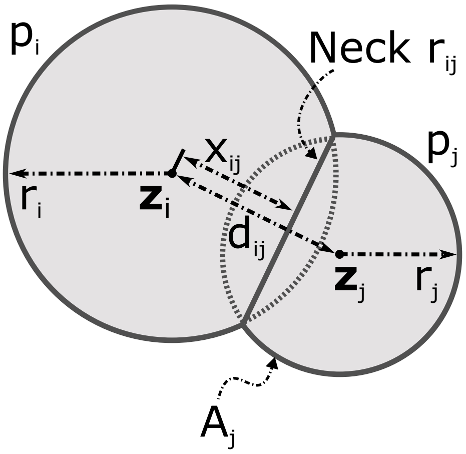

Fig. 3.4: Connectivity of primaries p_i and p_j, modelled as overlapping-spheres with radii r_i and r_j, is defined by their relative 3D coordinates, $\mathbf{z}_i$ and $\mathbf{z}_j$, specifying the centre-to-centre distance, d_{ij}, and neck radius, r_{ij} [81].

This informs the centre-to-centre separation, d_{ij},

$$d_{ij} = \left|\mathbf{z}_i - \mathbf{z}_j\right|, \tag{3.11}$$

which measures the degree of overlap between adjacent primary particles. From the primary coordinates and simple geometry, it is possible to specify the centre-to-neck distance, x_{ij},

$$x_{ij} = \frac{d_{ij}^2 - r_j^2 + r_i^2}{2d_{ij}}, \tag{3.12}$$

and the radius of the neck between adjacent primaries p_i and p_j, r_{ij},

$$r_{ij} = \left(r_i^2 - x_{ij}^2\right)^{\frac{1}{2}}. \tag{3.13}$$

$\mathbf{C}_q$ simply tracks the connectivity of the primary particles, i.e. which primary particles are adjacent in the aggregate. The value of each element, $C_{ij} \in \mathbf{C}_q$, depends on the relative positions of primary particles p_i and p_j,

$$C_{ij} = \begin{cases} 1 & \text{if } p_i, p_j \text{ are adjacent} \\ 0 & \text{if } p_i, p_j \text{ are not adjacent.} \end{cases} \tag{3.14}$$

The primary coordinates can be used to compute the diameter of gyration, d_{g}, which defines the aggregate size in terms of how its constituent primary particles contribute to its moment of inertia. This provides a means of defining the collision diameter, d_{c},

$$d_{\mathrm{c}}\left(P_q\right)^2 = \frac{4}{\sum_{i=1}^{n_q} m\left(p_i\right)} \sum_{i=1}^{n_q} m\left(p_i\right)\left(\left|\mathbf{z}_i\right|^2 + r_i^2\right), \tag{3.15}$$

without assuming a fractal structure to relate the aggregate composition to its size [81].

3.3 Gas phase chemistry model

This thesis studies the formation of solid titanium dioxide particles via the gas phase oxidation of titanium tetrachloride. The overall reaction produces chlorine as a by-product (Eq. (2.1)). As mentioned in Chapter 2, modelling studies up to the early 2000s used global kinetics to describe the process. A detailed gas phase mechanism was then developed by West et al. [160, 162], and extended by Nurkowski et al. [114] and Buerger et al. [16, 17]. This thesis uses the equations and parameters provided in West et al. [160, 162] without modification, which results in a series of nonlinear ODEs that specify the evolution of the gas phase concentrations as a function of gas composition, pressure and temperature as the term $\dot{w}_k$ in Eq. (3.2). The rates are in Arrhenius form, proportional to the product of the reacting species concentrations and exponentially increasing with temperature with the same general form as Eq. (3.20).

The mechanism describes the decomposition of the precursor, oxidation of titanium chlorides to form titanium oxychlorides, and chlorine chemistry. It includes 28 gas phase species (representative examples: $TiCl_4$, TiCl, TiOCl, $TiOCl_3$, $Ti_5O_6Cl_8$, Cl_2, ClO, Cl_2O) and one solid species (TiO_2). There are 66 gas phase reactions including thermal decomposition, abstraction, oxidation, chlorine/oxygen chemistry and dimerisation. The kinetic and thermodynamic parameters for the reactions and chemical species were obtained from a combination of experimental data and first-principles simulations.

The gas phase interacts with the particle system through inception (Section 3.4.1), surface reaction (Section 3.4.2) and bi-directional energy exchange (Chapter 6). In inception, gas phase titanium oxychlorides collide to form solid titania particles. In surface reaction, gas phase $TiCl_4$ and O_2 react on the particle surface, depositing new titania molecules directly.

3.4 Particle processes

Titania particles are produced from gas phase precursors and subsequently undergo structural changes due to different growth processes (Fig. 3.5). A generic expression for the evolution of the particle system was provided in Eq. (3.3). This illustrated that the concentration of particles of each type depends on the particle formation and growth rates.

The population balance model for titania includes inception, surface growth, coagulation and sintering processes and these will be described in more detail in Sections 3.4.1–3.4.4. It is worth noting that the detailed aggregate structure is known when a multivariate particle model is used; thus the processes and their rates can be resolved in terms of particle characteristics such as available surface area and particle morphology.

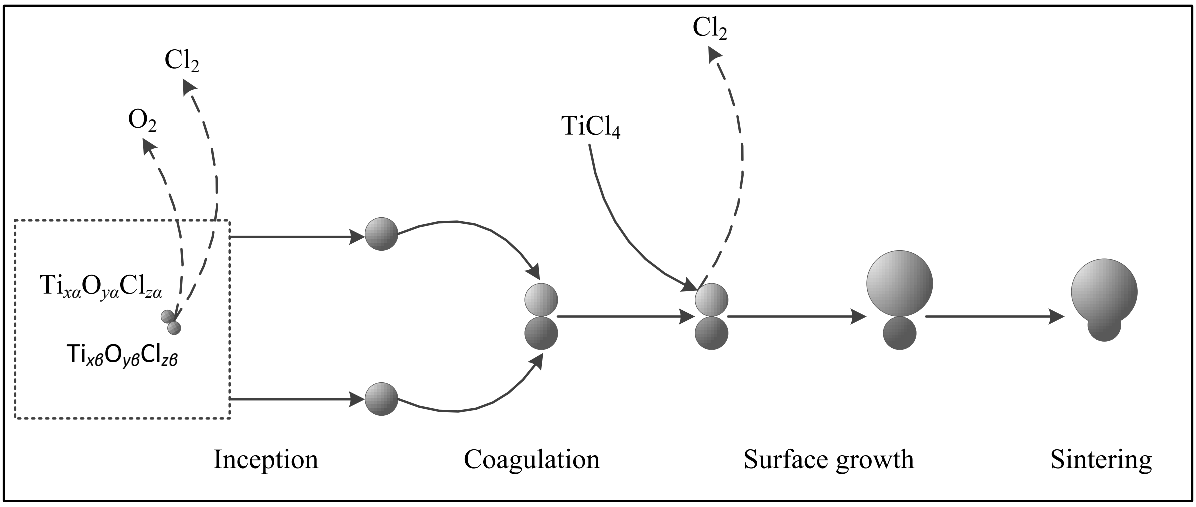

Fig. 3.5: Particle formation and growth processes for titania (note that these do not need to occur in the sequential manner shown in the figure).

3.4.1 Inception

Inception refers to the nucleation of primary particles as a result of collisions between pairs of precursor gas phase molecules. As in previous work [4, 143], possible particle inceptions are specified by the set of 105 bimolecular collision-limited reactions between any pair of titanium oxychloride species ($\mathrm{Ti}_x\mathrm{O}_y\mathrm{Cl}_z$, $x, y, z \geq 1$) generated by the gas phase mechanism,

$$\begin{aligned}\mathrm{Ti}_{x_\alpha}\mathrm{O}_{y_\alpha}\mathrm{Cl}_{z_\alpha} + \mathrm{Ti}_{x_\beta}\mathrm{O}_{y_\beta}\mathrm{Cl}_{z_\beta} \rightarrow &\left(x_\alpha + x_\beta\right)\mathrm{TiO}_{2(\mathrm{s})} \\ &+ \left(\frac{y_\alpha + y_\beta}{2} - x_\alpha - x_\beta\right)\mathrm{O}_2 + \left(\frac{z_\alpha + z_\beta}{2}\right)\mathrm{Cl}_2.\end{aligned} \tag{3.16}$$

The smallest particle formed in this mechanism has product stoichiometric coefficient $x_\alpha + x_\beta = 2$, which corresponds to a primary particle with diameter 0.491 nm. The inception rate,

$$I(x, \mathbf{C}, T) = \frac{K_\mathrm{I} N_\mathrm{A}^2}{2} \left[C_{\mathrm{Ti}_{x_\alpha}\mathrm{O}_{y_\alpha}\mathrm{Cl}_{z_\alpha}}\right] \left[C_{\mathrm{Ti}_{x_\beta}\mathrm{O}_{y_\beta}\mathrm{Cl}_{z_\beta}}\right], \qquad x \equiv \left(x_\alpha + x_\beta\right) \mathrm{TiO_2} \tag{3.17}$$

depends on the precursor species concentrations and a rate constant, K_I, that is determined using collision theory, which yields a constant specified by the transition regime [100] coagulation kernel (expression provided in Section 3.4.3) and parametrised by the collision diameters of the colliding molecules. A molecular collision diameter of 0.65 nm is used as proposed by West et al. [162]. The presence of Avogadro's constant (N_A) in Eq. (3.17) converts from molar to particle concentration and illustrates how interaction between the continuous description of the gas-phase and the discrete particle system is handled. Inception typically creates particles of the smallest size(s); thus continuous inception combined with particle growth processes yields bi-/multi-model particle size distributions with a sustained concentration of these small particles.

3.4.2 Surface reaction

Primary particles undergo growth due to reaction of gaseous species resulting in mass deposition on their surface,

$$\mathrm{TiCl_4} + \mathrm{O_2} \rightarrow \mathrm{TiO_{2(s)}} + 2\mathrm{Cl_2}. \tag{3.18}$$

Here, the heterogeneous surface reaction is assumed to be first-order in the concentrations of $\mathrm{TiCl_4}$ and $\mathrm{O_2}$, as in Akroyd et al. [4]. The growth rate is given by:

$$\beta_\mathrm{SG}(x, \mathbf{C}, T) = k_\mathrm{s} A(x) N_\mathrm{A} \left[C_{\mathrm{TiCl_4}}\right] \left[C_{\mathrm{O_2}}\right]. \tag{3.19}$$

The surface reaction constant, k_s, has Arrhenius form,

$$k_\mathrm{s} = k_1 \exp\left(-\frac{E_\mathrm{a}}{RT}\right), \tag{3.20}$$

where A refers to the surface area per unit volume of the particle population, T is the system temperature and values for the parameters k_1 and E_a were obtained by Lindberg et al. [78] by fitting data from the experiment of Pratsinis et al. [124]: $k_1 = 1.34 \times 10^3\ \mathrm{m\,s^{-1}\,m^3\,mol^{-1}}$ and $E_\mathrm{a} = 60\ \mathrm{kJ\,mol^{-1}}$. It is not currently possible to validate these values at the higher end of the temperature range pertinent to this work (ca. 1300 K–1500 K), or at high precursor concentrations, owing to the absence of relevant surface rate data. However, the Arrhenius form is still expected to be suitable in this range and, at present, there is no evidence to suggest a different reaction mechanism at elevated temperatures.

A geometric description of surface changes is required for primary particles in the overlapping-spheres particle model (Section 3.2.4). This is outlined by Lindberg et al. [81] in the paper that presented the overlapping-spheres model, but is summarised here for completeness. Each surface event results in addition of a discrete quantity of mass to a specific primary particle, p_i. This is modelled by increasing the radius of p_i, without changing the coordinates, $\mathbf{z}_j$, and radii, r_j, of adjacent primaries, p_j. Increasing the radius r_i alters the neck, r_{ij}, and the centre-to-neck distances, x_{ij} and x_{ji}, between connected primaries p_i and p_j. For a consistent definition of the particle, mass is redistributed between the primaries so that the mass on the i^{th} and j^{th} sides of the adjusted neck is assigned to primary particles p_i and p_j respectively.

3.4.3 Coagulation

Coagulation between two particles P_i and P_j involves collision and lasting point contact, creating a single structure by establishing a new connection between one primary particle from each original particle,

$$P_i\left(p_1,\ldots,p_{n_i},\mathbf{C}_i\right)+P_j\left(p_1,\ldots,p_{n_j},\mathbf{C}_j\right)\rightarrow P_k\left(p_1,\ldots p_{n_i},p_{n_i+1},\ldots,p_{n_i+n_j},\mathbf{C}_k\right).$$

Coagulation is viewed as addition in the particle type-space in the sense that two particles are combined to form a new particle comprising both of their masses (and structures). The change in particle concentration due to coagulation is described by the discrete or continuous form of the Smoluchowski equation [34] depending on the particle type-space $\mathcal{E}$,

$$\mathcal{K}\left(x,n,T\right)=\frac{1}{2}\sum_{\substack{y,z\in\mathcal{E}:\\ y+z=x}}K\left(y,z,T\right)n\left(y\right)n\left(z\right)-\sum_{y\in\mathcal{E}}K\left(x,y,T\right)n\left(x\right)n\left(y\right),\tag{3.21}$$

where the first term on the right hand side describes formation of particles of type x from suitable, smaller particle pairs $(x-y,y)\in\mathcal{U}\subset\mathcal{E}$, and the second, the loss of particles of type x when they collide with other particles of any size, $y\in\mathcal{E}$. When the type-space is continuous and univariate (e.g. mass), $\mathcal{E}=[0,\infty)$ and $\mathcal{U}=[0,x)$. In the case of a multivariate type-space, it is more challenging to write this expression as each dimension of the type-space must be included to consider all particle fragments that could yield a particle of type x. In a surface-volume model, this would require a double integral over each of the two descriptors: surface area and volume. For primary particle models, the complexity is even higher as the number of constituent primary particles per particle, the primary particle sizes and the degree of overlap between connected primary particles are all required to describe a structured particle.

The coagulation rate kernel and collision mechanism depend on properties of the particle pair and the system. In this thesis, different kernels will be denoted by the subscript of K, the types of the coagulating particles in its argument, i.e. x and y in $K(x, y, T)$, will be replaced by the pair of particles concerned where P_i has type x and P_j has type y, and the temperature will be dropped, i.e. $K(P_i, P_j)$. When particles are relatively small (e.g. similarly sized compared to gas molecules), the rate at which two particles collide, K, is governed by the free-molecular kernel [140],

$$K_{\mathrm{fm}}\left(P_i, P_j\right) = \varepsilon \sqrt{\frac{\pi k_{\mathrm{B}} T}{2}\left(\frac{1}{m\left(P_i\right)} + \frac{1}{m\left(P_j\right)}\right)}\left(d_{\mathrm{c}}\left(P_i\right) + d_{\mathrm{c}}\left(P_j\right)\right)^2. \tag{3.22}$$

Here, $\varepsilon = 2.2$ is the collision enhancement factor, k_{B} is the Boltzmann constant, Kn is the Knudsen number [140],

$$\mathrm{Kn}\left(P_i\right) = 4.74 \times 10^{-8} \frac{T}{\mathcal{P} d_{\mathrm{c}}\left(P_i\right)}, \tag{3.23}$$

and $\mathcal{P}$ is pressure. When particles are relatively large compared to the gas molecules, the slip-flow kernel [140],

$$K_{\mathrm{sf}}\left(P_i, P_j\right) = \frac{2 k_{\mathrm{B}} T}{3\mu}\left(\frac{1 + 1.257\mathrm{Kn}\left(P_i\right)}{d_{\mathrm{c}}\left(P_i\right)} + \frac{1 + 1.257\mathrm{Kn}\left(P_j\right)}{d_{\mathrm{c}}\left(P_j\right)}\right)\left(d_{\mathrm{c}}\left(P_i\right) + d_{\mathrm{c}}\left(P_j\right)\right), \tag{3.24}$$

is more appropriate. However, aerosol systems are typically best described by the transition regime coagulation kernel [140],

$$K_{\mathrm{tr}}\left(P_i, P_j\right) = \frac{K_{\mathrm{sf}}\left(P_i, P_j\right) K_{\mathrm{fm}}\left(P_i, P_j\right)}{K_{\mathrm{sf}}\left(P_i, P_j\right) + K_{\mathrm{fm}}\left(P_i, P_j\right)}, \tag{3.25}$$

representing coagulation in the intermediate regime between free molecular and slip-flow. This approach will be employed here.

Particles coagulating in different regimes experience different collision mechanisms. Most relevant to aerosol systems are ballistic cluster-cluster, diffusion-limited cluster agglomeration (respectively BCCA, DLCA) which produce different fractal-like structures. Eggersdorfer and Pratsinis [31] presented a comprehensive study of coagulating particles in different regimes. For fractal-like particles, the relative positions of primary particles in both coagulating particles matter and the coagulation model must account for geometry in determining the resulting aggregate structure.

A limitation of the combined surface area particle model (Section 3.2.3) is that the relative 3D positions of primary particles in each aggregate are not known; thus, coagulation cannot account for inaccessible points of contact. For the overlapping-spheres particle model with primary coordinate-tracking (Section 3.2.4), the relative positions of primary particles in both coagulating particles matter and the coagulation model must resolve the resulting aggregate structure. This is achieved using a BCCA algorithm with a random impact parameter as outlined by Lindberg et al. [81]. The collision direction is determined by rotating each particle around its centre of mass to a random orientation and a point of contact on one of the particles is chosen at random. Then a random impact is obtained by placing the second particle at an arbitrary position in the plane perpendicular to the collision direction. This process is illustrated in Fig. 3.6.

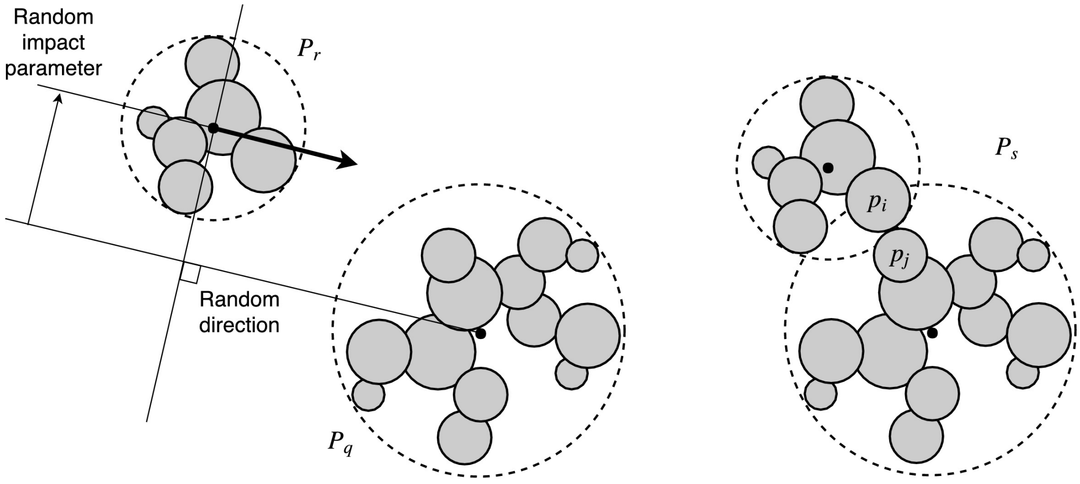

(a) (b)

Fig. 3.6: Ballistic cluster-cluster agglomeration with random impact parameter showing (a) Particles P_q and P_r before collision; and (b) newly created particle P_s with established point contact connecting primary particle p_i of P_r to primary particle p_j of P_q. Figure taken from Lindberg et al. [81] with permission.

3.4.4 Sintering

Coagulation creates point contact between neighbouring pairs of primary particles, p_i and p_j, and this is strengthened by sintering. Sintering is a process that triggers structural changes in connected primary particles, melding them together more cohesively to reduce their surface area and thus their surface free energy. This process is especially rapid at high temperatures.

As in previous work [161, 167], it is assumed that the excess radius over that of a volume-equivalent spherical particle decays exponentially resulting in a change in the common particle surface area, A_{ij},

$$\frac{dA_{ij}}{dt} = -\frac{1}{\tau_\mathrm{c}}\left(A_{ij} - A_{ij}^{\mathrm{sph}}\right). \tag{3.26}$$

A_{ij}^{sph} is the surface area of the volume-equivalent spherical particle and τ_c is the characteristic sintering time. Different expressions have been formulated for this parameter using different neck growth models such as grain boundary or surface diffusion [19] in attempt to find agreement with experimental results [115]. For example Kobata et al. [60] proposed,

$$\tau_\mathrm{c} = 7.44 \times 10^{16} T d_\mathrm{p}^4 \exp\left(\frac{258 \times 10^3}{RT}\right), \tag{3.27}$$

where d_p is the primary diameter in units of meters (m) to match the constant. This expression, which characterises titania particles sintering through grain boundary diffusion, is used to model sintering for the combined surface area particle model (Section 3.2.3), as in earlier work [103, 161, 167].

Sintering releases heat because the surface tension changes as particles sinter [74, 174]; and this phenomenon is particularly important when particles are very small (less than 10 nm [73]) because the energy released heats the particle surface, causing it to behave more like a liquid and sinter more rapidly. Tsantilis et al. [153] suggested that the sintering rate should account for the particle size dependence of the melting temperature, leading to a formulation for silica that depends on the ratio of the primary diameter and a given minimum primary diameter, $d_{\mathrm{p,min}}$. This increases the sintering rate for small particles. A similar formulation for titania was proposed by Buesser et al. [19] by fitting molecular dynamics data.

As with coagulation, the overlapping-spheres particle model requires a model that accounts for the particle geometry. Lindberg et al. [81] followed the approach of Eggersdorfer et al. [32] [79] and modelled sintering by grain boundary diffusion in terms of the rate of change of primary particle separation with characteristic time, τ_c,

$$\tau_\mathrm{c} = 9.112 \times 10^{17} T d_\mathrm{p}^4 \exp\left(\frac{258 \times 10^3}{RT}\left(1 - \frac{d_\mathrm{p,min}}{d_\mathrm{p}}\right)\right). \tag{3.28}$$

A minimum diameter of $d_\mathrm{p,min} = 4\,\mathrm{nm}$ was suggested [81] to increase the sintering rate for the smallest particles as determined by Buesser et al. [19] to be a critical size. The primary diameter used to compute the sintering rate between the pair (p_i, p_j) is

$$d_\mathrm{p} = \min\left(d_\mathrm{p}(p_i), d_\mathrm{p}(p_j)\right). \tag{3.29}$$

A (particle-model specific) 'sintering level', $s_{ij} \in [0,1]$, is defined to reflect the degree of cohesion between each neighbouring pair of primary particles p_i and p_j. Three values of sintering level should be highlighted here: a sintering level of $s_{ij} = 0$ represents particles in point contact with combined surface area, $A_{ij}^{(0)}$, equal to the sum of their areas, a sintering level of $s_{ij} = 1$ represents a fully-coalesced or loose primary particle, and a sintering level of $s_{ij} \geq 0.95$ is used as the cut-off in the model for performing coalescence [173]. Intermediate levels, $s_{ij} \in (0, 0.95)$, describe partially sintered particles, connected by a 'neck' of non-zero radius. The ability to describe such connections is one of the critical advantages of using a multivariate particle model for this work since the necks determine the milling energy requirement to post-process the particulate product to suitable sizes.

For the combined surface area model (Section 3.2.3), the sintering level is defined as the extent of decay towards a volume-equivalent sphere [140],

$$s_{ij} = \frac{\frac{A_{ij}^\mathrm{sph}}{A_{ij}} - \frac{A_{ij}^\mathrm{sph}}{A_{ij}^{(0)}}}{1 - \frac{A_{ij}^\mathrm{sph}}{A_{ij}^{(0)}}}. \tag{3.30}$$

For the overlapping-spheres particle model (Section 3.2.4), the sintering process reduces the centre-to-centre distance between connected primaries, creating an increase in the primary radii and the centre-to-centre distance of neighbouring pairs to conserve mass. The equations for how these properties alter as particles sinter are provided in the paper by Lindberg et al. [81] and not reproduced here. The sintering level is defined as the ratio of this neck radius, r_{ij}, to the radius of the smaller of the two primary particles,

$$s_{ij} = \tfrac{r_{ij}}{r_j}, \quad r_j \leq r_i. \tag{3.31}$$

3.5 Numerical methods

This section provides features of the numerical method and implementation details. The coupling between the phases is achieved using an operator splitting technique (Section 3.5.1) and the discrete particle phase (Section 3.5.2) is evolved using a stochastic numerical method (Section 3.5.3). Several advances have been proposed in previous work to improve performance and these are highlighted. Existing numerical challenges are discussed as these are relevant to the development of the new approach presented in Chapter 5. Key features of the algorithms discussed in Sections 3.5.1–3.5.3 are illustrated in Fig. 3.10, which appears at the end of this chapter, on page 55.

3.5.1 Operator splitting

The gas phase and particle processes are coupled due to mass transfer from the gas phase to the particle system during inception and surface growth, gas phase expansion and heat flux. The heat flux from particle processes was neglected in previous work (e.g. Celnik et al. [21] and Menz et al. [101]) for simplicity, on assumption that the particle volume fraction is negligible. This is addressed in Chapter 6 for cases where particles constitute a significant portion of the system's mass (as in industrial titania synthesis [50]) and are thus a relevant component of the energy model.

The gas phase is described by a set of 30 ordinary differential equations (ODEs) for composition and temperature. This system is suited to solution using an implicit ODE method. The particle phase is best treated as an ensemble of computational particles which evolves by discrete jump processes (i.e. a Monte Carlo method) because the particle type-space model is very high-dimensional and other approaches suffer the 'curse of dimensionality' which results in infeasible computational cost for more than a few dimensions. The Monte Carlo method used in this thesis is termed the direct simulation algorithm (DSA) (Section 3.5.3).

The coupling between the phases is achieved using the Strang operator splitting technique presented in Celnik et al. [21]. Celnik and co-authors presented an alternative, predictor-corrector approach [20] in later work. This was aimed at addressing source-sink issues between the phases and improving efficiency by not reinitialising the ODE solver so frequently. In the current work, the latter method was found to be considerably slower because the solver initialisation is a minor cost compared to the particle updates and the predictor-corrector algorithm employs iterative simulation of the particle processes. Source-sink issues can be mitigated by choosing sufficiently small splitting steps – this step size becomes a numerical parameter which must be considered during convergence studies [21, 140].

Operator splitting decomposes each differential equation (with reference to Eqs. (3.1)–(3.4)) into a sum of parts,

$$\begin{aligned}
\frac{dC_k}{dt} &= \underbrace{\mathcal{W}(\mathbf{C},T)+\mathcal{F}_{\mathrm{g}}(C_k)}_{\text{(I)}}+\underbrace{\mathcal{G}(\mathbf{C},T,n)}_{\text{(II)}}, && k=1,\ldots,N_{\mathrm{SP}},\\
\frac{dn(x)}{dt} &= \underbrace{\mathcal{I}(x,\mathbf{C},T)+\mathcal{K}(x,n,T)+\mathcal{S}(x,\mathbf{C},T)+\mathcal{F}_{\mathrm{p}}(n)}_{\text{(II)}}, && x\in\mathcal{E},
\end{aligned}$$

and then solves these separately. Strang splitting [149] is a particular variant in which accuracy is improved to second-order by use of overlapping time steps. For the systems considered here, the gas phase and particle phase are solved in separate steps, and changes to the gas phase due to particle processes are ‘split’ off from the ODE system and performed during discrete particle updates. To optimise time spent restarting the ODE solver while maintaining second order accuracy [21], the parts labelled (I) can be integrated for half a splitting time step at the beginning and end and successive integration of the parts labelled (II) and (I) can be performed successively for a chosen number of operator splitting steps in between these initial and final half-steps (Fig. 3.10, top panel). The core components of the coupled solver are outlined in Steps (1)–(3).

Step (1): $t\in\left[t_0,t_{1/2}\right]$, $t_{1/2}=t_0+\frac{\Delta t}{2}$
Solve the ODEs for changes in gas phase concentrations and temperature due to gas phase reactions and flow (I), starting with $\mathbf{C}(t_0)$, $T(t_0)$, $n(t_0,x)$,

$$\begin{aligned}
\frac{dC_k}{dt} &= \mathcal{W}(\mathbf{C},T)+\mathcal{F}_{\mathrm{g}}(C_k),\\
\frac{dn(x)}{dt} &= 0,
\end{aligned}$$

yielding $\mathbf{C}\left(t_{1/2}\right)$, $T\left(t_{1/2}\right)$, $n\left(t_{1/2},x\right)$.

Step (2): $t\in[t_0,t_1]$, $t_1=t_0+\Delta t$
Solve the PBE to update the particle system for particle processes and update the gas phase state accordingly to account for particle processes that consume/create gas species (II), starting with $\mathbf{C}\left(t_{1/2}\right)$, $T\left(t_{1/2}\right)$, $n\left(t_{1/2},x\right)$,

$$\begin{aligned}
\frac{dC_k}{dt} &= \mathcal{G}(\mathbf{C},T,n),\\
\frac{dn(x)}{dt} &= \mathcal{I}(x,\mathbf{C},T)+\mathcal{K}(x,n,T)+\mathcal{S}(x,\mathbf{C},T)+\mathcal{F}_{\mathrm{p}}(n),
\end{aligned}$$

yielding $\mathbf{C}(t_1)$, $T(t_1)$, $n(t_1,x)$.

Step (3): $t \in \left[t_{1/2}, t_1\right]$
Solve the ODEs for changes in gas phase concentrations and temperature due to gas phase reactions and flow (I), starting with $\mathbf{C}(t_1)$, $T(t_1)$, $n(t_1,x)$,

$$\begin{aligned}\frac{dC_k}{dt} &= \mathcal{W}(\mathbf{C},T) + \mathcal{F}_{\mathrm{g}}(C_k),\\ \frac{dn(x)}{dt} &= 0,\end{aligned}$$

yielding $\mathbf{C}'(t_1)$, $T'(t_1)$, $n'(t_1,x)$.

3.5.2 Discrete particle systems

The particle phase is modelled by considering a finite ensemble of discrete computational particles, P_q, $q = 1,\ldots,N \leq N_{\max}$, in a sample volume V_{smp} (Fig. 3.7). Each computational particle represents a certain concentration of physical particles, with the sample volume defining the scaling between the physical and simulated systems. For each computational particle, the list of its primary particles (with their individual compositions), the primary particle connectivity, and the available surface area are tracked throughout a simulation and used to specify the process rates.

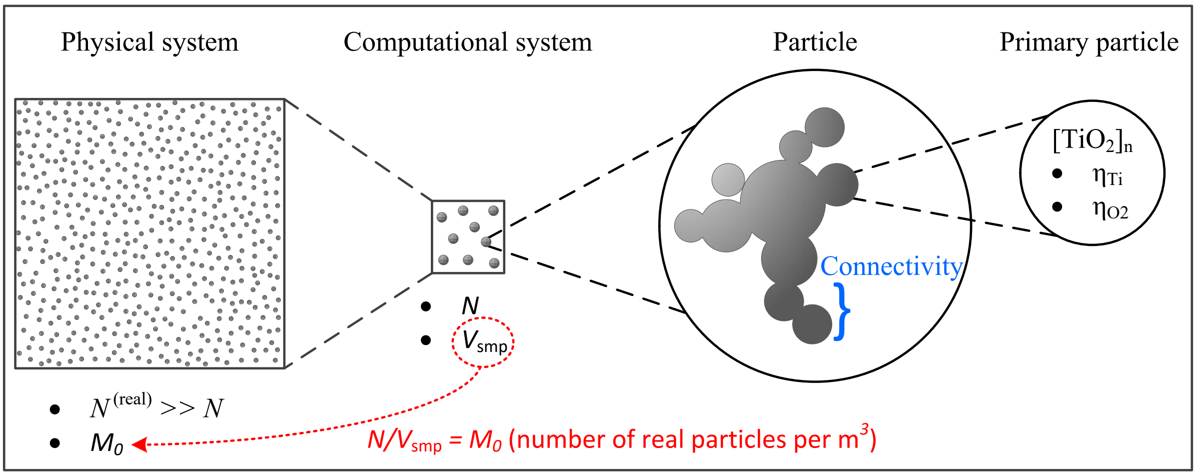

Fig. 3.7: Computational representation of the physical system, using N simulation particles in a sample volume V_{smp}, and primary particle connectivity and composition within the particle.

The user-defined upper limit on the number of computational particles in the simulation is given by $N_{\max}$. Theoretical convergence of the population balance equation as $N_{\max} \to \infty$

has been studied by Eibeck and Wagner [35], Patterson [116, 117] and Wells [159]. These studies analyse the mathematical formulation of the population balance equation and show that it recovers the correct behaviour in the limit of fine discretization in the particle space (i.e. for sufficiently large sample sizes). Such results are difficult to prove in general, but can be obtained by restricting what processes are studied, by careful construction of the jump operators defining the processes and by using weaker notions of convergence.

An important aspect of using these discrete particle systems is choice of suitable numerical parameters. Numerical convergence studies have already been mentioned in the context of choosing an appropriate splitting time step. More generally, numerical convergence studies are used to determine suitable simulation parameters to achieve a desired level of statistical accuracy. Other such simulation parameters are the maximum ensemble capacity, N_{max}, which is typically pre-defined, and the number of repeat runs, L. For linear particle processes, these two parameters have the same effect on the accuracy; however, this is not always the case – for example more than one particle is required to model coagulation, which is a nonlinear process because of particle interactions.

A common test is to hold the product $(N_{\text{max}} \times L)$ constant and increase N_{max}, checking the total error relative to a reference solution [81, 101, 140]. Initially, the discretization in error introduced by small N_{max} dominates; thus increasing N_{max} results in decreasing error with slope of '-1' on a log-scale plot. For sufficiently large N_{max}, the statistical error dominates and this is fixed for constant $N_{\text{max}} \times L$; thus, the error stabilises. This technique allows a modeller to choose suitable parameters to achieve a desired level of statistical resolution. Convergence studies are presented in Chapters 4 and 5 for the systems studied in this work.

The choice of numerical parameters requires consideration of the system being studied. For example, larger time steps can be accommodated if there is no danger of source-sink or related stiffness issues and narrow PSDs can be resolved with smaller particle ensembles. The sample volume, V_{smp}, is another parameter that was found to be important in this work. The sample volume provides the scaling between the real system and the model system,

$$M_0 = \frac{N^{\text{real}}}{V^{\text{real}}} = \frac{N}{V_{\text{smp}}}, \tag{3.32}$$

and as such is not an independent parameter if N is specified and the system has an inherent number density. However, the sample volume provides the scaling between the real and numerical rates. For example, for a unit real volume,

$$\mathcal{I}^{\text{num}}(x, \mathbf{C}, T) = \mathcal{I}^{\text{real}}(x, \mathbf{C}, T)\, V_{\text{smp}}. \tag{3.33}$$

In a small sample volume, there is a correspondingly low probability that events occur, leading to poor statistical resolution. Representatively more events occur in a large sample volume, and this can rapidly saturate an ensemble with a predefined capacity N_{max}. So-called doubling and contractions algorithms have been proposed to treat these issues by: (i) duplicating the ensemble and doubling the sample volume when too few particles exist; and (ii) randomly removing an existing ensemble particle and reducing the sample volume when capacity is exceeded and a particle addition event occurs. Doubling is illustrated in the paper by Shekar et al. [140] – for a coagulation process, it leads to zigzagging in the ensemble count as the ensemble constantly depletes and refills.

For systems with source and sink processes, doubling and contraction have a feedback effect in that they can eventually hone in on a suitable sample volume by iteratively compensating for the process rates (inception and inflow vs. coagulation and outflow). However, for doubling to occur, there needs to be sufficiently many initial particle inception events to provide some resolution, so the sample volume cannot be allowed to be too small. Excessive contractions caused by rapid inception or particle inflow events (Fig. 3.8, right-side schematic shows ensemble filling) rapidly randomize the ensemble – resulting in high error. Numerical studies demonstrating statistical error associated with removals [63] indicate that errors can worsen over time as the average particle size in the system increases because the change wrought by removal becomes more significant.

Because the numerical parameters are related to the real number density by Eq. (3.32), excessive contractions can be remedied by restarting simulations with (Fig. 3.8, left-side call-outs show restart options) a smaller sample volume (less numerical inception) or a larger pre-defined ensemble (more space for particles). Reducing the sample volume lowers the resolution that can be achieved in the PSD and increasing the ensemble size is memory intensive and expensive. In any event, this parameter can require time-consuming manual adaptation or enforce small steps to mitigate error. Simulation of changing process rates, for example due to transience or temperature gradients, can exacerbate this difficulty.

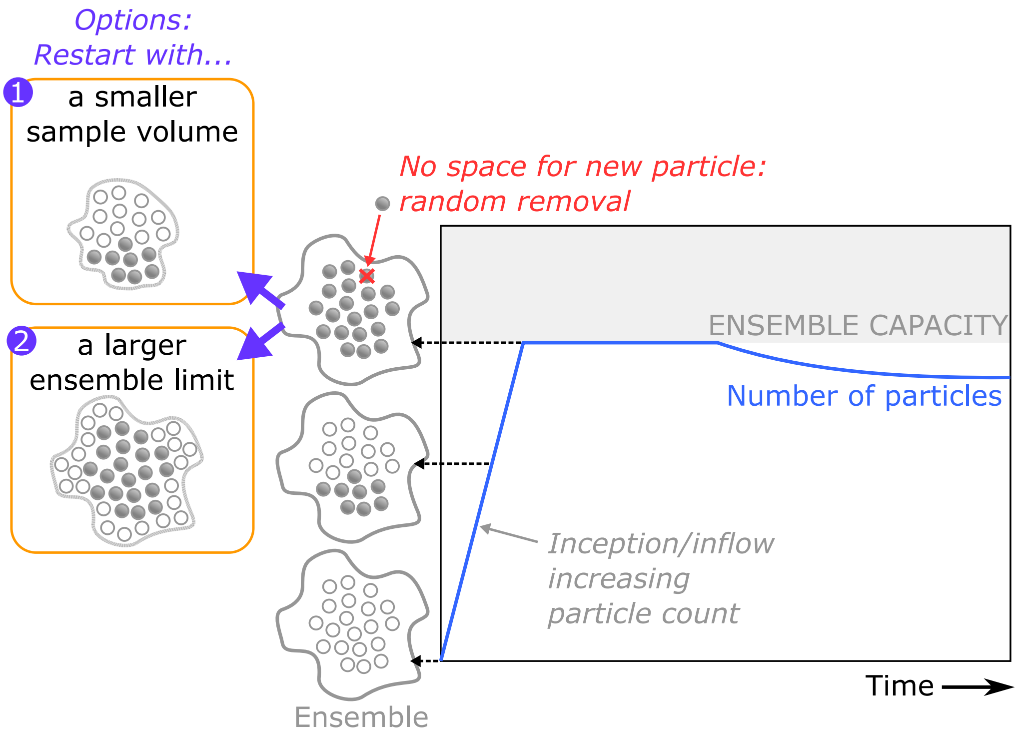

Fig. 3.8: Ensemble filling leading to random particle removal and prevention strategies for finite computational ensembles.

3.5.3 Direct simulation algorithm

The dynamics of the evolution of the discrete particle system are approximated by propagating discrete trajectories of individual particles using a stochastic simulation, an approach known as the Gillespie Algorithm [46]. Rather than solving the time evolution of the PBE solution, as in the ODE case, these trajectories constitute samples from the distribution of particles satisfying the PBE. Therefore, their properties can be be aggregated to describe macroscopic information about the particle phase, avoiding needing to perform integration in the high-dimensional particle type-space. The direct simulation algorithm (DSA) used in this work is a direct simulation Monte Carlo method that derives from algorithms proposed by Eibeck and Wagner [33] and Goodson and Kraft [48]. The system is treated as a Markov jump process [116] and particle formation and growth are modelled by performing randomly chosen updates directly on the discrete ensemble of computational particles at random times (Fig. 3.10, lower block). Here, 'random' refers to probabilistic choice of events and times in such a manner as to realize the correct behaviour of the system, and filter out unlikely behaviour, in the limit of many repetitions. The waiting time between events is drawn from an exponential distribution specified by the total process rate,

$$R_{\text{total}} = R_{\text{inception}} + R_{\text{surface reaction}} + R_{\text{coagulation}} \tag{3.34}$$

$$\tau \sim \exp\left(R_{\text{total}}\right). \tag{3.35}$$

so that the mean waiting time is the inverse of the total rate. The total process rate, R_{total}, is computed by summation of the rates of the formation and growth processes, R_{process}, where process $\in$ {inception,coagulation,surface reaction} and R_{process} is the numerical process rate, computed by summation over all particle types (i.e. for all simulation particles) of the respective rates provided by Eqs. (3.17), (3.19) and (3.21),

$$R_{\text{inception}} = V_{\text{smp}} \sum_{\{\alpha,\beta\}} I\left(P_{\text{inc}}^{\alpha\beta}, \mathbf{C}, T\right) \tag{3.36}$$

$$R_{\text{surface reaction}} = \sum_{i=1}^{N} \beta_{\text{SG}}\left(P_i, \mathbf{C}, T\right) \tag{3.37}$$

$$R_{\text{coagulation}} = \frac{1}{2V_{\text{smp}}} \sum_{i=1}^{N} \sum_{\substack{j=1 \\ j\neq i}}^{N} K\left(P_i, P_j\right), \tag{3.38}$$

where $P_{\text{inc}}^{\alpha\beta}$ is the particle incepted with type $x \equiv \left(x_\alpha + x_\beta\right)$ TiO_2 monomers with $\{\alpha,\beta\}$ the stoichiometry satisfying the inception process shown in Eq. (3.17).

The probability of selecting a particular process is given by the ratio of the individual and overall process rates,

$$\mathbb{P}\left(\text{process}\right) = \frac{R_{\text{process}}}{R_{\text{total}}}. \tag{3.39}$$

Once a process is selected, the particle system and gas phase are updated accordingly. The system time is then incremented by the associated waiting time and this exercise is iterated until the end of the DSA step. In this work, inception, coagulation and surface growth are modelled as stochastic processes and sintering is modelled as a continuous process.

Treatment of flow

Most studies using Monte Carlo methods presented in the literature do not include particle flow processes in the stochastic solver. These are typically not considered at all, or are treated by moving particles between cells in a separate step. This thesis considers networks of idealised flow reactors, building on the reactor network studies of Menz et al. [101]. Particle inflow to each reactor is treated as a stochastic process and outflow is performed continuously to minimise propagation of error [101]. In both cases, the residence time of the reactor (effectively the ratio of the flow rate to reactor volume) is used to determine the rate of flow events. Inflow requires that the distribution of particles in the feed stream is specified, possibly from an upstream reactor model. In each stochastic inflow event, a particle is sampled from this distribution, and then a number of copies are added to the reactor as determined by the ratio of sample volumes in the feed stream and the reactor in order to account for the number of real particles represented in each case. All particles have the same residence time, which implies that all particles travel at the same average velocity through the system and neglects variations arising from drag on larger aggregates. Continuous outflow can be achieved by either rescaling the sample volume or removing particles at the end of each time step to yield a representative decrease in particle number density, as determined by the flow rate and time interval. The reactors in the network are solved sequentially.

Efficient simulation techniques

A majorant kernel technique is used to compute the coagulation rate and perform coagulation events. Majorant kernels [33, 48, 99, 121, 132] provide a means to compute the coagulation rate and perform coagulation events more efficiently. The true total coagulation rate scales with the square of the number of particles in the system and is computationally expensive to compute because it involves double summation over all particle pairs and is typically a nonlinear function of the particle properties, for example, for the free molecular regime kernel (Eq. (3.22)), the total numerical coagulation rate, $R^{\mathrm{fm}}_{\mathrm{coagulation}}$, is:

$$R^{\mathrm{fm}}_{\mathrm{coagulation}} = \frac{1}{2V_{\mathrm{smp}}} \sum_{i=1}^{N} \sum_{\substack{j=1 \\ j\neq i}}^{N} \left[2.2 \sqrt{\frac{\pi k_{\mathrm{B}} T}{2} \left(\frac{1}{m(P_i)} + \frac{1}{m(P_j)} \right)} \left(d_{\mathrm{c}}(P_i) + d_{\mathrm{c}}(P_j) \right)^2 \right].$$

The majorant technique relies on finding an upper bound on the true coagulation rate that is less expensive to calculate. Continuing with the example of the free molecular kernel and defining the constant

$$\beta_1 = 4.4\sqrt{\frac{\pi k_{\mathrm{B}} T}{2}},$$

a valid majorant kernel, $\hat{K}_{\text{fm}}$, is [99]:

$$\hat{K}_{\text{fm}}\left(P_i,P_j\right)=\beta_1\left(\frac{1}{\sqrt{m\left(P_i\right)}}+\frac{1}{\sqrt{m\left(P_j\right)}}\right)\left(d_{\text{c}}\left(P_i\right)^2+d_{\text{c}}\left(P_j\right)^2\right). \tag{3.40}$$

The total coagulation rate is bound from above by the rate computed with the majorant kernel, $R^{\text{fm}}_{\text{coagulation}} \leq \hat{R}^{\text{fm}}_{\text{coagulation}}$, which is computed as:

$$\begin{aligned}\hat{R}^{\text{fm}}_{\text{coagulation}} =& \frac{\beta_1}{2V_{\text{smp}}}\sum_{i=1}^{N}\sum_{\substack{j=1\\ j\neq i}}^{N}\left[\frac{d_{\text{c}}\left(P_i\right)^2}{\sqrt{m\left(P_i\right)}}+\frac{d_{\text{c}}\left(P_i\right)^2}{\sqrt{m\left(P_j\right)}}+\frac{d_{\text{c}}\left(P_j\right)^2}{\sqrt{m\left(P_i\right)}}+\frac{d_{\text{c}}\left(P_j\right)^2}{\sqrt{m\left(P_j\right)}}\right]\\ =& \frac{\beta_1}{2V_{\text{smp}}}\left[\underbrace{(N-1)\sum_{i=1}^{N}\frac{d_{\text{c}}\left(P_i\right)^2}{\sqrt{m\left(P_i\right)}}}_{(1)}+\underbrace{\sum_{i=1}^{N}d_{\text{c}}\left(P_i\right)^2\sum_{i=1}^{N}\frac{1}{\sqrt{m\left(P_i\right)}}-\sum_{i=1}^{N}\frac{d_{\text{c}}\left(P_i\right)^2}{\sqrt{m\left(P_i\right)}}}_{(2)}\right]\end{aligned}$$

and does not require double summation – in fact, the sums of properties can be cached and updated efficiently as will be described next. The majorant rate is used to specify the frequency and probability of events (i.e. it is used as the coagulation rate in Eqs. (3.35) and (3.39)). Because it over-estimates the rate, the majorant over-predicts the frequency of events. This is corrected by using fictitious jumps – a coagulation event only occurs successfully with probability equal to the ratio of the true kernel to the majorant kernel for the chosen particle pair,

$$\mathbb{P}\left(\text{success}\right)=\frac{K\left(P_i,P_j\right)}{\hat{K}\left(P_i,P_j\right)}, \tag{3.41}$$

which only requires the real kernel be computed for a single pair of particles. This technique requires reasonable choice of majorant kernel – choosing a kernel much larger than the true kernel is inefficient because it requires frequent stops to attempt coagulation events that will ultimately not occur because they are found to be fictitious.

The slip-flow kernel does not require a majorant. Defining two constants

$$\beta_2=\frac{2k_{\text{B}}T}{3\mu}, \qquad \beta_3=1.257\times 4.74\times 10^{-8}\frac{T}{\mathcal{P}},$$

the slipflow kernel can be written

$$K_{\mathrm{sf}}\left(P_i,P_j\right)=\beta_2\left(2+\frac{d_{\mathrm{c}}\left(P_i\right)}{d_{\mathrm{c}}\left(P_j\right)}+\frac{d_{\mathrm{c}}\left(P_j\right)}{d_{\mathrm{c}}\left(P_i\right)}+\beta_3\left(\frac{1}{d_{\mathrm{c}}\left(P_i\right)}+\frac{d_{\mathrm{c}}\left(P_i\right)}{d_{\mathrm{c}}\left(P_j\right)^2}+\frac{d_{\mathrm{c}}\left(P_j\right)}{d_{\mathrm{c}}\left(P_i\right)^2}+\frac{1}{d_{\mathrm{c}}\left(P_j\right)}\right)\right). \tag{3.42}$$

The corresponding total numerical coagulation rate, $R^{\mathrm{sf}}_{\mathrm{coagulation}}$, is computed to be

$$\begin{aligned}
R^{\mathrm{sf}}_{\mathrm{coagulation}} =& \frac{\beta_2}{2V_{\mathrm{smp}}}\sum_{i=1}^{N}\sum_{\substack{j=1\\ j\neq i}}^{N}\left[2+\frac{d_{\mathrm{c}}\left(P_i\right)}{d_{\mathrm{c}}\left(P_j\right)}+\frac{d_{\mathrm{c}}\left(P_j\right)}{d_{\mathrm{c}}\left(P_i\right)}\right.\\
&\left.+\beta_3\left(\frac{1}{d_{\mathrm{c}}\left(P_i\right)}+\frac{d_{\mathrm{c}}\left(P_i\right)}{d_{\mathrm{c}}\left(P_j\right)^2}+\frac{d_{\mathrm{c}}\left(P_j\right)}{d_{\mathrm{c}}\left(P_i\right)^2}+\frac{1}{d_{\mathrm{c}}\left(P_j\right)}\right)\right]\\
=& \frac{\beta_2}{V_{\mathrm{smp}}}\left[\underbrace{N\left(N-1\right)}_{(1)}+\underbrace{\left(\sum_{i=1}^{N}d_{\mathrm{c}}\left(P_i\right)\sum_{i=1}^{N}\frac{1}{d_{\mathrm{c}}\left(P_i\right)}-N\right)}_{(2)}\right.\\
&\left.+\beta_3\left(\underbrace{\left(N-1\right)\sum_{i=1}^{N}\frac{1}{d_{\mathrm{c}}\left(P_i\right)}}_{(3)}+\underbrace{\left(\sum_{i=1}^{N}d_{\mathrm{c}}\left(P_i\right)\sum_{i=1}^{N}\frac{1}{d_{\mathrm{c}}\left(P_i\right)^2}-N\sum_{i=1}^{N}\frac{1}{d_{\mathrm{c}}\left(P_i\right)}\right)}_{(4)}\right)\right].
\end{aligned}$$

The free molecular terms labelled (1) and (2) and the slipflow terms labelled (1)–(4) yield the equations and selection properties given in Table 3.1 for coagulation rate terms and particle pairs respectively [99, 121]. The six selection probabilities in the third and fourth columns of Table 3.1 are derived from the corresponding coagulation rate terms in the second column, and are used to select particle pairs for coagulation according to their properties. The rate terms arise from summation of the majorant kernel over all particles. These are used to define probabilities of each selection process being chosen for a coagulation event.

Once a process is selected, the corresponding selection probabilities are used to choose a particle pair (that is, the particle property used to select a particle is specified by the relevant row and column of Table 3.1). Thus, the particle particle pairs with higher majorant rates are selected more often than the ones with lower rates. The real coagulation rate for the coagulating particle pair is compared to its majorant rate and this defines the probability of a real/fictitious event (Eq. (3.41)).

Table 3.1: Particle properties used to choose coagulation pair (P_i, P_j) based on transition regime majorant kernel terms.

Term	Equation	P_i	P_j
Free-molecular 1	$(N-1)\sum d_i^2 m_i^{-1/2}$	Uniform	$d_c(P_j)^2 m(P_j)^{-0.5}$
Free-molecular 2	$\sum d_i^2 \sum m_i^{-1/2} - \sum d_i^2 m_i^{-1/2}$	$d_c(P_i)^2$	$m(P_j)^{-0.5}$
Slip-flow 1	$N(N-1)$	Uniform	Uniform
Slip-flow 2	$\sum d_i \sum d_i^{-1} - N$	$d_c(P_i)$	$d_c(P_j)^{-1}$
Slip-flow 3	$(N-1)\sum d_i^{-1}$	Uniform	$d_c(P_j)^{-1}$
Slip-flow 4	$\sum d_i \sum d_i^{-2} - \sum d_i^{-1}$	$d_c(P_i)$	$d_c(P_j)^{-2}$

Binary tree data structures are used to store the primary particle lists for each computational particle [81], and the sums of particle properties (e.g. diameter, inverse mass, etc.) for the ensemble [133]. This provides an efficient means of selecting particles or primaries based on a specific property [120]. For $N_{\max}$ computational particles, the binary tree has $\log_2(N_{\max})$ levels and a particle is selected by traversing the tree by finding a suitable node on each level of the tree (Fig. 3.9, solid arrow). When a property changes, only one node per level needs to be updated (Fig. 3.9, dashed arrow). A consequence of this approach is that the maximum number of computational particles, $N_{\max}$, must be a power of 2; thus typical ensemble capacities could be $2^7 = 128$, $2^{10} = 1024$, $2^{17} = 131072$ etc.

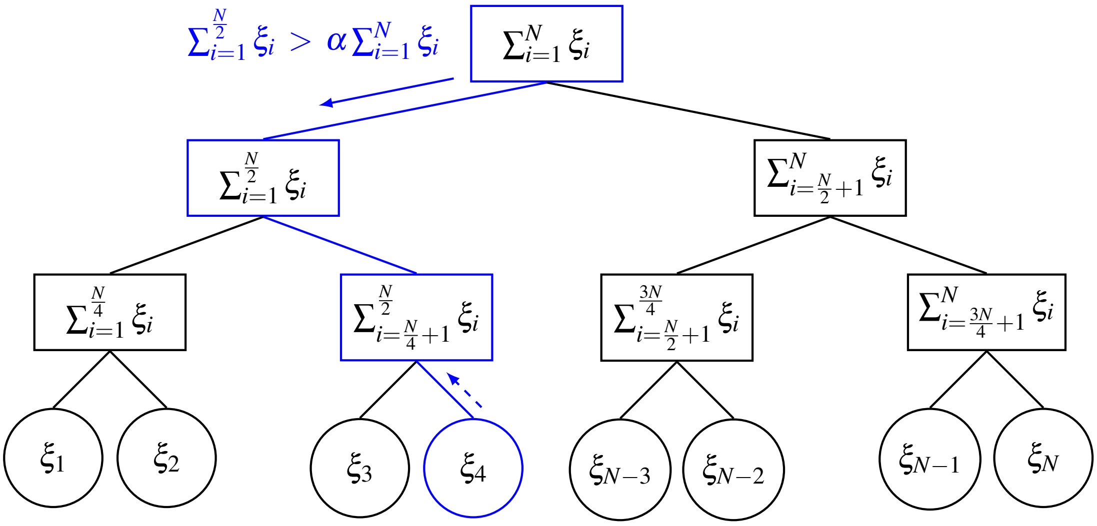

Fig. 3.9: Binary tree for particle property ξ showing particle selection using random value $\alpha \in (0,1)$ (follows blue path in direction of solid arrow) and update of cached values (follows blue path in direction of dashed arrow).

The linear process deferment algorithm (LPDA) is used for surface updates (here, surface growth and sintering). This was proposed by Patterson et al. [120] to aid simulations where surface growth dominates the solver time because the rate is much higher than the rates of other process (per Eqs. (3.34) and (3.35), this leads to very short wait times and frequent pauses to perform surface growth events; LPDA removes $R_{\text{surface reaction}}$ from the total rate, resulting in longer wait times and less frequent updates). It is noted that linear processes only affect single particles – i.e. changes to the particle surfaces occur independently of other particles in the system. These linear processes are held off and only performed at the end of each DSA step when all particles are updated for the amount of time that processes have been held off.

The risk with this is that particles picked for coagulation have incorrect surface structure because updates during the time step have been deferred. To mitigate this, surface updates are performed on the particles chosen for coagulation before they coagulate – thus checking that the majorant kernel is greater than the true kernel before combining particles during coagulation can also cancel out unlikely events after the surface update. As LPDA is a form of operator splitting, it requires small time steps to avoid altering the dynamics by decoupling the processes. In the original paper, LPDA was shown to be orders of magnitude faster for systems with high surface growth rates, without significant loss of simulation accuracy.

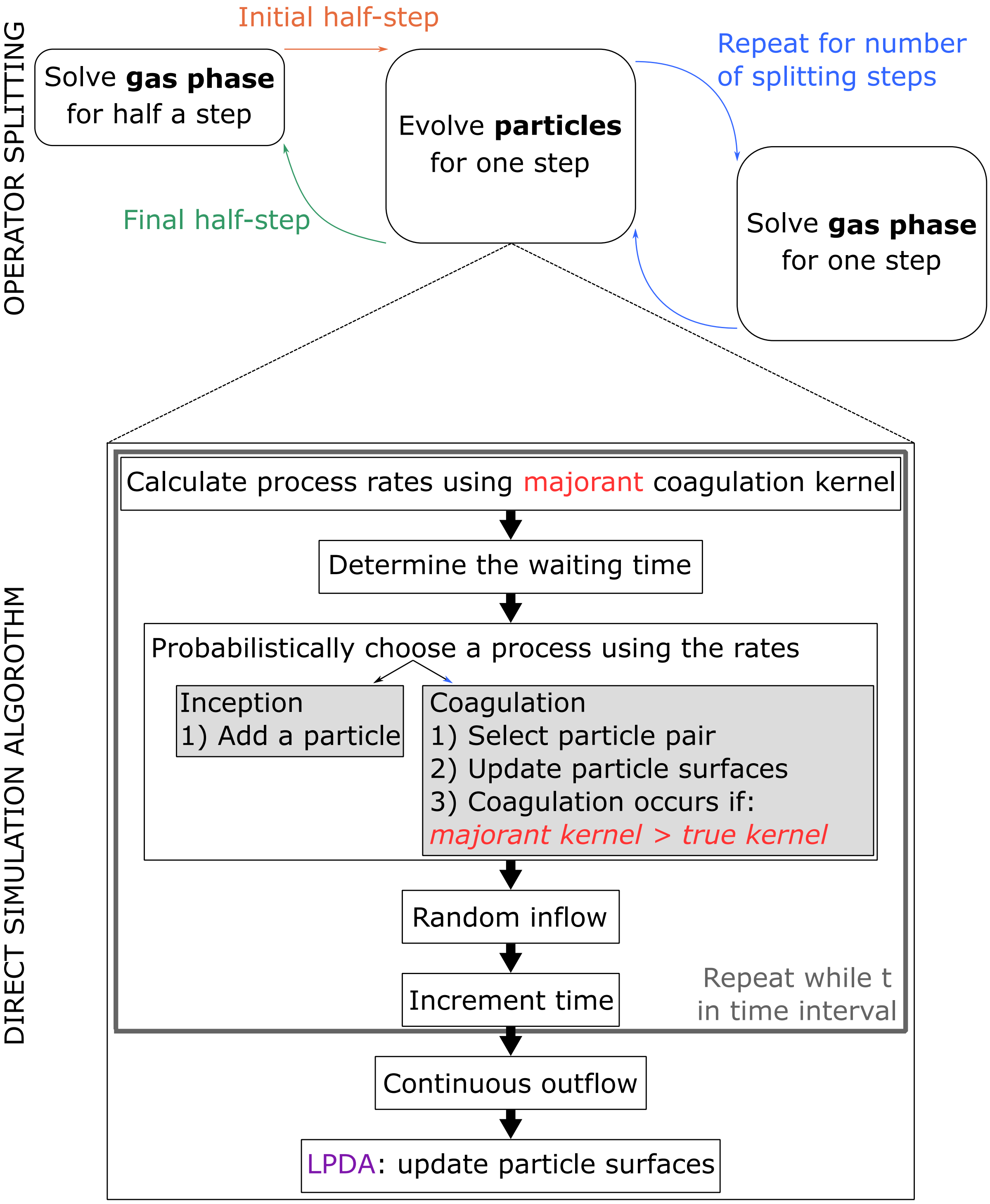

Fig. 3.10: Operator splitting procedure for coupling the gas and particle phases with inset showing key steps in the direct simulation algorithm for advancing the particle system.

Chapter 4

Detailed population balance modelling with simplified flow

This chapter presents a new model for simulating industrial titania synthesis with a detailed particle model. The industrial titania reactor has multiple reactant injections, a tubular working zone in which the exothermic reaction is completed, and a cooling zone. A network of continuously stirred tank reactors is used to model variation in composition around the feeds, and plug flow reactors with prescribed temperature gradients are used to describe the working and cooling zones. Particle morphology is characterized in terms of the distribution of different structural properties such as primary diameter and neck radius. Process conditions are shown to influence particle size – with larger particles formed at higher temperatures and lower throughputs. Qualitative similarities are highlighted between such findings and previous studies. The throughput studies are also in qualitative agreement with empirical industrial experience. There is scope for further extension of the model; however, it is suggested that insights of this type could be used to inform the design and operation of the industrial process. Material from this chapter was published in ***Paper 1*** *listed in the Declaration.*

4.1 Reactor model

This chapter develops a model for an industrially representative, multi-injection titania reactor. The reactor has two distinct zones (Fig. 4.1 shaded and unshaded parts). The dosing zone (the shaded part) is the first part of the reactor, with spatial coordinates $\theta \in \left[0, \mathcal{L}_{\text{dosing zone}}\right]$. High temperature oxygen enters the dosing zone at $\theta = 0$, and reactant gases $TiCl_4$ and O_2 are fed through the wall at three subsequent points (labelled f_2–f_4 in Fig. 4.1). The second part of the reactor, $\theta \in \left(\mathcal{L}_{\text{dosing zone}}, \mathcal{L}_{\text{working zone}}\right]$, is called the working zone (the unshaded part). Here, the gas phase reactions continue almost to completion and the particulate product undergoes further growth.

Temperature does not increase significantly in the dosing zone (profile shown qualitatively in Fig. 4.1) due to the effect of relatively cool reactant injections through the reactor wall. Temperature increases across the working zone (profile shown qualitatively in Fig. 4.1) due to heat release from the exothermic oxidation reaction. The temperature of the particulate product from the reactor is reduced in a cooler that is several times the reactor length.

An ideal reactor network (Fig. 4.2) is used to account for the axial variation in composition and temperature, while keeping the flow model simple enough to use a detailed particle model (Section 3.2.2) and comprehensive gas phase mechanism (Section 3.3). The reactor network consists of a linear sequence of eleven isothermal, constant volume, continuously stirred tank reactors (CSTRs) and two plug flow reactors (PFRs), with the gas and particle phases governed by Eqs. (3.2) and (3.4) respectively.

The CSTRs are used as a dynamic model of the reactor dosing zone because good mixing is assumed to occur near the dosing points. It is noted that this assumption forms the basis of the current reactor network study. Although a realistic CFD study is presently out of reach, particularly in conjunction with the detailed particle and chemistry models used in this work, it would be useful to investigate the multiphase flow behaviour, including energy exchanges and reaction kinetics, in more detail at a later stage to validate this assumption for the industrial reactor. Fresh $TiCl_4$ and O_2 reactants are injected to every third CSTR in the network. These injection streams have volumetric feed fractions f_2, f_3 and f_4 (cf. dosing point labels in Fig. 4.1 and labelled stream arrows in Fig. 4.2) relative to the total volumetric inflow to the corresponding reactor. Two PFRs with prescribed positive and negative temperature gradients are used to model the reactor working zone and the cooler respectively, resulting in a linear temperature profile across these sections.

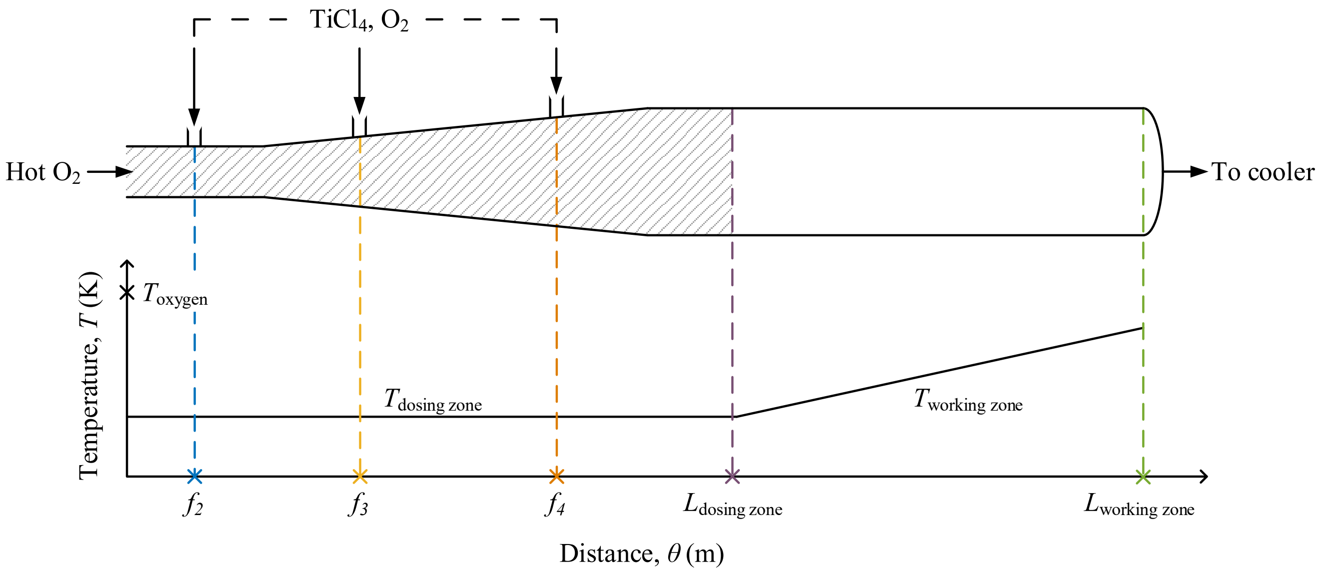

Fig. 4.1: Schematic of an industrial titania reactor showing dosing (shaded) and working (unshaded) zones and location of each feed stage relative to the reactor length $\mathcal{L} = \mathcal{L}_{\text{dosing zone}} + \mathcal{L}_{\text{working zone}}$ (zones not drawn to scale). The labels f_2, f_3, f_4 designate reactant feed points. A rough axial temperature profile is indicated for each zone in the lower part of the figure.

Typical industrial conditions are used (Table 4.1), and include an approximately equimolar ratio of $TiCl_4$ to O_2 in feeds f_2, f_3 and f_4 [4, 50] and a pressure of around 4 bar (absolute). The first feed, f_1, is predominantly O_2 with a small quantity of $TiCl_4$.

Reactors are initialised containing only inert argon and the simulations are conducted for 20τ to obtain steady state results, which was empirically observed to be well sufficient for concentrations and particle moments and properties to stabilise.

4.2 Process modelling results

The developed reactor network model is used to study distributions of the size and structural characteristics of titania particles formed under industrial synthesis conditions. The combined surface area particle model is used (Section 3.2.3) to describe the particle structure. Particle growth is investigated in detail for a base case simulation in Sections 4.2.1 and 4.2.2. In Section 4.2.3, a parametric study is used to compare the product size and structure resulting from different process conditions. A brief discussion of numerical considerations follows in Section 4.3.

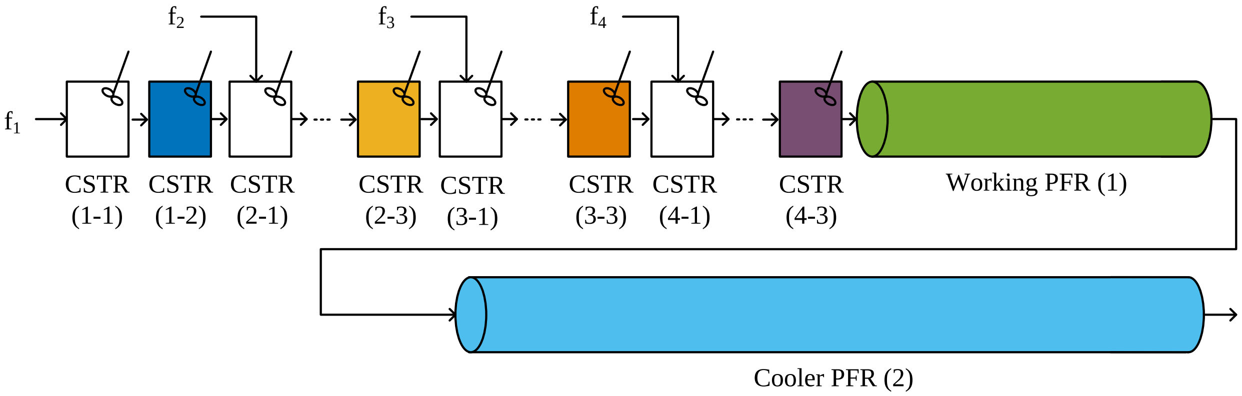

Fig. 4.2: Reactor network with feed f_i to CSTR (i-1), i.e. the first reactor in the i^{th} section, $i = 1, \ldots, 4$. Results will be shown for CSTRs (1-2), (2-3), (3-3), (4-3) and PFRs (1) and (2).

Table 4.1: Base case operating conditions in each reactor in the network, where D, W and C are the dosing, working and cooling zones and f is the volumetric feed fraction to the reactor.

Reactor (CSTR #)	Zone -	Feed fraction f (-)	Residence time τ (ms)	Temperature T (K)
CSTR (1-1)	D	1.0	2.0	1200
CSTR (1-2)	D	0	2.0	1200
CSTR (2-1)	D	0.50	5.0	1200
CSTR (2-2)	D	0	5.0	1200
CSTR (2-3)	D	0	5.0	1200
CSTR (3-1)	D	0.30	5.0	1200
CSTR (3-2)	D	0	5.0	1200
CSTR (3-3)	D	0	5.0	1200
CSTR (4-1)	D	0.40	5.0	1200
CSTR (4-2)	D	0	5.0	1200
CSTR (4-3)	D	0	5.0	1200
PFR (1)	W	0	160	1200–1600
PFR (2)	C	0	1500	1600–400

4.2.1 Baseline assessment of particle structure

Particle properties evolve along the reactor network (Fig. 4.3), providing insight into formation and growth in the different process stages. Key particle properties include the number of primary particles per particle (Fig. 4.3(a)), the collision diameter (Fig. 4.3(b)), the mean primary particle diameter (Fig. 4.3(c)), and the mean particle neck radius (Fig. 4.3(d)). The inception, coagulation and surface processes produce free primary particles and non-spherical aggregates, resulting in broad property distributions. In addition to the mean values and discrete distributions, smoothed distributions are useful to guide the eye and highlight trends across the reactor–cooler. These were obtained by fitting the simulation data with scaled kernel density estimates using the Matlab *ksdensity* function [90]. This assumes that the data is (log)normally distributed and specified by its bandwidth (i.e. the sample standard deviation. The default adaptive bandwidth was used, and the fits normalised to show particle number density. The fourth sub-figure in each panel of Fig. 4.3 compares the kernel estimates after the reactor and cooler. The neck radius (Fig. 4.3(d)) is computed by relating the common surface area and volume of a primary pair to the surface area and volume of point-contacting mass equivalent spheres. These features provide geometric information about the distance between the particle centres and the area of overlap as outlined by Lindberg et al. [78].

As expected, particle inception dominates near the beginning of the reactor due to the high reactant concentration and lack of particle surface area for surface reaction. Thus, most aggregates consist of one or several small primary particles and have small collision diameters (Fig. 4.3, CSTR (1-2)). The near-zero mean neck radius indicates that most aggregated particles are only in point contact. Further down the dosing zone, the distributions become increasingly broad as the particles become more polydisperse and more significantly connected (Fig. 4.3, CSTR (4-3)). Coagulation increases the mean collision diameters and number of primary particles per aggregated particle. Surface growth increases the primary diameters and the neck radii become larger due to sintering between neighbouring primaries. Because coagulation is fast relative to sintering under the base case conditions, a significant portion of the particles remains in point contact across the reactor (Fig. 4.3(d), CSTR (4-3)).

In the working zone and cooler, the gas phase precursor is depleted and there is no further substantial change in mean primary diameter (Fig. 4.3(c), PFR (1)). Coagulation and sintering continue, producing increasingly broad, flat distributions with large mean collision and neck diameters (Figs. 4.3(a), 4.3(b), 4.3(d) PFR (1)). While sintering can also change mean primary diameter by merging primary particles in the absence of gas precursor (cf. Eqs. (3.8) and (3.26)), this effect is not observed to contribute substantially in this zone either.

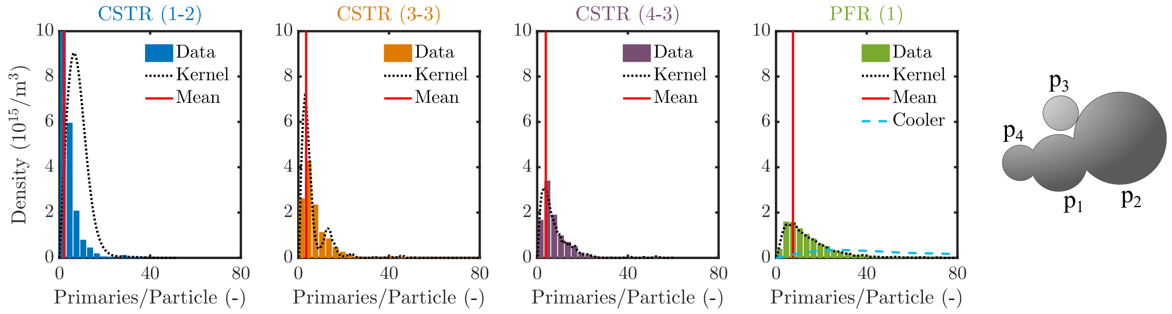

(a) Number of primaries per particle

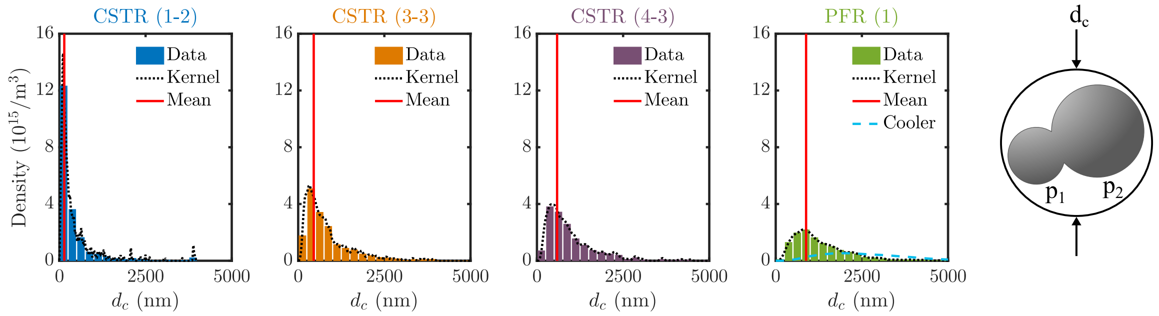

(b) Collision diameter, d_c

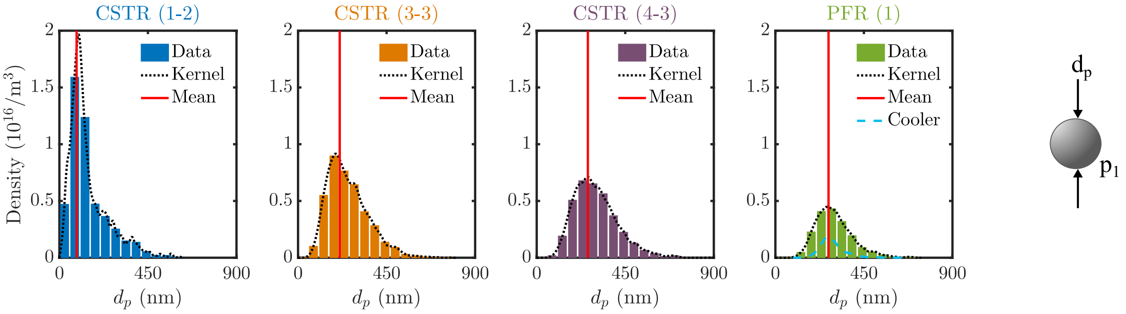

(c) Primary diameter, d_p

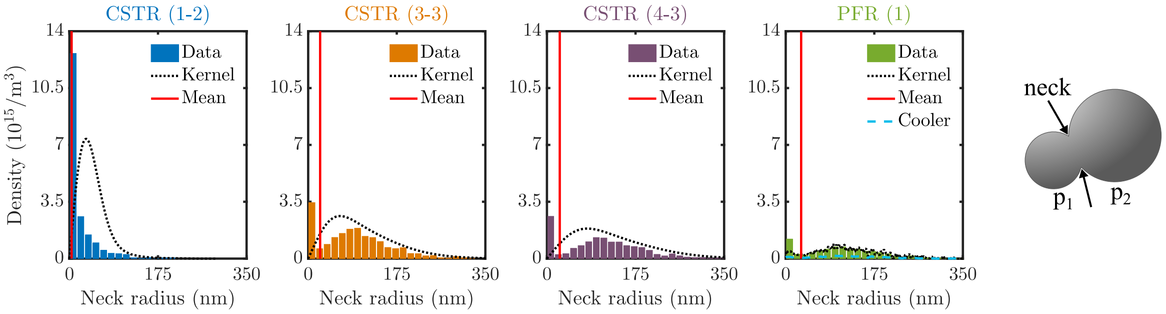

(d) Neck radius

Fig. 4.3: Raw simulation data, kernel density estimate and mean of the PSD in CSTRs (1-2), (3-3), (4-3) and PFR (1); and kernel density estimate for PFR (2). Right-hand schematics illustrate each property.

4.2.2 Transient evolution of particle properties

The transient evolution of the particle collision diameter distribution is explored at times 0.05τ, 0.5τ, τ and 5τ ($\tau = 2$ ms) in CSTR (1-1). Lognormal kernel density estimates (Appendix B) for the collision diameter distribution are fitted to the data at each of the specified times (Fig. 4.4). At 0.05τ, the distribution consists of a single peak, that is just larger than the incepting particle size (0.49 nm). The mean of the distribution is larger for 0.5τ and τ respectively due to coagulation (increasing the particle collision diameter) and surface growth (indirectly contributing to a larger collision diameter by increasing the primary diameters). The absence of a peak at the incepting particle size suggests that coagulation is rapid, especially for the smallest particles. By 5τ, the steady state has been established and this is observed to consist of a bimodal distribution, with a peak centred at the incepting particle size and a second peak at approximately 550 nm. These observations indicate that the characteristic time of the coagulation process is relatively short compared to the CSTR residence time.

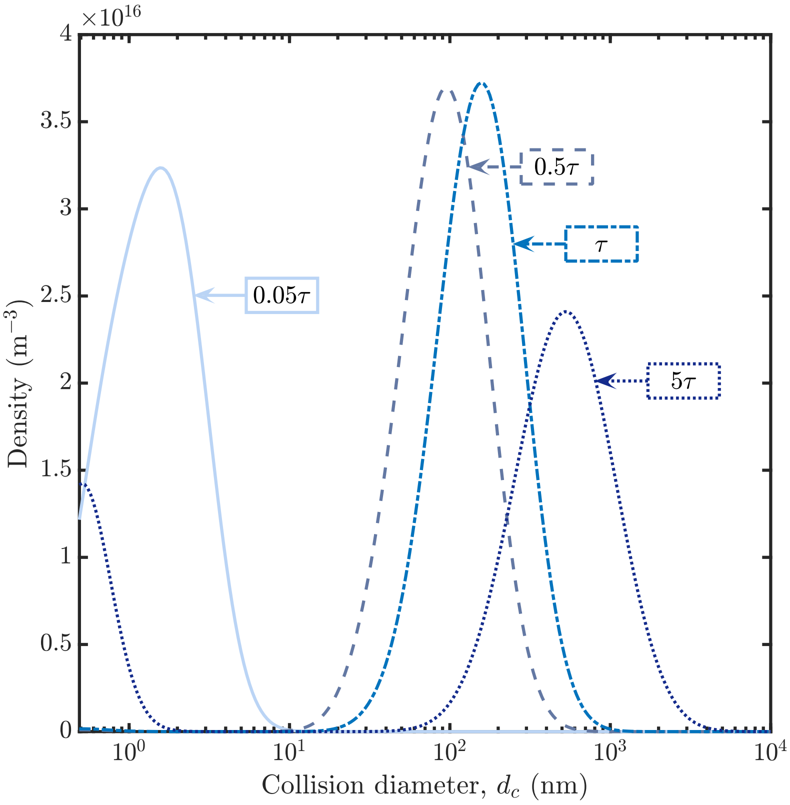

Fig. 4.4: Lognormal kernel estimates (with $\sigma = 0.4$) for the collision diameter simulation data, for four time points during transience in CSTR (1-1) with $\tau = 2$ ms. Extension below 0.49 nm is a consequence of the continuous smoothing kernel.

4.2.3 Sensitivity to process conditions and configuration

The effect of changing configuration and operating conditions on the particle properties is explored to demonstrate the potential to use the detailed model to understand the process and important operating parameters. Three reactor configurations (test cases described in rows 1–3 of Table 4.2), two temperatures (test cases in rows 1 and 4 of Table 4.2) and two residence times (test cases in rows 1 and 5 of Table 4.2) are considered. The configuration is varied by moving the location of the three feed sites to different CSTRs in the network (Fig. 4.5).

Table 4.2: Operational parameters used in test cases varying feed injection points (f_i), temperature and flow rate. Varying the injection points determines which CSTRs receive feeds f_2–f_4, and varying the flow rate specifies the set of reactor residence times relative to the base case (BC) set of residence times, $\{\tau\}_{\mathrm{bc}}$.

Test case	Temperature	Injection points	Residence time
-	T (K)	f_2, f_3, f_4 (CSTR #)	$\{\tau\}$ (ms)
Base case	1200	3, 6, 9	$1 \times \{\tau\}_{\mathrm{bc}}$
Early dosage	1200	2, 3, 4	$1 \times \{\tau\}_{\mathrm{bc}}$
Late dosage	1200	9, 10, 11	$1 \times \{\tau\}_{\mathrm{bc}}$
Low temperature	1100	3, 6, 9	$1 \times \{\tau\}_{\mathrm{bc}}$
High throughput	1200	3, 6, 9	$\frac{1}{2} \times \{\tau\}_{\mathrm{bc}}$

The effect of temperature and residence time on the particle size and structure is summarised using the arithmetic mean and geometric standard deviation (GSTD) of the aggregate and primary particle diameters, the number of primaries per particle and the number density (Fig. 4.6 and Table 4.3). These properties are chosen so as to accommodate qualitative comparison with literature studies and plant experience, in the absence of relevant laboratory measurement or measured plant data. The geometric standard deviation is typically used to quantify particle polydispersity [30].

In the base case, particle inception dominates near the reactor inlet, causing an early increase in the number density (Fig. 4.6). The surface reaction proceeds rapidly across the dosing zone, near the fresh feed points, and a sharp increase in the mean primary diameter is observed. The mean primary diameter remains almost constant in the reactor working zone and the cooler because the rate of surface reaction is diminished at the significantly lower reactant concentrations downstream of the dosing stages. The final mean primary diameter is 277 nm.

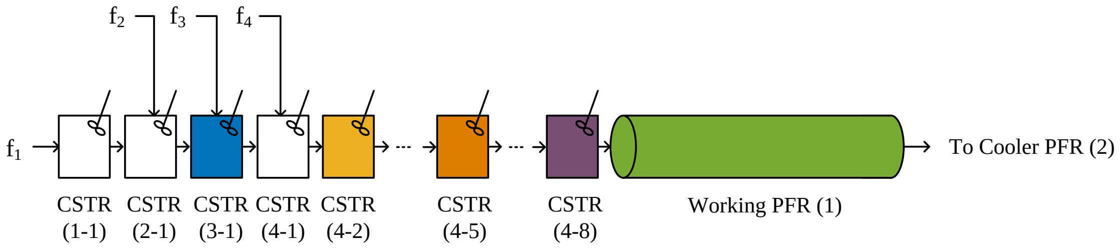

(a) Early dosage injections

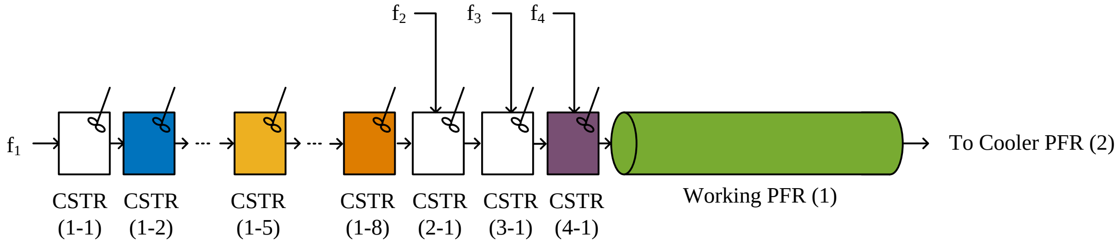

(b) Late dosage injections

Fig. 4.5: Reactor network configurations with different dosing points corresponding to (a) early dosage injections and (b) late dosage injections, compared to the base case reactor dosing scheme, in which f_2, f_3 and f_4 were allocated to the third, sixth and ninth CSTRs respectively.

Coagulation occurs throughout the reactor and cooler, as can be seen in the increasing collision diameter and decreasing particle number density, and the development of aggregate structures shown in the simulated transmission electron microscopy (TEM) images (Fig. 4.6). The final particulate product consists of aggregates with a mean size of 2000 nm, composed of 32 primary particles per particle on average, with a mean neck radius of 38 nm, indicating partial sintering between neighbouring, connected primary particles.

Increasing the reactor temperature increased the mean collision diameter and decreased the mean primary diameter and number density (indicated with dashed arrows in Fig. 4.6). These trends can be explained by comparing the relative rates of the different processes at different temperatures. The particle process rates are higher at higher temperatures, and the effect of temperature on the inception and coagulation rates is relatively large compared to the effect on surface growth.

Akhtar et al. [1] used an aerosol reactor to investigate the effect of temperature in the range 1200 K–1723 K. There, the PSD was found to shift to larger particle sizes with increased temperature and a theoretical study showed an increase in coagulation. As in the current work,

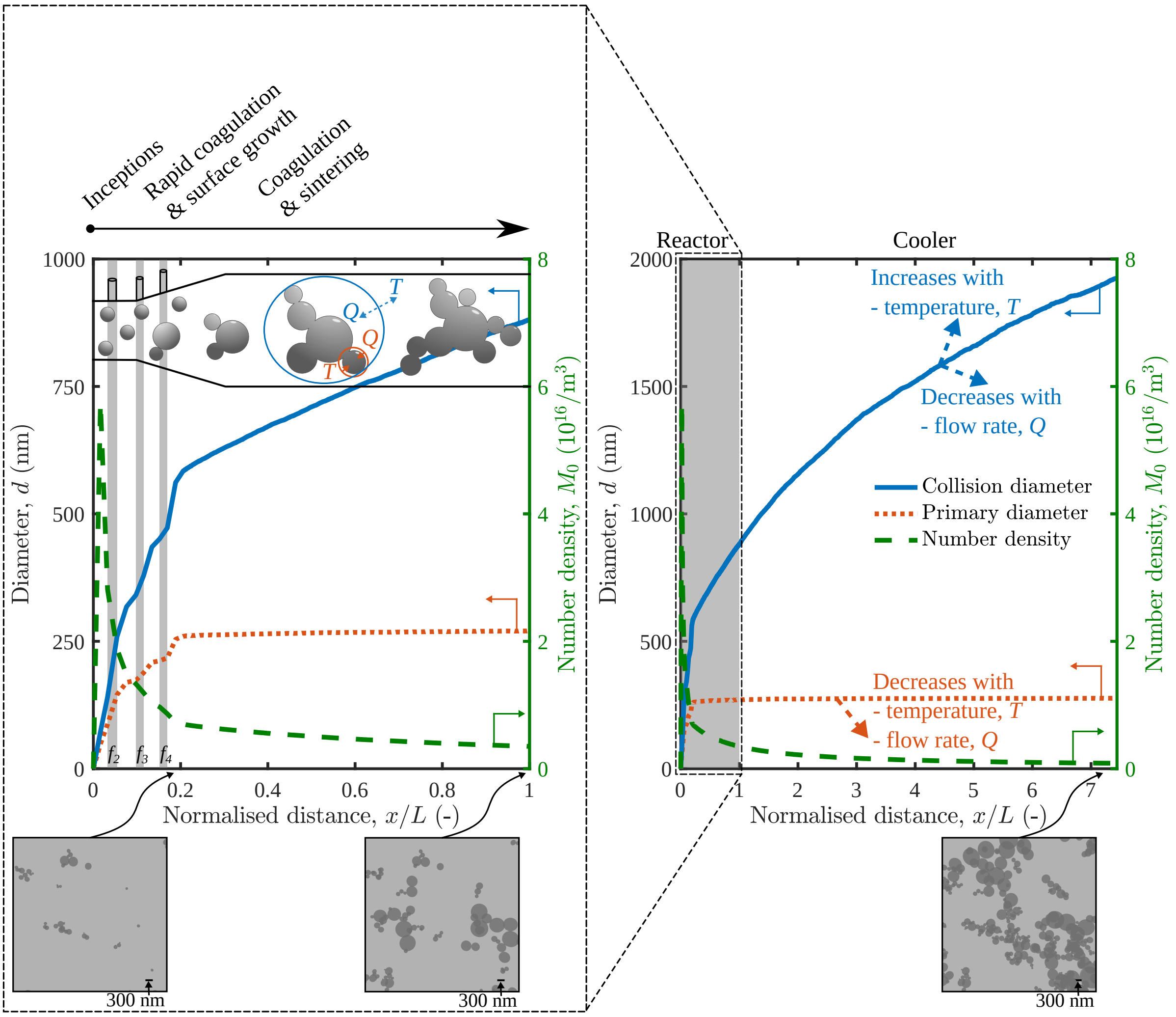

Fig. 4.6: Evolution of particle size (left axis) and number density (right axis) across the reactor and cooler (normalised by reactor length $\mathcal{L}$) for the base conditions. Dashed arrows show the effects of increasing temperature T and throughput Q. The simulated TEM images were generated using the freeware ray tracing program, POV-Ray, to visualise the surface data for a sample of computational particles.

there was little change in the geometric standard deviation (Table 4.3). Nakaso et al. [109] also observed that, for temperatures in the range studied here, higher temperatures produced larger particles consisting of smaller primaries, and lower temperatures resulted in less dense aggregates of larger primaries. Other studies also report this effect [178]. The primary diameter might begin to increase again for temperatures higher than the ones investigated here due to complete sintering between primary particles [109].

Increasing the flow rate produced smaller primary and aggregate particles (indicated with dashed arrows in Fig. 4.6), and a higher number density because the particles had less time to grow. Again, this is supported by the trend reported in the literature [1] and this finding also agrees with empirical experience of the industrial process.

In this chapter, the same base case temperature profile was used for the early and late dosing cases. This is sufficient for the current study; however, the effect of dosing configuration is more complicated in general, since it determines the concentration profile and temperature exotherm. At this juncture, it is noted that it would be useful to have the flexibility to allow temperature to change with dosing strategy to account for reactions and mixing. This will be addressed in Chapter 6. Here, the early dosing configuration created slightly smaller particles and a higher particle number concentration while the late dosing configuration produced significantly smaller primary particles (Table 4.3).

A smaller mean particle size is desirable in the commercial process so as to reduce milling requirements to produce a high-quality product. This short study suggests that the use of high throughput, with rapid quenching at the end of the working zone and in the cooler, is necessary to minimise coagulation and sintering of the pigmentary particles and thereby improve product quality with lower cost because of reduced milling requirements.

Table 4.3: Mean and geometric standard deviation (GSTD, σ_g) of collision diameter and primary diameter and mean number density after the cooler for each case in Table 4.2.

Test case	Mean	GSTD	Mean	GSTD	Mean
-	$\bar{d}_\mathrm{c}$, nm	$\sigma_g\left(d_\mathrm{c}\right)$	$\bar{d}_\mathrm{p}$, nm	$\sigma_g\left(d_\mathrm{p}\right)$	$\bar{M}_0$, m^{-3}
Base case	2000	1.79	277	1.23	8.14×10^{14}
Early dosage	1910	1.77	272	1.21	8.44×10^{14}
Late dosage	1990	1.77	246	1.27	8.07×10^{14}
Low temperature	1800	1.74	356	1.23	9.02×10^{14}
High throughput	1590	1.76	251	1.23	15.1×10^{14}

4.3 Numerical considerations

The direct simulation algorithm (DSA) was used to produce the results presented in this chapter. The stochastic weighted algorithm (SWA) used by Menz et al. [101] was found to produce comparable statistical errors across the network. However, in contrast to that previous study for CSTR networks with recycles, SWA was not found to reduce the statistical error in the first particle moments. This is possibly because the current reactor network is linear, where the previous study reported that recycles compounded the error.

The average relative statistical error, $\overline{\varepsilon}_{\mathrm{stat}}$, is defined for a given combination of maximum ensemble capacity, $N_{\max}$, and number of repeat runs, L, by

$$\overline{\varepsilon}_{\mathrm{stat},\xi}^{(N_{\max},L)} = \frac{1}{M}\sum_{k=1}^{M} \frac{\alpha_{0.999}}{\sqrt{L-1}} \frac{\sigma_{\xi}^{(N_{\max},L)}(t_k)}{\mu_{\xi}^{(N_{\max},L)}(t_k)}, \tag{4.1}$$

where M is the number of time steps included in the calculation, σ_ξ is the sample standard deviation in the property ξ, μ_ξ is its mean value and $\alpha_{0.999} = 3.29$ is the coefficient associated with a confidence level of 99.9 % for the normal distribution [101]. The statistical error and convergence are investigated in terms of particle properties used in the previous results (Sections 4.2.1–4.2.3) and the particle mass moments,

$$M_j(t) = \frac{1}{V_{\mathrm{smp}}}\sum_{i=1}^{N(t)} (\rho V_i)^j,\ j = 0,1,2. \tag{4.2}$$

Here, ρ is the mass density of $\mathrm{TiO_2}$, taken as $4.26\,\mathrm{g\,cm^{-3}}$, and V_i is the volume of particle P_i. The statistical errors in the collision diameter, the primary diameter, the number of primary particles per particle and the lower order mass moments are assessed for CSTR (2-1) for base case simulation conditions with $N_{\max} = 2^{14}$ computational particles and $L = 10$ repeat runs (Fig. 4.7(b)). The statistical errors are observed to increase in the higher order moments as was found in other works [101, 121]. The statistical errors in properties that are of interest in this chapter are sufficiently low. Numerical convergence (discussed in Section 3.5.2) with increasing computational particles and $N_{\max} \times L = 2^{17}$ is studied by considering the mean particle size properties and mass density for CSTR (2-1) for the base case simulation conditions (Fig. 4.7(a)). Convergence in all three properties has been obtained by $N_{\max} = 2^{14} = 16384$, the value used for the process modelling studies in this chapter, as judged by the small changes to these values upon increasing the ensemble size further.

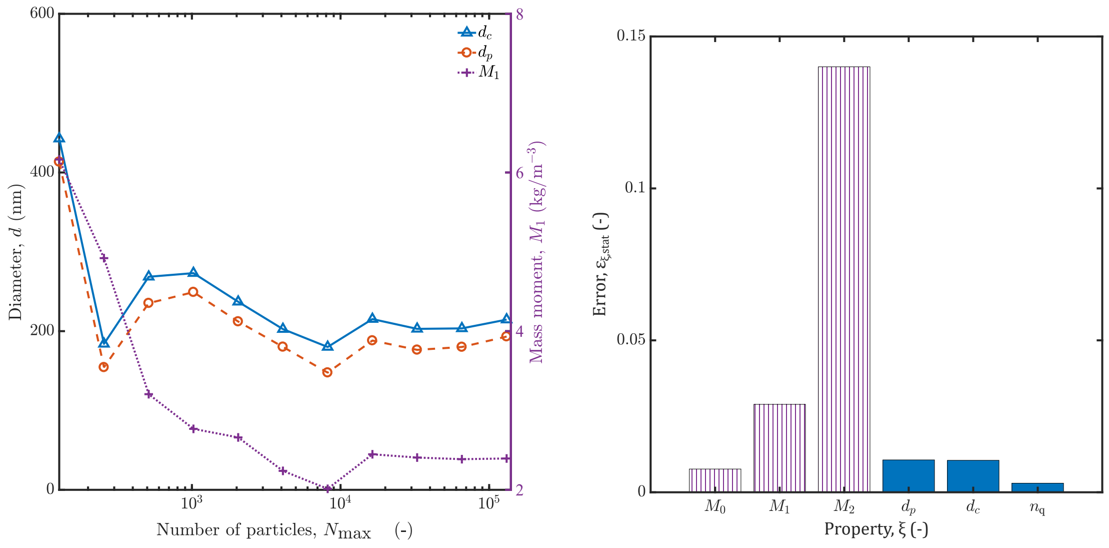

(a) Numerical convergence

(b) Statistical error

Fig. 4.7: Convergence behaviour of the particle mass moments and size characteristics in CSTR (2-1) showing (a) convergence as a function of ensemble capacity, N_{max}, with diameters and mass moment shown on left and right vertical axes respectively; and (b) statistical error, with moments and size characteristics represented by striped and filled bars respectively.

A comment on the solver time

The solver time with 2^{14} particles was approximately 33 h on a 3 GHz Intel Xeon X5472 processor with 8 GB of RAM, running 64-bit CentOS Linux 7. While this is not intractably computationally expensive, it is significantly longer than one would hope. For example, this would make an extensive parameter sweep aimed at fitting process response surfaces extremely expensive since the number of points needed to do this accurately increases with the number of independent variables considered. This also illustrates why full fluid dynamics coupling is currently out of scope.

4.4 Chapter summary

This chapter presented a model for studying titania synthesis in an industrial reactor. Important features of the model include an ideal reactor network to treat flow behaviour and describe variations in composition and temperature; and detailed population balance dynamics for the particle system, coupled to a comprehensive chemical mechanism. The use of a high-dimensional particle model allows for many internal coordinates of the particles to be tracked, and these provide important information about aggregate structure. Aggregate size and morphology are critical factors in determining end-product quality, which in turn impacts milling requirements in the industrial process. It is thus useful to obtain as much information as possible about the particle aggregates.

The distributions of number of primary particles, collision diameter, primary particle diameter, and neck radius were tracked across the system. The pigmentary product leaving the cooler was found to consist of partially sintered groups of connected primary particles, creating particles several times larger than their constituent primaries on average. This agrees with literature commentary on industrial titania product characteristics [50]. The degree of cohesion has implications for milling requirements to produce particles of the requisite size in the industrial process. The sensitivity study found that increasing temperature resulted in the formation of larger particles, composed of smaller primary particles, owing to the relative rates of the particle processes at different temperatures. As discussed in Section 4.2.3, these findings are consistent with previous studies. Higher throughput produced smaller particles due to the limited time for reaction and particle growth. This is supported by empirical experience of the industrial process. Thus, although there is not currently industrial data to compare such trends quantitatively, the effects of operational changes were found to agree qualitatively with previously observed trends. The work reported in this chapter serves as proof-of-concept for the use of a reactor network with a detailed population balance model to simulate industrial titania synthesis. The developed reactor model was shown to be sensitive to changes in operational parameters and design choices; however, the imposed temperature profile limits flexibility in this respect. Thus, a desirable next step is to include the energy balance in the system equations in order to apply the model to a wider range of conditions and configurations. This development is covered in Chapter 6.

A principal concern is the numerical performance of the current framework with very rapid process rates resulting from the high concentration and high temperature industrial conditions. The simulations described in this chapter required large particle ensembles (2^{14} computational particles) to resolve the particle size distribution, and small time steps to capture the coupling between rapid gas phase and particle processes. This is clearly computationally expensive (order of days to run). An unseen consequence of the fast process dynamics is that choice of suitable parameters (e.g. sample volume) is non-trivial. Transient changes in the numerical rates of processes such as inception can result in poor resolution of the PSD – thus reducing efficiency. This is worsened with an energy balance which introduces temperature gradients and further dynamic rate changes. Thus, it is crucial to address challenges in the simulation algorithm to mitigate these issues, and this is the subject of Chapter 5.

Chapter 5

A new hybrid particle model and algorithm

This chapter presents a new algorithm for solving population balance equations that is capable of improving efficiency and robustness to parameter choice of existing methods while remaining exactly equivalent. A hybrid particle-number and particle model is proposed for type-spaces spanning spherical and aggregate particles. Small primary particles are tracked efficiently by storing only the number of particles with each possible monomer count. For larger particles, aggregate structure is resolved in detail using a high-dimensional particle model for discrete computational entities. This approach is exact for univariate primary particle models in that it makes no additional simplifications. Algorithms are provided to solve the population balance equations with a hybrid type-space. The new method is shown to work well for large particle ensembles, where simplified updates are up to 50 % *cheaper than updating an equivalent ensemble of detailed particles. These computational savings can be traded for greater statistical resolution. The cost of growth updates on large aggregates cannot be avoided; however, runtime improvements are not the principal advantage. The hybrid method is attractive even in cases with high growth rates as its primary purpose is to decrease sensitivity to numerical parameters by preventing saturation of the ensemble with simple particles at high inception rates. Material from this chapter was published in* ***Paper 2*** *listed in the Declaration.*

5.1 Population balance equation

This chapter develops a novel hybrid model for the particle type-space. The PBE is presented for a generic type-space in the current section. Following this, two particle systems are defined using particle-number and detailed particle models (Section 5.2). The processes that transfer mass between the particle systems are then described in general terms and the stochastic method is outlined (Section 5.3). Numerical studies are presented for the convergence behaviour and performance of the hybrid particle model, compared to a single particle model (Section 5.4). Various simplified TiO_2 test cases are used in these studies, and the relevant rate forms are provided explicitly alongside these. The new algorithms for the hybrid particle model are provided in Appendix A.1.

The concentration of particles of a given multivariate type $x \in \mathcal{E}$, where $\mathcal{E}$ is called the type-space and describes all possible particles, can be described by the Smoluchowski coagulation equation [121], extended to include inception, surface changes and flow. Here, flow is considered in an isothermal, constant volume, continuously stirred tank reactor (CSTR),

$$\begin{aligned}\frac{dn(x)}{dt} =& I(x,\mathbf{C},T) + \frac{1}{2}\sum_{\substack{y,z\in\mathcal{E}:\\ y+z=x}} K(y,z,T)\,n(y)\,n(z)\\ &- \sum_{y\in\mathcal{E}} K(x,y,T)\,n(x)\,n(y)\\ &+ \sum_{\substack{y\in\mathcal{E}:\\ g_{\mathrm{SG}}(y)=x}} \beta_{\mathrm{SG}}(y,\mathbf{C},T)\,n(y) - \beta_{\mathrm{SG}}(x,\mathbf{C},T)\,n(x)\\ &+ \frac{1}{\tau_{\mathrm{CSTR}}}\sum_{j=1}^{N_{\mathrm{in}}} f^{[j]}\left(n_{\mathrm{in}}^{[j]}(x) - n(x)\right).\end{aligned} \tag{5.1}$$

$n(x)$ is the concentration of particles of type x, $I(x,\mathbf{C},T)$ is the rate of inception of particles of type x, $K(x,y,T)$ is the rate at which particles of type x coagulate – that is collide and remain in point contact – with particles of type y, $\beta_{\mathrm{SG}}(y,\mathbf{C},T)$ is the rate at which particles of type y undergo surface changes and $g_{\mathrm{SG}}(y)$ is the particle type that is produced, and τ_{CSTR} is the residence time in the CSTR. In the case of N_{in} inflow streams, $f^{[j]}$ is the volumetric feed fraction of the j^{th} stream. Process rates and parameters for the titania process were provided in Section 3.4. Simplified expressions used for testing the new hybrid model in this Chapter will be defined in Section 5.4.

5.2 Particle systems

Monte Carlo methods employ a finite ensemble of computational particles to model the diverse assortment of particles in the physical system. A computational particle P_q has a distinct, possibly multivariate type, x. In this chapter, a hybrid particle-number/particle model is proposed wherein the particle type-space is split such that $\mathcal{E} = (\mathcal{M} \cup \mathcal{X})$. This allows different levels of detail to be used to describe particles in the spaces $\mathcal{M}$ and $\mathcal{X}$ (Fig. 5.1).

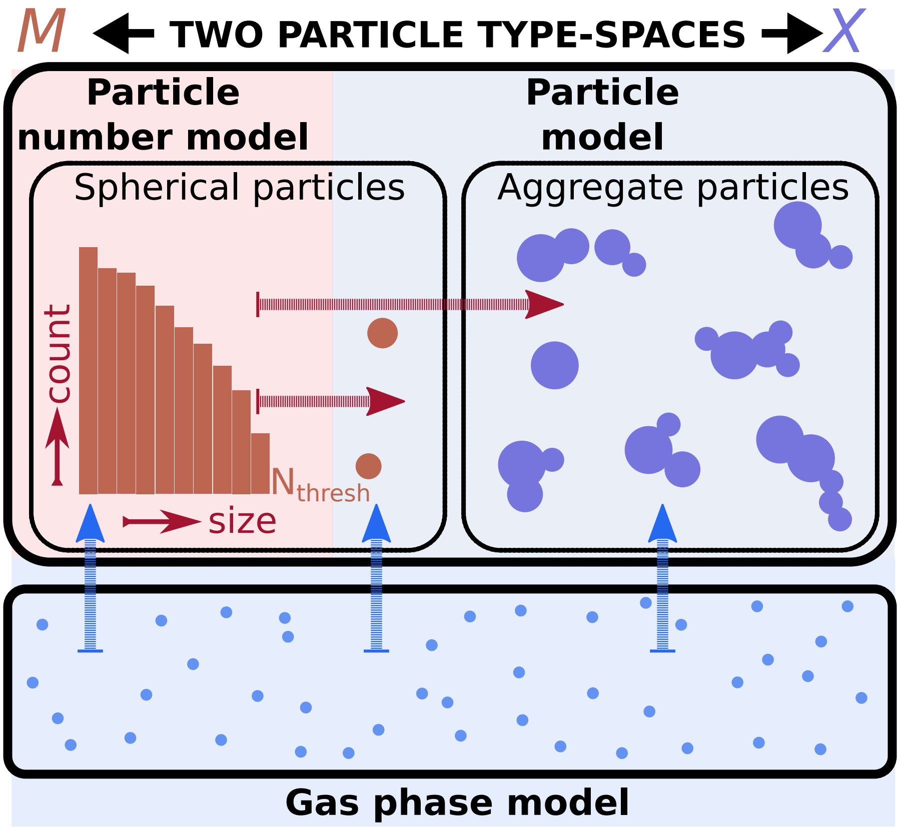

Fig. 5.1: Mass transfer from the gas phase to the particle systems by inception and surface reaction, and mass transfer from the particle-number model to the particle model by coagulation and surface growth beyond the threshold size (N_{thresh}).

5.2.1 Space of small, spherical particles, $\mathcal{M}$

Let the particle type-space consisting of small, spherical particles (primary particles) be defined as $\mathcal{M}$. Particles in this space have a single internal coordinate for number of monomers, with different sizes $i \in [1, N_{\text{thresh}}]$ where $i = 1$ is a single molecular unit and N_{thresh} is the size of the largest particle that is tracked by the particle-number model before transfer to the space of aggregate particles, $\mathcal{X}$. In principle, the size threshold N_{thresh} could be chosen to be arbitrarily large such that all spherical particles are defined in $\mathcal{M}$ where $\mathcal{M} = \mathbb{N}$. However, this will not be practically useful for implementation so a finite threshold is chosen, resulting in a space of *small*, spherical particles. In the titania mechanism, the smallest particle contains 2 TiO_2 monomers. An example threshold choice of $N_{\text{thresh}} = 10^4$ TiO_2 monomers results in ten thousand tracked particle sizes and corresponds to a maximum diameter of approximately 8.5 nm for particles in the space $\mathcal{M}$. To increase the maximum diameter to 50 nm requires more than two million numbers to be tracked ($N_{\text{thresh}} = 2.1 \times 10^6$). The particle-number (PN) system is written:

$$z_{\mathcal{M}}(t) = \left(y_1, \ldots, y_{N_{\text{thresh}}}\right),$$

where

$$y_i(t) \in \mathcal{M}, \quad i = 1, \ldots, N_{\text{thresh}}, \quad t \geq 0,$$

and $N_i = N(y_i)$ is the number of particles that have type y_i (note that notation N subscript i or j refers to the number of particles at these indices, while N with subscript "thresh" refers to the threshold number of monomers in a particle to be tracked in this model). The concentration of particles with type $y_i \in \mathcal{M}$ is $N_i \cdot V_{\text{smp}}^{-1}$. The type-space $\mathcal{M}$ can be represented efficiently as it requires only a vector in $\mathbb{R}^{N_{\text{thresh}}}$ to produce the PSD from the number of particles in each size class.

5.2.2 Space of large particles and aggregates, $\mathcal{X}$

Let $\mathcal{X}$ be the type-space for spherical particles containing more than N_{thresh} monomers and all aggregate particles containing more than one primary particle. Particles in $\mathcal{X}$ need to be defined by both morphology and composition and for this the combined surface area particle model (Section 3.2.3) is used. A particle P_q is made up of an unordered list of primary particles, p_i, each of which is described by its chemical composition (Figs. 3.2(a) and 3.2(b)), and a record of the connectivity of the primary particles:

$$P_q = \left(p_1, \ldots, p_{n_q}, \mathbf{C}_q\right).$$

In this chapter, the data structure of each particle stores a connectivity matrix $\mathbf{C}_q$ to track adjacent primary particles and their combined surface area (Figs. 3.2(b) and 3.3). The particle model has been comprehensively described by Sander et al. [133] and Shekar et al. [140]. The combined surface area in C_{ij} must be updated if connected primary particles p_i, p_j undergo surface processes. Sintering is not considered in the studies presented in this chapter which employ simplified process models to interrogate the hybrid model's performance. Sintering only affects aggregates and can be included in the algorithm for updating these particles as usual, without modifying the new approach.

The particle system is composed of $N(t) \leq N_{\max}$ such particles (at time t):

$$z_{\mathcal{X}}(t) = \left(x_1, \ldots, x_{N(t)}\right),$$

where

$$x_i(t) \in \mathcal{X}, \quad i = 1, \ldots, N(t), \quad t \geq 0.$$

The concentration of particles with type $x_i \in \mathcal{X}$ is V_{smp}^{-1} assuming each computational particle represents the same quantity of physical particles. The description of multivariate particle types x_i requires much more information for each particle; thus, a more sophisticated data structure is required to store each distinct particle.

5.2.3 Mass transfer between the particle systems

The change in the PSD with time is described by Eq. (5.1). In the hybrid particle model, the PSD spans two type-spaces; thus, it is necessary to define how the particle processes affect both particle systems $z_{\mathcal{M}}(t)$, $z_{\mathcal{X}}(t)$.

Interaction with a gas phase system

The systems of interest in this work (i.e. flame synthesis) typically involve a gas phase precursor as well as several intermediate species. Formation and reaction processes in the gas phase (see the mass balances described by Eq. (3.2)) must be described by a chemical mechanism. Particle synthesis follows from collision between gas phase species that results in a stable configuration of molecular units (inception, with concentration- and temperature-dependent rate I in Eq. (5.1)). Particle growth occurs due to the reaction of gas phase species on the particle surface (surface growth, with concentration- and temperature-dependent rate β_{SG} in Eq. (5.1)), producing a polydisperse primary particle size distribution.

Inception

Particle inception from the gas phase intermediates occurs at a rate, I, that depends on the gas phase concentrations and the temperature. The inception process only acts on the space of spherical primaries, $\mathcal{M}$, and not on the space of large particles, $\mathcal{X}$. In this chapter, it is assumed that a dimer unit containing 2 TiO_2 monomers is the only incepting size; however, the description is transferable to any monomer index corresponding to a stable particle composition. Because inception creates particles at size index 2 and particles do not lose mass, there are never particles at size index 1 – i.e. $N_1 = 0$ at all times. Primary particles of type $y_i \in \mathcal{M}$ are created and this is modelled by incrementing the count at index i in the particle-number model (Fig. 5.2).

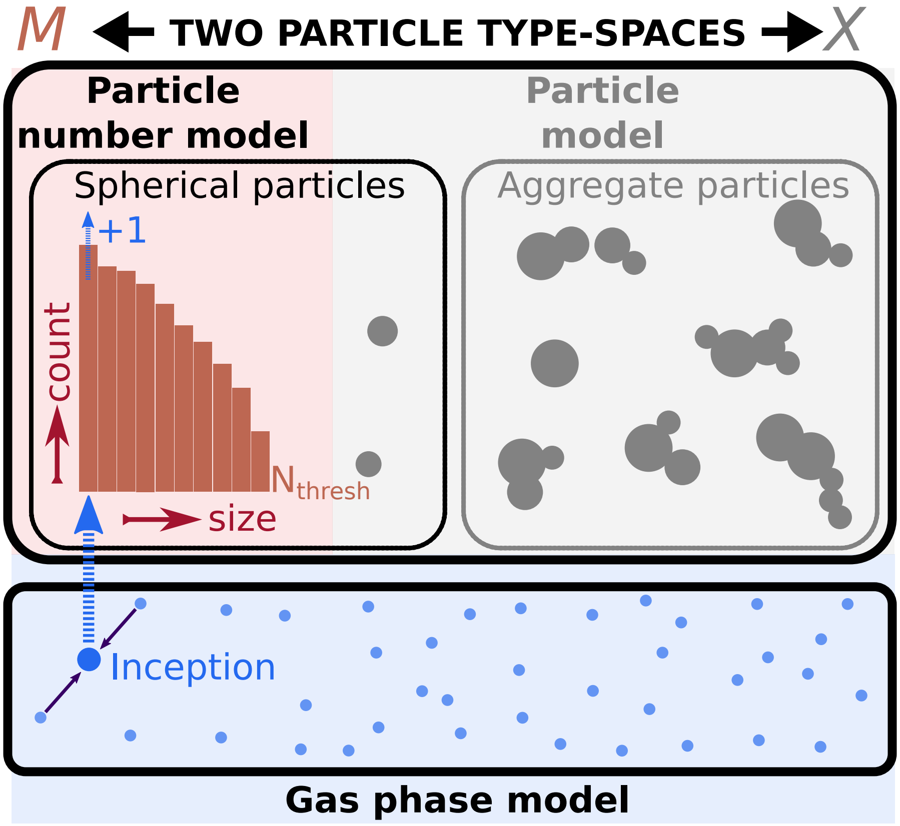

Fig. 5.2: Interaction between the gas phase and the particle-number system by inception of primary particles following gas phase collisions.

Surface growth

All particles in the two type-spaces experience surface growth, at a rate, β_{SG}, that is dependent on the gas phase reactant concentrations and temperature, and the particle surface area. Surface growth results in a change in particle type according to the surface growth function, g_{SG}, with the following effects:

1. A particle described by the particle-number model with type $y_i \in \mathcal{M}$ is transformed to type $y_j = g_{\mathrm{SG}}(y_i)$, $i < j$. If the new size is still in $\mathcal{M}$, i.e. $j \leq N_{\mathrm{thresh}}$, the indices i and j are altered accordingly (Fig. 5.3, small, solid horizontal arrows indicating movement towards larger size indices).
2. If the new size exceeds the threshold size, i.e. $j > N_{\mathrm{thresh}}$, the particle is transferred to the detailed particle model, by creation of a new particle consisting of a single primary, with type $x_j \in \mathcal{X}$ (Fig. 5.3, curved horizontal arrow indicating transfer to the particle model).
3. Particles of type $x \in \mathcal{X}$, are transformed to larger type $y = g_{\mathrm{SG}}(x)$, $y \in \mathcal{X}$ (Fig. 5.3, dashed arrows showing surface increase of discrete particle).

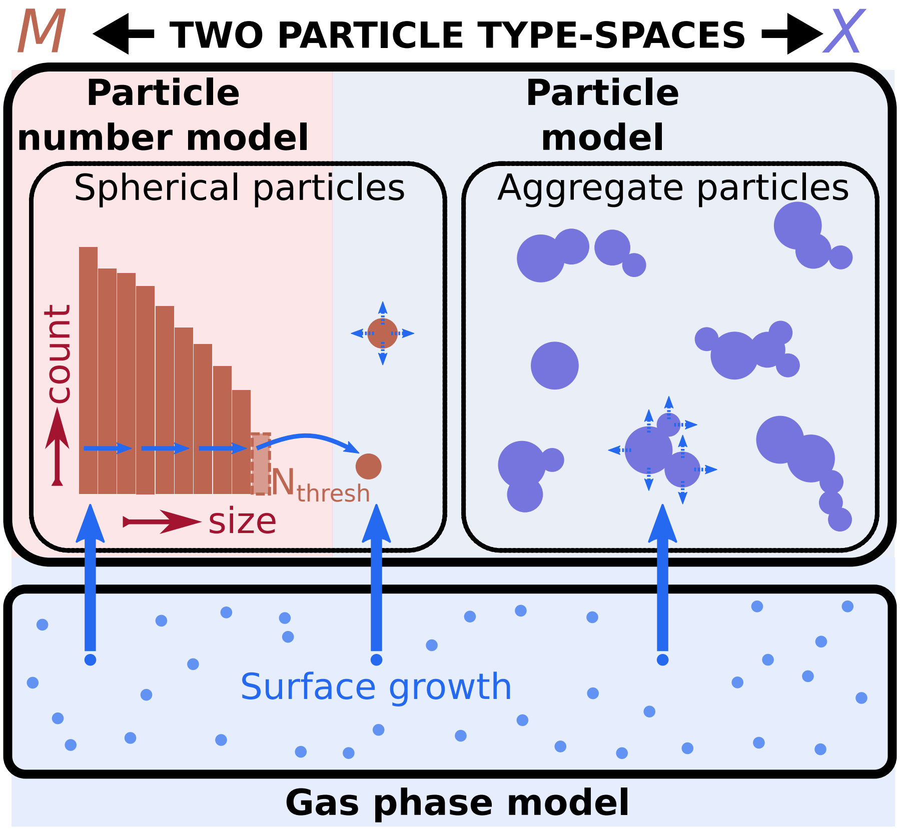

Fig. 5.3: Interaction between the gas phase and both particle systems by surface reaction (surface reaction beyond the threshold size N_{thresh} in the particle-number model causes transfer of particles to the particle model).

Coagulation

Coagulation events occur between any two particles across both type-spaces $(\mathcal{M} \cup \mathcal{X})$. This transfers particles from the particle-number model (space $\mathcal{M}$) to the detailed particle model (space $\mathcal{X}$) (Fig. 5.4). Coagulation between two particle-number model particles forms a new aggregate in the particle model (this process acts as a source term for the particle model) and reduces the number of particle-number particles by two. Coagulation between two particle model particles reduces by one the number of particles in the particle model system. Coagulation between one particle from each space reduces the number of particles in the particle-number model by one. The PN particle is attached to the coagulating particle model particle, conserving the count in the particle model.

The coagulation operator $\mathcal{K}$ acts on $(\mathcal{M} \cup \mathcal{X})^2$ and produces particles in $\mathcal{X}$. The symmetric coagulation kernel for each particle pair is $K(x,y,T)$ where $x,y \in (\mathcal{M} \cup \mathcal{X})$. The rate $K(x,y,T)$ is defined by the type of coagulation process considered. The constant rate kernel and transition regime kernel used in this chapter are presented in more detail alongside the relevant numerical study. Because the primary particle model in $\mathcal{X}$ is one-dimensional, there is no difference between the description of single primary particles in $\mathcal{M}$ and $\mathcal{X}$. Thus, the rate is derived in the same manner for particles in either space.

For the discrete particle systems:

$$\begin{aligned} x_i &\in z_{\mathcal{X}}(t),\ i = 1,\ldots,N(t) \\ y_i &\in z_{\mathcal{M}}(t),\ i = 1,\ldots,N_{\text{thresh}}, \end{aligned}$$

the total rate can be written by considering collisions between particle pairs $(y_i, y_j) \in \mathcal{M}$, $(x_i, x_j) \in \mathcal{X}$ or $(y_i, x_j) \in (\mathcal{M} \cup \mathcal{X})$:

$$\begin{aligned} R_{\text{coagulation}} = &\frac{1}{2V_{\text{smp}}} \sum_{i=1}^{N(t)} \sum_{\substack{j=1 \\ j \neq i}}^{N(t)} K(x_i, x_j, T) \\ &+ \frac{1}{2V_{\text{smp}}} \sum_{i=1}^{N_{\text{thresh}}} \sum_{\substack{j=1 \\ j \neq i}}^{N_{\text{thresh}}} K(y_i, y_j, T) N(y_i) N(y_j) \\ &+ \frac{1}{V_{\text{smp}}} \sum_{i=1}^{N_{\text{thresh}}} K(y_i, y_i, T) N(y_i) (N(y_i) - 1) \\ &+ \frac{1}{V_{\text{smp}}} \sum_{i=1}^{N(t)} \sum_{j=1}^{N_{\text{thresh}}} K(x_i, y_j, T) N(y_j). \end{aligned} \tag{5.2}$$

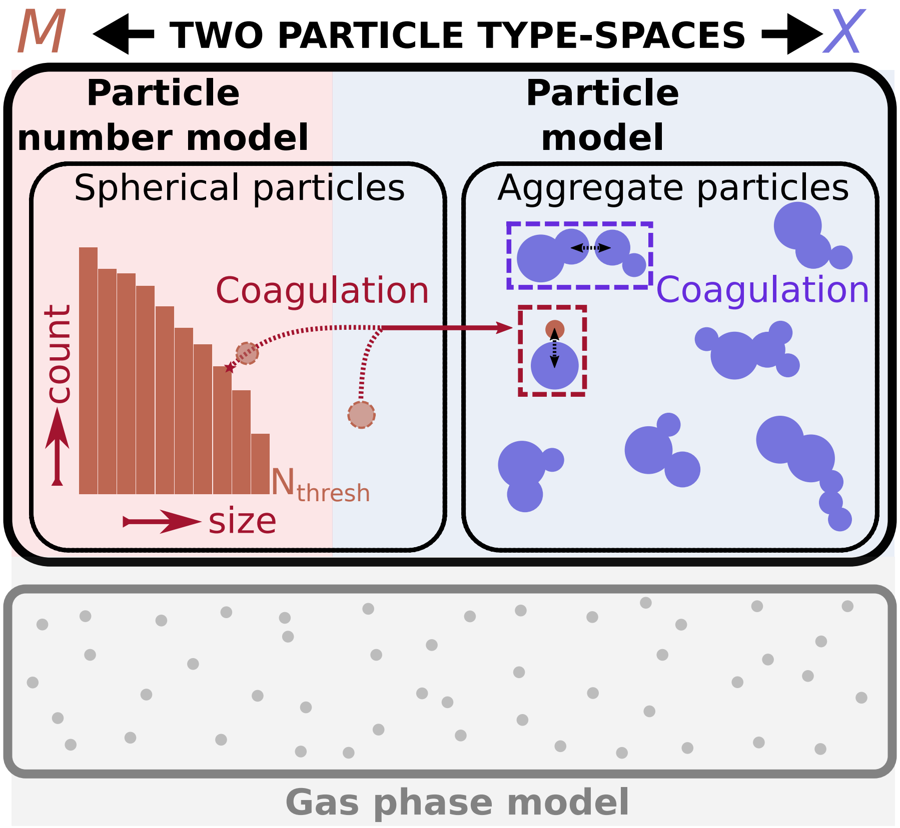

Fig. 5.4: Interaction between the particle systems by coagulation.

Inflow

In a CSTR with particles in the inflow streams, particle inflow occurs with rate $\tau_{\mathrm{CSTR}}^{-1}$ and particles can be added to both spaces with the following effects:

1. If $y_{\mathrm{in}} = y_i \in \mathcal{M}$, the number of particles at the i^{th} index of the particle-number model is incremented: $N_i \leftarrow N_i + 1$, $i \in [1, N_{\mathrm{thresh}}]$.
2. If $x_{\mathrm{in}} \in \mathcal{X}$, a new particle with type x_{in} is added to the detailed particle system, i.e. $z_{\mathcal{X}}(t) \leftarrow \{z_{\mathcal{X}}(t), P(x_{\mathrm{in}})\}$.

Outflow

In a CSTR, particle outflow occurs with rate $\tau_{\mathrm{CSTR}}^{-1}$ and particles can be removed as follows:

1. If $y_{\mathrm{out}} = y_i \in \mathcal{M}$, the number of particles at the i^{th} index of the particle-number model is decremented: $N_i \leftarrow N_i - 1$, $i \in [1, N_{\mathrm{thresh}}]$.

2. If $x_{\text{out}} \in \mathcal{X}$, the particle $P(x_{\text{out}})$ is removed from the detailed particle system, i.e. $z_{\mathcal{X}}(t) \leftarrow \{z_{\mathcal{X}}(t) \setminus P(x_{\text{out}})\}$.

5.3 Stochastic numerical method

Strang operator splitting is used to couple the solution of the gas phase chemistry using an ODE solver and the solution of the particle population balance equations using a stochastic method in which the different events are performed probabilistically. This approach has been described elsewhere [21, 140] but is adapted here to handle the interaction between the two type-space models (Algorithm 1 in Appendix A.1). In $\mathcal{M}$, the properties (mass, diameter, etc.) corresponding to each size index in the particle-number space are stored at the simulation outset and only the total particle numbers at each index,

$$N_i,\ i = 1, \ldots, N_{\text{thresh}},$$

and the property sums,

$$\xi(z_{\mathcal{M}}) = \sum_{i=1}^{N_{\text{thresh}}} N_i \xi_i,$$

are updated at runtime. The gas phase chemistry is first updated for half a time step, after which a direct simulation algorithm (DSA) is used to advance the particle population balance equations for a full time step, over a number of smaller splitting steps. Each splitting step involves repeatedly sampling a waiting time from an exponential distribution defined by the total process rate, choosing an inception or coagulation event according to their relative rates and updating the relevant particle system to reflect this event (Algorithm 2 in Appendix A.1).

If the selected process is inception, the particle-number model is adjusted by incrementing the count of particles at the index corresponding to the number of monomers in the incepting particle,

$$N_1 \leftarrow N_1 + 1,$$

and the cached property sums for the particle-number system are updated,

$$\xi(z_{\mathcal{M}}(t)) \leftarrow \xi(z_{\mathcal{M}}(t)) + \xi_1.$$

If the selected process is coagulation, a particle pair $\left(P_i, P_j\right)$ is selected using kernel-specific selection criteria. Majorant kernels are used in this work to simplify computation of the total coagulation rate. Fictitious jumps are used to recover the correct distribution of coagulation events, i.e. particles selected for coagulation are only updated with probability:

$$\mathbb{P}_{i,j} = K\left(P_i, P_j\right) \cdot \hat{K}\left(P_i, P_j\right)^{-1}.$$

If a particle is selected from the particle-number class ($P_i \in \mathcal{M}$), the index corresponding to its monomer count is decremented,

$$N_i \leftarrow N_i - 1,$$

and the cached property sums are updated,

$$\xi\left(z_{\mathcal{M}}\left(t\right)\right) \leftarrow \xi\left(z_{\mathcal{M}}\left(t\right)\right) - \xi_i.$$

A new particle is created by cloning the i^{th} particle from the pre-initialised particle-number list. If both particles are selected from the particle-number system, the first is added to the ensemble at this stage,

$$z_{\mathcal{X}}\left(t\right) \leftarrow \left\{z_{\mathcal{X}}\left(t\right), P_i\right\},$$

and the second coagulates with it. Coagulation events join the colliding particles, combining their list of primaries and creating one new connection point [133].

The surface growth and sintering of adjacent primary particles is performed using a linear process deferment algorithm (LPDA) because the surface growth rate is disproportionately fast relative to the rates of inception and coagulation and would greatly increase the frequency of stopping solving to perform particle updates if performed within stochastic steps. This is also a form of operator splitting which defers the particle processes that occur independently for each particle and performs them either at the end of a splitting step t_{split}, or during the step if the particle is selected for coagulation. This algorithm was introduced by Patterson et al. [120] to improve computational efficiency by reducing the number of times per step the algorithm halts to perform stochastic events. The splitting step is chosen to control the number of deferred particle surface updates that occur relative to the stochastic inception and coagulation events. Suitable step sizes and more details are given in the original paper [120].

The particle-number counts are updated for surface growth in a second LPDA-type sub-scheme (Algorithm 4 in Appendix A.1). This loops over all particle indices and computes the surface area dependent growth rate, samples the number of monomers to add from a Poisson distribution using this rate parameter (as in the original LPDA), and uses this to determine a new index, which is incremented accordingly,

$$\begin{aligned} n_{\text{add,index}} &\sim \text{Poi}\left(\beta_{\text{SG}}\left(A_{\text{index}}\right)\right) \\ \text{newIndex} &\leftarrow \left(\text{index} + n_{\text{add,index}}\right). \end{aligned}$$

If the new index is larger than the threshold size, a new particle is created by cloning the template particle, $P^{\text{tmp}}_{\text{thresh}}$, which is a primary particle of size N_{thresh} monomers, from the pre-initialised particle-number list. The required number of monomers,

$$\left(\text{newIndex} - N_{\text{thresh}}\right),$$

is added and the new particle is then transferred to the detailed particle system.

Particle inflow and outflow are performed after each splitting step. The number of particles expected to enter or leave the system over this time is sampled from a Poisson distribution with rate parameter $1/\tau_{\text{CSTR}}$. Particles are added by uniform selection from the list of particles in the inflow stream(s) followed by increasing the particle-number count ($y_{\text{in}} \in \mathcal{M}$) or adding a particle to the ensemble ($x_{\text{in}} \in \mathcal{X}$). For each chosen particle, on average $\left(V_{\text{smp}}/V^{\text{in}}_{\text{smp}}\right)$ copies are added. Particles are removed by uniform selection followed by decreasing the particle-number count ($y_{\text{out}} \in \mathcal{M}$) or deletion ($x_{\text{out}} \in \mathcal{X}$).

5.3.1 Selecting particles according to their properties

Two particle selection processes are of interest. Uniform selection is used to choose particles to add or remove in flow events, and a pair of particles to collide with a constant coagulation kernel. For more realistic coagulation kernels, selection of a pair of particles might depend on properties of the respective particles, for example in the majorant proposed for the transition regime kernel (Table 3.1), coagulation between small particles and large particles is often favoured. The selection algorithm is outlined in more detail in Algorithm 5 in Appendix A.1.

Random uniform selection

For the particle-number model with $y_i \in \mathcal{M}$, the index i of the selected particle is selected such that:

$$\mathbb{P}\left(\text{index} = i\right) = \frac{N_i}{\sum_{i=1}^{N_\text{thresh}} N_i} \qquad \forall i \in \{1,\ldots,N_\text{thresh}\}. \tag{5.3}$$

For the detailed particle model with $x_i \in \mathcal{X}$, particles $P\left(x_i\right)$ are selected such that:

$$\mathbb{P}\left(P_i\right) = \frac{1}{N\left(t\right)} \qquad \forall i \in \{1,\ldots,N\left(t\right)\}. \tag{5.4}$$

Selection according to particle properties

Let ξ be a property of the particles that is defined for either type-space, such as mass or diameter. For the particle-number model with $y_i \in \mathcal{M}$, the index i of the selected particle is determined using the property ξ as a weighting such that:

$$\mathbb{P}\left(\text{index} = i\right) = \frac{N_i \xi_i}{\sum_{j=1}^{N_\text{thresh}} N_j \xi_j} \qquad \forall i \in \{1,\ldots,N_\text{thresh}\}. \tag{5.5}$$

For the detailed particle model with $x_i \in \mathcal{X}$, particles $P\left(x_i\right)$ are selected using the property ξ as a weighting such that:

$$\mathbb{P}\left(P_i\right) = \frac{\xi\left(P_i\right)}{\sum_{j=1}^{N(t)} \xi\left(P_j\right)} \qquad \forall i \in \{1,\ldots,N\left(t\right)\}. \tag{5.6}$$

5.4 Numerical studies

5.4.1 Comparison with single particle type-space model

The performance of the hybrid approach is compared with a single particle type-space model in which the discrete ensemble describes the full type-space, which is modelled with a detailed particle model, and primary particles are represented by stochastic entities in the ensemble alongside aggregate particles. The latter has been the standard approach for detailed population balance models to date and is well documented in the existing literature [99, 141]. In this chapter, the implementation using the detailed particle model for the full type-space will be referred to as the standard approach or direct simulation algorithm (DSA). Because the detailed particle model describes primary particles as spheres, the two approaches are expected to be equivalent for the same particle processes because the models are inherently the same. This gives a means to validate the algorithm for the hybrid approach against the DSA. The DSA has already been compared to deterministic methods in the literature for example Maisels et al. [83], Menz et al. [101]; thus a comparison is not presented here.

Titanium dioxide (TiO_2) is taken as the particulate species and the gas phase mechanism of West et al. [160, 162] is used, although simplified artificial rates are used for easier analysis of the model behaviour. The TiO_2 system is of industrial interest; however modelling efforts are hindered by the computational cost of high process rates under industrially relevant conditions. The performance is assessed by: comparative convergence behaviour (the double type-space should not affect the solution since the particle-number indices fully encode the particle space at the level of primary particles defined by monomer count); solver time savings; and reduction in required ensemble size.

For continuous functions ϕ, the following convergence property holds as the sample volume, V_{smp}, increases:

$$\int_{\mathcal{M}} \phi\left(y\right) n\left(t, dy\right) = \lim_{V_{\text{smp}} \to \infty} \frac{1}{V_{\text{smp}}} \sum_{i=1}^{N_{\text{thresh}}} N_i \phi\left(y_i\left(t\right)\right).$$

Here, the concentration measure $n\left(t, dy\right)$ is used in place of the density $n\left(t, y\right)$ to allow for particle type-spaces with continuous and discrete components [121]. Likewise, for particles of type $x_i \in \mathcal{X}$ and concentration V_{smp}^{-1},

$$\int_{\mathcal{X}} \phi\left(x\right) n\left(t, dx\right) = \lim_{V_{\text{smp}} \to \infty} \frac{1}{V_{\text{smp}}} \sum_{i=1}^{N(t)} \phi\left(x_i\left(t\right)\right).$$

Test cases

Two test cases are considered: a batch reactor and a continuously stirred tank reactor (CSTR) with no particles in the inflow. A spherical particle model is used in the first case and a detailed model is used in the second case. Both reactors are constant volume, at 1200 K and 4 bar (absolute). The molar composition of the initial mixture in the batch reactor and the inflow stream in the CSTR is 47 % $TiCl_4$ and 53 % O_2. The CSTR is initialised with argon. Their residence times are 6 ms and 10 ms respectively. Time steps of 0.01 ms and 0.1 ms are used respectively, with 10 splitting steps per step (convergence with decreasing splitting step was studied by Shekar et al. [140]).

A constant inception rate is used, with the inception particle size taken to be 0.49 nm (2 TiO_2 units). Thus the particle-number model will always have zero particles at index 1. In the first case, the coagulation rate is constant $K = \tilde{K}$, and in the second case, a transition regime coagulation kernel $K = K_{\text{tr}}$ is used (Eq. (5.13)). In both cases, sintering of neighbouring primary particles is not considered – note that the particle-number model does not introduce an assumption of instantaneous sintering because in the current studies all coagulation events involving the particle-number particles transfer them to the discrete particle ensemble. The surface growth reaction adds TiO_2 units to the particle surface and the rate depends on surface area only,

$$\beta_{\text{SG}}(P_i) = \frac{\tilde{\beta}}{N_{\text{A}}} \cdot A(P_i), \qquad \forall (P_i) \in \mathcal{M} \cup \mathcal{X}.$$

Convergence tests

For given property ξ, a simulation with M timesteps, L repeat runs and a maximum ensemble size of $N_{\max}$ has mean value $\mu_\xi^{(N_{\max},L)}(t_k)$ at time t_k, $k \in [1,M]$,

$$\mu_\xi^{(N_{\max},L)}(t_k) = \frac{1}{L}\sum_{l=1}^{L} \xi^{(N_{\max},l)}(t_k), \tag{5.7}$$

and standard deviation $\sigma_\xi^{(N_{\max},L)}(t_k)$ at time t_k, $k \in [1,M]$,

$$\sigma_\xi^{(N_{\max},L)}(t_k) = \sqrt{\frac{1}{L-1}\sum_{l=1}^{L} \left(\xi^{(N_{\max},l)}(t_k)\right)^2 - \left(\mu_\xi^{(N_{\max},L)}(t_k)\right)^2}. \tag{5.8}$$

The relative statistical error,

$$\overline{\varepsilon}_{\text{stat},\xi}^{(N_{\max},L)}(t_k) = \frac{\alpha_{0.99}}{\sqrt{L-1}} \cdot \frac{\sigma_\xi^{(N_{\max},L)}(t_k)}{\mu_\xi^{(N_{\max},L)}(t_k)}, \tag{5.9}$$

is used to assess the random error in repeat simulations at a given confidence level (99 % used here, with $\alpha_{0.99}$ from the t-distribution).

The average relative total error,

$$\overline{\varepsilon}_{\text{total},\xi}^{(N_{\max},L)} = \frac{1}{M}\sum_{k=1}^{M}\frac{\left|\mu_{\xi}^{(N_{\max},L)}(t_k) - \xi^{*}(t_k)\right|}{\xi^{*}(t_k)}, \tag{5.10}$$

is used to assess the relative difference compared to a true solution ξ^*. Here, the 'true' solution is approximated by the solution with $N_{\max} = 2^{18}$ and $L = 10$ and the convergence study is performed for $N_{\max} \in \{2^5, 2^6, 2^7, \ldots, 2^{17}\}$, with $N_{\max} \times L = 2^{18}$.

The properties used to illustrate convergence behaviour in this chapter include particle number concentration, $M_0(t)$,

$$M_0(t) = \frac{N(z_{\mathcal{M}}(t)) + N(z_{\mathcal{X}}(t))}{V_{\text{smp}}}, \tag{5.11}$$

and the average particle collision diameter, d_{c},

$$d_{\text{c}}(P_i) = \frac{6V_i}{A_i} n_i^{\frac{1}{1.8}}, \tag{5.12}$$

which is a measure of average particle size in terms of its volume, V_i, A_i and number of primaries n_i, and is an example of a property that is of importance in applications. The denominator of the exponent is the particle fractal dimension and the value of 1.8 is typically used for aerosols formed by coagulation in the transition regime [140].

Solver time

Tests were run on one Intel Xeon E5-2640 CPU (2.40 GHz) of a 40 processor node with 200 GB RAM, running Red Hat Enterprise Linux version 7.2.

Case 1: Constant rates batch reactor with spherical particle model

The constant rates case with spherical particle model is used to demonstrate proof of concept – under trivial constant rate conditions, the particle-number/particle model matches the convergence behaviour of the particle model (Figs. 5.5 and 5.6). The convergence tests were performed with $I = 10^{16}$ cm^{-3}s^{-1}, $\tilde{\beta} = 10^{24}$ cm^{-5}s^{-1} and $\tilde{K} = 1.5 \times 10^{-15}$ cm^{-3}s^{-1}. A constant majorant kernel is used for coagulation and this has value $\hat{K} = 1.5\tilde{K}$.

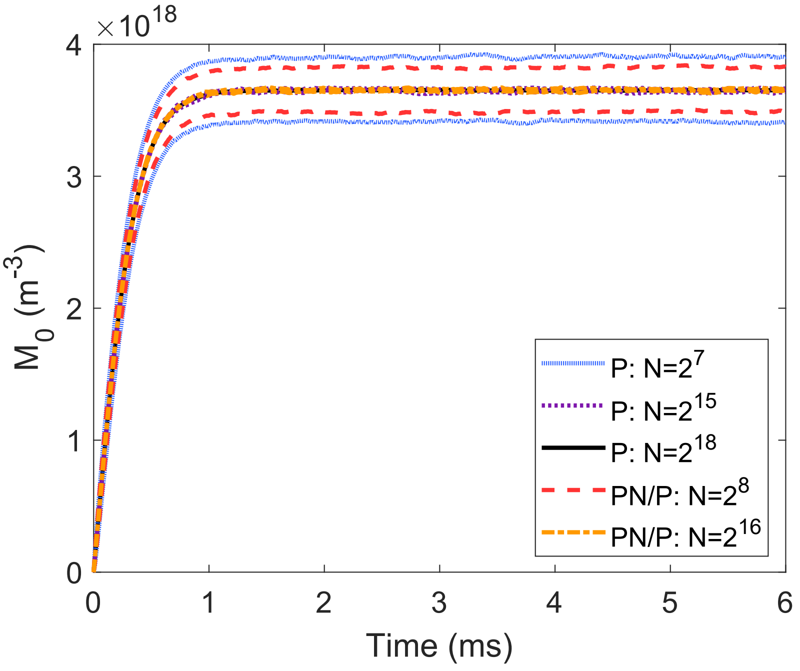

(a) Number density

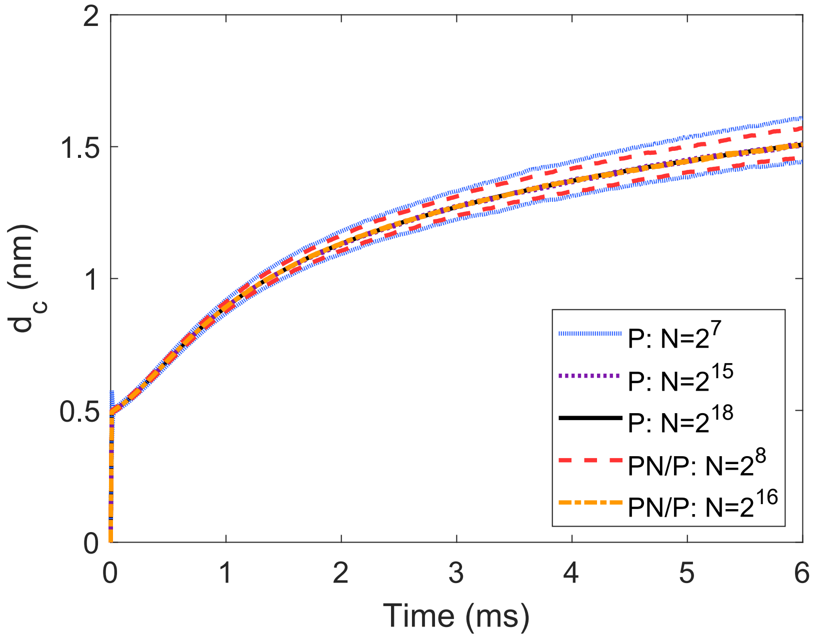

(b) Collision diameter

Fig. 5.5: Transient (a) number density and (b) collision diameter in convergence study maintaining $N_{\text{max}} \times L = 2^{18}$ – the solid black line is the high fidelity solution and one standard deviation above and below the mean are shown as dotted lines for odd (particle model) and dashed lines for even (particle-number/particle model with $N_{\text{thresh}} = 10^2$) powers of 2 (case 1).

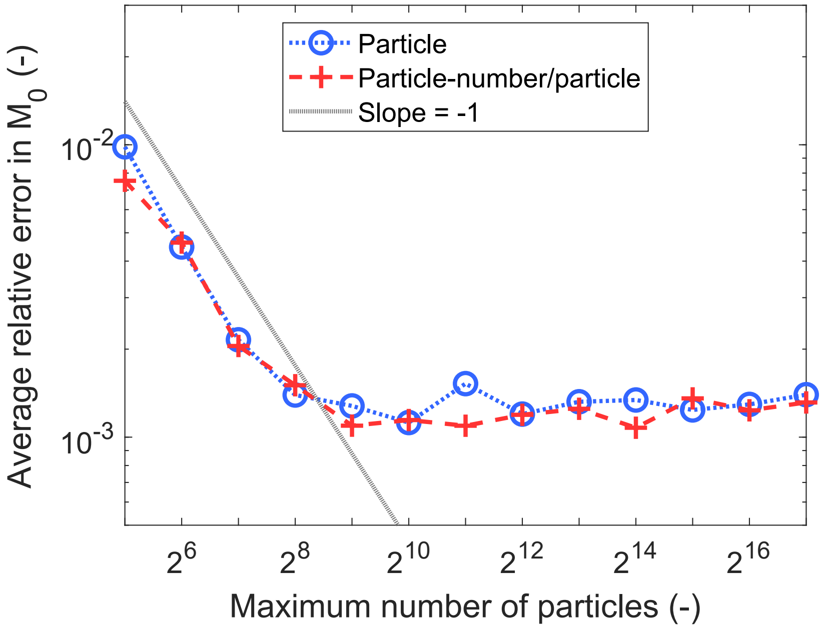

(a) Number density

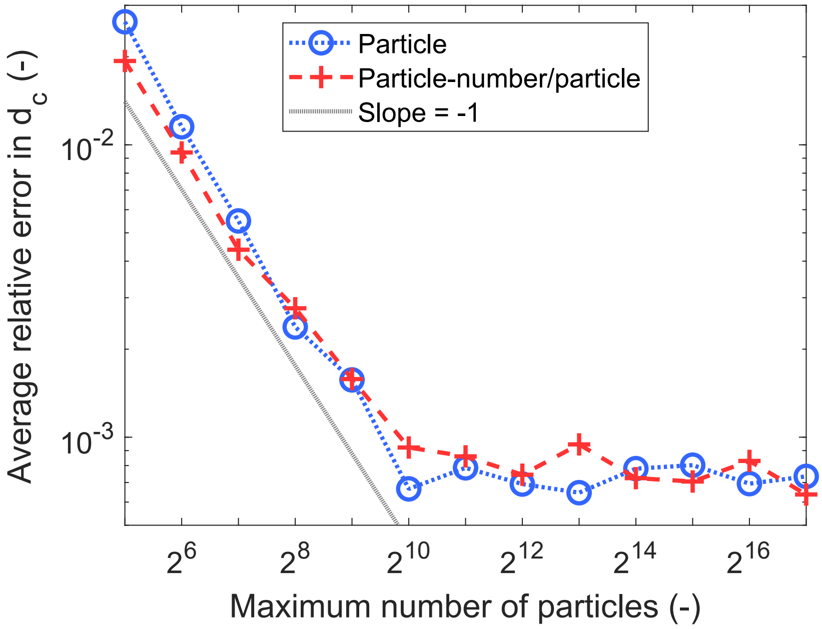

(b) Particle diameter

Fig. 5.6: Convergence of (a) number density and (b) collision diameter, maintaining $N_{\text{max}} \times L = 2^{18}$ – average relative total error (Eq. (5.10)) of the particle model and particle-number/particle model ($N_{\text{thresh}} = 10^2$) compared to the high fidelity solution (case 1 conditions).

The spherical particle model assumes each coagulation event is followed by instant coalescence to form a larger, spherical particle, so both type-spaces hold the same information; however it should be possible to store/update this information more efficiently in a vector than a discrete ensemble. Surface growth events are performed once per particle since particles are not composed of distinct primaries and choice of particles for coagulation and outflow is done by random selection (uniform selection criterion for Algorithm 5 in Appendix A.1). Thus the opportunities for improving run time with the PN/P model are limited; however, as expected it is more economical, especially for large ensembles (Table 5.1).

Table 5.1: Single run times for particle (P) and particle-number/particle (PN/P) models with $N_{\text{thresh}} = 10^2$ in the convergence study with case 1 conditions.

Particles N_{max}	Repeats L	Single run time P (min)	Single run time PN/P (min)
2^7	2048	0.118	0.117
2^8	1024	0.130	0.126
2^9	512	0.154	0.143
2^{10}	256	0.201	0.176
2^{11}	128	0.336	0.265
2^{12}	64	0.583	0.425
2^{13}	32	1.18	0.797
2^{14}	16	1.76	1.15
2^{15}	8	3.06	1.94
2^{16}	4	5.79	3.68
2^{17}	2	12.3	7.99
2^{18}	1	26.1	16.5

Case 2: Transition kernel CSTR with detailed particle model

The transition regime coagulation kernel,

$$K_{\text{tr}}\left(P_i,P_j\right) = \frac{K_{\text{sf}}\left(P_i,P_j\right) K_{\text{fm}}\left(P_i,P_j\right)}{K_{\text{sf}}\left(P_i,P_j\right) + K_{\text{fm}}\left(P_i,P_j\right)}, \forall \left(P_i,P_j\right) \in \mathcal{M} \cup \mathcal{X}, \tag{5.13}$$

is chosen because it is relevant to real synthesis conditions and depends on the properties of each particle which makes its evaluation more costly. The transition regime kernel is computed from the harmonic mean of the slip-flow and free-molecular kernels (K_{sf}, K_{fm}). The slip-flow kernel is sufficiently simple not to require a majorant kernel (Eq. (3.42)). A majorant for the free-molecular kernel can be formed using inequalities for the nonlinear terms (Eq. (3.40)). This expression is useful because it does not require computation of the nonlinear terms for each particle pair to find the total rate. The rates for each kernel are split into several terms, computed as the sum of different particle properties across both type-spaces, and these terms define particle selection rules used to choose a pair of particles (rates and selection rules in terms of particle properties are given in Table 3.1). Surface growth is performed on every primary particle in each aggregate. The average relative error is compared with ten runs of the particle model with $N_{\max} = 2^{18}$. The convergence tests were performed with $I = 10^{12}$ cm^{-3}s^{-1} and $\tilde{\beta} = 10^{24}$ cm^{-5}s^{-1}.

Although the rates used in this case are more complicated, the simulation with two type-space models converges on the same properties as the single type-space approach (Figs. 5.7–5.9). Slight discrepancies between the PN/P model and the high fidelity solution with the particle model may exist due to differences in the ordering of particles – i.e. a list in increasing size order vs. an unordered list of particles as formed could influence which particle is selected in Algorithm 5 in Appendix A.1 – but it is clear from the comparison of the steady state particle size distributions (Fig. 5.8) that the algorithm for the PN/P model finds the same solution. Differences in run time (Fig. 5.10) are more significant than in the study with the spherical particle model. This is especially noticeable for large ensembles where updates to the particle-number list are much more efficient than updates to distinct particles and a speed up of approximately 50 % is observed for the ensembles with $2^{17} = 131072$ particles. For small ensembles, the PN/P model is more efficient in a narrower range of threshold values because with larger thresholds, time spent searching through and updating the particle-number list becomes relatively expensive compared with using a small set of discrete particles. In general, a threshold of $N_{\text{thresh}} = 10^4 = 10000$ was found to work well for the current conditions.

Reduced solver time is useful if CPU time is constrained; however the main benefit is that this allows an increase in the sample volume in the PN/P model, i.e. use of a time equivalent sample volume (TESV, Table 5.2 column 5), or an increase in the number of repeat runs in the PN/P model, i.e. use of time equivalent runs (TER, Table 5.2 column 6), to gain additional accuracy for comparable CPU cost (Fig. 5.9, solid vertical lines illustrate reduced error with additional repeats for same computational cost). The TESV is the sample volume for which the average run time of the PN/P model matches that of the particle model. The TER is computed from the ratio of the average solver times ($\bar{t}$) for the particle and particle-number/particle simulations,

$$L^{\text{TER}} = \frac{\bar{t}_{\text{P}}}{\bar{t}_{\text{PN/P}}} \cdot L. \tag{5.14}$$

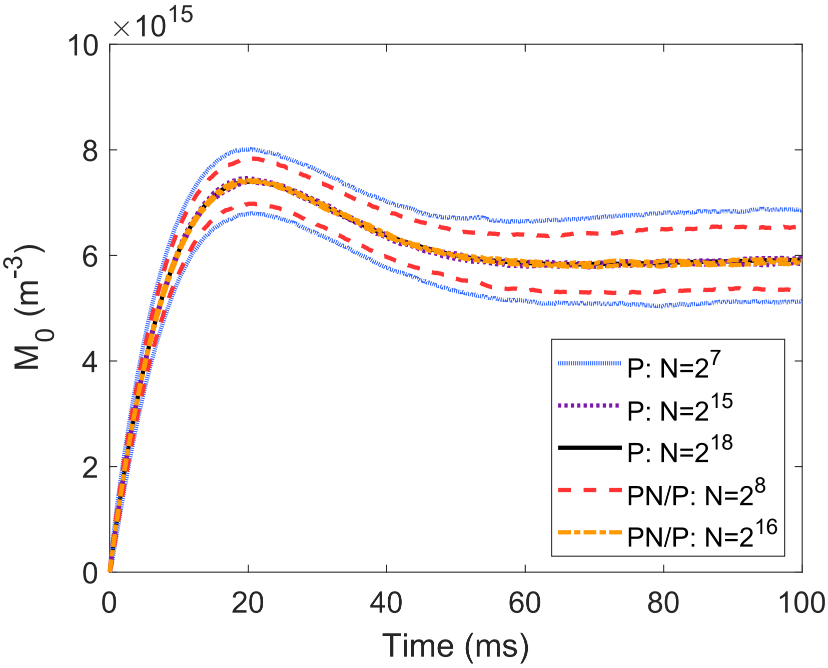

(a) Number density

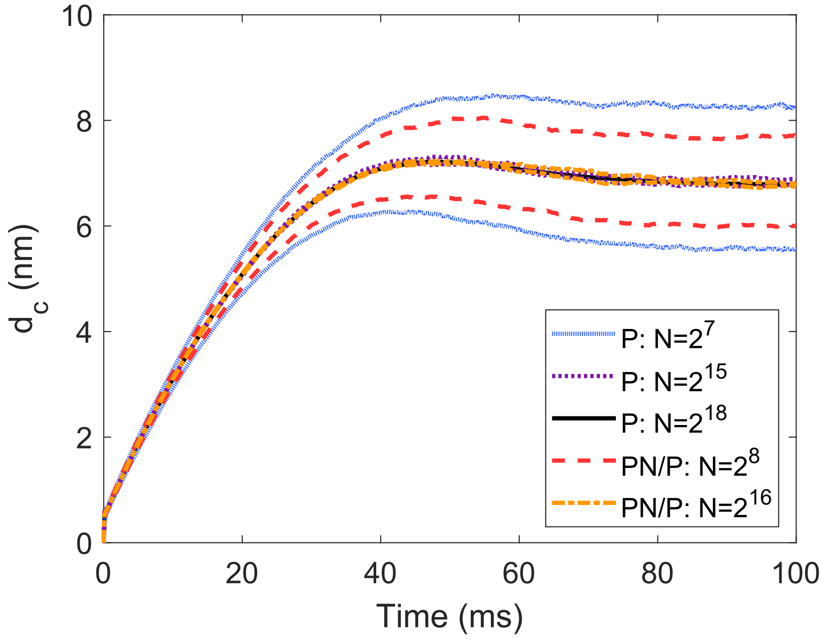

(b) Collision diameter

Fig. 5.7: Transient (a) number density and (b) collision diameter in convergence study maintaining $N_{\max} \times L = 2^{18}$ – the solid black line is the high fidelity solution and one standard deviation above and below the mean are shown as dotted lines for odd (particle model) and dashed lines for even (particle-number/particle model with $N_{\text{thresh}} = 10^4$) powers of 2 (case 2 conditions).

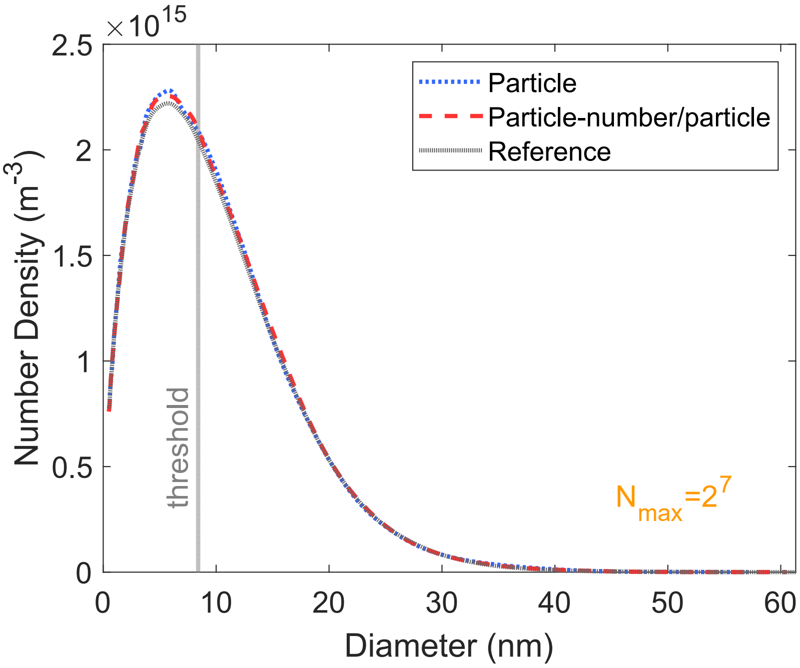

(a) $N_{\max} = 2^7$

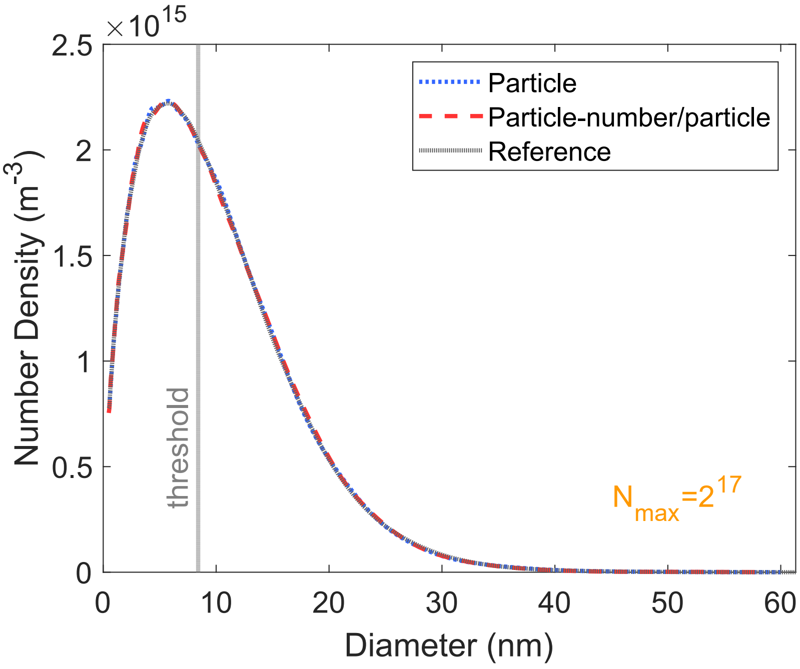

(b) $N_{\max} = 2^{17}$

Fig. 5.8: Kernel density estimates (bandwidth 0.07) for primary particle size distributions from particle model and particle-number/particle model with $N_{\text{thresh}} = 10^4$ and ensemble capacities of (a) $N_{\max} = 2^7$ and (b) $N_{\max} = 2^{17}$ compared with reference solution with $N_{\max} = 2^{18}$ and $L = 10$.

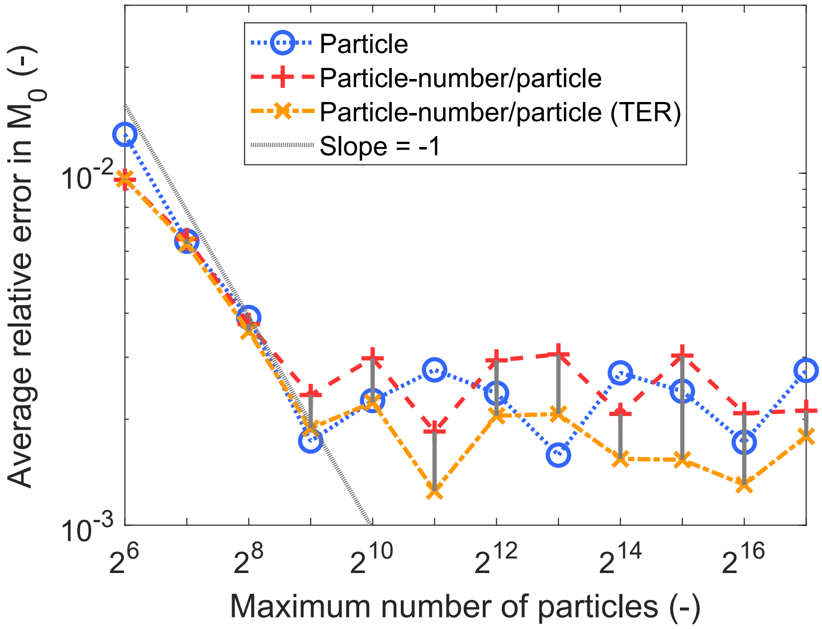

(a) Number density

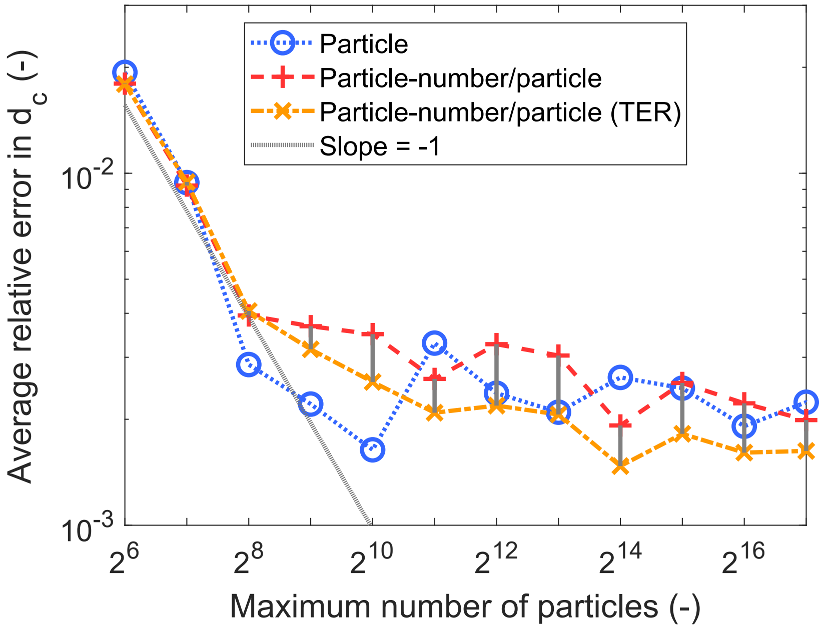

(b) Particle diameter

Fig. 5.9: Convergence of (a) number density and (b) collision diameter, maintaining $N_{\max} \times L = 2^{18}$ – average relative total error (Eq. (5.10)) of the particle model, particle-number/particle model ($N_{\text{thresh}} = 10^4$), and PN/P model with time equivalent runs (TER) compared to the high fidelity solution (case 2 conditions).

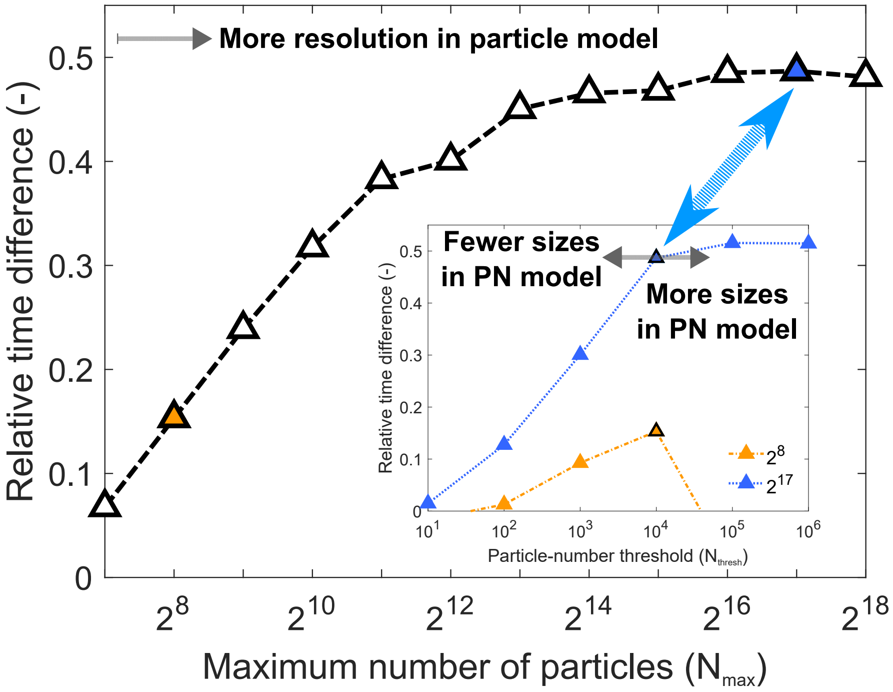

Fig. 5.10: Relative time difference maintaining $N_{\text{max}} \times L = 2^{18}$ for pure particle model and particle-number(PN)/particle model with inset showing effect of threshold value N_{thresh} (case 2 conditions).

Table 5.2: Single run times, sample volume increase and additional repeats that can be achieved with solver time savings gained from PN/P model with $N_{\text{thresh}} = 10^4$ (case 2 conditions).

Particles N_{max}	Repeats L	Single run time P (min)	Single run time PN/P (min)	TESV ratio $V_{\text{smp}}^{\text{TESV}} \cdot V_{\text{smp}}^{-1}$	TER L^{TER}
2^7	2048	0.339	0.316	1.67	2196
2^8	1024	0.436	0.369	1.67	1209
2^9	512	0.636	0.484	1.70	672
2^{10}	256	1.05	0.717	1.74	375
2^{11}	128	1.96	1.21	1.81	207
2^{12}	64	3.46	2.07	1.88	107
2^{13}	32	6.46	3.55	1.90	58
2^{14}	16	9.23	4.93	1.95	30
2^{15}	8	16.6	8.83	1.97	15
2^{16}	4	31.3	16.1	2.00	8
2^{17}	2	62.2	31.9	2.00	4
2^{18}	1	124	64.6	2.03	2

The PN/P model removes most of the solo primary particles from the discrete particle ensemble, which allows the discrete ensemble to be used almost exclusively to resolve more complicated aggregate particles for the same computational cost and ensemble memory overhead by using a larger sample volume, as shown in the simulated imaging pictures in Fig. 5.11 (generated using the ray-tracing program *POV-Ray* to draw particles with sizes specified according to the simulation data). This ensures that maximum utility is obtained from the detailed particle model without 'wasting' ensemble space and time on structurally simple particles. Increasing the sample volume increases the rate of numerical inceptions. The sample volume was chosen to ensure that the discrete ensemble never reached its maximum capacity in these studies, preventing random removals in all cases so that the statistical noise did not increase.

An alternative approach is to maintain a more economical memory foot-print by initialising a smaller ensemble for tracking fewer distinct particles. This could be useful for systems that have an initial burst of particle inception due to high concentration of the gas phase precursor yielding a high initial number density. In such a system, doubling and contraction algorithms are often necessary with a discrete ensemble since demand for capacity varies with time. The particle-number list can store arbitrarily many incepting particles so the ensemble can be customized to the size required to store aggregates only.

The effect of exceeding the ensemble capacity is illustrated further in Fig. 5.12. With a single discrete particle model, increasing the sample volume by a factor of three from the previous conditions results in contractions in the interval $t \in [4.8, 20]$ ms (shown in Fig. 5.12(a) with a horizontal arrow) because there is no space for new particles in the discrete ensemble so inceptions are accommodated by randomly removing an existing particle from the ensemble and scaling the sample volume to preserve the particle number density. With the hybrid type-space model, particle inceptions contribute to the particle-number space, $\mathcal{M}$, instead of being added to the ensemble space, $\mathcal{X}$. This list storage (shown in Fig. 5.12(a) with a vertical arrow) prevents the ensemble from flooding; thus no particles are removed.

Particle removal randomizes the system when the particles are polydisperse. This can be seen in Fig. 5.12(b): tripling the sample volume significantly increases the total error for the particle model (cf. bars labelled "P: V_{smp}" and bars labelled "P: $3V_{\text{smp}}$") whereas it reduces the total error for the hybrid model (*cf.* bars labelled "PN/P: V_{smp}" and bars labelled "PN/P: $3V_{\text{smp}}$") due to the increased statistical significance of events in the larger sample volume.

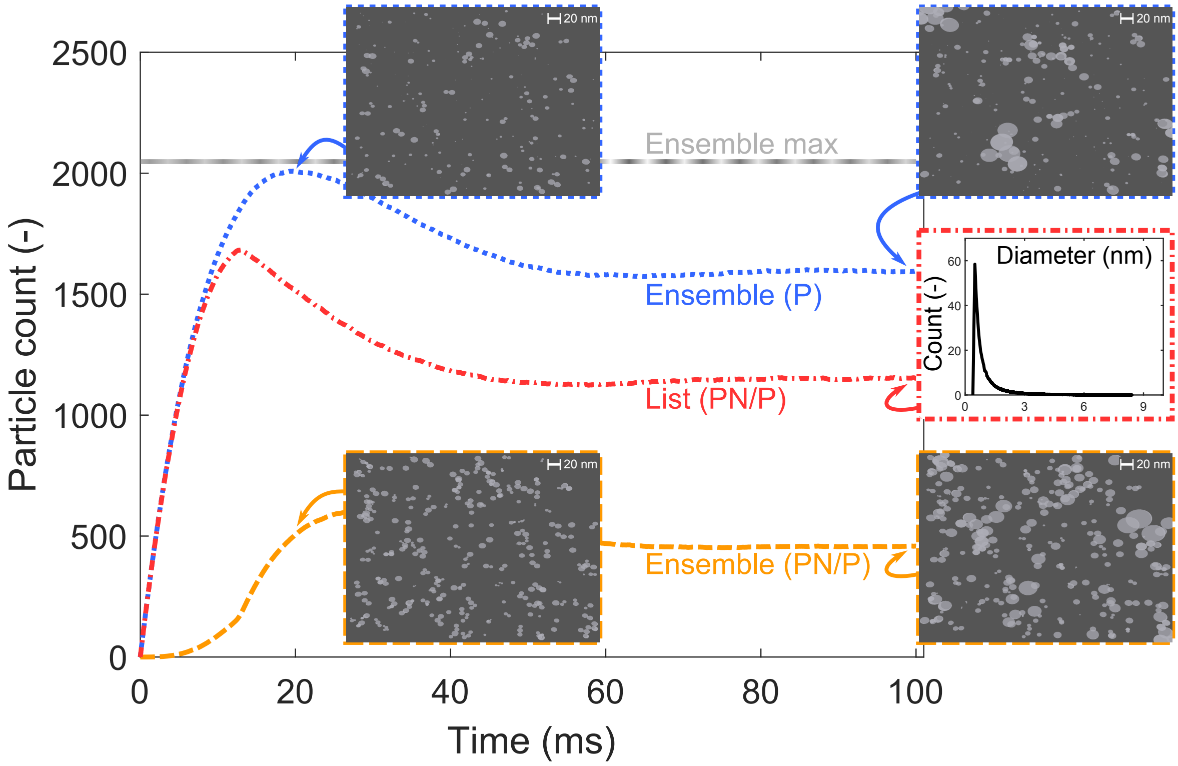

Fig. 5.11: Particle counts in the ensemble and particle-number list for particle model (P) and particle-number/particle model (PN/P), with inset simulated SEMs of 200 tracked ensemble particles at 20 ms and 100 ms (scale bar shows 20 nm) for $N_{\text{max}} = 2^{11}$ and $N_{\text{thresh}} = 10^4$ (PN/P with runtime equivalent sample volume).

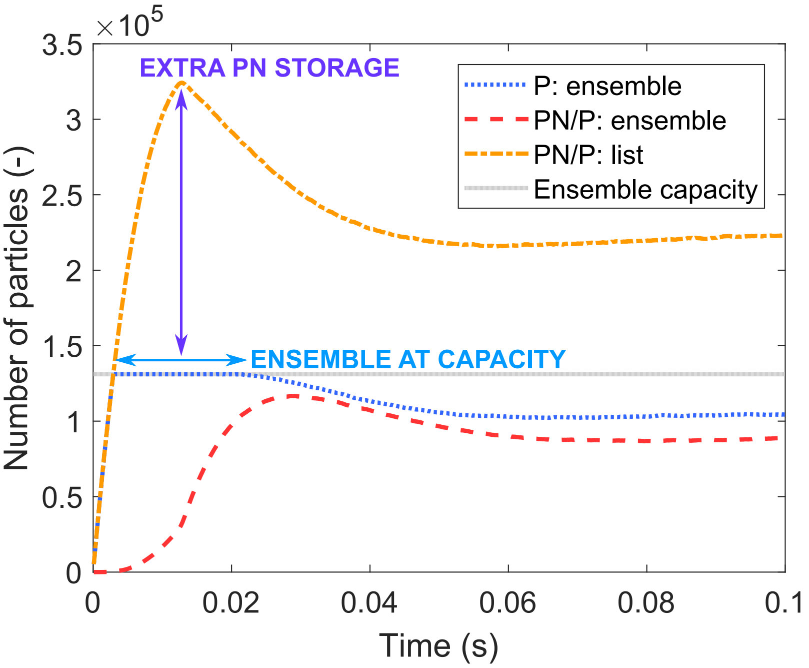

(a) Particle counts in $3V_{\text{smp}}$ case

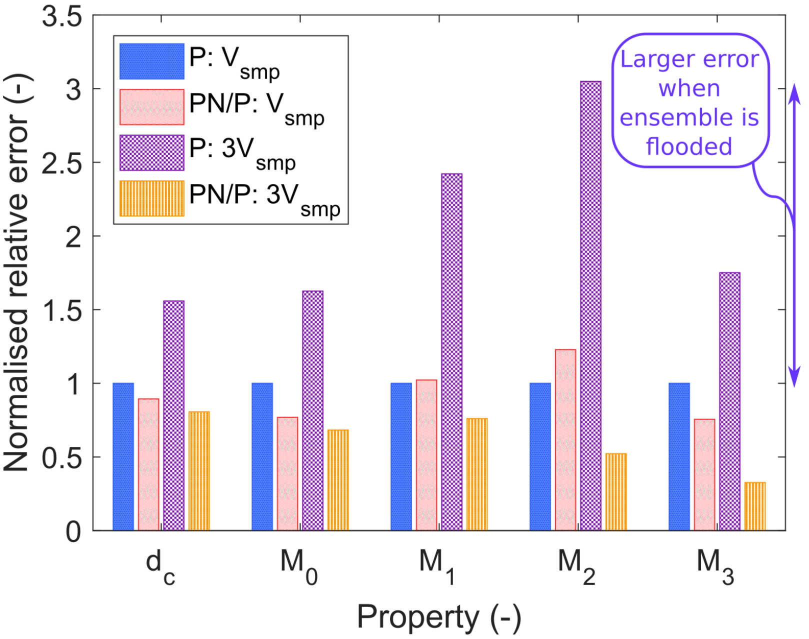

(b) Average error in converged solutions

Fig. 5.12: Effect of exceeding ensemble capacity with $N_{\text{max}} = 2^{17}$: (a) illustration of finite ensemble operating at capacity (horizontal arrow) and extra storage of particles in the particle-number model (vertical arrow); and (b) normalised total relative error in: particle model; PN/P model ($N_{\text{thresh}} = 10^4$); particle model with triple sample volume; and PN/P model with triple sample volume (case 2 conditions).

CSTR with particle inflow

A second CSTR is added in series with the first using the conditions from case 2. The residence times are both 10 ms, and the outflow from CSTR 1 is the only inflow stream to CSTR 2. This case demonstrates the use of the particle-number/particle inflow algorithm (Algorithm 3 in Appendix A.1) as there are particles in the outflow from CSTR 1. The primary PSD shifts towards larger particles in CSTR 2 due to further surface growth (Fig. 5.13).

This study also provides insight into the transient statistical error behaviour (Eq. (5.9)) in a flow reactor. As shown in previous work [101], the error increases before reaching a plateau as the system reaches steady state. The same sample volume was used for both reactors. For the second CSTR with the particle model, random removal events occurred from ca. τ_{CSTR2}, reducing the sample volume (shown as a dashed black line in 5.14(b)). The sample volume in the second CSTR was constant for the particle-number model, due to use of the particle-number list to store inflowing and incepting particles. Thus, the steady statistical error in the second CSTR was slightly lower (Fig. 5.14(b)).

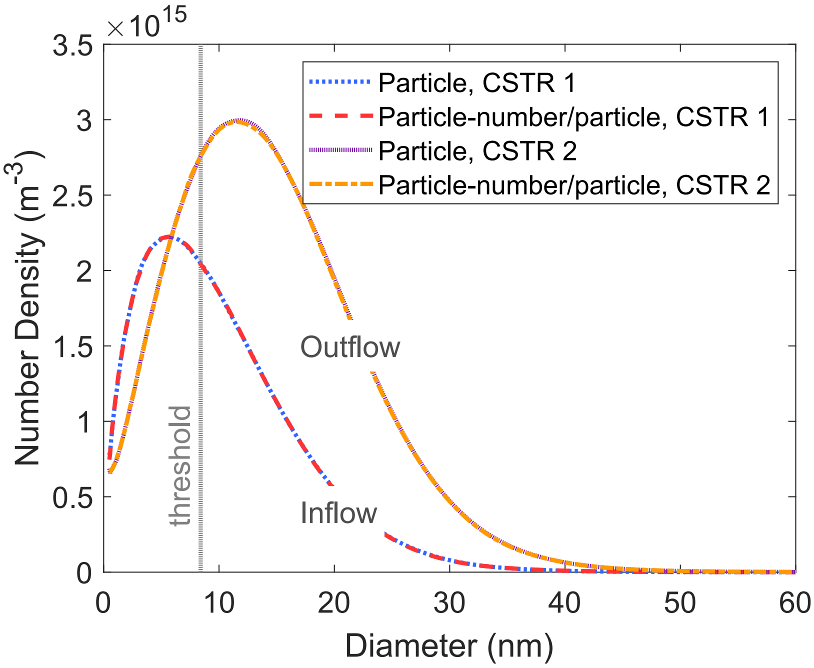

Fig. 5.13: Steady state kernel density estimate of the primary particle size distribution in the inflow and outflow from CSTR 2 (bandwidth of 0.07), for the particle and particle-number/particle ($N_{\mathrm{thresh}} = 10^4$) models with $N_{\mathrm{max}} = 2^{14}$ and $L = 160$.

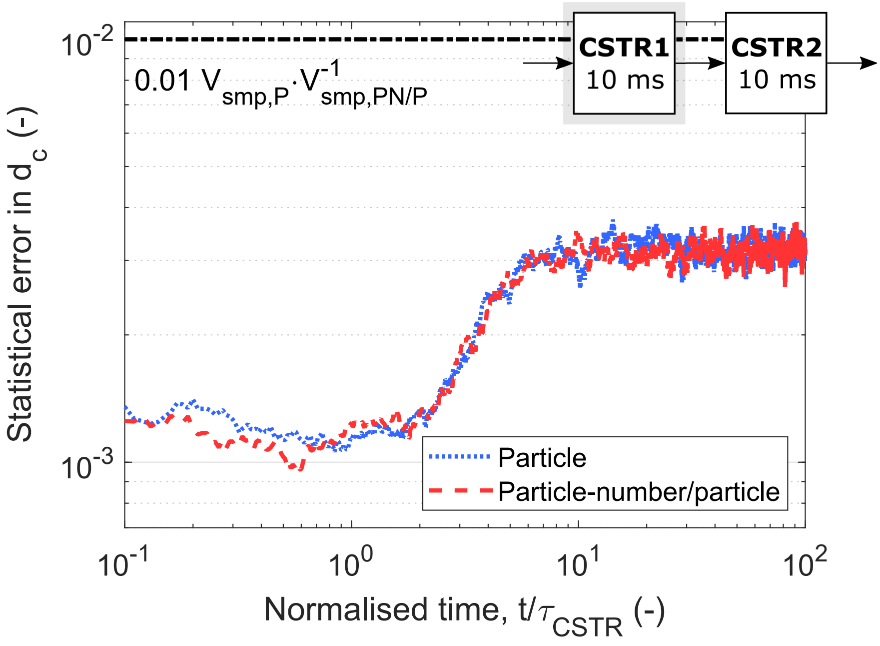

(a) CSTR 1

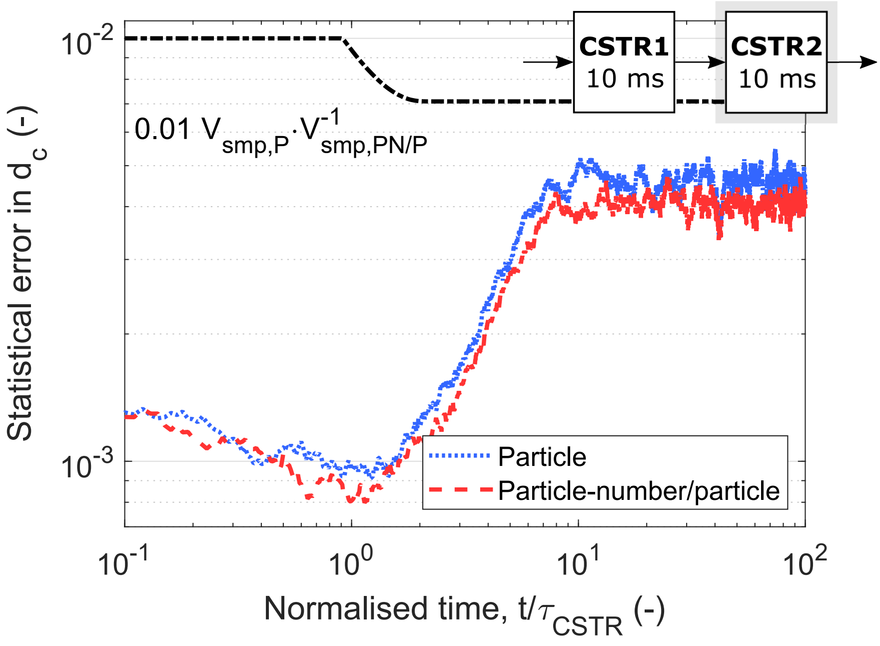

(b) CSTR 2

Fig. 5.14: Transient statistical error at 99 % confidence level, using t-distribution values, in a pair of CSTRs connected in series: (a) CSTR 1 and (b) CSTR 2, for the particle and particle-number/particle ($N_{\mathrm{thresh}} = 10^4$) models with $N_{\max} = 2^{14}$ and $L = 160$.

5.4.2 Model performance in different rate regimes

Performance of the PN/P model is assessed in different rate regimes using the conditions in Table 5.3, for the CSTR from case 2 with a transition regime coagulation kernel and a detailed particle model for the aggregate type-space.

Table 5.3: Inception and surface reaction rate constants used in rate study.

Process	Units	Rate constants			
Inception	$[\mathrm{cm}^{-3}\cdot\mathrm{s}^{-1}]$	1×10^{6}	1×10^{9}	1×10^{12}	1×10^{13}
Surface reaction	$[\mathrm{cm}^{-5}\cdot\mathrm{s}^{-1}]$	1×10^{18}	1×10^{21}	1×10^{24}	

The process rates are coupled since the coagulation rate increases quadratically with number density and depends on properties of the particles such as diameter. To simplify the analysis, the average ratio of the rates is used in Figs. 5.15–5.17:

$$\text{Mean rate ratio (inception:coagulation)} = \frac{1}{M}\sum_{m=1}^{M}\frac{R_{\text{inception}}(t_m)}{R_{\text{coagulation}}(t_m)}$$

$$\text{Mean rate ratio (surface reaction:coagulation)} = \frac{1}{M}\sum_{m=1}^{M}\frac{R_{\text{surface reaction}}(t_m)}{R_{\text{coagulation}}(t_m)}.$$

The mean count ratio is used to assess the utility of the particle-number list for storing particles and refers to the average particle-number count divided by the average ensemble count:

$$\text{Mean count ratio} = \frac{1}{M}\sum_{m=1}^{M}\frac{N(z_{\mathcal{M}}(t_m))}{N(z_{\mathcal{X}}(t_m))}.$$

The PN/P model offers considerable performance advantages over the use of a single detailed particle model for conditions that result in a large number of solo primary particles (when inception dominates coagulation). In these cases, most of the particles in the system can be stored in the particle-number list, significantly reducing the ensemble size requirements (Fig. 5.15).

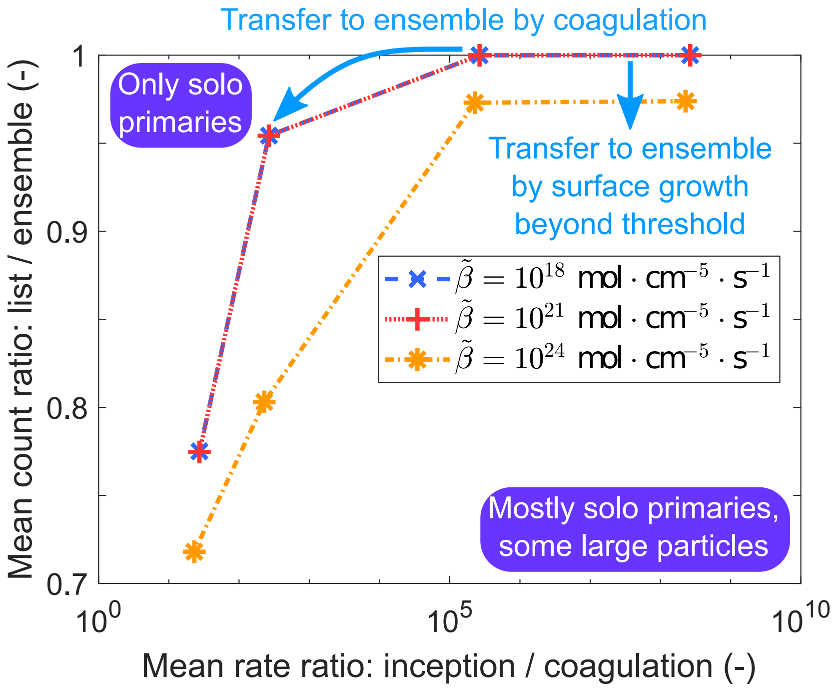

Fig. 5.15: Ratio of particles in the particle-number list to particles in the ensemble in the PN/P model for different ratios of inception rate to coagulation rate (using threshold $N_{\text{thresh}} = 2^{17}$).

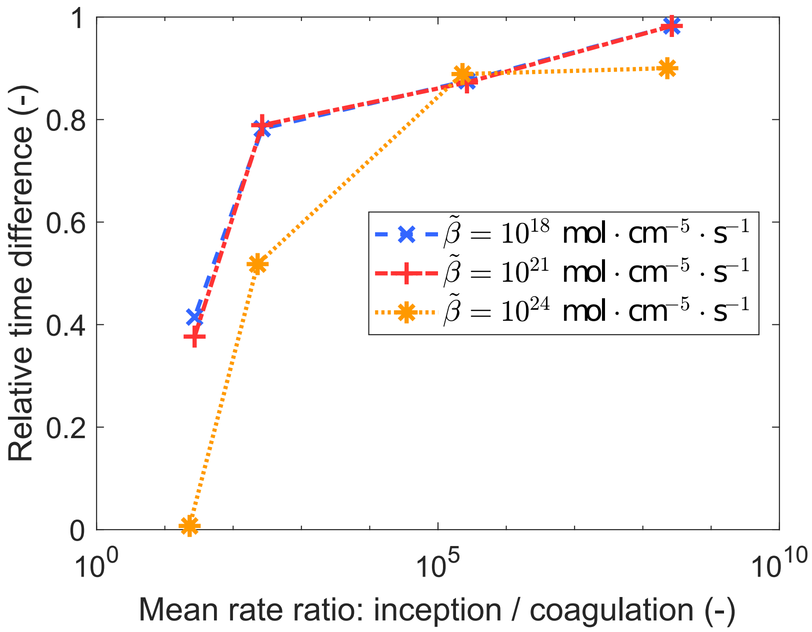

Fig. 5.16: Solver time difference for different ratios of inception rate to coagulation rate (using threshold $N_{\text{thresh}} = 2^{17}$).

Conditions with high surface growth and similar coagulation and inception rates do not see significant solver time advantage with the PN/P model (Fig. 5.16) because the coagulation processes produce large aggregates and the surface updates for these complex structures dominate the solver time; however, there are still significantly many primary particles in the particle-number list under these conditions and the option to use a smaller particle ensemble could still be attractive due to improved memory efficiency. Future work could consider methods for mitigating the aggregate update cost.

When the surface growth rate is very high, primary particles grow rapidly and are pulled out of the particle-number system into the particle system unless a large threshold value is used to store the primaries in the particle-number system for as long as possible (Fig. 5.17). The number density of very large primaries becomes lower with increasing index (Fig. 5.18), so use of a high threshold (e.g. $N_{\text{thresh}} = 10^4$) achieves limited additional particle storage; however, since the updates to the particle-number model are comparatively inexpensive even for large thresholds, it is reasonable to use a large threshold to avoid wasting ensemble space on single primary particles.

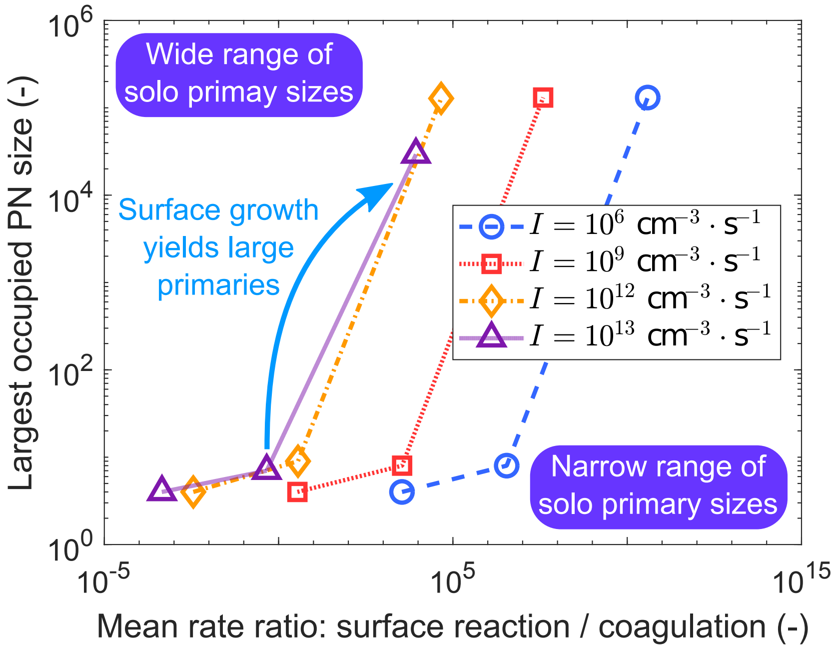

Fig. 5.17: Largest occupied particle-number (PN) size for different ratios of surface reaction rate to coagulation rate (using threshold $N_{\text{thresh}} = 2^{17}$).

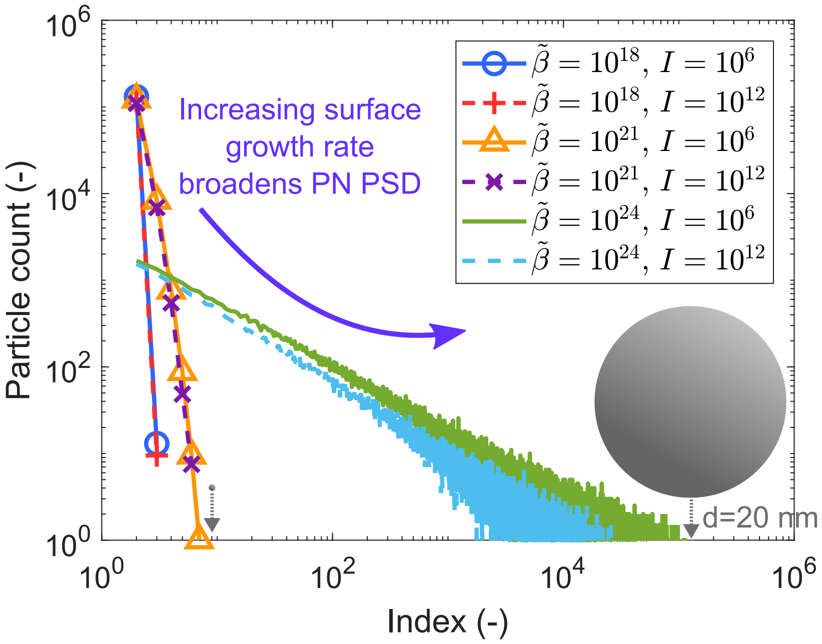

Fig. 5.18: Particle-number (PN) size distributions at t_f for different ratios of surface reaction rate to coagulation rate (using threshold $N_{\text{thresh}} = 2^{17}$).

5.5 Chapter summary

This chapter has presented a stochastic population balance algorithm that uses a detailed particle model to resolve complex particles and a particle-number model for simple particles. This improves computational resolution of particles when the PSD is broad and aggregate particle morphology is important. It is more robust to selection of ensemble size because (practically) arbitrarily many primary particles can be stored in the number list and a larger sample volume can be tolerated for a given ensemble size, without causing random removal of particles. Because updating particles in the list only requires updating a counter, this approach is also more efficient in general. The improved efficiency is expected to be particularly important under high concentration conditions, such as modelling industrial particle synthesis.

For low surface growth rates, the required threshold to store all primaries is small because the range of primary sizes is narrow; however, under high surface growth conditions, it is advantageous to use a larger threshold in order to accommodate the wider range of primary sizes and benefit from the more efficient update structure of the particle-number list. The new hybrid model is less effective when the coagulation rate is very high, because the computational complexity associated with very large aggregate particles dominates the solver time.

The two primary advantages of the hybrid scheme are reduced sensitivity to selection of numerical parameters, i.e. robustness to parameter choice, and improved efficiency. Two foreseeable benefits of better efficiency are:

1. It can be up to 50 % faster than a single detailed particle type-space model when the surface growth rate is high and the surface updates to ensemble particles are expensive. This speed-up can be traded for a larger sample volume to achieve a greater statistical accuracy for comparable cost and memory. One possible application where this would make a significant improvement is if particle–particle heat transfer effects were included as the surface updates for each particle would be very costly.

2. When the inception/coagulation ratio is large, most particles can be stored in the particle-number list, reducing the particle ensemble capacity required to resolve the aggregate particles. This smaller ensemble has a lower memory footprint. This also assists tailoring the ensemble to the size needed to store aggregate particles, by avoiding initial periods of high inception when the precursor concentration is high, without resorting to contraction and doubling algorithms.

A number of adaptations are possible for different systems:

1. If the internal coordinate is not ‘quantized’ (multiples of a monomer subunit), the indexing can be converted to sections of larger width at the cost of introducing some approximation error within the sections.

2. For more efficiency, it might be assumed that collisions between small particles result in instant coalescence, allowing these collisions to be performed in the particle-number model. This could be controlled using the sintering rate to determine where this assumption is near to the actual behaviour.

3. Weighted particle methods such as described by Patterson et al. [121] could be employed to reduce the number of particles injected to the ensemble by surface growth beyond the threshold.

In the following chapter, the new algorithm will be applied to study industrial synthesis of titania to extend the approach developed in Chapter 4 and address numerical challenges that previously precluded more detailed study. The extended model includes the system energy balance and a more sophisticated description of particle morphology.

Chapter 6

Studying titania synthesis using a hybrid particle model

In this chapter, the new hybrid particle model developed in Chapter 5 is applied to study industrial synthesis of titanium dioxide. Motivated by findings from the initial reactor study in Chapter 4, an energy balance including important heat release contributions from the particle processes is modelled to create a more flexible framework. The performance gains with the hybrid model enable inclusion of the system energy balance and a more sophisticated particle model which allows study of particle formation in extensive detail. The detailed particle model resolves properties of the particulate product that determine product quality and post-processing efficiency including particle size and degree of primary particle overlap, i.e. sintering. These are explored for different process design choices and the PSD and morphology are shown to be sensitive to variations in reactant temperature and dosing strategy – higher temperature injections produce more sintered particles, more frequent injections narrow the PSD and chlorine dilution reduces particle size and variance. Visualisations of simulated particle structures can now be compared with electron microscopy of a typical raw industrial product. This comparison illustrates similar aggregate characteristics with slightly larger primary particles. Material from this chapter was published in ***Paper 3*** *listed in the Declaration.*

6.1 Extensions to reactor model

A reactor network approach is employed to model the system, as in Chapter 4. This includes continuously stirred tank reactors (CSTRs) in series with one reactant injection per CSTR 'stage' for the dosing zone, and subsequent plug flow reactors (PFRs) for the tubular working and cooling zones. Chapter 4 modelled the reactor at constant temperature, with a stipulated temperature profile in the working zone to model completion of the exothermic reactions. This limited the model's flexibility and constrained investigation of different design choices. This motivated the inclusion of the energy balance in the current chapter where the intention is to investigate process conditions and reactor configurations such as stream temperatures and dosing strategies respectively. The hybrid particle-number/particle (PN/P) model developed in Chapter 5 is used to describe the particle type-space with the overlapping-spheres particle model (Section 3.2.4).

This section provides system mass and energy balance equations (Section 6.1.1) for non-isothermal, constant pressure reactors and motivates cases to be studied (Section 6.1.2). Extensions to the stochastic numerical method are developed in Section 6.2 and process modelling results for the different cases are presented in Section 6.3, which highlights use of the developed reactor framework to characterise particle structures and their sensitivity to process design and operational choices.

6.1.1 System equations

For each CSTR with characteristic residence time τ_{CSTR}, the two-phase system including gas phase reactants, intermediates and by-products, and solid-phase particulate product is described by coupled equations for the change in number density $n(x)$ of particles of type x, the change in concentration C_k of gas phase species k, and the change in temperature T due to both reactions and flow. In the following formulation, phase coupling includes gas phase expansion with the expansion coefficient Γ [21, 101] to enable constant pressure (i.e. variable volume) modelling. The PFRs are modelled as batch reactors by changing the time/distance coordinates. The mass and energy balances for a batch reactor take the same form as Eqs. (6.1)–(6.2), without the flow terms ($\tau_{\mathrm{CSTR}}^{-1} \times (\ldots)$). The thermodynamic data for rutile $\mathrm{TiO_2}$ is taken from the NIST-JANAF thermochemical tables [23].

The particle number density evolves according to the population balance equation,

$$\begin{aligned}\frac{dn(x)}{dt} =& I(x,\mathbf{C},T)+\frac{1}{2}\sum_{\substack{y,z\in\mathcal{E}:\\ y+z=x}} K(y,z,T)\,n(y)\,n(z)-\sum_{y\in\mathcal{E}} K(x,y,T)\,n(x)\,n(y)\\ &+\sum_{\substack{y\in\mathcal{E}:\\ g_{\mathrm{SG}}(y)=x}} \beta_{\mathrm{SG}}(y,\mathbf{C},T)\,n(y)-\beta_{\mathrm{SG}}(x,\mathbf{C},T)\,n(x)\\ &+\frac{1}{\tau_{\mathrm{CSTR}}}\sum_{j=1}^{N_{\mathrm{in}}} f^{[j]}\left(n_{\mathrm{in}}^{[j]}(x)-n(x)\right)-\Gamma(n,\mathbf{C},T)\,n(x).\end{aligned}\tag{6.1}$$

Here, $g_{\mathrm{SG}}:\mathcal{E}\to\mathcal{E}$ describes change in particle type, β_{SG} is the rate of change in type due to surface processes (growth/sintering), and $f^{[j]}$ is the volumetric feed fraction of inlet stream j, $j\in[1,N_{\mathrm{in}}]$. The effect of gas phase molar density change is included in the expansion coefficient, Γ,

$$\begin{aligned}\Gamma(n,\mathbf{C},T)=\frac{1}{V}\frac{dV}{dt}=\frac{1}{\rho_{\mathrm{g}}}&\left[\sum_{k=1}^{N_{\mathrm{sp}}}\left[\dot{w}_k(\mathbf{C},T)+\dot{g}_k(n,\mathbf{C},T)\right]\right.\\ &\left.+\frac{1}{\tau_{\mathrm{CSTR}}}\sum_{j=1}^{N_{\mathrm{in}}} f^{[j]}\left(\rho_{\mathrm{g,in}}^{[j]}-\rho_{\mathrm{g}}\right)\right]+\frac{1}{T}\frac{dT}{dt}.\end{aligned}\tag{6.2}$$

Here, $\dot{w}_k$ and $\dot{g}_k$ are the molar production rates of species k by gas phase and particle reactions respectively at constant volume and $\rho_{\mathrm{g,in}}^{[j]}$ is the gas phase molar density in the j^{th} inflow stream. The gas phase chemistry evolves according to the set of equations for each species,

$$\frac{\mathrm{d}C_k}{\mathrm{d}t}=\dot{w}_k(\mathbf{C},T)+\dot{g}_k(n,\mathbf{C},T)+\frac{1}{\tau_{\mathrm{CSTR}}}\sum_{j=1}^{N_{\mathrm{in}}} f^{[j]}\left(C_{k,\mathrm{in}}^{[j]}-C_k\right)-\Gamma(n,\mathbf{C},T)\,C_k.\tag{6.3}$$

Here, $C_{k,\mathrm{in}}^{[j]}$ is the concentration in the j^{th} inflow stream. The energy balance for the system provides a description of the change in temperature, T,

$$\begin{aligned}\left(\rho_{\mathrm{g}}\overline{C}_{\mathrm{P,g}}+\rho_{\mathrm{p}}C_{\mathrm{P,p}}\right)\frac{\mathrm{d}T}{\mathrm{d}t}=&\sum_{k=1}^{N_{\mathrm{sp}}}\left[-\dot{w}_k(\mathbf{C},T)\hat{H}_k-\dot{g}_k(n,\mathbf{C},T)\hat{H}_k\right]-\dot{g}_{\mathrm{p}}(n,\mathbf{C},T)\hat{H}_{\mathrm{p}}\\ &+\frac{1}{\tau_{\mathrm{CSTR}}}\sum_{j=1}^{N_{\mathrm{in}}} f^{[j]}\left[\sum_{k=1}^{N_{\mathrm{sp}}} C_{k,\mathrm{in}}^{[j]}\left(\hat{H}_{k,\mathrm{in}}-\hat{H}_k\right)+C_{\mathrm{p,in}}^{[j]}\left(\hat{H}_{\mathrm{p,in}}-\hat{H}_{\mathrm{p}}\right)\right].\end{aligned}\tag{6.4}$$

Here, ρ_g and ρ_p are the gas phase and particle molar densities respectively, $\overline{C}_{P,g}$ and $C_{P,p}$ are the bulk gas and the particle constant pressure heat capacities, $\hat{H}_k$ is the specific molar enthalpy of species k and N_{sp} is the number of gas phase species. Particle processes contribute to the heat flux in the reaction terms ($\dot{g}_k\hat{H}_k$) and the particle flow term. Inter-phase heat transfer is assumed to be instantaneous because of the large surface area to volume ratio of small particles and the highly turbulent convective flow in typical reactor conditions – this simplification neglects radiative and conductive heat transfer to avoid modelling temperature in each particle separately. The particles are added to the thermal bulk of the system by the term $\rho_p C_{P,p}$.

6.1.2 Reactor network configurations

The reactor network model presented in Chapter 4 consisted of eleven CSTRs in series, with a new feed injection every three CSTRs, followed by two PFRs. The choice of dosing zone model was intended to reduce the degree of mixing achieved at each dosing point, introducing an element of plug flow behaviour to each dosing stage. Although it is unlikely that the injections result in perfect mixing at each stage, current knowledge of the flow behaviour in the reactor is insufficient to quantify the patterns in each stage. Thus, in this chapter, a simpler configuration will be used as the base case – and this will be used as a reference point to speculate about other network designs for dosing strategies.

The base case network has a four-CSTR dosing zone (Fig. 6.1, lower network), and is used to investigate the predicted final particle structure, and to study sensitivity of the particle structure to a 20 % increase/decrease in temperature of the injection streams (f_1–f_4). Subsequent studies investigate two aspects of dosing strategy that have influenced the operation of the industrial process: injection spatial frequency and chlorine dilution. In all cases, the network parameters are chosen such that the total mass of injected reactants and reactor volume are conserved.

The reactor network configuration is adjusted to achieve the stated research goals; however, in all studies the initial CSTR is supplied with hot O_2 gas in stream f_0 and the i^{th} CSTR is supplied with reactants in injection stream f_i (injection conditions in Table 6.1 and flow conditions in Table 6.2). Injection spatial frequency is investigated by varying the network length using: an eight-CSTR dosing zone, with CSTRs receiving half of the successive original injections (Fig. 6.1, upper inset, flow conditions in Table C.1 in Appendix C); and a twelve-CSTR dosing zone, with CSTRs receiving one third of the original injections (not pictured, flow conditions given in Table C.2 in Appendix C). Chlorine dilution is investigated for the four-CSTR configuration with chlorine injected into CSTR (4) at different flow fractions, f_{Cl_2}, and temperatures (Fig. 6.1, dotted arrow, conditions in Table 6.3).

Table 6.1: Stream conditions for all studies.

	Temperature (K)	$TiCl_4$ mole fraction	O_2 mole fraction
Injection f_1	600	0.26	0.74
Injection f_2–$f_{4/8/12}$	600	0.58	0.42
Hot oxygen f_0	2750	0.0	1.0

Table 6.2: Reactor volumetric feed fractions and residence times for 4 dosing-point study.

	Injection fraction	Upstream fraction	Residence time (ms)
CSTR (1)	0.42	0.58	3.0
CSTR (2)	0.25	0.75	15
CSTR (3)	0.26	0.74	15
CSTR (4)	0.23	0.77	15
PFR (1)	0.0	1.0	160
PFR (2)	0.0	1.0	1500

Table 6.3: Injection flow fractions and chlorine flow fractions and temperatures for 4 dosing-point study.

Molar flow rate	Injection f_4	Chlorine f_{Cl_2}	Temperature (K)
2× all $TiCl_4$ added in f_4	0.19	0.20	600
2× all $TiCl_4$ added in f_1–f_3	0.15	0.33	600
1× all $TiCl_4$ added in f_1–f_3	0.21	0.11	300

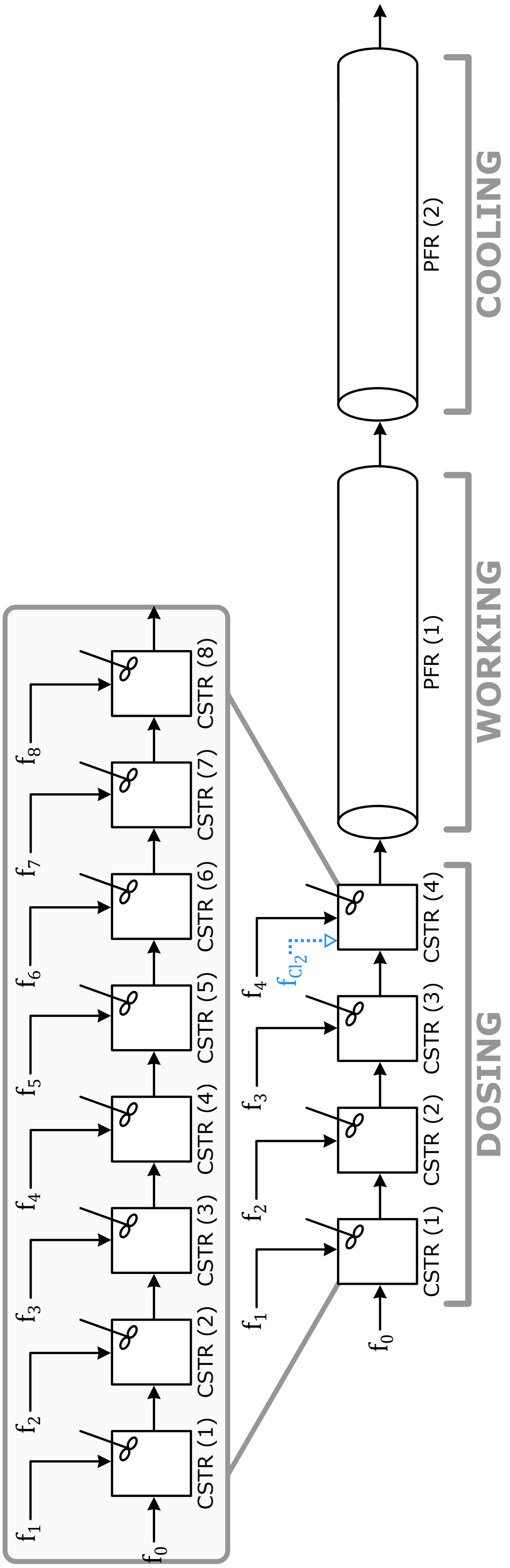

Fig. 6.1: Alternative reactor network configurations with four/eight CSTRs with reactant injections f_1–f_4/f_8, hot oxygen flow f_0 to CSTR (1), optional chlorine dilution $f_{\mathrm{Cl_2}}$ to CSTR (4), and two subsequent PFRs for completion of reactions (1) and cooling (2). Chlorine dilution only studied in four-CSTR network.

6.2 Stochastic numerical method

The gas and particle systems are treated separately using an operator splitting approach [21] which allows solving the gas phase kinetics (Eqs. (6.3)–(6.2)) with an ordinary differential equation (ODE) solver and evolving the particle size distributions (Eq. (6.1)) with a Monte Carlo method. The hybrid particle type-space models are incorporated using an adapted direct simulation algorithm (DSA) (as developed in Chapter 5, see Appendix A.1) that handles particle choice from the combined set of particles in the particle-number list and particle ensemble, and provides machinery for performing particle processes for each type-space. Simulation efficiency is enhanced using majorant kernels [33, 121], doubling [83], the linear process deferment algorithm (LPDA) [120], and a binary tree data structure [133].

6.2.1 Inclusion of heat release from particle processes

This chapter adds particle contributions to the energy balance by incorporating temperature updates during stochastic events (see Algorithm 6 in Appendix A.2). This mirrors how operator splitting treats changes in concentration of the gas phase due to particle events [21]. To do this, a discrete update is needed. A simulation particle, P_q, represents a molar concentration of

$$C\left(P_q\right) = \frac{1}{V_{\mathrm{smp}}} \cdot \frac{1}{N_{\mathrm{A}}} \left[\frac{(\mathrm{particles})}{\mathrm{m}^3} \cdot \frac{\mathrm{mol}}{(\mathrm{particles})}\right],$$

in the sample volume V_{smp}. For species k, the concentration change resulting from N_{event} particle events of a given type, j, is

$$\Delta C_k = \nu_k^{(j)} \left(\frac{N_{\mathrm{event}}}{V_{\mathrm{smp}} N_{\mathrm{A}}}\right) \left[\frac{\mathrm{mol}}{\mathrm{m}^3}\right]. \tag{6.5}$$

Here, $\nu_k^{(j)}$ is the stoichiometry for the k^{th} species in the j^{th} process. From Eq. (6.4), this triggers a discrete temperature change given by

$$\Delta T^{(j)} = -\left(\frac{1}{\rho_{\mathrm{g}} \overline{C}_{\mathrm{P,g}} + \rho_{\mathrm{p}} C_{\mathrm{P,p}}}\right) \left(\frac{N_{\mathrm{event}}}{V_{\mathrm{smp}} N_{\mathrm{A}}}\right) \left(\sum_{k=1}^{N_{\mathrm{sp}}} \nu_k^{(j)} \hat{H}_k + \nu_{\mathrm{p}}^{(j)} \hat{H}_{\mathrm{p}}\right) \; [\mathrm{K}], \tag{6.6}$$

when j is a reaction process (i.e. inception or surface growth) and

$$\Delta T^{(j)} = \left(\frac{1}{\rho_{\mathrm{g}} \overline{C}_{\mathrm{P,g}} + \rho_{\mathrm{p}} C_{\mathrm{P,p}}}\right) \left(\frac{N_{\mathrm{event}} \nu_{\mathrm{p}}^{\mathrm{in}}}{V_{\mathrm{smp}}^{\mathrm{in}} N_{\mathrm{A}}}\right) \left(\frac{\hat{H}_{\mathrm{p,in}} - \hat{H}_{\mathrm{p}}}{\tau_{\mathrm{CSTR}}}\right) \; [\mathrm{K}], \tag{6.7}$$

when j is an inflow process (note that the inflow stream may have a different sample volume, $V^{\mathrm{in}}_{\mathrm{smp}}$ to the reactor sample volume) and $v^{\mathrm{in}}_{\mathrm{p}}$ refers to the composition of the incoming particle. The temperature is incrementally adjusted by $\Delta T^{(j)}$ for each event of type j.

6.2.2 Numerical parameters

All studies use the simulation parameters in Table 6.4. The number of ensemble particles is chosen based on the previous convergence studies for industrially representative conditions (Fig. 4.7(a) and Fig. 5.9). The ensemble capacity used here is half the size as in Chapter 4 to reduce the wall time; however, four times the repeat runs are used to ensure comparable or improved accuracy (these can be performed in parallel). Small time steps and many splitting steps are required in the reactor stages due to the strong coupling between the gas phase kinetics and the particle growth dynamics. Larger steps are possible for modelling the cooling stage because there is no significant gas phase coupling by this point (due to near-complete depletion of the precursor).

Table 6.4: Simulation parameters used in all studies.

	Value
Ensemble capacity, N_{max}	2^{13}
Repeat runs, L	2^{5}
Particle-number threshold, N_{thresh}	10^{5}
Step size, Δt_{step} (s)	10^{-5}
Splitting steps per step, n_{splits}	10^{2}
Step size for cooling, $\Delta t^{\mathrm{cooler}}_{\mathrm{step}}$ (s)	10^{-4}
Splitting steps per step for cooling, $n^{\mathrm{cooler}}_{\mathrm{splits}}$	10^{1}

6.2.3 Model performance

Chapter 5 proposed a particle-number/particle (PN/P) model to improve robustness with respect to numerical parameters and efficiency of Monte Carlo simulations of particle synthesis in conditions associated with high process rates. This demonstrated significant computational savings tracking small particles with a particle-number model, which also reduces the risk of ‘contractions’ (random removals triggered when there is no space in the ensemble for inception of new particles). This robustness with respect to ensemble size choice is now demonstrated for industrially relevant conditions with physically meaningful kinetics.

Robustness of the PN/P model is illustrated by considering the particle loading (number of particles stored in each sub-system model) across the reactor network. In the four CSTRs, where fresh precursor triggers rapid inception of new particles, the majority of particles in the system are small, single primaries that are stored in the particle-number model (Fig. 6.2, dotted lines). In fact, the total number of particles in the system, especially in CSTR (1) and CSTR (4), is frequently greater than would be tolerated using only an ensemble pre-initialised with $N_{\text{max}} = 2^{13}$ (Fig. 6.2, solid line). Using only a finite ensemble would require random removals to reduce the sample volume until the numerical inception rate was suitable, with each removal eliminating a particle that had been resolved with computational effort.

CSTRs (1), (2) and (4) also demonstrates another advantage of the cheap storage of additional small particles – higher numerical inception rates during transient periods or temperature increase can be handled more robustly. Aggregates become more common in PFR (1), as many primaries collide and sinter. Here, the detailed particle model (Fig. 6.2, dashed lines) incorporates the full complexity required to describe aggregate particles fully, providing a ‘best-of-both-worlds’ approach. From the studies in Chapter 5, the greatest improvement in efficiency is achieved in the CSTR network, where primary particles can be updated and selected more efficiently using the particle-number representation.

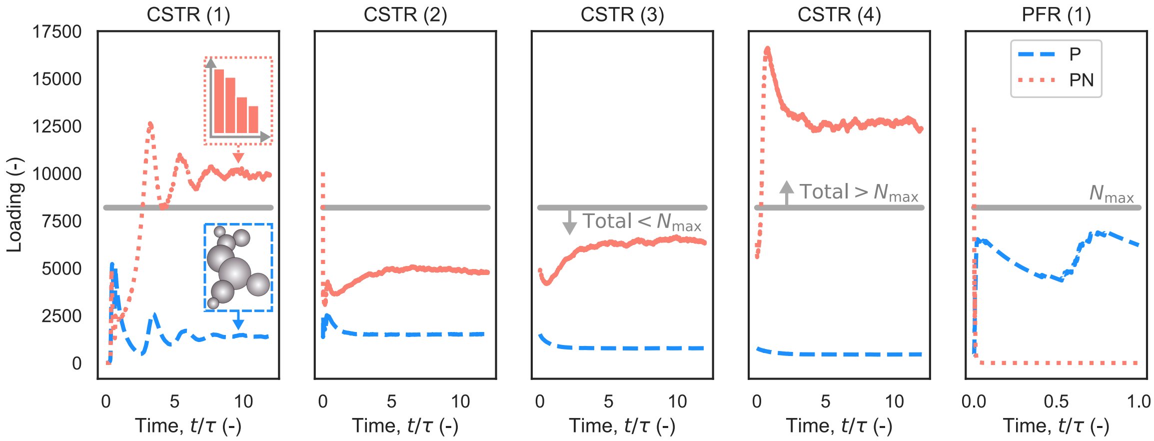

Fig. 6.2: Number of particles stored in the particle-number list (PN) and the particle ensemble (P) in each reactor in the network. Solid line shows the ensemble maximum ($N_{\text{max}} = 2^{13}$).

6.3 Process modelling results

The work presented in this chapter aims to contribute novel understanding of industrial titania synthesis through detailed population balance modelling facilitated by enhanced robustness of the new hybrid type-space approach in cases with high inception rates. Understanding particle morphology is crucial because it determines the product properties and is controlled by process conditions that are challenging to study experimentally. The proposed reactor model is now used to investigate particulate properties for the base case conditions, and then to study sensitivity to different reactor parameters as outlined in Section 6.1.

6.3.1 Baseline assessment of particulate structure

Several driving questions are considered regarding particle morphology and the outlook for controlling the synthesis process. Relevant features of particle morphology include: collision diameter, primary particle diameter, number of primary particles, and degree of sintering/neck formation. The geometric mean primary diameter, $\overline{d}_{\mathrm{p,g}}$, is computed for each particle P_q from the product of its n_q primary particle diameters,

$$\overline{d}_{\mathrm{p,g}}\left(P_q\right) = \left(\prod_{i=1}^{n_q} d_{\mathrm{p}}\left(p_i\right)\right)^{\frac{1}{n_q}}. \tag{6.8}$$

This is used to calculate the geometric standard deviation (GSTD, σ_{g}) in primary particle diameter, which is used to assess typical product character in the sense that the extent of non-uniformity of particle sizes leads to more variable end-product properties such as light scattering ability and tint,

$$\sigma_{\mathrm{g}}\left(P_q\right) = \exp\left(\sqrt{\frac{1}{n_q}\sum_{i=1}^{n_q}\left(\ln\left(\frac{d_{\mathrm{p}}\left(p_i\right)}{\overline{d}_{\mathrm{p,g}}\left(P_q\right)}\right)\right)^2}\right). \tag{6.9}$$

What is the primary particle size distribution in the aggregates?

The final aggregate particle size distribution is broad, spanning hundreds of nanometers to several microns (Fig. 6.3(a)), with a mean diameter of 1.85 µm. The primary particles are much smaller on average, with a mean diameter of 373 nm. This is relatively large compared to the targeted industrial range of around 200 nm–300 nm given by Park and Park [115]; however, it is within the bounds of other hot wall and flame studies they list with similar temperatures and residence times. As this is an idealised representation of the industrial reactor (Section 4.1), some discrepancy is not surprising. The primary particles in the cooled outflow are significantly polydisperse, with a geometric standard deviation in diameter of 1.6.

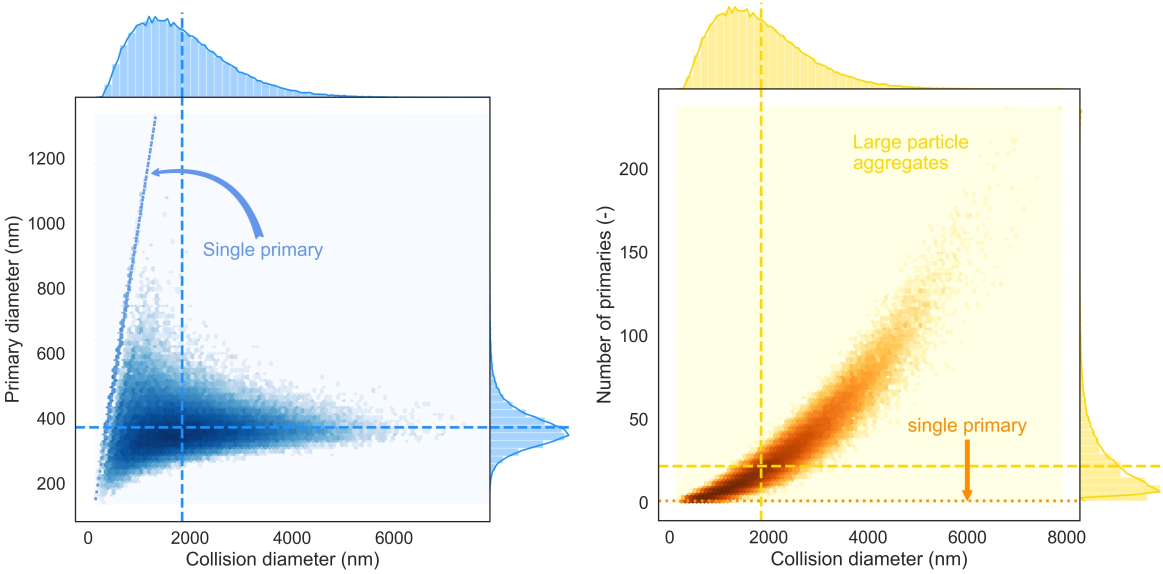

(a) Aggregate and primary sizes (b) Aggregate size and composition

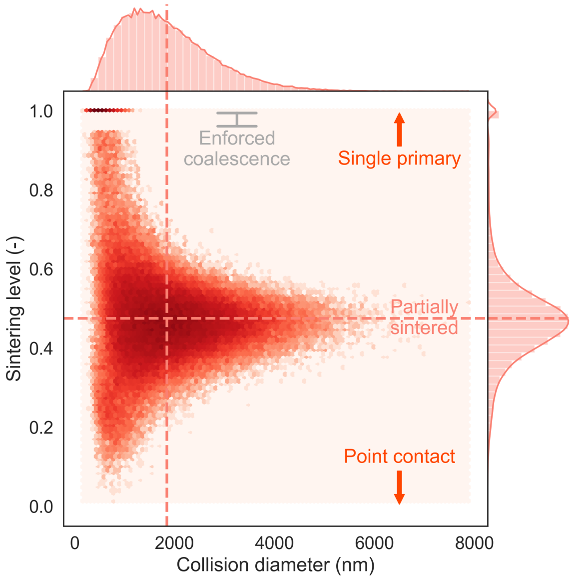

(c) Aggregate size and cohesion

Fig. 6.3: Joint property distributions with marginal kernel density estimates (bandwidths: 0.01) and histograms for the cooled particles. Dashed lines indicate property mean values and dotted line indicates single primaries. Note lognormal marginal distributions not centred on mean value lines.

What is the aggregate composition?

Cooled aggregates consist of 22 connected primary particles (Fig. 6.3(b)) on average, although free primary particles and many larger aggregates containing 50–150 primaries also exist. Some free primary particles (see dotted line in Fig. 6.3(a)) have sizes significantly above the desired range; however, in general aggregate size increases with the number of constituent particles and the marginal distributions of both primary particles and aggregates have long tails.

How strongly connected are the primary particles?

When two particles coagulate, the resulting particle initially has point contact where the collision occurred. When the neighbouring particles sinter or undergo surface growth at temperatures relevant to this study, the area of their connection increases, rendering an aggregate that is increasingly difficult to break down by mechanical force. There is limited aggregate sintering in the dosing zone, where the sintering levels range between 0 (point contact) and 1 (fully sintered/free primary). Neck growth occurs to a larger extent in the PFRs, where there is also less inception of free primaries, and this yields a more compact sintering level distribution with most particles somewhat sintered. The average sintering level of the cooled product is 0.48, i.e. the final particulate product consists of strongly bonded primaries (Fig. 6.3(c) – the absence of simulation particles with sintering levels in the band 0.95–1.0 is an artefact of the model that enforces coalescence for particles with $s_{ij} > 0.95$).

The cumulative distributions of primary and neck diameters (Fig. 6.4) demonstrate the high level of sintering more quantitatively for the cooled product. Approximately 75 % of the population has primary particle diameters in the range 100 nm–400 nm (indicated with solid lines in Fig. 6.4); however, some 20 % of the neck diameters fall in this range too. The neck diameter has severe implications for the ease of separation of particles to achieve a desired size – crystals with significant necks may not be easily split into smaller primary particles, whereas small necks are easy to break with post-process milling. Models for milling of aggregate particles could be used to further inform process understanding and such models could also consider other factors such as the distance of a primary pair from the centre of mass of the particle to determine fragmentation efficiency [78].

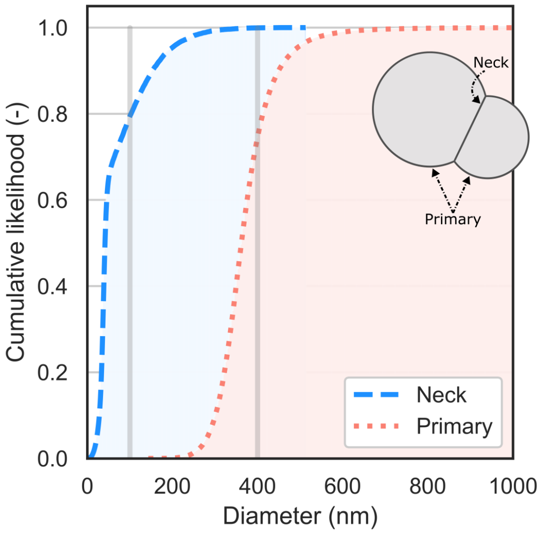

Fig. 6.4: Cumulative distribution of cooled particle primary and neck diameters with 100 nm–400 nm range indicated as solid vertical lines.

6.3.2 Sensitivity to process conditions and configuration

Ideally, a model for the industrial process should inform optimal process design, including operating conditions and strategies to enhance product quality and minimise cost of post-processing steps such as milling. The questions that follow illustrate the degree of process/model sensitivity to such design choices.

What is the effect of injection temperature?

Reactor temperature is an important parameter: decomposition of the $TiCl_4$ is endothermic, so energy is required to initiate the process. With the exothermic oxidation step, there is a risk of thermal runaway or hotspot development, which would negatively affect product quality. The reactant injections offer one means to control temperature. The baseline injection temperature of 600 K is in the scope of what could be used in the industrial process. The temperature range of 480 K–720 K chosen for this study is fairly broad and is not likely to be plausible in the real process. These values were selected as the upper and lower test points to provide an idea of the possible influence exerted by this process parameter and assess the extent to which it is important for determining particle structure.

The outlet temperature from PFR (1) shows unsurprising correlation with increasing or decreasing reactant injection temperature (Table 6.5), but only a moderate change was observed in this study (increasing the temperature of the reactant stream reduces the thermal cooling it can provide to the exothermic oxidation process); however, the reaction goes to near-completion in all three cases. It does not follow the same path in each case (cf. $TiCl_4$ decomposition, reaction with oxygen to form intermediates and inception vs. $TiCl_4$ oxidation on the particle surface), so there is some discrepancy in the observed temperature changes.

Table 6.5: Effect of injection temperature on reactor outlet temperature.

Injection temperature (K)	PFR (1) outlet temperature (K)
480	1536.7
600	1629.0
720	1703.8

Effects of temperature on the particles are more difficult to analyse due to the complex nature of interdependent processes that occur in the multi-injection system, with all particle processes accelerated by increasing temperature. The collision diameter distributions in the CSTR network are slightly bimodal, with a small peak near the incepting particle size (0.49 nm) and a larger peak in the 100 nm–1000 nm range. These peaks change with temperature: the hotter system induced by a higher injection temperature (Fig. 6.5, dotted line) has the largest inception mode, with lower reactant concentration driving lower surface growth, and higher temperature increasing sintering (cf. Fig. 6.5, dashed line). Downstream, in PFR (1), there is little/no evidence of an inception peak and the distributions are similar due to coagulation. The number density decreases along the network due to coagulation, and the main difference in distributions is a reduction in number density with increasing temperature.

Assessment of the mean geometric standard deviation in primary size (Fig. 6.6(a)) across the network shows a similar homogenization in PFR (1). The higher temperature systems seem to produce less disparate primaries throughout all stages and this could help to yield a more consistent product; however, the final GSTD shows no clear influence of temperature. The increase in GSTD between the CSTR network, which models the dosing zone, and the end of PFR (1), which models the working zone, can be attributed to additional surface growth and high-temperature sintering-to-coalescence in the final reactor zone, which has an order of magnitude longer residence time.

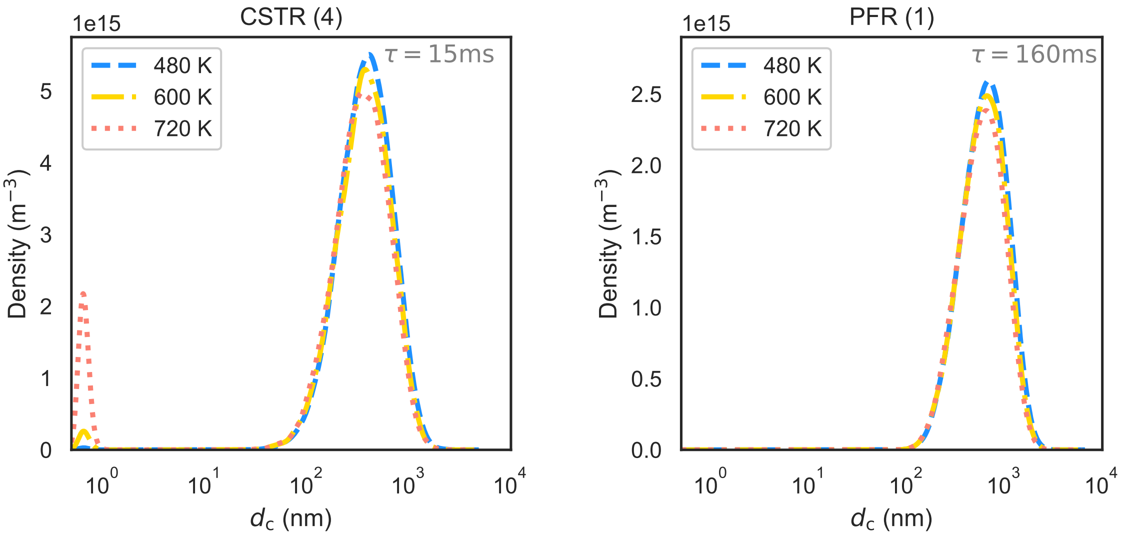

(a) After dosing (b) After reactor

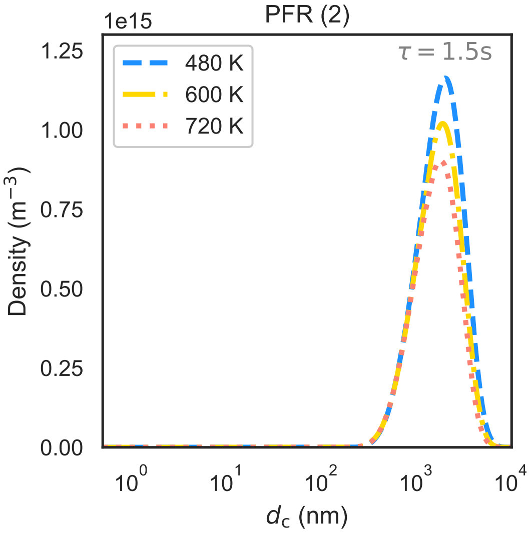

(c) After cooling

Fig. 6.5: Scaled kernel density estimates (bandwidth: 0.1) of collision diameter distributions in the reactor network after the (a) dosing zone, (b) reactor and (c) cooler with different injection temperatures (note vertical axis limits differ to resolve different number densities in the three reactors).

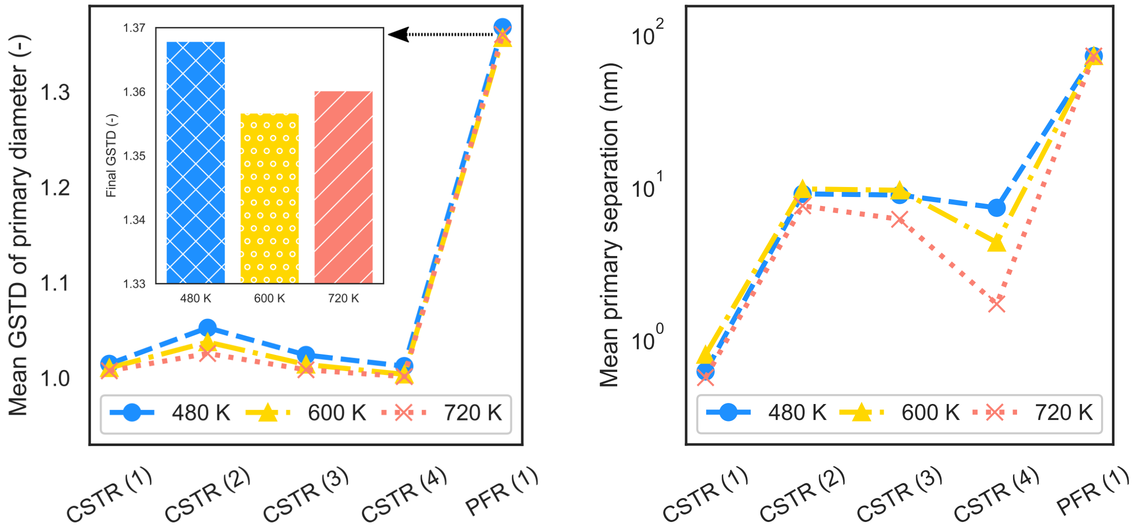

(a) GSTD (b) Separation

Fig. 6.6: Mean (a) GSTD in primary diameter and (b) primary particle separation across the reactor network for different injection temperatures.

The detailed particle model provides insight beyond comparing particle diameter distributions. The size distribution of the necks between connected primaries can also be assessed (Fig. 6.7). This highlights interesting features of the relationship between temperature and particle structure: (i) there are more inceptions at higher temperatures, lowering the average neck size in the CSTR network (free primaries have no necks and small particles coalesce rapidly); (ii) the neck distribution is bimodal in PFR (1) where most of the remaining free primary particles coagulate (cf. loss of the small peak between Fig. 6.5(a) and Fig. 6.5(b)), with a large peak for necks less than 100 nm in radius and a smaller peak for necks above this size; and (iii) higher temperature increases the sintering rate, yielding a larger mean size for the small-radius mode without significant change in the large-radius mode.

Comparison of the separation between connected primaries also highlights different sintering behaviour: primaries are closer together in the hotter (720 K) study (Fig. 6.6(b)). Insights about particle cohesion could be used to choose process conditions that result in lower post-processing requirements to separate primaries to achieve suitable pigment sizes.

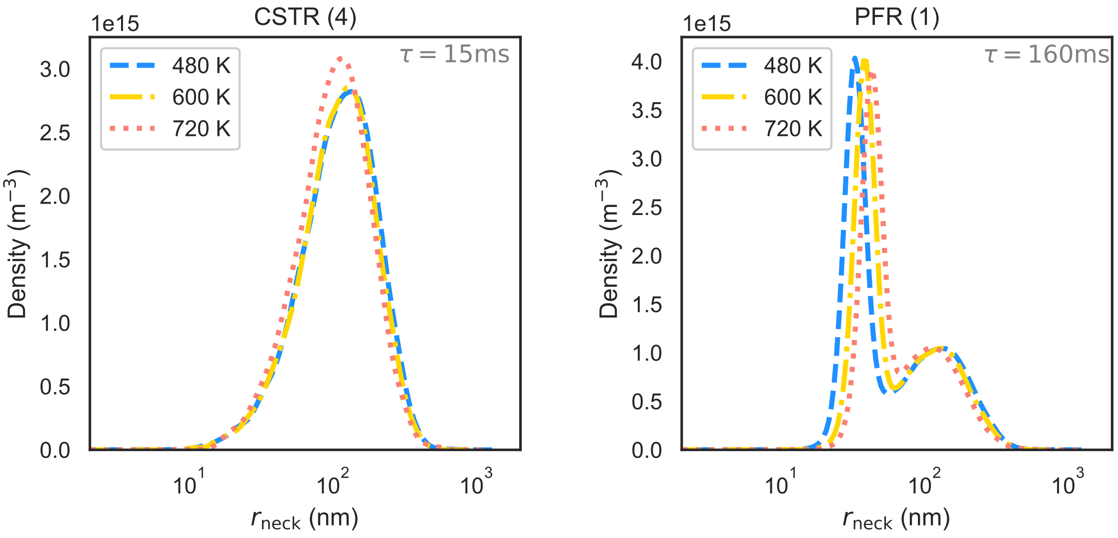

(a) After dosing

(b) After reactor

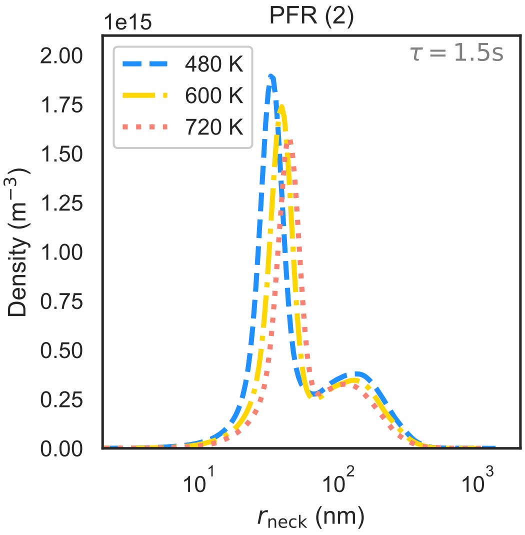

(c) After cooling

Fig. 6.7: Scaled kernel density estimates (bandwidth: 0.1) of neck radius distributions in the reactor network after the (a) dosing zone, (b) reactor and (c) cooler with different injection temperatures (note vertical axis limits differ to resolve different number densities in the three reactors). Free primaries (“$r_{\text{neck}} = 0\,\text{nm}$”)) not represented on log-scale plot.

How do dosing strategies alter particle size and polydispersity?

The dosing scheme is modified by increasing the number of CSTRs (each with a fresh reactant feed) to achieve smaller, more frequent injections (cf. Fig. 6.1, upper/lower networks). This reduces the range of geometric standard deviations in primary diameters in the aggregates and, to a lesser extent, produces smaller primary particles on average (Fig. 6.8). These findings indicate that increasing the spatial frequency of reactant injections produces a higher quality, more consistent product which is in keeping with observation of the multi-injection, industrial process.

To study the differences further, five particles are extracted for each configuration using 'k-mediod' clustering [111] based on the property sets, Σ_q:

$$\Sigma_q = \left\{ d_\mathrm{c}\left(P_q\right), \overline{d}_\mathrm{p}\left(P_q\right), n_q\left(P_q\right), \overline{s}\left(P_q\right) \right\}.$$

Σ_q thus accounts for the aggregate collision diameter, average primary diameter, number of primaries and average sintering level – the properties used to assess particle structure for the base case conditions. K-medoids clustering is a variant of k-means clustering that forces the cluster centroids to be elements of the set being clustered, i.e. particles [59]. The number of cluster centres was selected by inspection with 5 being chosen to keep the number of centres manageable while maintaining apparent cluster separation. It was observed that metrics of clustering success (e.g. silhouette scores [59]) were weak functions of the number of clusters for $k \leq 10$. The five clusters group the particle system according to principal observations of these characteristics.

Increasing the frequency of injections reduces the range of primary particle sizes, producing mediods with more similar primary size properties and eliminating the large diameter centre, cluster 5, observed for the four-injection configuration (Fig. 6.9(a)). The five clusters have disparate primary counts in all cases (Fig. 6.9(b)), with clusters 1–3 containing fewer than ten primaries and clusters 4–5 including particles with more than ten primaries. The twelve-injection configuration has the largest upper bound on primary count.

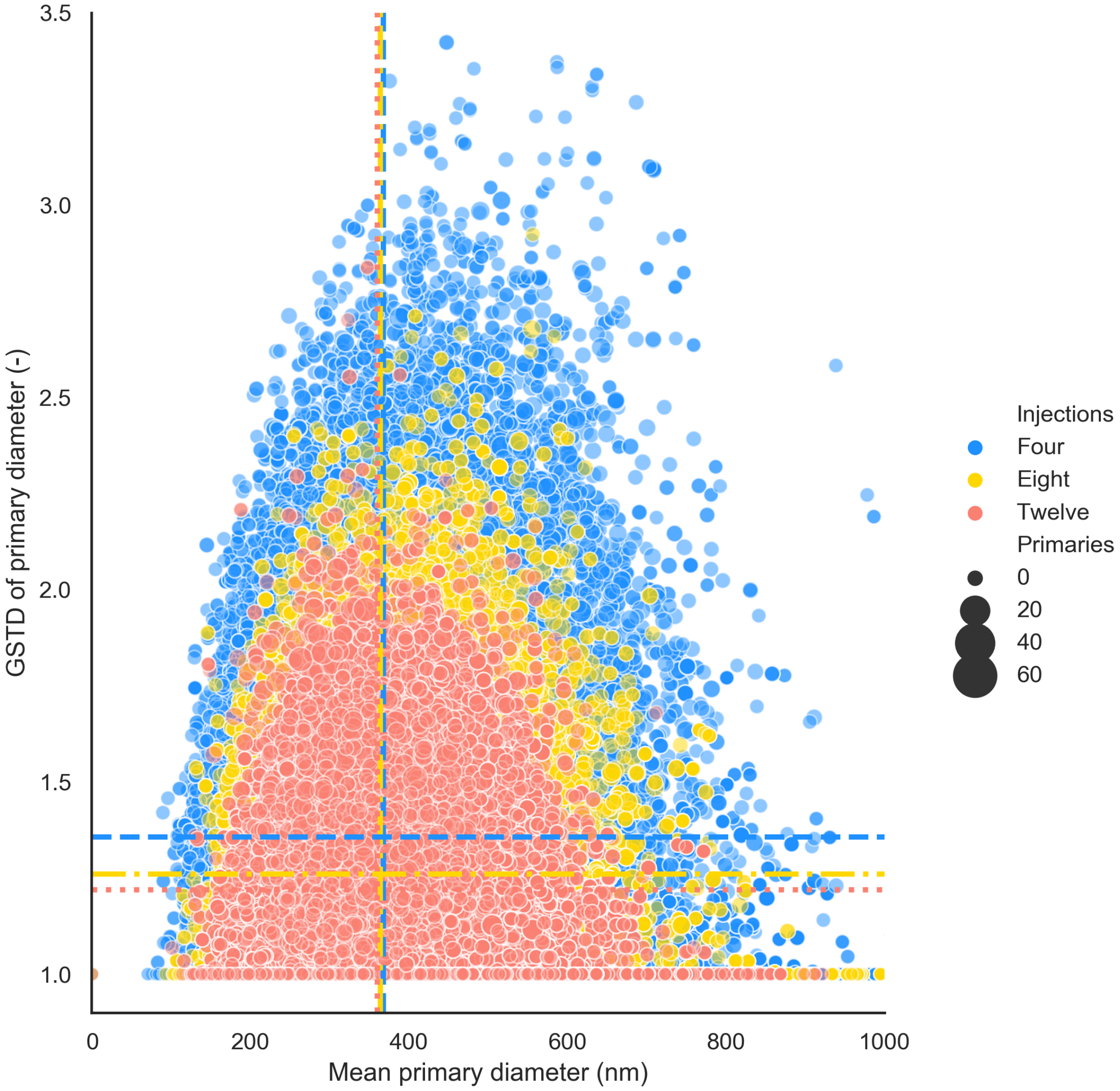

Fig. 6.8: Mean and geometric standard deviation (GSTD) of primary diameters in each aggregate for different reactant dosing frequencies at the end of the reactor (i.e. after PFR (1)). The marker sizes reflect the relative number of primaries in the aggregate. The dashed lines indicate the mean values for the sample.

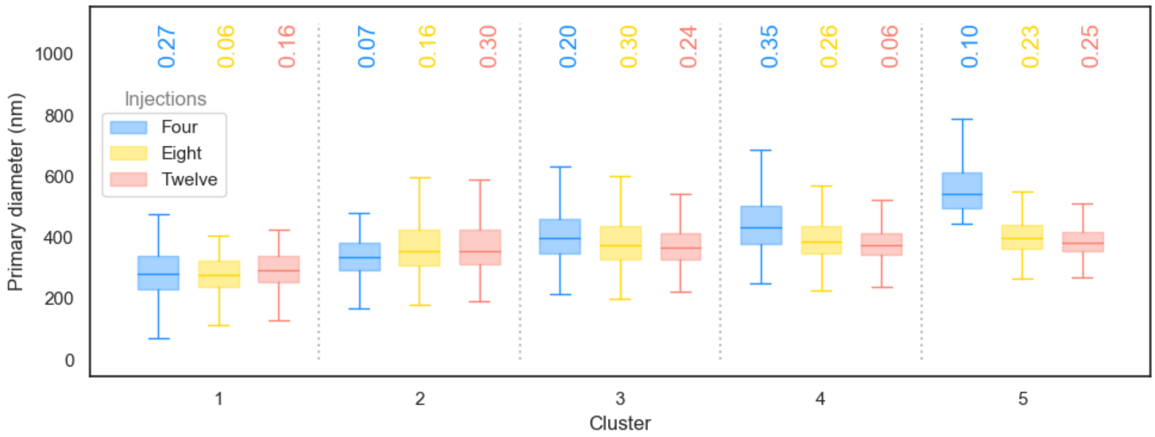

(a) Primary diameter clusters

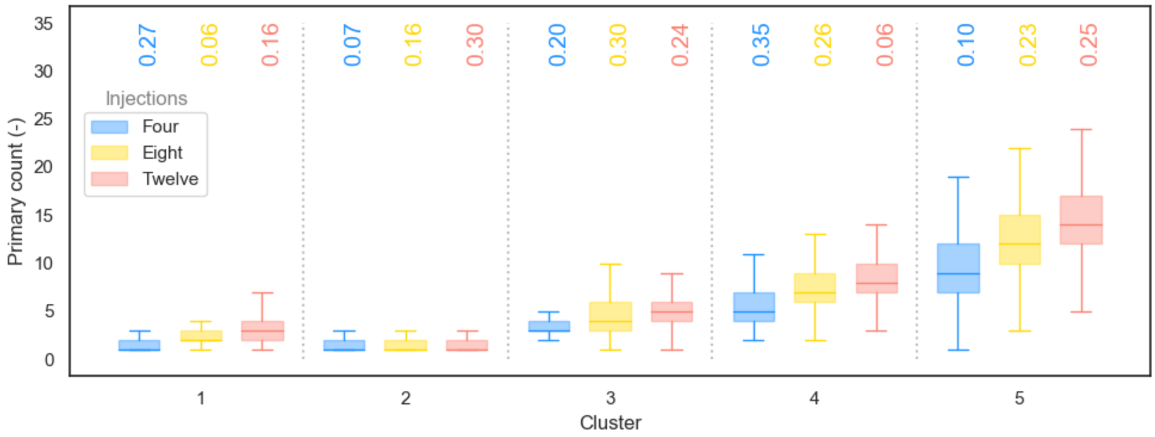

(b) Primary count clusters

Fig. 6.9: Comparison of (a) primary diameter and (b) primary count for 5 particle centres selected using k-mediod clustering. The numbers above the boxes indicate the portion of the total sample in the cluster.

Does chlorine dilution affect particle size and structure?

Synthesis of titania from $TiCl_4$ produces chlorine as a by-product. The chlorine can be recycled to the chlorination stage that produces $TiCl_4$ or cooled and re-injected into the reactor [8, 107] to reduce temperature, dilute the system or inhibit the surface oxidation process, all of which target reduced particle size. Three chlorine dilution strategies are assessed (Table 6.3): adding 20 % by volume at 600 K, adding 33 % by volume at 600 K and adding 11 % by volume at 300 K. These cases assess some extremes on possible chlorine strategies: dilution at the injection temperature versus dilution around room temperature; dilution with double the flow rate of the stage injection, versus dilution with the maximum chlorine produced up to this point.

The developed PSDs are altered in all three new schemes (Fig. 6.10). The injection of chlorine produces a larger peak around the inception size in CSTR (4) (see dashed/dotted lines cf. original in solid grey). In contrast to the base case, this is still present after PFR (1) in all chlorine cases. The small-particle peak vanishes by the end of the cooling stage due to coagulation; however, there is still discrepancy in the final distributions with a smaller mean particle size, lower standard deviation and reduced range (Table 6.6).

The mean primary particle size is also reduced in all cases, although the difference is smaller. Dosing with chlorine also shifts the particle neck distributions (Fig. 6.11), producing a larger density of small necks (600 K injections) or reducing the mean size of the small necks (large injections at both temperatures). Thus injection of chlorine could be an effective strategy to control particle size and polydispersity. The most significant reduction in mean and polydispersity is observed for the case with 33 % Cl_2 at 600 K – this suggests that cooling the separated chlorine to room temperature for this purpose is less useful than increasing the chlorine flow rate.

Table 6.6: Effect of chlorine dosing on final particle collision diameter distributions – range, arithmetic mean and standard deviation (STD), with ratios computed using respective base case value as the denominator to demonstrate relative effect.

Case	Range (nm)	Mean (nm)	STD (nm)	Mean ratio	STD ratio
0 % Cl_2 base case	7710	1850	913	1.00	1.00
19 % Cl_2 at 600 K	6830	1750	876	0.948	0.959
33 % Cl_2 at 600 K	6351	1550	784	0.841	0.858
11 % Cl_2 at 300 K	7040	1640	818	0.891	0.896

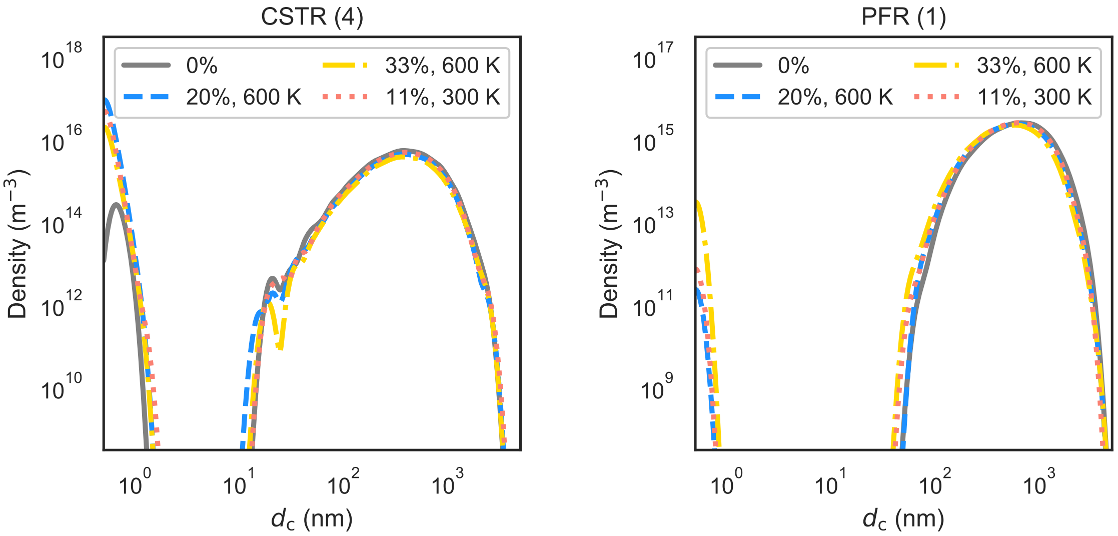

(a) After dosing

(b) After reactor

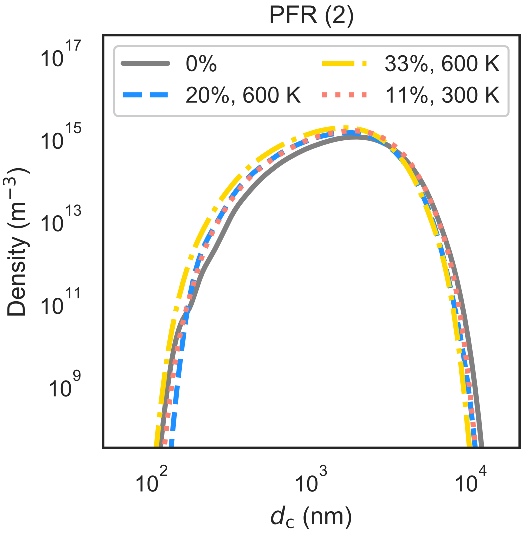

(c) After cooling

Fig. 6.10: Kernel density estimates (bandwidth: 0.1) of collision diameter distributions immediately after (a) CSTR (4) (where chlorine is injected), (b) PFR (1) and (c) PFR (2) with solid line showing 0 % addition for comparison (note axis limits differ).

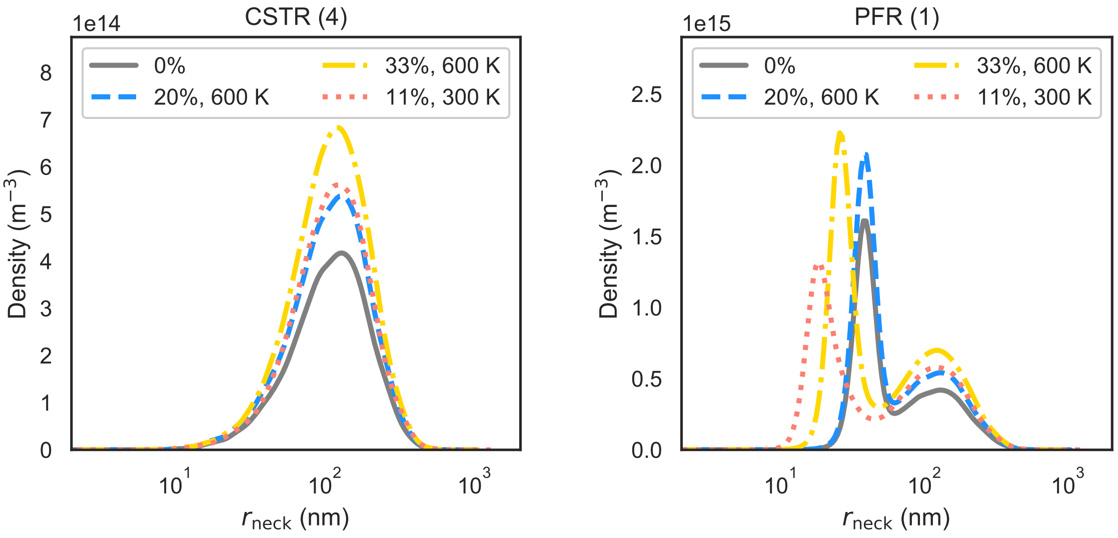

(a) After dosing (b) After reactor

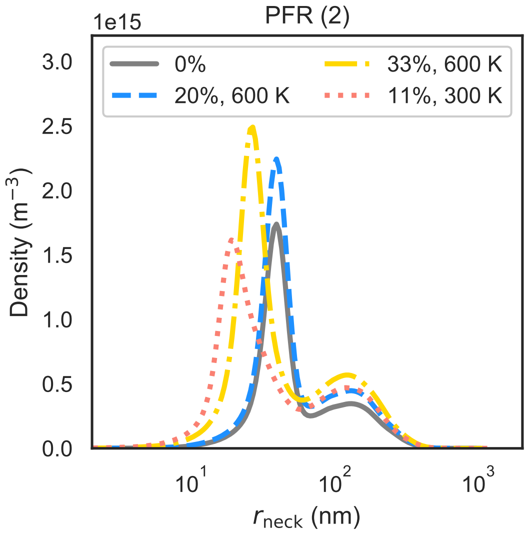

(c) After cooling

Fig. 6.11: Scaled kernel density estimates (bandwidth: 0.1) of neck radius distributions in the reactor network after (a) CSTR (4), (b) PFR (1) and (c) PFR (2), with different chlorine injections (note vertical axis limits differ to resolve different number densities in the three reactors). Free primaries (“$r_{\text{neck}} = 0\,\text{nm}$”)) not represented on log-scale plot.

6.3.3 Characterisation of fractal structure

The fractal-like nature of aerosol particles can be characterised by relating the primary and aggregate diameters with the number of primary particles in the aggregate,

$$n_q\left(P_q\right) = k_{\mathrm{f}}\left(\frac{d_{\mathrm{g}}\left(P_q\right)}{\bar{d}_{\mathrm{p}}\left(P_q\right)}\right)^{D_{\mathrm{f}}}. \tag{6.10}$$

D_{f} is the fractal dimension, k_{f} is the fractal pre-factor and $d_{\mathrm{g}}\left(P_q\right)$ is the radius of gyration of particle P_q (Eq. (3.15)). The fractal dimension is often used to classify particle structure, with a fractal dimension of 3.0 corresponding to a spherical particle and lower fractal dimensions indicating more open, linear particle shapes. Fractal dimensions can be defined by simulating coagulation for populations of coagulating monodisperse (uniform properties) and polydisperse (distribution of properties) primary particles [30].

For monodisperse primary particles BCCA should produce a fractal dimension of 1.9. Polydispersity has been shown to alter fractal structure [32]. Eggersdorfer and Pratsinis [30] found that, for a BCCA coagulation model, increasing primary particle polydispersity (as measured by the GSTD) produces decreasing fractal parameters in the GSTD range 1.0–2.0, with approximate corresponding parameter values in the ranges 1.4–1.1 for k_{f} and 1.9–1.7 for D_{f}. The fractal structure of particles has been shown to be a strong function of the particle growth processes. Schmid et al. [136] found significant dependence on the relationship between the coagulation and sintering processes and Eggersdorfer et al. [32] note that sintering tends to increase the fractal dimension (particle aggregates more compact/spherical) whilst polydispersity decreases the fractal dimension (particle aggregates more open). Aerosol particles typically have a fractal dimension in the range 1.6–2.5 [32]. Elucidating the fractal structure relationship is important because it provides information about the particle geometry, which governs product properties such as light scattering propensity but also determines local chemical activity and heat transfer properties [32].

The polydispersity is classified using the geometric standard deviation in primary particle diameters. In other work, this has parametrized the lognormal distribution of primary particles used as a starting point in simulations to determine fractal dimension. The advantage of the current work is that it provides sufficient detail in the particle model to estimate the fractal structure of particles that have polydispersity arising from real processes (e.g. sintering, surface reaction) in the industrial reactor. The fractal structures created in the different test cases presented in this chapter were characterised by fitting (Fig. 6.12) the simulation data using Eq. (6.10). In general, the relationship observed by Eggersdorfer and Pratsinis [30] was found to hold (Table 6.7) for fractal dimension, with lower D_f values predicted for the cases with higher polydispersity. The prefactor values are higher than reported in the previous study. However, the prefactors and fractal dimensions are sensitive to the minimum primary particle count cut-off used in the fitting, with larger values of D_f and smaller values of k_f resulting from exclusion of aggregates with only a few primaries. There is a trade-off in prediction uncertainty as points are excluded in this cut-off (Fig. 6.12, density histogram). The fractal fit provides a reasonable description of the full set of aggregates, in spite of weaker agreement at the edges of the spectrum due to low number density of particles with the largest primary counts and reduced applicability of fractal models to particles with few primaries.

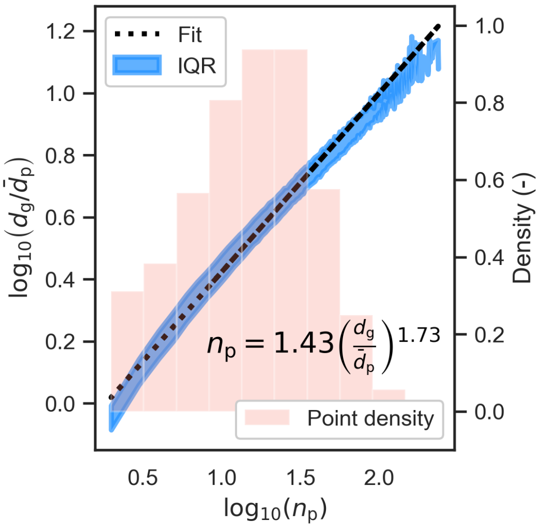

Fig. 6.12: Fitted fractal relationship (dashed line) between the logarithms of number of primary particles per particle and particle-to-primary diameter ratio for the base case simulation data. The interquartile range (IQR, i.e. middle 50 %) is indicated by the filled area and the fitted slope and intercept parameters are shown in context as the exponent and prefactor of the equation in the lower right. The histogram indicates density of data for different aggregate sizes.

It is useful to relate the simulated particle properties to a well-known, mean structural property because this provides a simple method of assessing how process conditions affect particle geometry – a relationship that can be challenging to investigate experimentally. However, it should be noted that the BCCA model used here applies best to particle coagulating in the free-molecular, rather than the transition, regime. For larger particles, a diffusion-limited cluster-cluster model would be more appropriate. Lindberg et al. [81] reported that no appreciable difference was observed when testing these two coagulation models in hot wall reactor simulations. There is further a relatively narrow gap between the fractal dimensions predicted by ballistic and diffusion-limited aggregation. Thus, this caveat is not expected to undermine the utility of the current study assessing the trend in geometries predicted for different process design choices.

Table 6.7: Fitted fractal parameters and mean geometric standard deviation (GSTD) in primary diameters from simulation data.

Case	Fractal dimension	Fractal pre-factor	GSTD
	D_f	k_f	σ_g
600 K, 4 injections	1.73	1.43	1.60
480 K, 4 injections	1.73	1.41	1.62
720 K, 4 injections	1.73	1.44	1.59
600 K, 8 injections	1.78	1.46	1.42
600 K, 12 injections	1.80	1.48	1.35

6.3.4 Comparison of simulated and real particle images

The model data can be used to simulate scanning electron microscopy (SEM) images, providing a view of the developed particles that is directly comparable with images of real particles coming out of a titania reactor. Comparison of a real particle image (Fig. 6.13) with the simulated images (Fig. 6.14) shows qualitatively similar properties such as highly non-spherical aggregate structures composed of many smaller, partially sintered primary particles; however, these images also highlight the many relatively large primary particles produced in the simulations, especially for the non-diluted case (Fig. 6.14(a)).

This observation supports the preceding comments on size ranges compared to those reported for the industrial process. The simulations undertaken in this study employed industrially representative conditions, but are not a perfect match for the exact conditions used to generate the real particles from which the image is created. There is uncertainty in the numerical rates used – associated with generation of constants from first-principles calculations and by fitting to data from less severe process conditions – which is amplified by the fast dynamics of this process. Images with and without chlorine dilution (Fig. 6.14(a) cf. Fig. 6.14(b)–6.14(d)) do, however, illustrate effectiveness of injecting cool chlorine in reducing particle/aggregate size by cooling and diluting the system – which is likely closer to the industrial operation in any case. These simulated SEM images highlight the utility of the detailed particle model in providing morphological information about the particles for visualisation.

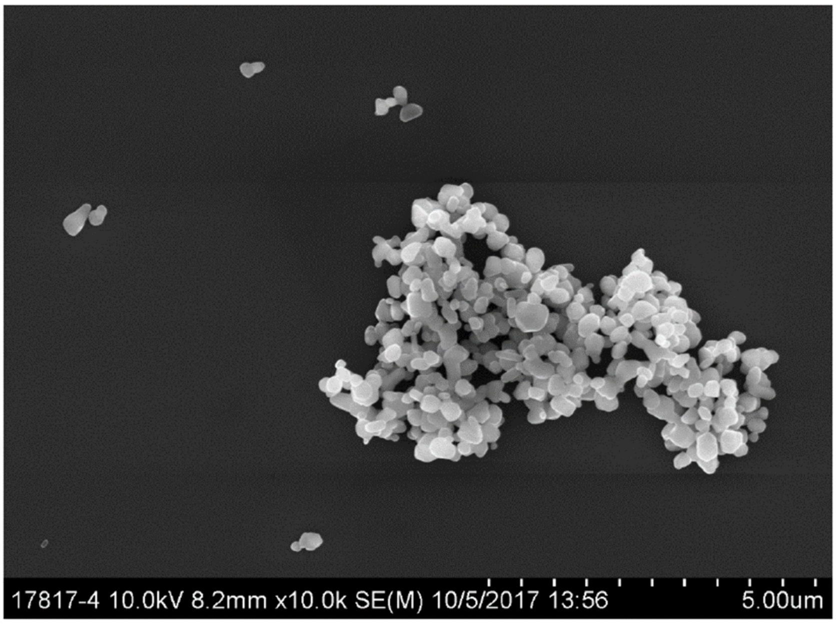

Fig. 6.13: Real particle SEM (image courtesy of, and with permission from, Venator).

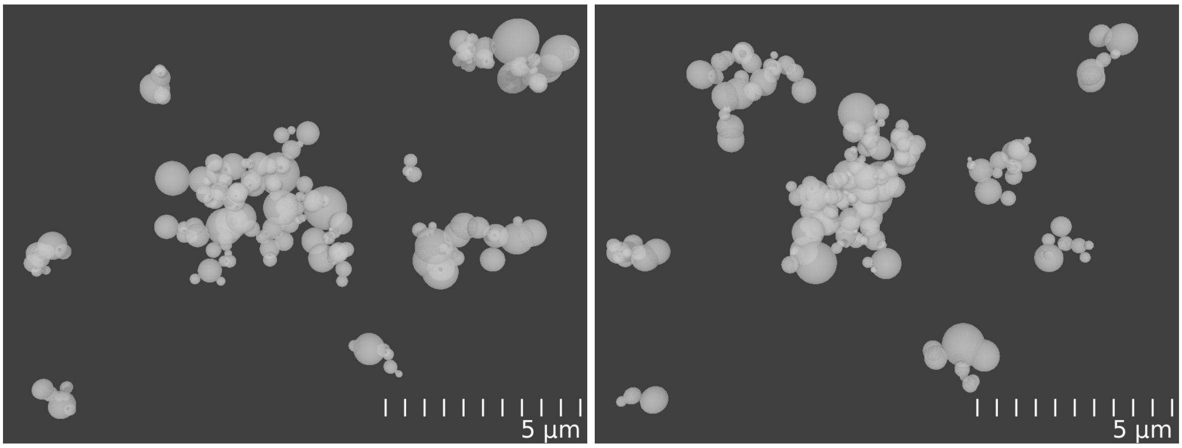

(a) 0 % Cl_2 (b) 20 % Cl_2, 600 K

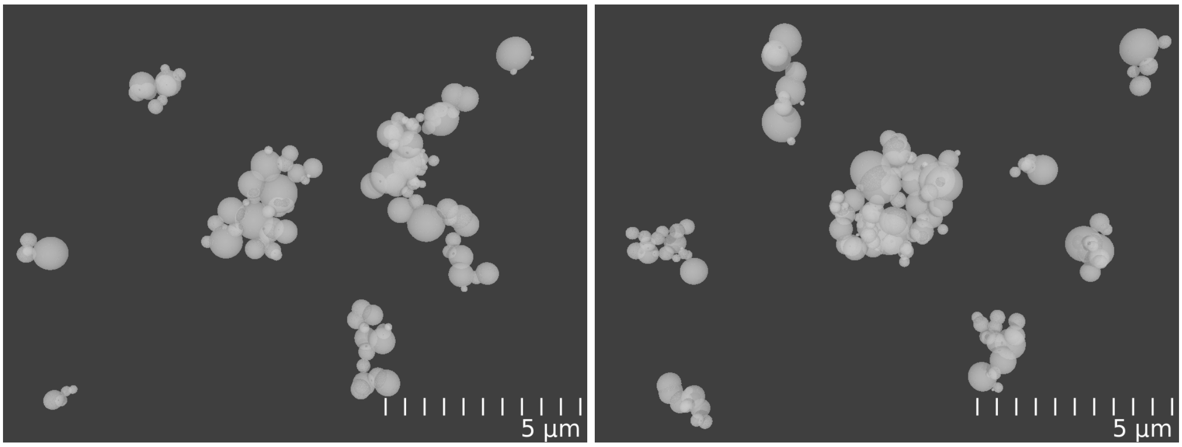

(c) 33 % Cl_2, 600 K (d) 11 % Cl_2, 300 K

Fig. 6.14: Simulated SEMs for cooled particle product.

6.4 Chapter summary

This chapter has presented the addition of a system energy balance equation that includes heat released from particle processes into the gas phase, and has outlined steps for inclusion of this heat release from particle processes in the operator splitting algorithm. It has demonstrated use of the recently proposed particle-number/particle algorithm to aid simulation of titania synthesis under industrially relevant conditions. The new algorithm provides additional robustness with respect to the selection of ensemble size and efficiency that can be exploited to study rapid particle inception and growth, even in the presence of exotherms and transience, using a complicated type-space model.

The overlapping-spheres particle model was used to provide insight into the development of complex aggregate structures in the industrial synthesis of pigmentary titania. The final particle population exhibits broad aggregate size distributions, with a range of sintering levels (necks) and primary numbers, and this has implications for ease of post-processing to achieve a desired product specification. The neck radius and degree of primary separation were studied in addition to properties of the particle size distribution, and it was shown that changing reactant dosing temperature alters the development of particle attachment characteristics that are important for post-processing efficiency.

Reactant dosing strategy is also important – with more frequent dosage creating a narrower range of particle properties. Of course, in practice there may be reactor design limitations on the number of feasible injection points and the studies shown here should be supported by insights from computational fluid dynamics studies of mixing behaviour (realistically the computational cost of performing these studies simultaneously is currently infeasible; thus mixing is commonly studied independently without detailed particle models [57, 179]); however, in general the reduction in particle size and geometric deviation for increasing injection points agrees with industrial practice where multiple injection points are employed. Chlorine dosage was also shown to reduce the average size, standard deviation and range of the distribution of particles, providing another option for achieving desired sizes in the industrial process.

Comparison of simulated images with an SEM image from a titania plant provides a useful qualitative assessment of model predictive capacity. Simulated imaging also allows different conditions to be explored in terms of the morphology developed.

Chapter 7

Conclusions

7.1 Conclusions of the thesis

This thesis investigated population balance modelling tools for particulate synthesis with high process rates, focussing on the industrial titania process. Population balance modelling is widely used to study particle systems, including aerosol synthesis, and popular classes of numerical methods are documented extensively in the literature. Existing methods offer different degrees of efficiency, scalability with increasing dimensions, resolution of particle property distributions and ease of coupling with fluid and gas dynamics. This thesis developed a framework for detailed population balance modelling of industrial particle synthesis that includes a modular reactor model, and a novel hybrid particle model. The new framework enables efficient simulation of high-rate particle processes, allowing detailed numerical characterisation of particles produced in industrial titania synthesis.

Titania is an important inorganic chemical across many applications. Pigmentary particles produced in an industrial titania reactor are non-spherical and consist of many primary particles that are bonded together by high-temperature sintering. Process conditions influence particle size and aggregate morphology. As these characteristics govern end-product properties such as opacity and tint, it is critical to understand how synthesis conditions influence particle growth dynamics. Data for industrial titania synthesis is scarce due to limitations imposed on experiments and measurements by the harsh process environment. Existing modelling studies typically consider more dilute, laboratory-scale flow reactors and flames. A numerical framework for studying particle synthesis in the industrial reactor must be capable of resolving detailed particle structure and account for complicated reactor geometry.

This thesis proposed a modular reactor model to provide simplified, tractable treatment of the most important features of the flow field – multiple injection points at which reactant mixing can occur, and temperature gradients in the reactor and cooler. A continuously stirred tank reactor (CSTR) network is used to model the dosing zone and plug flow reactors (PFRs) are used to model the reaction and cooling zones. The reactor network model has two main advantages: (i) it provides a cheap approximation of flow characteristics in different parts of the reactor and facilitates focussing computational effort on resolving particle structure and coupling with gas phase kinetics; and (ii) it allows flexible modelling of different reactor configurations, for example to control the spatial configuration of dosing.

The utility of this approach was demonstrated using an 11-CSTR and 2-PFR network, with an imposed temperature profile based on plant expectations for the respective zones. Results of this study provided characterisation of the particle size distributions across the reactor, including primary particle size, neck radius (degree of sintering) and number of primary particles per aggregate. To inform process understanding, the model was used to test sensitivity to different design choices. It was found that higher reactor temperatures produce larger particles composed of smaller primary particles, while higher throughput produces smaller aggregates composed of smaller primaries. These observations are qualitatively supported by a combination of plant experience and literature studies. The imposed temperature profile was found to limit flexibility in these studies since temperature is likely to develop in a path-dependent manner. Thus, a further contribution of this thesis is the incorporation of heat release from the particle processes in the energy balance to allow modelling of temporal and spatial temperature dynamics. Initial work in this direction proved challenging due to numerical problems, exacerbated by feedback effects caused by temperature dynamics.

The serious numerical difficulties described above necessitated a new, more efficient method. This thesis developed a novel hybrid particle model with associated simulation algorithm to address this. The intention of this component of the work was to provide more efficient treatment of the numerics with lower sensitivity to numerical parameters for the rapid process rates associated with concentrated, high temperature systems in order to aid resolution of a broad particle size distribution and support inclusion of a system energy balance. The hybrid particle model was proposed based on the observation that small, newly-incepted particles do not require a representation as detailed as that of complicated aggregates. Primary particles are tracked efficiently with a particle-number model, while full aggregate structural information is provided for larger particles using a detailed particle model. Performance of the new approach was tested for simplified kinetics and it was shown to provide lower sensitivity to ensemble size choice and more efficient simulations under a wide range of process rates. The hybrid model is theoretically exactly equivalent for univariate primary particle systems, as was verified empirically by comparison with previous particle models.

The new hybrid model enables simulation of the industrial process within the reactor network framework, with extensions to model the energy balance and provide more complete resolution of particle structure. The operator splitting algorithm was adapted to incorporate the effect of heat release from particle processes, which had previously been excluded due to the low volume fraction of particles in other studies. The improved numerical performance of the new method facilitates the use of a recently-proposed, highly-detailed particle model that tracks relative primary coordinates for each aggregate particle. This allows reconstruction of the 3D structure without any assumption on the fractal dimension of the particle. This model was used as the detailed particle model in a second study of the industrial titania reactor using the new hybrid particle model and associated simulation algorithm.

The hybrid model was shown to provide robust handling of different particle loadings across the reactor network, to allow characterisation of particle property distributions for industrially relevant conditions, and to enable thorough investigation of process design choices. Critically, the new model has sufficient flexibility and its algorithms are sufficiently efficient to provide solutions to questions of interest to practitioners. It allows interrogation of dosing configuration, dilution strategy, operating temperature, etc., using a high-dimensional particle model that provides detailed information about aggregate morphology. In the penultimate chapter of this thesis, simulated images of structured particles observed under different production conditions were compared with a scanning electron microscopy (SEM) image of product particles from the industrial reactor, showing qualitative similarity.

Taken together, this thesis has advanced the state-of-the-art in terms of detailed resolution of the morphology of TiO_2 particles under industrially relevant synthesis conditions. The developed framework improves the efficiency and robustness to parameter choice of previous methods and supports detailed investigation into the relationship between process conditions and product quality. The techniques presented here are expected to have broader applicability to simulation of other aerosol products and particle processes in general.

7.2 Suggestions for future work

It is anticipated that future work could be beneficial on three fronts: further development of the reactor and particle models; improvement of the numerical method; and application to new systems with similar features. These are discussed in Sections 7.2.1–7.2.3.

7.2.1 Model development

There are several opportunities for developing the particle models in future work. Improvements to incorporate more physically realistic details are naturally desirable. A feature not represented in the current particle model is crystal phase. Xu et al. [171] demonstrated a simple phase-transformation model in a CFD-population balance Monte Carlo simulation for flame synthesis of TiO_2. Models to account for crystal phase in the detailed particle model are currently being investigated by other members of the Computational Modelling group in the context of flame synthesis with a TTIP precursor. Although the pigment-producing process mostly produces rutile titania, which is thermodynamically dominant under its process conditions, phase transformation could have some influence on modelling early particle structure. The particle-number model was found to assist in efficient simulations but currently is only exactly equivalent for a univariate primary particle model. Extension to a 2D particle-number model capable of tracking rutile and anatase phases could also allow application to systems such as carbon black synthesis (where carbon and hydrogen are important species).

There is scope for work in two areas of the particle process models. The current model for surface growth kinetics is limited by availability of relevant experimental data – parameters were fitted using data from the study of Pratsinis et al. [124] under more moderate conditions, using a kinetic expression proposed in previous work to fit observed experimental dynamics. There are many challenges associated with obtaining data under the industrial conditions and currently no such data exists. If this restriction is lifted in the future, relevant results could be used to investigate kinetic parameters or even growth laws, for example rate inhibition by chlorine, or surface evaporation. Secondly, the current system energy balance assumes pseudo steady dynamics which provides a far simpler model for heat flux as it avoids needing to track temperature for each ensemble particle. If future work identifies a need to account for heat transfer dynamics (for example radiative heat loss or melting of small particles), an additional internal coordinate could be included for each particle and a heat transfer splitting step could be added. This would increase computational cost significantly.

At the system level, modelling of fluid dynamics is simplified in the ideal reactor network. This is necessary in order to use a detailed particle model with current computational resources; however, with ongoing improvements in computing power, it should be possible for future studies in this field to investigate fluid dynamics for the reactor geometry. It was originally intended that surface structure data provided by this project could be used in subsequent work to study milling, which is applied as a post-process in the industrial synthesis. This would provide insight into the link between synthesis conditions and ease-of-milling to achieve end-product specifications.

Finally, surrogate models [38] could be fitted to the simulation data to provide a fast, potentially real-time evaluation of different operational choices. This would require many simulations covering the range of likely process conditions and is thus a computationally expensive exercise; however, it could aid process understanding and optimisation of particle properties.

7.2.2 Method optimisation

While the different Monte Carlo runs are "embarrassingly parallel", each run is still expensive and could possibly benefit from local parallelisation. This is challenging for the system presented in this thesis because of phase-coupling and particle interactions (e.g. coagulation); however, it should be possible to implement shared-memory parallelisation of single particle processes (e.g. surface growth or sintering). Initial overtures in this direction found that common memory access created read-write conflicts which limited the utility of this approach.

Combination of the hybrid particle model with weighted particle methods is a possible area for development. Weighted methods represent particle concentrations differentially, allowing more efficient resolution of larger or more rare particles. There is some similarity between the particle-number approach of the hybrid model, which accounts for many particles of a particular type using a single number, and assigning a differentiated particle weight to account for the concentration of a particular type of particle. Combination of the two techniques could provide optimal ensemble utility.

7.2.3 New applications

The hybrid approach provided the necessary efficiency and robustness to parameter choice to study industrial titania synthesis, and there is interest in extending the model to allow study of organic systems (e.g. carbon black) that exhibit similar fast process dynamics. This would require a two-dimensional (or more) particle-number model in order to track, for example, carbon-to-hydrogen ratios in soot. It is expected that the extension of the algorithm presented in this thesis would be straightforward.

As it allows resolution of complex aggregates without requiring large allocated ensembles of stochastic particles (by tracking small particles with the particle-number counter), the hybrid model could be used to aid coupling population balance modelling to CFD. The requirement of a large particle ensemble for physically realistic systems rapidly makes CFD simulations intractable. Weighted particle methods have been suggested to limit ensemble requirements with CFD coupling – thus, the hybrid model combined with weighted particles could offer even greater performance benefits.

The reactor network approach provides a convenient framework for addressing flow in complex geometries and could be suitable for studying other aerosol processes such as silica and carbon black. More generally, it is applicable to other well-mixed systems which are described by detailed population balance equations, including granulation [94] and crystallization processes. Thus, the framework presented in this thesis for detailed population balance modelling using a hybrid particle model in a reactor network provides an efficient platform for future use in a range of applications.

Nomenclature

Upper-case Roman

A	Surface area	$[\mathrm{m}^2]$
C	Concentration	$[\mathrm{mol\,m}^{-3}]$
$\mathbf{C}$	Connectivity matrix	
C_P	Constant pressure heat capacity	$[\mathrm{J\,K}^{-1}\,\mathrm{mol}^{-1}]$
D_f	Fractal dimension	
E_a	Arrhenius activation energy	$[\mathrm{kJ\,mol}^{-1}]$
F	Ratio	
$\hat{H}$	Specific molar enthalpy	$[\mathrm{J\,mol}^{-1}]$
I	Inception rate	$[\mathrm{mol\,m}^{-3}\,\mathrm{s}^{-1}]$
K	General coagulation kernel	$[\mathrm{m}^{-3}\,\mathrm{s}^{-1}]$
$\tilde{K}$	Coagulation constant	
$\hat{K}$	Majorant coagulation kernel	
Kn	Knudsen number	
L	Number of repeat runs	
$\mathcal{L}$	Length	$[\mathrm{m}]$
M	Number of time steps	
M_0	0th number moment	$[\mathrm{m}^{-3}]$
M_k	k^th mass moment	$[(\mathrm{kg\,m}^{-3})^{k}]$
MW	Molecular weight	$[\mathrm{g\,mol}^{-1}]$
N	Number	
N_A	Avogadro's constant	$[\mathrm{mol}^{-1}]$
P	Particle	
Poi	Poisson distribution	
Q	System state	

R	Rate	[process specific]
T	Temperature	[K]
U	Uniform distribution	
V	Volume	[m^3]

Lower-case Roman

c	Constant	
d	Diameter	[nm]
d_{ij}	Centre-to-centre distance of primary particles i and j	[nm]
f	Volumetric feed fraction	
g	Surface growth type-change function	
$\dot{g}$	Molar rate due to particle process	[$\mathrm{mol\,m^{-3}}$]
k_B	Boltzmann constant	[$\mathrm{J \cdot K^{-1}}$]
k_f	Fractal prefactor	
k_s	Surface growth rate constant, Arrhenius form	[$\mathrm{m\,s^{-1}\,m^3\,mol^{-1}}$]
k_1	Arrhenius constant	[$\mathrm{m\,s^{-1}\,m^3\,mol^{-1}}$]
m	Mass	[kg]
n	Particle number concentration	[$\mathrm{m^{-3}}$]
n_q	Primary count for particle P_q	
p	Primary particle	
r	Radius	[nm]
s	Sintering level	
t	Time	[s]
v	Primary particle volume	[m^3]
w	Statistical weight	
$\dot{w}$	Molar rate due to particle process	[$\mathrm{mol\,m^{-3}}$]
x	Particle type variable	
x_{ij}	Centre-to-neck distance from primary particle i to j	
y	Particle type variable	
z	Particle system	
$\mathbf{z}$	Primary centre of mass coordinates	[nm]

Upper-case Greek

Γ	Gas phase expansion coefficient	

Σ	Property set	
Ω	Physical domain	

Lower-case Greek

α	Random variable	
β	Surface growth rate	$[\mathrm{m^2\,m^{-3}\,s^{-1}}]$
$\tilde{\beta}$	Surface growth constant	
γ	Weighted random variable	
ε	Collision enhancement factor	
$\bar{\varepsilon}$	Average relative error	
η	Number of components	
θ	Axial coordinate for the reactor	$[\mathrm{m}]$
μ	Viscosity	$[\mathrm{Pa\,s}]$
μ_ξ	Mean values of property ξ	
ν	Stoichiometry	
π	Pi (constant)	
ξ	Property	
ρ	Mass/molar density	$[\mathrm{kg\,m^{-3}/mol\,m^{-3}}]$
σ	Standard deviation	
τ	Residence time	$[\mathrm{s}]$
τ_c	Characteristic time	$[\mathrm{s}]$
ϕ	Arbitrary continuous function	
ω	External coordinates	

Superscripts

in	Inflow
out	Outflow
sph	Sphere
$*$	Denotes reference solution

Subscripts

add	Added
bc	Base case
c	Collision

coag	Coagulation
fm	Free-molecular
g	geometric
i	Index variable
in	Inflow
inc	Inception
j	Index variable
k	Index variable
max	Maximum
out	Outflow
pri	Primary particle
q	Index variable
sf	Slip-flow
SG	Surface growth
smp	Sample
sp	Species
split	Splitting time
stat	Statistical
thresh	Threshold
tmp	Template
tr	Transition
1	Denotes monomer size (first) index

Symbols

$\mathcal{E}$	Generic particle type-space	
$\mathcal{F}$	Flow operator	
$\mathcal{G}$	Particle process gas phase operator	
$\mathcal{K}$	Coagulation operator	
$\mathcal{I}$	Inception operator	
$\mathcal{L}$	Reactor length	[m]
$\mathcal{M}$	Small particle type-space	
$\mathbb{N}_0$	Set of natural numbers including zero	
$\mathcal{P}$	Pressure	[Pa]
$\mathbb{P}$	Mathematical probability	

$\mathbb{R}_0^+$	The set of positive real numbers including zero
$\mathcal{S}$	Surface growth operator
$\mathcal{W}$	Gas phase process operator
$\mathcal{X}$	Large particle type-space
$\mathbb{1}$	Indicator function
$\forall$	For all

Abbreviations

BCCA	Ballistic cluster-cluster algorithm
CFD	Computational fluid dynamics
CSTR	Continuous stirred tank reactor
DNS	Direct numerical simulation
DSA	Direct simulation algorithm
DQMOM	Direct quadrature method of moments
ERN	Equivalent reactor network
(G)STD	(Geometric) standard deviation
IQR	Interquartile range (middle 50 % of data)
LPDA	Linear process deferment algorithm
MOMIC	Method of moments with interpolative closure
NDF	Number density function
ODE	Ordinary differential equation
PBE	Population balance equation
PDF	Probability density function
PFR	Plug flow reactor
PN/P	Particle-number/particle
PSD	Particle size distribution
QMOM	Quadrature method of moments
SQMOM	Sectional quadrature method of moments
SWA	Stochastic weighted algorithm
SEM	Scanning electron microscopy
TEM	Transmission electron microscopy
TER	Time-equivalent repeats
TESV	Time-equivalent sample volume
TTIP	Titanium tetraisopropoxide

Definitions

A

Agglomerate	Particle formed of primary particles loosely attached by physical forces (not modelled in this thesis, but used in the literature e.g. Eggersdorfer and Pratsinis [31])
Aggregate	Particle formed of primary particles attached by chemical forces (modelled in this thesis as resulting from coagulation with/without sintering and surface growth, also simply referred to as particle)

C

Coagulation	Collision of two particles resulting in lasting point contact
Coagulation kernel	Mathematical operator (function) that maps from elements of the particle type-space to a real number, specifying the rate of collision between two particles
Contraction	Numerical process of removing a particle selected at random from the finite computational ensemble when the ensemble capacity is exceeded and rescaling the sample volume to maintain the correct number density

Cooling zone	Describes the part of the industrial titania reactor where cooling occurs

D

Detailed particle model	Multivariate particle model that tracks lists of primary particles and their connectivity
Dimer	Chemical complex formed when two molecules (monomers) are bonded together, minimum configuration of solid titania used in this work
Dosing zone	Describes the part of the industrial titania reactor where reactants are injected stage-wise
Doubling	Numerical process of duplicating all computational particles and doubling the sample volume to improve statistical resolution

E

Ensemble	Collection of computational particles
Exotherm	Used here to refer to the increasing temperature gradient resulting from release of energy due to oxidation
External coordinates	Define particle positions in physical space

G

Gas phase expansion coefficient	Scalar that tracks the change in working volume of the gas phase

H

Hybrid particle model	Combination of multiple particle models to provide different descriptions for particles with different properties; type of particle model proposed in this work to treat small particles simply and resolve complicated particles

I

Ideal reactor	Simplified reactor flow model which assumes perfect mixing (CSTR) or no axial mixing (PFR)
Inception	Collision of gas phase precursors to form solid particles
Internal coordinates	Define particle types in property space

J

Jump process	Stochastic process with discrete changes in state triggered by events occur at random time intervals

K

Kernel density estimate	Method used here to fit a smooth, (log)normally distributed, probability density function to estimate the particle property distributions (also referred to as KDE)

M

Majorant kernel	Mathematical operator (function) that generates output values larger than those generated by the coagulation kernel (providing an upper bound on the coagulation rate)
Method	Numerical technique used to solve a problem
Model	Description of a process or feature

N

Neck	Connection between adjacent primary particles, formed by coagulation and extended by sintering or surface growth
Number density	Number of particles (of a specific type) in a given volume

Numerical diffusion	Artificial smoothing introduced when using a numerical method that discretizes the state-space, creating a discrepancy between the real and simulated behaviour of the system

P

Particle-number model	Model for the particle system that tracks the number of particles with a given property; used here to model primary particles with integer numbers of TiO_2 molecules less than a threshold size
Precursor	Chemical species required to form a certain product (e.g. $TiCl_4$ is a *precursor* in the titania process, providing the Ti that is used to form gas phase intermediate species that collide to form solid TiO_2, and titanium oxychloride intermediates such as TiOCl are *precursors* in this inception process)
Polydisperse	Refers to particle populations with a range of characteristic properties (e.g. non-uniform primary particle diameters)
Primary particles	The simplest particles considered here formed as stable collections of molecules by inception from the gas phase, undergo growth due to surface reaction and can become attached to each other in collisions (also called ‘primaries’)

R

Rutile	One of the dominant crystal phases of titanium dioxide, of interest in production of pigments due to its high refractive index and associated light scattering behaviour

S

Sintering	Process of compaction that occurs in adjacent primary particle pairs, strengthening their chemical bond and leading to the development of necks at the point of connection
State-space	Mathematical description of the combined space of internal (type) and external (location) coordinates for the particles
Statistical weight	Numerical property assigned to simulation particles to provide flexibility to model different physical concentrations of particles with a single computational entity; can help to resolve rare parts of the particle size distribution [121]

T

Titania	Titanium dioxide, TiO_2
Transience	Non-steady, dynamic behaviour of a system
Type-space	Mathematical description of particle property (e.g. mass, composition, geometry) space, defines description of different particle types

W

Waiting time	Time between jump process events (an exponentially distributed random variable)
Working zone	Describes the part of the industrial titania reactor immediately after the dosing zone where the reactions are completed

References

[1] M. K. Akhtar, Y. Xiong, and S. E. Pratsinis. Vapor synthesis of titania powder by titanium tetrachloride oxidation. *Journal of Aerosol Science*, 22(SUPPL. 1):S35–S38, 1991. ISSN 00218502. doi:10.1016/S0021-8502(05)80028-X.

[2] M. K. Akhtar, G. G. Lipscomb, and S. E. Pratsinis. Monte Carlo Simulation of Particle Coagulation and Sintering. *Aerosol Science and Technology*, 21(1):83–93, 1994. ISSN 0278-6826. doi:10.1080/02786829408959698.

[3] J. Akroyd, A. J. Smith, L. R. McGlashan, and M. Kraft. Numerical investigation of DQMoM-IEM as a turbulent reaction closure. *Chemical Engineering Science*, 65(6): 1915–1924, 2010. ISSN 00092509. doi:10.1016/j.ces.2009.11.010.

[4] J. Akroyd, A. J. Smith, R. Shirley, L. R. McGlashan, and M. Kraft. A coupled CFD-population balance approach for nanoparticle synthesis in turbulent reacting flows. *Chemical Engineering Science*, 66(17):3792–3805, 2011. ISSN 00092509. doi:10.1016/j.ces.2011.05.006.

[5] C. Artelt, H. J. Schmid, and W. Peukert. On the impact of accessible surface and surface energy on particle formation and growth from the vapour phase. *Journal of Aerosol Science*, 36(2):147–172, 2005. ISSN 00218502. doi:10.1016/j.jaerosci.2004.08.003.

[6] C. Artelt, H. J. Schmid, and W. Peukert. Modelling titania formation at typical industrial process conditions: effect of surface shielding and surface energy on relevant growth mechanisms. *Chemical Engineering Science*, 61(1):18–32, 2006. ISSN 00092509. doi:10.1016/j.ces.2004.12.053.

[7] M. M. Attarakih, C. Drumm, and H.-J. Bart. Solution of the population balance equation using the sectional quadrature method of moments (SQMOM). *Chemical Engineering Science*, 64(4):742–752, 2009. ISSN 00092509. doi:10.1016/j.ces.2008.05.006.

[8] G. Auer, P. Woditsch, A. Westerhaus, J. Kischkewitz, W.-d. Griebler, M. Rohe, and M. Liedekerke. Pigments, Inorganic, 2. White Pigments. In *Ullmann's Encyclopedia of Industrial Chemistry*, pages 1–36. Wiley-VCH Verlag GmbH & Co. KGaA, Weinheim, Germany, 2017. doi:10.1002/14356007.n20_n01.pub2.

[9] H. Babovsky. A hybrid numerical scheme for aerosol dynamics. In *Numerical Mathematics and Advanced Applications*, pages 425–432. Springer, 2008. ISBN 978-3-540-69776-3. doi:0.1007/978-3-540-69777-0.

[10] M. Balthasar, F. Mauss, A. Knobel, and M. Kraft. Detailed modeling of soot formation in a partially stirred plug flow reactor. *Combustion and Flame*, 128(4):395–409, 2002. ISSN 00102180. doi:10.1016/S0010-2180(01)00344-3.

[11] C. Bartsch, V. John, and R. I. Patterson. Simulations of an ASA flow crystallizer with a coupled stochastic-deterministic approach. *Computers & Chemical Engineering*, 124: 350–363, 2019. ISSN 00981354. doi:10.1016/j.compchemeng.2019.01.012.

[12] A. Bouaniche, L. Vervisch, and P. Domingo. A hybrid stochastic/fixed-sectional method for solving the population balance equation. *Chemical Engineering Science*, 209:115198, 2019. ISSN 00092509. doi:10.1016/j.ces.2019.115198.

[13] J.-P. Bourgade and F. Filbet. Convergence of a finite volume scheme for coagulation-fragmentation equations. *Mathematics of Computation*, 77(262):851–883, 2007. ISSN 0025-5718. doi:10.1090/S0025-5718-07-02054-6.

[14] N. Brilliantov, P. L. Krapivsky, A. Bodrova, F. Spahn, H. Hayakawa, V. Stadnichuk, and J. Schmidt. Size distribution of particles in Saturn's rings from aggregation and fragmentation. *Proceedings of the National Academy of Sciences*, 112(31):9536–9541, 2015. ISSN 0027-8424. doi:10.1073/pnas.1503957112.

[15] M. C. Bruns and O. A. Ezekoye. Development of a hybrid sectional quadrature-based moment method for solving population balance equations. *Journal of Aerosol Science*, 54:88–102, 2012. ISSN 00218502. doi:10.1016/j.jaerosci.2012.07.003.

[16] P. Buerger, J. Akroyd, S. Mosbach, and M. Kraft. A systematic method to estimate and validate enthalpies of formation using error-cancelling balanced reactions. *Combustion and Flame*, 187:105–121, 2018. ISSN 15562921. doi:10.1016/j.combustflame.2017.08.013.

[17] P. Buerger, J. Akroyd, and M. Kraft. Extended first-principles thermochemistry for the oxidation of titanium tetrachloride. *Combustion and Flame*, 199:441–450, 2019. ISSN 00102180. doi:10.1016/j.combustflame.2018.07.021.

[18] B. Buesser and S. E. Pratsinis. Design of Nanomaterial Synthesis by Aerosol Processes. *Annual Review of Chemical and Biomolecular Engineering*, 3(1):103–127, 2012. ISSN 1947-5438. doi:10.1146/annurev-chembioeng-062011-080930.

[19] B. Buesser, A. J. Gröhn, and S. E. Pratsinis. Sintering Rate and Mechanism of TiO_2 Nanoparticles by Molecular Dynamics. *The Journal of Physical Chemistry C*, 115(22): 11030–11035, 2011. ISSN 1932-7447. doi:10.1021/jp2032302.

[20] M. Celnik, R. I. A. Patterson, M. Kraft, and W. Wagner. A predictor–corrector algorithm for the coupling of stiff ODEs to a particle population balance. *Journal of Computational Physics*, 228(8):2758–2769, 2009. ISSN 00219991. doi:10.1016/j.jcp.2008.12.030.

[21] M. S. Celnik, R. I. A. Patterson, M. Kraft, and W. Wagner. Coupling a stochastic soot population balance to gas-phase chemistry using operator splitting. *Combustion and Flame*, 148(3):158–176, 2007. ISSN 00102180. doi:10.1016/j.combustflame.2006.10.007.

[22] M. S. Celnik, M. Sander, A. Raj, R. H. West, and M. Kraft. Modelling soot formation in a premixed flame using an aromatic-site soot model and an improved oxidation rate. *Proceedings of the Combustion Institute*, 32(1):639–646, 2009. ISSN 15407489. doi:10.1016/j.proci.2008.06.062.

[23] M. W. Chase. *NIST-JANAF Thermochemical Tables*. American Institute of Physics, New York, 4 edition, 1998.

[24] X. Chen and S. S. Mao. Titanium Dioxide Nanomaterials: Synthesis, Properties, Modifications, and Applications. *Chemical Reviews*, 107(7):2891–2959, 2007. ISSN 0009-2665. doi:10.1021/cr0500535.

[25] J. C. Deberry, M. Robinson, M. D. Pomponi, A. J. Beach, Y. Xiong, and K. Akhtar. Controlled vapor phase oxidation of titanium tetrachloride to manufacture titanium dioxide, 2002. US Patent 6,387,347.

[26] E. Debry, B. Sportisse, and B. Jourdain. A stochastic approach for the numerical simulation of the general dynamics equation for aerosols. *Journal of Computational Physics*, 184(2):649–669, 2003. ISSN 00219991. doi:10.1016/S0021-9991(02)00041-4.

[27] L. DeVille, N. Riemer, and M. West. Convergence of a generalized Weighted Flow Algorithm for stochastic particle coagulation. *Journal of Computational Dynamics*, 6(1): 69–94, 2019. ISSN 2158-2491. doi:10.3934/jcd.2019003.

[28] R. DeVille, N. Riemer, and M. West. Weighted Flow Algorithms (WFA) for stochastic particle coagulation. *Journal of Computational Physics*, 230(23):8427–8451, 2011. ISSN 00219991. doi:10.1016/j.jcp.2011.07.027.

[29] DuPont Titanium Technologies. Polymers, light and science of TiO_2 (h-88382-6). https://www.chemours.com/Titanium_Technologies/es_US/tech_info/literature/Plastics/PL_B_Polymers_Light_Science.pdf, 2007. Accessed: 2019-10-08.

[30] M. L. Eggersdorfer and S. E. Pratsinis. The Structure of Agglomerates Consisting of Polydisperse Particles. *Aerosol Science and Technology*, 46(3):347–353, 2012. ISSN 0278-6826. doi:10.1080/02786826.2011.631956.

[31] M. L. Eggersdorfer and S. E. Pratsinis. Agglomerates and aggregates of nanoparticles made in the gas phase. *Advanced Powder Technology*, 25(1):71–90, 2014. ISSN 09218831. doi:10.1016/j.apt.2013.10.010.

[32] M. L. Eggersdorfer, D. Kadau, H. J. Herrmann, and S. E. Pratsinis. Aggregate morphology evolution by sintering: Number and diameter of primary particles. *Journal of Aerosol Science*, 46:7–19, 2012. ISSN 00218502. doi:10.1016/j.jaerosci.2011.11.005.

[33] A. Eibeck and W. Wagner. An Efficient Stochastic Algorithm for Studying Coagulation Dynamics and Gelation Phenomena. *SIAM Journal on Scientific Computing*, 22(3): 802–821, 2000. ISSN 1064-8275. doi:10.1137/S1064827599353488.

[34] A. Eibeck and W. Wagner. Stochastic Particle Approximations for Smoluchoski's Coagulation Equation. *The Annals of Applied Probability*, 11(4):1137–1165, 2001. ISSN 10505164. doi:10.1214/aoap/1015345398.

[35] A. Eibeck and W. Wagner. Stochastic interacting particle systems and nonlinear kinetic equations. *The Annals of Applied Probability*, 13(3):845–889, 2003. ISSN 1050-5164. doi:10.1214/aoap/1060202829.

[36] H. S. Fogler. *Elements of chemical reaction engineering*. Prentice Hall, Upper Saddle River, N.J., 5 edition, 2016.

[37] M. Formenti, F. Juillet, P. Meriaudeau, S. Teichner, and P. Vergnon. Preparation in a hydrogen-oxygen flame of ultrafine metal oxide particles. Oxidative properties toward hydrocarbons in the presence of ultraviolet radiation. *Journal of Colloid and Interface Science*, 39(1):79–89, 1972. ISSN 00219797. doi:10.1016/0021-9797(72)90144-0.

[38] A. I. J. Forrester, A. Sóbester, and A. J. Keane. *Engineering Design via Surrogate Modelling: A Practical Guide*. John Wiley & Sons, Chichester, UK, 2008. ISBN 9780470770801. doi:10.1002/9780470770801.

[39] M. Frenklach. Method of moments with interpolative closure. *Chemical Engineering Science*, 57(12):2229–2239, 2002. ISSN 00092509. doi:10.1016/S0009-2509(02)00113-6.

[40] M. Frenklach and S. J. Harris. Aerosol dynamics modeling using the method of moments. *Journal of Colloid and Interface Science*, 118(1):252–261, 1987. ISSN 00219797. doi:10.1016/0021-9797(87)90454-1.

[41] S. C. Garrick and G. Wang. Modeling and simulation of titanium dioxide nanoparticle synthesis with finite-rate sintering in planar jets. *Journal of Nanoparticle Research*, 13 (3):973–984, 2011. ISSN 1388-0764. doi:10.1007/s11051-010-0097-x.

[42] M. J. Gázquez, J. P. Bolívar, R. Garcia-Tenorio, and F. Vaca. A Review of the Production Cycle of Titanium Dioxide Pigment. *Materials Sciences and Applications*, 05(07): 441–458, 2014. ISSN 2153-117X. doi:10.4236/msa.2014.57048.

[43] F. Gelbard and J. H. Seinfeld. Numerical solution of the dynamic equation for particulate systems. *Journal of Computational Physics*, 28(3):357–375, 1978. ISSN 00219991. doi:10.1016/0021-9991(78)90058-X.

[44] A. P. George, R. D. Murley, and E. R. Place. Formation of TiO_2 aerosol from the combustion supported reaction of $TiCl_4$ and O_2. *Faraday Symposia of the Chemical Society*, 7:63, 1973. ISSN 0301-5696. doi:10.1039/fs9730700063.

[45] R. N. Ghoshtagore. Mechanism of Heterogeneous Deposition of Thin Film Rutile. *Journal of The Electrochemical Society*, 117(4):529, 1970. ISSN 00134651. doi:10.1149/1.2407561.

[46] D. T. Gillespie. An Exact Method for Numerically Simulating the Stochastic Coalescence Process in a Cloud. *Journal of the Atmospheric Sciences*, 32(10):1977–1989, 1975.

[47] R. A. Gonzalez, C. D. Musick, and J. N. Tilton. Process for controlling agglomeration in the manufacture of TiO_2, 1996. US Patent 5,508,015.

[48] M. Goodson and M. Kraft. An Efficient Stochastic Algorithm for Simulating Nanoparticle Dynamics. *Journal of Computational Physics*, 183(1):210–232, 2002. ISSN 00219991. doi:10.1006/jcph.2002.7192.

[49] E. Goudeli, M. L. Eggersdorfer, and S. E. Pratsinis. Aggregate characteristics accounting for the evolving fractal-like structure during coagulation and sintering. *Journal of Aerosol Science*, 89:58–68, 2015. ISSN 00218502. doi:10.1016/j.jaerosci.2015.06.008.

[50] M. C. Heine and S. E. Pratsinis. Agglomerate TiO_2 Aerosol Dynamics at High Concentrations. *Particle & Particle Systems Characterization*, 24(1):56–65, 2007. ISSN 09340866. doi:10.1002/ppsc.200601076.

[51] R. Hong, Z. Ren, J. Ding, and H. Li. Experimental investigation and particle dynamic simulation for synthesizing titania nanoparticles using diffusion flame. *Chemical Engineering Journal*, 108(3):203–212, 2005. ISSN 13858947. doi:10.1016/j.cej.2005.02.011.

[52] D. Hou, C. S. Lindberg, M. Y. Manuputty, X. You, and M. Kraft. Modelling soot formation in a benchmark ethylene stagnation flame with a new detailed population balance model. *Combustion and Flame*, 203:56–71, 2019. ISSN 00102180. doi:10.1016/j.combustflame.2019.01.035.

[53] M. J. Hounslow, R. L. Ryall, and V. R. Marshall. A discretized population balance for nucleation, growth, and aggregation. *AIChE Journal*, 34(11):1821–1832, 1988. ISSN 0001-1541. doi:10.1002/aic.690341108.

[54] R. Irizarry. Fast Monte Carlo methodology for multivariate particulate systems—I: Point ensemble Monte Carlo. *Chemical Engineering Science*, 63(1):95–110, 2008. ISSN 00092509. doi:10.1016/j.ces.2007.09.007.

[55] R. Irizarry. Fast Compartmental Monte Carlo Simulation of Population Balance Models: Application to Nanoparticle Formation in Nonhomogeneous Conditions. *Industrial & Engineering Chemistry Research*, 51(47):15484–15496, 2012. ISSN 0888-5885. doi:10.1021/ie3011116.

[56] T. Johannessen, S. E. Pratsinis, and H. Livbjerg. Computational analysis of coagulation and coalescence in the flame synthesis of titania particles. *Powder Technology*, 118(3): 242–250, 2001. ISSN 00325910. doi:10.1016/S0032-5910(00)00401-0.

[57] E. V. Kartaev, V. P. Lukashov, S. P. Vashenko, S. M. Aulchenko, O. B. Kovalev, and D. V. Sergachev. An Experimental Study of the Synthesis of Ultrafine Titania Powder in Plasmachemical Flow-Type Reactor. *International Journal of Chemical Reactor Engineering*, 12(1):377–396, 2014. ISSN 2194-5748. doi:10.1515/ijcre-2014-0001.

[58] V. Kartaev, V. Emelkin, M. Ktalkherman, S. Aulchenko, S. Vashenko, and V. Kuzmin. Formation of counter flow jet resulting from impingement of multiple jets radially injected in a crossflow. *Experimental Thermal and Fluid Science*, 68:310–321, 2015. ISSN 08941777. doi:10.1016/j.expthermflusci.2015.05.009.

[59] L. Kaufman and P. J. Rousseeuw. *Finding groups in data: an introduction to cluster analysis*, volume 344. John Wiley & Sons, 2009.

[60] A. Kobata, K. Kusakabe, and S. Morooka. Growth and transformation of TiO_2 crystallites in aerosol reactor. *AIChE Journal*, 37(3):347–359, 1991. ISSN 0001-1541. doi:10.1002/aic.690370305.

[61] J. Koch, W. Hackbusch, and K. Sundmacher. $\mathcal{H}$-matrix methods for linear and quasi-linear integral operators appearing in population balances. *Computers & Chemical Engineering*, 31(7):745–759, 2007. ISSN 00981354. doi:10.1016/j.compchemeng.2006.07.012.

[62] W. Koch and S. Friedlander. The effect of particle coalescence on the surface area of a coagulating aerosol. *Journal of Colloid and Interface Science*, 140(2):419–427, 1990. ISSN 00219797. doi:10.1016/0021-9797(90)90362-R.

[63] G. Kotalczyk and F. Kruis. A Monte Carlo method for the simulation of coagulation and nucleation based on weighted particles and the concepts of stochastic resolution and merging. *Journal of Computational Physics*, 340:276–296, 2017. ISSN 00219991. doi:10.1016/j.jcp.2017.03.041.

[64] M. Kraft. Modelling of Particulate Processes. *KONA Powder and Particle Journal*, 23: 18–35, 2005. ISSN 0288-4534. doi:10.14356/kona.2005007.

[65] F. E. Kruis, K. A. Kusters, S. E. Pratsinis, and B. Scarlett. A Simple Model for the Evolution of the Characteristics of Aggregate Particles Undergoing Coagulation and Sintering. *Aerosol Science and Technology*, 19(4):514–526, 1993. ISSN 0278-6826. doi:10.1080/02786829308959656.

[66] F. E. Kruis, A. Maisels, and H. Fissan. Direct simulation Monte Carlo method for particle coagulation and aggregation. *AIChE Journal*, 46(9):1735–1742, 2000. ISSN 00011541. doi:10.1002/aic.690460905.

[67] F. E. Kruis, J. Wei, T. van der Zwaag, and S. Haep. Computational fluid dynamics based stochastic aerosol modeling: Combination of a cell-based weighted random walk method and a constant-number Monte-Carlo method for aerosol dynamics. *Chemical Engineering Science*, 70:109–120, 2012. ISSN 00092509. doi:10.1016/j.ces.2011.10.040.

[68] S. Kumar and D. Ramkrishna. On the solution of population balance equations by discretization–I. A fixed pivot technique. *Chemical Engineering Science*, 51(8):1311–1332, 1996. ISSN 00092509. doi:10.1016/0009-2509(96)88489-2.

[69] S. Kumar and D. Ramkrishna. On the solution of population balance equations by discretization–II. A moving pivot technique. *Chemical Engineering Science*, 51(8): 1333–1342, 1996. ISSN 00092509. doi:10.1016/0009-2509(95)00355-X.

[70] S. Kumar and D. Ramkrishna. On the solution of population balance equations by discretization–III. Nucleation, growth and aggregation of particles. *Chemical Engineering Science*, 52(24):4659–4679, 1997. ISSN 00092509. doi:10.1016/S0009-2509(97)00307-2.

[71] K. F. Lee, R. I. A. Patterson, W. Wagner, and M. Kraft. Stochastic weighted particle methods for population balance equations with coagulation, fragmentation and spatial inhomogeneity. *Journal of Computational Physics*, 303:1–18, 2015. ISSN 00219991. doi:10.1016/j.jcp.2015.09.031.

[72] S.-Y. Lee and S.-J. Park. TiO_2 photocatalyst for water treatment applications. *Journal of Industrial and Engineering Chemistry*, 19(6):1761–1769, 2013. ISSN 1226086X. doi:10.1016/j.jiec.2013.07.012.

[73] K. E. Lehtinen and M. R. Zachariah. Energy accumulation in nanoparticle collision and coalescence processes. *Journal of Aerosol Science*, 33(2):357–368, 2002. ISSN 00218502. doi:10.1016/S0021-8502(01)00177-X.

[74] K. E. J. Lehtinen and M. R. Zachariah. Effect of coalescence energy release on the temporal shape evolution of nanoparticles. *Physical Review B*, 63(20):205402, 2001. ISSN 0163-1829. doi:10.1103/PhysRevB.63.205402.

[75] H. Li, S. Zhang, and Q. Zhong. Effect of nitrogen doping on oxygen vacancies of titanium dioxide supported vanadium pentoxide for ammonia-SCR reaction at low temperature. *Journal of Colloid and Interface Science*, 402:190–195, 2013. ISSN 00219797. doi:10.1016/j.jcis.2012.10.033.

[76] S. Li, Y. Ren, P. Biswas, and S. D. Tse. Flame aerosol synthesis of nanostructured materials and functional devices: Processing, modeling, and diagnostics. *Progress in Energy and Combustion Science*, 55:1–59, 2016. ISSN 03601285. doi:10.1016/j.pecs.2016.04.002.

[77] Y. Lin, K. Lee, and T. Matsoukas. Solution of the population balance equation using constant-number Monte Carlo. *Chemical Engineering Science*, 57(12):2241–2252, 2002. ISSN 00092509. doi:10.1016/S0009-2509(02)00114-8.

[78] C. Lindberg, J. Akroyd, and M. Kraft. Developing breakage models relating morphological data to the milling behaviour of flame synthesised titania particles. *Chemical Engineering Science*, 166:53–65, 2017. ISSN 00092509. doi:10.1016/j.ces.2017.03.016.

[79] C. S. Lindberg, M. Y. Manuputty, J. Akroyd, and M. Kraft. A two-step simulation methodology for modelling stagnation flame synthesised aggregate nanoparticles. *Combustion and Flame*, 202:143–153, 2019. ISSN 00102180. doi:10.1016/j.combustflame.2019.01.010.

[80] C. S. Lindberg, M. Y. Manuputty, P. Buerger, J. Akroyd, and M. Kraft. Numerical simulation and parametric sensitivity study of titanium dioxide particles synthesised in a stagnation flame. *Journal of Aerosol Science*, 138:105451, 2019. ISSN 00218502. doi:10.1016/j.jaerosci.2019.105451.

[81] C. S. Lindberg, M. Y. Manuputty, E. K. Yapp, J. Akroyd, R. Xu, and M. Kraft. A detailed particle model for polydisperse aggregate particles. *Journal of Computational Physics*, 397:108799, 2019. ISSN 00219991. doi:10.1016/j.jcp.2019.06.074.

[82] J. Loeffler, S. Das, and S. C. Garrick. Large Eddy Simulation of Titanium Dioxide Nanoparticle Formation and Growth in Turbulent Jets. *Aerosol Science and Technology*, 45(5):616–628, 2011. ISSN 0278-6826. doi:10.1080/02786826.2010.551147.

[83] A. Maisels, F. Einar Kruis, and H. Fissan. Direct simulation Monte Carlo for simultaneous nucleation, coagulation, and surface growth in dispersed systems. *Chemical Engineering Science*, 59(11):2231–2239, 2004. ISSN 00092509. doi:10.1016/j.ces.2004.02.015.

[84] L. Malyshkin and J. Goodman. The Timescale of Runaway Stochastic Coagulation. *Icarus*, 150(2):314–322, 2001. ISSN 00191035. doi:10.1006/icar.2001.6587.

[85] M. Y. Manuputty, J. Akroyd, S. Mosbach, and M. Kraft. Modelling TiO_2 formation in a stagnation flame using method of moments with interpolative closure. *Combustion and Flame*, 178:135–147, 2017. ISSN 00102180. doi:10.1016/j.combustflame.2017.01.005.

[86] M. Y. Manuputty, J. A. H. Dreyer, Y. Sheng, E. J. Bringley, M. L. Botero, J. Akroyd, and M. Kraft. Polymorphism of nanocrystalline TiO_2 prepared in a stagnation flame: formation of the TiO_2-II phase. *Chemical Science*, 10(5):1342–1350, 2019. ISSN 2041-6520. doi:10.1039/C8SC02969E.

[87] M. Y. Manuputty, C. S. Lindberg, M. L. Botero, J. Akroyd, and M. Kraft. Detailed characterisation of TiO_2 nano-aggregate morphology using TEM image analysis. *Journal of Aerosol Science*, 133:96–112, 2019. ISSN 00218502. doi:10.1016/j.jaerosci.2019.04.012.

[88] D. L. Marchisio and R. O. Fox. Solution of population balance equations using the direct quadrature method of moments. *Journal of Aerosol Science*, 36(1):43–73, 2005. ISSN 00218502. doi:10.1016/j.jaerosci.2004.07.009.

[89] D. L. Marchisio, J. T. Pikturna, R. O. Fox, R. D. Vigil, and A. A. Barresi. Quadrature method of moments for population-balance equations. *AIChE Journal*, 49(5):1266–1276, 2003. ISSN 00011541. doi:10.1002/aic.690490517.

[90] MathWorks. R2016a Documentation: 'ksdensity', Kernel smoothing function estimate for univariate and bivariate data. https://www.mathworks.com/help/stats/ksdensity.html?searchHighlight=ksdensity, 2016. Accessed: 2016-11-09.

[91] S. Matveev, A. Smirnov, and E. Tyrtyshnikov. A fast numerical method for the Cauchy problem for the Smoluchowski equation. *Journal of Computational Physics*, 282:23–32, 2015. ISSN 00219991. doi:10.1016/j.jcp.2014.11.003.

[92] S. A. Matveev, D. A. Zheltkov, E. E. Tyrtyshnikov, and A. P. Smirnov. Tensor train versus Monte Carlo for the multicomponent Smoluchowski coagulation equation. *Journal of Computational Physics*, 316:164–179, 2016. ISSN 00219991. doi:10.1016/j.jcp.2016.04.025.

[93] R. McGraw. Description of aerosol dynamics by the quadrature method of moments. *Aerosol Science and Technology*, 27(2):255–265, 1997. ISSN 15217388. doi:10.1080/02786829708965471.

[94] A. D. McGuire, S. Mosbach, K. F. Lee, G. Reynolds, and M. Kraft. A high-dimensional, stochastic model for twin-screw granulation – Part 1: Model description. *Chemical Engineering Science*, 188:221–237, 2018. ISSN 00092509. doi:10.1016/j.ces.2018.04.076.

[95] M. Mehta, Y. Sung, V. Raman, and R. O. Fox. Multiscale Modeling of TiO_2 Nanoparticle Production in Flame Reactors: Effect of Chemical Mechanism. *Industrial & Engineering Chemistry Research*, 49(21):10663–10673, 2010. ISSN 0888-5885. doi:10.1021/ie100560h.

[96] M. Mehta, V. Raman, and R. O. Fox. On the role of gas-phase and surface chemistry in the production of titania nanoparticles in turbulent flames. *Chemical Engineering Science*, 104(2013):1003–1018, 2013. ISSN 00092509. doi:10.1016/j.ces.2013.10.039.

[97] J. M. Meichtry, H. J. Lin, L. de la Fuente, I. K. Levy, E. A. Gautier, M. A. Blesa, and M. I. Litter. Low-Cost TiO_2 Photocatalytic Technology for Water Potabilization in Plastic Bottles For Isolated Regions. Photocatalyst Fixation. *Journal of Solar Energy Engineering*, 129(1):119, 2007. ISSN 01996231. doi:10.1115/1.2391317.

[98] W. J. Menz and M. Kraft. The Suitability of Particle Models in Capturing Aggregate Structure and Polydispersity. *Aerosol Science and Technology*, 47(7):734–745, 2013. ISSN 0278-6826. doi:10.1080/02786826.2013.788244.

[99] W. J. Menz and M. Kraft. A new model for silicon nanoparticle synthesis. *Combustion and Flame*, 160(5):947–958, 2013. ISSN 00102180. doi:10.1016/j.combustflame.2013.01.014.

[100] W. J. Menz, R. I. A. Patterson, W. Wagner, and M. Kraft. Application of stochastic weighted algorithms to a multidimensional silica particle model. *Journal of Computational Physics*, 248:221–234, 2013. ISSN 00219991. doi:10.1016/j.jcp.2013.04.010.

[101] W. J. Menz, J. Akroyd, and M. Kraft. Stochastic solution of population balance equations for reactor networks. *Journal of Computational Physics*, 256:615–629, 2014. ISSN 00219991. doi:10.1016/j.jcp.2013.09.021.

[102] P. Mitchell and M. Frenklach. Particle aggregation with simultaneous surface growth. *Physical Review E*, 67(6):061407, 2003. ISSN 1063-651X. doi:10.1103/PhysRevE.67.061407.

[103] N. Morgan, C. Wells, M. Goodson, M. Kraft, and W. Wagner. A new numerical approach for the simulation of the growth of inorganic nanoparticles. *Journal of Computational Physics*, 211(2):638–658, 2006. ISSN 00219991. doi:10.1016/j.jcp.2005.04.027.

[104] N. Morgan, M. Kraft, M. Balthasar, D. Wong, M. Frenklach, and P. Mitchell. Numerical simulations of soot aggregation in premixed laminar flames. *Proceedings of the Combustion Institute*, 31(1):693–700, 2007. ISSN 15407489. doi:10.1016/j.proci.2006.08.021.

[105] M. Mueller, G. Blanquart, and H. Pitsch. Hybrid Method of Moments for modeling soot formation and growth. *Combustion and Flame*, 156(6):1143–1155, 2009. ISSN 00102180. doi:10.1016/j.combustflame.2009.01.025.

[106] H. Mühlenweg, A. Gutsch, A. Schild, and S. Pratsinis. Process simulation of gas-to-particle-synthesis via population balances: Investigation of three models. *Chemical Engineering Science*, 57(12):2305–2322, 2002. ISSN 00092509. doi:10.1016/S0009-2509(02)00119-7.

[107] C. D. Musick, A. H. Reid Jr, and L. Zhang. Titanium dioxide nanopowder manufacturing process, 2007. US Patent 7,208,126.

[108] K. Nakaso, T. Fujimoto, T. Seto, M. Shimada, K. Okuyama, and M. M. Lunden. Size Distribution Change of Titania Nano-Particle Agglomerates Generated by Gas Phase Reaction, Agglomeration, and Sintering. *Aerosol Science and Technology*, 35(5):929–947, 2001. ISSN 0278-6826. doi:10.1080/02786820126857.

[109] K. Nakaso, K. Okuyama, M. Shimada, and S. E. Pratsinis. Effect of reaction temperature on CVD-made TiO_2 primary particle diameter. *Chemical Engineering Science*, 58(15): 3327–3335, 2003. ISSN 00092509. doi:10.1016/S0009-2509(03)00213-6.

[110] T. Nguyen, F. Laurent, R. Fox, and M. Massot. Solution of population balance equations in applications with fine particles: Mathematical modeling and numerical schemes. *Journal of Computational Physics*, 325:129–156, 2016. ISSN 00219991. doi:10.1016/j.jcp.2016.08.017.

[111] A. Novikov. PyClustering: Data mining library. *Journal of Open Source Software*, 4 (36):1230, 2019. doi:10.21105/joss.01230.

[112] I. V. Novosselov and P. C. Malte. Development and Application of an Eight-Step Global Mechanism for CFD and CRN Simulations of Lean-Premixed Combustors. *Journal of Engineering for Gas Turbines and Power*, 130(2):021502, 2008. ISSN 07424795. doi:10.1115/1.2795787.

[113] I. V. Novosselov, P. C. Malte, S. Yuan, R. Srinivasan, and J. C. Y. Lee. Chemical Reactor Network Application to Emissions Prediction for Industial DLE Gas Turbine. In *Volume 1: Combustion and Fuels, Education*, volume 2006, pages 221–235. ASME, 2006. ISBN 0-7918-4236-3. doi:10.1115/GT2006-90282.

[114] D. Nurkowski, A. W. Jasper, J. Akroyd, and M. Kraft. Theoretical study of the Ti–Cl bond cleavage reaction in $TiCl_4$. *Zeitschrift für Physikalische Chemie*, 231(9):1489–1506, 2017.

[115] H. K. Park and K. Y. Park. Control of Particle Morphology and Size in Vapor-Phase Synthesis of Titania, Silica and Alumina Nanoparticles. *KONA Powder and Particle Journal*, 32(32):85–101, 2015. ISSN 0288-4534. doi:10.14356/kona.2015018.

[116] R. I. A. Patterson. Convergence of Stochastic Particle Systems Undergoing Advection and Coagulation. *Stochastic Analysis and Applications*, 31(5):800–829, 2013. ISSN 0736-2994. doi:10.1080/07362994.2013.817245.

[117] R. I. A. Patterson. Properties of the solutions of delocalised coagulation and inception problems with outflow boundaries. *Journal of Evolution Equations*, 16(2):261–291, 2016. ISSN 1424-3199. doi:10.1007/s00028-015-0302-6.

[118] R. I. A. Patterson and M. Kraft. Models for the aggregate structure of soot particles. *Combustion and Flame*, 151(1-2):160–172, 2007. ISSN 00102180. doi:10.1016/j.combustflame.2007.04.012.

[119] R. I. A. Patterson and W. Wagner. A Stochastic Weighted Particle Method for Coagulation–Advection Problems. *SIAM Journal on Scientific Computing*, 34(3):B290–B311, 2012. ISSN 1064-8275. doi:10.1137/110843319.

[120] R. I. A. Patterson, J. Singh, M. Balthasar, M. Kraft, and J. R. Norris. The Linear Process Deferment Algorithm: A new technique for solving population balance equations. *SIAM Journal on Scientific Computing*, 28(1):303–320, 2006. ISSN 1064-8275. doi:10.1137/040618953.

[121] R. I. A. Patterson, W. Wagner, and M. Kraft. Stochastic weighted particle methods for population balance equations. *Journal of Computational Physics*, 230(19):7456–7472, 2011. ISSN 00219991. doi:10.1016/j.jcp.2011.06.011.

[122] S. E. Pratsinis. Flame aerosol synthesis of ceramic powders. *Progress in Energy and Combustion Science*, 24(3):197–219, 1998. ISSN 03601285. doi:10.1016/S0360-1285(97)00028-2.

[123] S. E. Pratsinis and P. T. Spicer. Competition between gas phase and surface oxidation of $TiCl_4$ during synthesis of TiO_2 particles. *Chemical Engineering Science*, 53(10): 1861–1868, 1998. ISSN 00092509. doi:10.1016/S0009-2509(98)00026-8.

[124] S. E. Pratsinis, H. Bai, P. Biswas, M. Frenklach, and S. V. R. Mastrangelo. Kinetics of Titanium(IV) Chloride Oxidation. *Journal of the American Ceramic Society*, 73(7): 2158–2162, 1990. ISSN 0002-7820. doi:10.1111/j.1151-2916.1990.tb05295.x.

[125] S. S. R. Putluru, L. Schill, A. D. Jensen, B. Siret, F. Tabaries, and R. Fehrmann. Mn/TiO_2 and Mn-Fe/TiO_2 catalysts synthesized by deposition precipitation—promising for selective catalytic reduction of NO with NH_3 at low temperatures. *Applied Catalysis B: Environmental*, 165:628–635, 2015. ISSN 09263373. doi:10.1016/j.apcatb.2014.10.060.

[126] V. Raman and R. O. Fox. Modeling of Fine-Particle Formation in Turbulent Flames. *Annual Review of Fluid Mechanics*, 48:159–190, 2016. ISSN 0066-4189. doi:10.1146/annurev-fluid-122414-034306.

[127] D. Ramkrishna. *Population balances: Theory and applications to particulate systems in engineering*. Academic Press, San Diego, 1 edition, 2000. ISBN 0125769709.

[128] A. D. Randolph and M. A. Larson. *Theory of particulate processes: analysis and techniques of continuous crystallization*. Academic Press, San Diego, 2 edition, 1988. ISBN 0125796528.

[129] S. Rigopoulos. PDF method for population balance in turbulent reactive flow. *Chemical Engineering Science*, 62(23):6865–6878, 2007. ISSN 00092509. doi:10.1016/j.ces.2007.05.039.

[130] S. Rigopoulos. Population balance modelling of polydispersed particles in reactive flows. *Progress in Energy and Combustion Science*, 36(4):412–443, 2010. ISSN 03601285. doi:10.1016/j.pecs.2009.12.001.

[131] A. Roussos, A. Alexopoulos, and C. Kiparissides. Part III: Dynamic evolution of the particle size distribution in batch and continuous particulate processes: A Galerkin on finite elements approach. *Chemical Engineering Science*, 60(24):6998–7010, 2005. ISSN 00092509. doi:10.1016/j.ces.2005.06.021.

[132] K. Sabelfeld, S. Rogasinsky, A. Kolodko, and A. Levykin. Stochastic algorithms for solving Smolouchovsky coagulation equation and applications to aerosol growth simulation. *Monte Carlo Methods and Applications*, 2(1):41–87, 1996. ISSN 0929-9629. doi:10.1515/mcma.1996.2.1.41.

[133] M. Sander, R. H. West, M. S. Celnik, and M. Kraft. A Detailed Model for the Sintering of Polydispersed Nanoparticle Agglomerates. *Aerosol Science and Technology*, 43(10): 978–989, 2009. ISSN 0278-6826. doi:10.1080/02786820903092416.

[134] M. Sander, R. I. A. Patterson, A. Braumann, A. Raj, and M. Kraft. Developing the PAH-PP soot particle model using process informatics and uncertainty propagation. *Proceedings of the Combustion Institute*, 33(1):675–683, 2011. ISSN 15407489. doi:10.1016/j.proci.2010.06.156.

[135] A. Schild, A. Gutsch, H. Mühlenweg, and S. E. Pratsinis. Simulation of nanoparticle production in premixed aerosol flow reactors by interfacing fluid mechanics and particle dynamics. *Journal of Nanoparticle Research*, 1(2):305–315, 1999. ISSN 13880764. doi:10.1023/A:1010025121980.

[136] H. J. Schmid, B. Al-Zaitone, C. Artelt, and W. Peukert. Evolution of the fractal dimension for simultaneous coagulation and sintering. *Chemical Engineering Science*, 61(1):293–305, 2006. ISSN 00092509. doi:10.1016/j.ces.2004.11.068.

[137] T. Seto, M. Shimada, and K. Okuyama. Evaluation of Sintering of Nanometer-Sized Titania Using Aerosol Method. *Aerosol Science and Technology*, 23(2):183–200, 1995. ISSN 0278-6826. doi:10.1080/02786829508965303.

[138] F. Sewerin and S. Rigopoulos. An LES-PBE-PDF approach for modeling particle formation in turbulent reacting flows. *Physics of Fluids*, 29(10):105105, 2017. ISSN 1070-6631. doi:10.1063/1.5001343.

[139] B. H. Shah, D. Ramkrishna, and J. D. Borwanker. Simulation of particulate systems using the concept of the interval of quiescence. *AIChE Journal*, 23(6):897–904, 1977. ISSN 0001-1541. doi:10.1002/aic.690230617.

[140] S. Shekar, W. J. Menz, A. J. Smith, M. Kraft, and W. Wagner. On a multivariate population balance model to describe the structure and composition of silica nanoparticles. *Computers & Chemical Engineering*, 43:130–147, 2012. ISSN 00981354. doi:10.1016/j.compchemeng.2012.04.010.

[141] S. Shekar, A. J. Smith, W. J. Menz, M. Sander, and M. Kraft. A multidimensional population balance model to describe the aerosol synthesis of silica nanoparticles. *Journal of Aerosol Science*, 44:83–98, 2012. ISSN 00218502. doi:10.1016/j.jaerosci.2011.09.004.

[142] R. Shirley, Y. Liu, T. S. Totton, R. H. West, and M. Kraft. First-Principles Thermochemistry for the Combustion of a $TiCl_4$ and $AlCl_3$ Mixture. *The Journal of Physical Chemistry A*, 113(49):13790–13796, 2009. ISSN 1089-5639. doi:10.1021/jp905244w.

[143] R. Shirley, J. Akroyd, L. A. Miller, O. R. Inderwildi, U. Riedel, and M. Kraft. Theoretical insights into the surface growth of rutile TiO_2. *Combustion and Flame*, 158(10):1868–1876, 2011. ISSN 00102180. doi:10.1016/j.combustflame.2011.06.007.

[144] R. Singh and V. Raman. Two-dimensional direct numerical simulation of nanoparticle precursor evolution in turbulent flames using detailed chemistry. *Chemical Engineering Journal*, 207-208:794–802, 2012. ISSN 13858947. doi:10.1016/j.cej.2012.07.064.

[145] A. J. Smith, C. G. Wells, and M. Kraft. A new iterative scheme for solving the discrete Smoluchowski equation. *Journal of Computational Physics*, 352:373–387, 2018. ISSN 00219991. doi:10.1016/j.jcp.2017.09.045.

[146] M. Smith and T. Matsoukas. Constant-number Monte Carlo simulation of population balances. *Chemical Engineering Science*, 53(9):1777–1786, 1998. ISSN 00092509. doi:10.1016/S0009-2509(98)00045-1.

[147] P. T. Spicer, O. Chaoul, S. Tsantilis, and S. E. Pratsinis. Titania formation by $TiCl_4$ gas phase oxidation, surface growth and coagulation. *Journal of Aerosol Science*, 33(1): 17–34, 2002. ISSN 00218502. doi:10.1016/S0021-8502(01)00069-6.

[148] V. Stadnichuk, A. Bodrova, and N. Brilliantov. Smoluchowski aggregation-fragmentation equations: Fast numerical method to find steady-state solutions. *International Journal of Modern Physics B*, 29(29):1550208, 2015. ISSN 0217-9792. doi:10.1142/S0217979215502082.

[149] G. Strang. On the Construction and Comparison of Difference Schemes. *SIAM Journal on Numerical Analysis*, 5(3):506–517, 1968. ISSN 0036-1429. doi:10.1137/0705041.

[150] Y. Sung, V. Raman, and R. O. Fox. Large-eddy-simulation-based multiscale modeling of TiO_2 nanoparticle synthesis in a turbulent flame reactor using detailed nucleation chemistry. *Chemical Engineering Science*, 66(19):4370–4381, 2011. ISSN 00092509. doi:10.1016/j.ces.2011.04.024.

[151] T. H. Tsang and A. Rao. Comparison of Different Numerical Schemes for Condensational Growth of Aerosols. *Aerosol Science and Technology*, 9(3):271–277, 1988. ISSN 0278-6826. doi:10.1080/02786828808959214.

[152] S. Tsantilis and S. E. Pratsinis. Evolution of primary and aggregate particle-size distributions by coagulation and sintering. *AIChE Journal*, 46(2):407–415, 2000. ISSN 00011541. doi:10.1002/aic.690460218.

[153] S. Tsantilis, S. E. Pratsinis, and H. Briesen. Sintering Time for Silica Particle Growth. *Aerosol Science and Technology*, 34(3):237–246, 2001. ISSN 15217388. doi:10.1080/02786820119149.

[154] S. Tsantilis, H. Kammler, and S. Pratsinis. Population balance modeling of flame synthesis of titania nanoparticles. *Chemical Engineering Science*, 57(12):2139–2156, 2002. ISSN 00092509. doi:10.1016/S0009-2509(02)00107-0.

[155] S. Vemury and S. E. Pratsinis. Dopants in Flame Synthesis of Titania. *Journal of the American Ceramic Society*, 78(11):2984–2992, 1995. ISSN 0002-7820. doi:10.1111/j.1151-2916.1995.tb09074.x.

[156] G. Wang and S. C. Garrick. Modeling and Simulation of Titania Synthesis in Two-dimensional Methane–air Flames. *Journal of Nanoparticle Research*, 7(6):621–632, 2005. ISSN 1388-0764. doi:10.1007/s11051-005-4966-7.

[157] H. Wang. Formation of nascent soot and other condensed-phase materials in flames. *Proceedings of the Combustion Institute*, 33(1):41–67, 2011. ISSN 15407489. doi:10.1016/j.proci.2010.09.009.

[158] J. Wei and F. Kruis. GPU-accelerated Monte Carlo simulation of particle coagulation based on the inverse method. *Journal of Computational Physics*, 249:67–79, 2013. ISSN 00219991. doi:10.1016/j.jcp.2013.04.030.

[159] C. G. Wells. A stochastic approximation scheme and convergence theorem for particle interactions with perfectly reflecting boundary conditions. *Monte Carlo Methods and Applications*, 12(3):291–342, 2006. ISSN 0929-9629. doi:10.1515/156939606778705182.

[160] R. H. West, G. J. O. Beran, W. H. Green, and M. Kraft. First-Principles Thermochemistry for the Production of TiO_2 from $TiCl_4$. *The Journal of Physical Chemistry A*, 111(18): 3560–3565, 2007. ISSN 1089-5639. doi:10.1021/jp0661950.

[161] R. H. West, M. S. Celnik, O. R. Inderwildi, M. Kraft, G. J. O. Beran, and W. H. Green. Toward a Comprehensive Model of the Synthesis of TiO_2 Particles from $TiCl_4$. *Industrial & Engineering Chemistry Research*, 46(19):6147–6156, 2007. ISSN 0888-5885. doi:10.1021/ie0706414.

[162] R. H. West, R. A. Shirley, M. Kraft, C. F. Goldsmith, and W. H. Green. A detailed kinetic model for combustion synthesis of titania from $TiCl_4$. *Combustion and Flame*, 156(9):1764–1770, 2009. ISSN 00102180. doi:10.1016/j.combustflame.2009.04.011.

[163] K. Woan, G. Pyrgiotakis, and W. Sigmund. Photocatalytic Carbon-Nanotube–TiO_2 Composites. *Advanced Materials*, 21(21):2233–2239, 2009. ISSN 09359648. doi:10.1002/adma.200802738.

[164] S. Wu, E. K. Yapp, J. Akroyd, S. Mosbach, R. Xu, W. Yang, and M. Kraft. A moment projection method for population balance dynamics with a shrinkage term. *Journal of Computational Physics*, 330:960–980, 2017. ISSN 00219991. doi:10.1016/j.jcp.2016.10.030.

[165] M. Wulkow, A. Gerstlauer, and U. Nieken. Modeling and simulation of crystallization processes using parsival. *Chemical Engineering Science*, 56(7):2575–2588, 2001. ISSN 00092509. doi:10.1016/S0009-2509(00)00432-2.

[166] Y. Xiong and S. E. Pratsinis. Gas phase production of particles in reactive turbulent flows. *Journal of Aerosol Science*, 22(5):637–655, 1991. ISSN 00218502. doi:10.1016/0021-8502(91)90017-C.

[167] Y. Xiong and S. E. Pratsinis. Formation of agglomerate particles by coagulation and sintering – Part I. A two-dimensional solution of the population balance equation. *Journal of Aerosol Science*, 24(3):283–300, 1993. ISSN 00218502. doi:10.1016/0021-8502(93)90003-R.

[168] Y. Xiong, M. Kamal Akhtar, and S. E. Pratsinis. Formation of agglomerate particles by coagulation and sintering—Part II. The evolution of the morphology of aerosol-made titania, silica and silica-doped titania powders. *Journal of Aerosol Science*, 24(3): 301–313, 1993. ISSN 00218502. doi:10.1016/0021-8502(93)90004-S.

[169] Z. Xu and H. Zhao. Simultaneous measurement of internal and external properties of nanoparticles in flame based on thermophoresis. *Combustion and Flame*, 162(5): 2200–2213, 2015. ISSN 00102180. doi:10.1016/j.combustflame.2015.01.018.

[170] Z. Xu, H. Zhao, and C. Zheng. Accelerating population balance-Monte Carlo simulation for coagulation dynamics from the Markov jump model, stochastic algorithm and GPU parallel computing. *Journal of Computational Physics*, 281:844–863, 2015. ISSN 00219991. doi:10.1016/j.jcp.2014.10.055.

[171] Z. Xu, H. Zhao, and H. Zhao. CFD-population balance Monte Carlo simulation and numerical optimization for flame synthesis of TiO_2 nanoparticles. *Proceedings of the Combustion Institute*, 36(1):1099–1108, 2017. ISSN 15407489. doi:10.1016/j.proci.2016.07.008.

[172] E. K. Yapp, D. Chen, J. Akroyd, S. Mosbach, M. Kraft, J. Camacho, and H. Wang. Numerical simulation and parametric sensitivity study of particle size distributions in a burner-stabilised stagnation flame. *Combustion and Flame*, 162(6):2569–2581, 2015. ISSN 00102180. doi:10.1016/j.combustflame.2015.03.006.

[173] E. K. Yapp, R. I. A. Patterson, J. Akroyd, S. Mosbach, E. M. Adkins, J. Houston Miller, and M. Kraft. Numerical simulation and parametric sensitivity study of optical band gap in a laminar co-flow ethylene diffusion flame. *Combustion and Flame*, 167:320–334, 2016. ISSN 00102180. doi:10.1016/j.combustflame.2016.01.033.

[174] H. Zhang and J. F. Banfield. Thermodynamic analysis of phase stability of nanocrystalline titania. *Journal of Materials Chemistry*, 8(9):2073–2076, 1998. ISSN 09599428. doi:10.1039/a802619j.

[175] H. Zhao, C. Zheng, and M. Xu. Multi-Monte Carlo method for particle coagulation: description and validation. *Applied Mathematics and Computation*, 167(2):1383–1399, 2005. ISSN 00963003. doi:10.1016/j.amc.2004.08.014.

[176] H. Zhao, F. E. Kruis, and C. Zheng. Reducing Statistical Noise and Extending the Size Spectrum by Applying Weighted Simulation Particles in Monte Carlo Simulation of Coagulation. *Aerosol Science and Technology*, 43(8):781–793, 2009. ISSN 0278-6826. doi:10.1080/02786820902939708.

[177] H. Zhao, F. E. Kruis, and C. Zheng. A differentially weighted Monte Carlo method for two-component coagulation. *Journal of Computational Physics*, 229(19):6931–6945, 2010. ISSN 00219991. doi:10.1016/j.jcp.2010.05.031.

[178] E. Zhou, Z.-F. Yuan, Z. Wang, X.-G. Fang, and J.-Z. Gong. Mechanism of scaling on oxidation reactor wall in TiO_2 synthesis by chloride process. *Transactions of Nonferrous Metals Society of China*, 16(2):426–431, 2006. ISSN 10036326. doi:10.1016/S1003-6326(06)60073-3.

[179] M. Zhou, H. Jiang, Y. Hu, Z. Lu, H. Jiang, and C. Li. Evaluation of mixing performance for the industrial-scale radial multiple jets-in-crossflow mixing structure. *Chemical Engineering and Processing - Process Intensification*, 141:107534, 2019. ISSN 02552701. doi:10.1016/j.cep.2019.107534.

Appendix A

Algorithms

A.1 Hybrid particle model

Algorithm 1: Operator-splitting algorithm using particle-number/particle model

```
Input: $\mathbf{C}(t_0)$, $T(t_0)$, $z_{\mathcal{X}}(t_0)$, $z_{\mathcal{M}}(t_0)$, $z_{\mathcal{X}}^{[\text{in}]}(t_0)$, $z_{\mathcal{M}}^{[\text{in}]}(t_0)$, $N_{\text{thresh}}$, $N_{\text{max}}$, $V_{\text{smp}}$[a], $t_0$, $t_f$.
Output: $\mathbf{C}(t_f)$, $T(t_f)$, $z_{\mathcal{X}}(t_f)$, $z_{\mathcal{M}}(t_f)$, $N(z_{\mathcal{M}}(t_f))$.
Set $t \leftarrow t_0$, $\mathbf{C} \leftarrow \mathbf{C}(t_0)$, $T \leftarrow T(t_0)$, $z_{\mathcal{X}} \leftarrow z_{\mathcal{X}}(t_0)$, $z_{\mathcal{M}} \leftarrow z_{\mathcal{M}}(t_0)$, $\Delta t = t_f - t_0$.
Solve gas phase ODEs (i.e. Eq. (3.2) or Eqs. (6.2)–(6.4)) for $\left[t, t+\frac{\Delta t}{2}\right]$: $\mathbf{C} \leftarrow \mathbf{C}\left(t+\frac{\Delta t}{2}\right)$, $T \leftarrow T\left(t+\frac{\Delta t}{2}\right)$.
while $t < t_f$ do
    Calculate overall rates of non-deferred inception and coagulation processes (Eqs. (3.36) and (3.38)):
        $$R_{\text{total}} = R_{\text{inception}} + R_{\text{coagulation}}.$$
    Calculate the maximum splitting time $t_{\text{split}}$ given $R_{\text{total}}$.
    Set $t_{\text{flow}} \leftarrow t$, $\Delta t_{\text{split}} \leftarrow t_{\text{split}} - t$.
    while $t < t_{split}$ do
        Alg. 2 is used to treat the inception and coagulation and increase the time.
        Alg. 3 is used to treat particle inflow and outflow over the time $\Delta t_{\text{flow}} \leftarrow (t - t_{\text{flow}})$.
        Set $t_{\text{flow}} \leftarrow t$.
    end
    for $i = 1, \ldots, N(t)$ do
        Do surface growth and sintering updates on $P_i$ over $\Delta t_{\text{split}}$ and update $\mathbf{C}$, $T$.
    end
    Update particle-number list $z_{\mathcal{M}}$ for surface growth over $\Delta t_{\text{split}}$ (Alg. 4).
end
Solve gas phase ODEs (i.e. Eq. (3.2) or Eqs. (6.2)–(6.4)) for $\left[t+\frac{\Delta t}{2}, t+\Delta t\right]$: $\mathbf{C} \leftarrow \mathbf{C}(t+\Delta t)$, $T \leftarrow T(t+\Delta t)$.
```

---

[a] Initially $V_{\text{smp}} = N_{\text{max}}/M_0^{\text{max}}$ where M_0^{max} is an estimate of the maximum number density.

Algorithm 2: Waiting time algorithm using particle-number/particle model

```
Input: $\mathbf{C}(t_0), T(t_0), z_{\mathcal{X}}(t_0), z_{\mathcal{M}}(t_0), N_{\mathrm{thresh}}, N_{\max}, V_{\mathrm{smp}}, t_0, t_{\mathrm{split}}$.
Output: $\mathbf{C}(t_f), T(t_f), z_{\mathcal{X}}(t_f), z_{\mathcal{M}}(t_f), t_f$.
Set $t \leftarrow t_0, \mathbf{C} \leftarrow \mathbf{C}(t_0), T \leftarrow T(t_0), z_{\mathcal{X}} \leftarrow z_{\mathcal{X}}(t_0), z_{\mathcal{M}} \leftarrow z_{\mathcal{M}}(t_0)$.
Calculate overall rates of non-deferred inception and coagulation processes (Eqs. (3.36) and (3.38)):
    $$R_{\mathrm{total}} = R_{\mathrm{inception}} + R_{\mathrm{coagulation}}.$$
Select a waiting time $\tau \sim \exp(R_{\mathrm{total}})$.
if $t + \tau < t_{split}$ then
    Choose process $\in$ {inception, coagulation} using:
        $$\mathbb{P}(\mathrm{process}) = R_{\mathrm{process}} \cdot {R_{\mathrm{total}}}^{-1}.$$
    if $process = inception$ then
        Update property sums for change in number of particles at index 1.
            $$N_1 \leftarrow (N_1 + 1); \qquad N(z_{\mathcal{M}}) \leftarrow (N(z_{\mathcal{M}}) + 1).$$
        Update gas phase $\mathbf{C}$, $T$.
    else if $process = coagulation$ then
        Pick $(P_i, P_j) \in (z_{\mathcal{X}} \cup z_{\mathcal{M}})$ (Alg. 5), update for surface growth and allow coagulation with probability
          (see Eqs. (3.22)–(3.25), (3.40) and (3.42)):
            $$\mathbb{P}(\mathrm{success}) = K_{\mathrm{tr}}(P_i, P_j) \cdot \hat{K}_{\mathrm{tr}}(P_i, P_j)^{-1}.$$
        if $Coagulation\ allowed$ then
            if $(P_k \in \mathcal{M}, k = \{i, j\})$ then
                Update property sums for change in number of particles at index $k$.
                    $$N_k \leftarrow (N_k - 1); \qquad N(z_{\mathcal{M}}) \leftarrow N(z_{\mathcal{M}}) - 1.$$
            end
            if $(P_i \in \mathcal{M}, P_j \in \mathcal{M})$ then
                if $N(z_{\mathcal{X}}) = N^{max}$ then
                    Uniformly choose a particle $P_j \in z_{\mathcal{X}}$ and set
                        $$z_{\mathcal{X}} \leftarrow z_{\mathcal{X}} \setminus P_j; \qquad V_{\mathrm{smp}} \leftarrow V_{\mathrm{smp}} \cdot \frac{N(z_{\mathcal{X}}) + N(z_{\mathcal{M}})}{N(z_{\mathcal{X}}) + N(z_{\mathcal{M}}) + 1}.$$
                end
                Add $P_i$ to the ensemble:
                    $$z_{\mathcal{X}} \leftarrow \{z_{\mathcal{X}}, P_i\}; \qquad N(z_{\mathcal{X}}) \leftarrow (N(z_{\mathcal{X}}) + 1).$$
            end
            Perform coagulation $P_i \leftarrow (P_i + P_j)$.
        end
    end
    Set $t \leftarrow (t + \tau)$.
else
    Set $t \leftarrow t_{\mathrm{split}}$.
end
```

Algorithm 3: Particle flow algorithm using particle-number/particle model

```
Input: $z_{\mathcal{X}}(t_0)$, $z_{\mathcal{M}}(t_0)$, $z_{\mathcal{X}}^{[\text{in}]}(t_0)$, $z_{\mathcal{M}}^{[\text{in}]}(t_0)$, $N_{\text{thresh}}$, $N_{\max}$, $\Delta t_{\text{flow}}$, $V_{\text{smp}}$, $V_{\text{smp}}^{\text{in}}$.
Output: $z_{\mathcal{X}}(t_f)$, $z_{\mathcal{M}}(t_f)$.
Set $z_{\mathcal{X}} \leftarrow z_{\mathcal{X}}(t_0)$, $z_{\mathcal{M}} \leftarrow z_{\mathcal{M}}(t_0)$, $z_{\mathcal{X}}^{[\text{in}]} \leftarrow z_{\mathcal{X}}^{[\text{in}]}(t_0)$, $z_{\mathcal{M}}^{[\text{in}]} \leftarrow z_{\mathcal{M}}^{[\text{in}]}(t_0)$, $F_{\text{smp}} = V_{\text{smp}}/V_{\text{smp}}^{\text{in}}$, $n_{\text{copies}} = \lfloor F_{\text{smp}} \rfloor$.
Select number, $n$, of particles for inflow:
    $$n \sim \text{Poi}\left(\Delta t_{\text{flow}} \cdot \tau^{-1} \cdot \left(N\left(z_{\mathcal{M}}^{[\text{in}]}\right) + N\left(z_{\mathcal{X}}^{[\text{in}]}\right)\right)\right).$$
while $n > 0$ do
    Uniformly select a particle $P_i$ (Alg. 5) and set $n \leftarrow (n-1)$.
    if $\lfloor F_{smp} \rfloor \neq F_{smp}$ then
        $\gamma \sim \text{BernoulliDistribution}\left(F_{\text{smp}}\right)$
        $n_{\text{copies}} \leftarrow n_{\text{copies}} + \gamma$
    end
    if $P_i \in \mathcal{M}$ then
        $$N_i \leftarrow \left(N_i + n_{\text{copies}}\right).$$
    else
        while $n_{copies} > 0$ do
            if $N(z_{\mathcal{X}}) = N^{max}$ then
                Uniformly choose a particle $P_j \in z_{\mathcal{X}}$ and set
                $$z_{\mathcal{X}} \leftarrow z_{\mathcal{X}} \setminus P_j; \qquad V_{\text{smp}} \leftarrow V_{\text{smp}} \cdot \frac{N(z_{\mathcal{X}}) + N(z_{\mathcal{M}})}{N(z_{\mathcal{X}}) + N(z_{\mathcal{M}}) + 1}.$$
            end
            Add $P_i$ to the ensemble:
            $$z_{\mathcal{X}} \leftarrow (z_{\mathcal{X}}, P_i); \qquad n_{\text{copies}} \leftarrow n_{\text{copies}} - 1.$$
        end
    end
end
Select number, $n$, of particles for outflow:
    $$n \sim \text{Poi}\left(\Delta t_{\text{flow}} \cdot \tau^{-1} \cdot (N(z_{\mathcal{M}}) + N(z_{\mathcal{X}}))\right).$$
while $n > 0$ do
    Uniformly select a particle $P_i$ (Alg. 5) and set $n \leftarrow (n-1)$.
    if $P_i \in \mathcal{M}$ then
        $$N_i \leftarrow (N_i - 1).$$
    else
        Remove $P_i$ from the ensemble:
        $$z_{\mathcal{X}} \leftarrow z_{\mathcal{X}} \setminus P_i.$$
    end
end
```

Algorithm 4: Update particle-number lists

```
Input: $\mathbf{C}(t_0)$, $T(t_0)$, $z_{\mathcal{X}}(t_0)$, $z_{\mathcal{M}}(t_0)$, $N_{\text{thresh}}$, $N_{\max}$, $V_{\text{smp}}$, $\Delta t_{\text{split}}$, template particle of size $N_{\text{thresh}}$: $P^{\text{tmp}}_{\text{thresh}}$.
Output: $\mathbf{C}(t_f)$, $T(t_f)$, $z_{\mathcal{M}}(t_f)$.
Set $n_{\text{add,total}} \leftarrow 0$.
Compute expected surface growth factor (see Eq. (3.18)):
    $$\tilde{\beta} \leftarrow \tilde{\beta}(\mathbf{C}, T)\,\Delta t_{\text{split}}.$$
for $index = N_{thresh}, \ldots, 1$ do
    if $N_{index} > 0$ then
        Choose number of units to add from:
            $$n_{\text{add,index}} \sim \text{Poi}\left(\tilde{\beta} A(P_{\text{index}})\right).$$
        Set newIndex $\leftarrow (\text{index} + n_{\text{add,index}})$.
        if $newIndex > index$ then
            Update $n_{\text{add,total}} \leftarrow (n_{\text{add,total}} + n_{\text{add,index}})$.
            if $newIndex \leq N_{thresh}$ then
                Update property sums for change in number at index, newIndex.
                Set $N_{\text{newIndex}} \leftarrow (N_{\text{newIndex}} + N_{\text{index}})$.
                Set $N_{\text{index}} \leftarrow 0$.
            else
                Update property sums for change in number at index.
                Update total particle number:
                    $$N(z_{\mathcal{M}}) \leftarrow (N(z_{\mathcal{M}}) - N_{\text{index}}).$$
                Set $N_{\text{index}} \leftarrow 0$.
                Copy template particle:
                    $$P_{\text{new}} \leftarrow P^{\text{tmp}}_{\text{thresh}}.$$
                Add $(\text{newIndex} - N_{\text{thresh}})$ monomers to $P_{\text{new}}$.
                for $j = 1, \ldots, N_{index}$ do
                    if $N(z_{\mathcal{X}}) = N^{max}$ then
                        Uniformly choose a particle $P_j \in z_{\mathcal{X}}$ and set
                            $$z_{\mathcal{X}} \leftarrow z_{\mathcal{X}} \setminus P_j; \qquad V_{\text{smp}} \leftarrow V_{\text{smp}} \cdot \frac{N(z_{\mathcal{X}}) + N(z_{\mathcal{M}})}{N(z_{\mathcal{X}}) + N(z_{\mathcal{M}}) + 1}.$$
                    end
                    Add $P_{\text{new}}$ to the ensemble:
                        $$z_{\mathcal{X}} \leftarrow \{z_{\mathcal{X}}, P_{\text{new}}\}.$$
                end
            end
        end
    end
end
Update gas phase $\mathbf{C}$, $T$ for $n_{\text{add,total}}$ surface growth events.
```

Algorithm 5: Particle selection algorithm using particle-number/particle model

```
Input: $z_{\mathcal{X}}(t)$, $z_{\mathcal{M}}(t)$, selection criterion ‘choose according to property $\xi$’.
Output: Selected particle $P_i$.
Define the sums of properties in each space (note these properties are cached):

    $\Sigma_{\mathcal{M}} \leftarrow \sum_{i=1}^{N_{\text{thresh}}} N_i \xi_i;$    $\Sigma_{\mathcal{X}} \leftarrow \sum_{i=1}^{N(t)} \xi(P_i);$    $\Sigma_{\text{total}} \leftarrow \Sigma_{\mathcal{M}} + \Sigma_{\mathcal{X}}.$

Choose a uniform random number: $\alpha \sim \mathrm{U}(0,1)$.
Set $\gamma \leftarrow \alpha \Sigma_{\text{total}}$.
if $\gamma \leq \Sigma_{\mathcal{M}}$ then
    /* Select index $i$ from particle-number list $z_{\mathcal{M}}$ */
    $j \leftarrow 1$.
    while $j \leq N_{thresh}$ do
        if $\gamma \leq (N_j \xi_j)$ then
            $i \leftarrow j$.
        else
            $\gamma \leftarrow (\gamma - N_j \xi_j)$.
            $j \leftarrow (j+1)$.
        end
    end
    Create the new particle $P_i$.[a]
else
    /* Select particle $P_i$ from particle ensemble $z_{\mathcal{X}}$ */
    $\gamma \leftarrow \alpha \Sigma_{\text{total}} - \Sigma_{\mathcal{M}}$.
    $j \leftarrow 1$.
    while $j \leq N(t)$ do
        if $\gamma \leq \xi(P_j)$ then
            $i \leftarrow j$.
        else
            $\gamma \leftarrow (\gamma - \xi(P_j))$.
            $j \leftarrow (j+1)$.
        end
    end
    Use the ensemble particle $P_i$.
end
```

---

[a] Clone the particle with index *i* from reference particle list

A.2 Operator-splitting with temperature updates

Algorithm 6: Simplified Strang operator-splitting scheme with heat release due to particulate processes added in the particle solver step (***emphasised in bold italics***).

```
Input: State $((\mathbf{C}_0, T_0, \Gamma_0), (z_{\mathcal{M},0}, z_{\mathcal{X},0}))$, sample volume $V_{\mathrm{smp},0}$, time $t_0$, final time $t_f$
Output: State $((\mathbf{C}_f, T_f, \Gamma_f), (z_{\mathcal{M},f}, z_{\mathcal{X},f}))$, sample volume $V_{\mathrm{smp},f}$
Set $t \leftarrow t_0$, $\Delta t \leftarrow (t_f - t_0)$, $(\mathbf{C}, T, \Gamma) \leftarrow (\mathbf{C}_0, T_0, \Gamma_0)$, $(z_{\mathcal{M}}, z_{\mathcal{X}}) \leftarrow (z_{\mathcal{M},0}, z_{\mathcal{X},0})$, $V_{\mathrm{smp}} \leftarrow V_{\mathrm{smp},0}$.
while $t < t_f$ do
    Solve gas phase chemistry (i.e. Eqs. (6.2)–(6.4)) for $[t, t + \frac{\Delta t}{2}] \rightarrow$ update $(\mathbf{C}, T, \Gamma)$.
    Set $t_{\mathrm{process}} \leftarrow t$.
    Scale sample volume for gas phase expansion $\Gamma$.
    Compute total process rate $R(z_{\mathcal{M}}, z_{\mathcal{X}})$.
    while $t_{process} < t + \Delta t$ do
        Choose update time $\tau \sim \exp(R)$.
        if $t_{process} + \tau < t + \Delta t$ then
            Choose and perform a particle process $\rightarrow$ update $(z_{\mathcal{M}}, z_{\mathcal{X}})$.
            Compute changes to gas phase (i.e. Eqs. (6.5)–(6.6)) $\rightarrow$ update $(\mathbf{C}, T, \Gamma)$.
            Scale sample volume for gas phase expansion $\Gamma$.
            Increment $t_{\mathrm{process}} \leftarrow t_{\mathrm{process}} + \tau$.
        end
    end
    Solve gas phase chemistry (i.e. Eqs. (6.2)–(6.4)) for $[t + \frac{\Delta t}{2}, t + \Delta t] \rightarrow (\mathbf{C}, T, \Gamma)$.
    Scale sample volume for gas phase expansion $\Gamma$.
    Increment $t \leftarrow t + \Delta t$.
end
```

Appendix B

Kernel density estimates

Kernel density estimates are used to fit smooth distributions for particle properties such as diameter (e.g. Fig. 4.4). Within the aerosol science community, it is common to scale the estimate to obtain a lognormal fit for the particle size distribution in terms of concentration, i.e. particles per cubic meter. The probability density function of the collision diameter, $f\left(d_{\mathrm{c}}\right)$, is estimated as the sum of lognormal distributions (for N stochastic particles in sample volume V_{smp}):

$$f\left(d_{\mathrm{c}},\sigma\right)=\frac{1}{N}\sum_{n=1}^{N}\frac{1}{d_{\mathrm{c}}\sigma\sqrt{2\pi}}\exp\left(-\frac{\left(\ln\left(d_{\mathrm{c}}\right)-\ln\left(d_{\mathrm{c}}^{(n)}\right)\right)^{2}}{2\sigma^{2}}\right). \tag{B.1}$$

Here, $d_{\mathrm{c}}^{(n)}$ is the collision diameter of the n^{th} particle and σ is the standard deviation of the distribution, a parameter which can be modified to control the degree of smoothing. The number density is given by:

$$g\left(d_{\mathrm{c}}\right)=\frac{dn}{d\left(d_{\mathrm{c}}\right)}=\frac{N}{V_{\mathrm{smp}}}f\left(d_{\mathrm{c}}\right) \tag{B.2}$$

and, from this:

$$\frac{dn}{d\ln\left(d_{\mathrm{c}}\right)}=d_{\mathrm{c}}\frac{dn}{d\left(d_{\mathrm{c}}\right)}=d_{\mathrm{c}}g\left(d_{\mathrm{c}}\right). \tag{B.3}$$

Appendix C

Conditions for alternative networks

Tables C.1 and C.2 provide conditions for reactor networks used to investigate the spatial frequency of dosing injections in Chapter 6. The injection and upstream fractions refer to relative contributions to the total volumetric feed to the reactor from the injection and previous reactor outflow streams.

Table C.1: Reactor volumetric feed fractions and residence times for 8-dosing-point study.

	Injection fraction	Upstream fraction	Residence time (ms)
CSTR (1)	0.26	0.74	1.9
CSTR (2)	0.21	0.79	1.5
CSTR (3)	0.15	0.85	8.6
CSTR (4)	0.13	0.87	7.5
CSTR (5)	0.15	0.85	8.6
CSTR (6)	0.13	0.87	7.5
CSTR (7)	0.13	0.87	8.6
CSTR (8)	0.12	0.88	7.5

Table C.2: Reactor volumetric feed fractions and residence times for 12-dosing-point study.

	Injection fraction	Upstream fraction	Residence time (ms)
CSTR (1)	0.19	0.81	1.4
CSTR (2)	0.16	0.84	1.2
CSTR (3)	0.14	0.86	1.0
CSTR (4)	0.10	0.90	6.0
CSTR (5)	0.09	0.91	5.5
CSTR (6)	0.08	0.92	5.0
CSTR (7)	0.11	0.89	6.1
CSTR (8)	0.10	0.90	5.5
CSTR (9)	0.09	0.91	5.0
CSTR (10)	0.09	0.91	5.9
CSTR (11)	0.08	0.92	5.4
CSTR (12)	0.08	0.92	5.0